UNIVERSITA' DEGLI STUDI DI PARMA

Dottorato di ricerca in Scienza e Tecnologia dei Materiali Innovativi

Ciclo XXVII (2012-2014)

Tailoring surfaces and interface properties by kinetically activated processes controlled by Supersonic Beam Deposition

Coordinatore:
Chiar.mo Prof. Enrico Dalcanale

Tutor:
Dott. Salvatore Iannotta

Tutor:
Dott. Roberto Verucchi

Dottorando: Roberta Tatti

2015

Index

Chapter 1

Introduction

1.1 Surface and interfaces

Materials science is one of the fast developing fields with high impact, in particular from the point of view of functional materials. It is multidisciplinary in its own nature, involving skills coming from physics, chemistry, biology, engineering, but it requires approaches spanning from theoretical to basic research, up to technology with realization of devices and prototypes. For these reasons there are several typical "common topics" like materials synthesis, characterization, theoretical modelling as well as their physical/chemical, electronic, optical, structural, morphological properties. At the same time, comprehension of the aforementioned material features leads to its application in sensing, electronics, optoelectronics and thus realization of the relative devices.

Considering most of these applicative fields, widely diffused is the use of materials in form of thin films, where "thin" refers to micro- and nano-metric thicknesses, and of nanostructures, mono-, bi- but also three-dimensional. The role of "surfaces" in determining the final properties of materials is crucial not only because we are dealing with very high surface-to-volume ratio, but because most of processes at the basis of applicative devices occur in the upper most atomic layers, involving the creation and evolution of interfaces with other species and, most of the times, they are "intrinsically" at the nanoscale.

The comprehension of these processes thus requires investigations tools that are able to acquire information right at the nanoscale, in particular from the surfaces and interfaces of

materials involved. To this end, techniques that are able to extract signals only from the topmost layers are advisable, such as Atomic Force Microscopy and Transmission Electron Microscopy, able to study surfaces morphology and structure down to the nanoscale, while electronic properties are better addressed using, for example, surface electron spectroscopies like X-ray ad UV induced electron photoemission. However, also techniques like Raman or X-ray diffraction even if they are not intrinsically "nanometric", when used in specific experimental conditions, can enhance surface contribution and can give important information on materials having nanometric dimensions.

The chemical species typically involved are inorganic, organic and hybrid organic/inorganic species. Great efforts are devoted to inducing the synthesis of new materials, aiming at controlling functional and multifunctional properties possibly by design. In particular our interest is on the ability to improve the functionality of materials and surfaces by functionalization, achieving new physical/chemical properties as well as new chemical species, able to possibly conjugate characteristics of both parent materials but mainly adding new "abilities" and functionalities.

That is probably the highest challenge of material science, the multifunctionality.

Though the panorama is so wide that any kind of specific example would lead to understatements, some relevant cases may be cited and will be addressed in this Thesis work. The growth of organic and inorganic materials in form of thin films showing better and wider properties thanks to activation of specific electronic, structural, morphological properties has attracted great attention for applications in electronics and optoelectronics. At present, among inorganics, one of the most promising material is considered by far graphene, and promising means that its amazing properties are often view as a sort of panacea in a number of scientific fields and applications. On the other end, the inorganic surface functionalization by organic single molecules or polymers is one of the most challenging approaches to prepare biocompatible materials, paving the way for very promising biomedical applications for biosensing, lab-on-a-chip devices and towards theragnostics.

In this Thesis we will address the aforementioned scientific issues, developing concepts being topics in materials science community by using original approaches, focusing our attention on the control and activation of processes that are able to drive thin film growth

and synthesis towards the creation of multifunctional chemical species and hybrid materials.

1.2 The supersonic seeded beam approach

Materials synthesis, in particular thin films growth, can be achieved with different techniques, able to work in air, controlled atmosphere, vacuum and starting from precursors in solid, liquid or gaseous state. Concerning inorganics, the strong requests coming from electronics led to the development of several techniques, mainly in vacuum, having in common the growth of materials in different forms but with high purity, high control on structure and morphology, tuning of electronic properties, dimensional scalability from the micro- to the nano-scale. Chemical Vapour Deposition, Molecular Beam Epitaxy, Atomic Layer Deposition are probably the most known techniques working in vacuum environment, and have shown to be suitable for growth and synthesis of both inorganics and organics in form of thin films and nanostructures like quantum dots, nanowires.

Recently, it has been developed and proposed a different approach based on the use of supersonic molecular beams seeded by organic precursors, molecules. Its main difference with respect to aforementioned techniques in vacuum is the possibility to control the kinetics properties of the particles and aggregates in the beam, among all the kinetic and internal energies. While the latter is reduced to equivalent temperatures of few kelvins, the former can reach values as high as tens of eV. In this way, it is possible to achieve materials synthesis in conditions that are far from thermodynamic equilibrium, as happens for Molecular Beam Epitaxy where kinetic and internal energies are typically tenths of eV and hundreds of kelvins, inducing and activating chemical/physical processes at interfaces otherwise forbidden or unlikely.

The so called Supersonic Molecular Beam Deposition (SuMBD) has shown to be a viable approach for the growth of highly ordered organic thin films, synthesis of inorganic materials, functionalization of surfaces in conditions where other techniques are not able to achieve reliable results. Different relevant examples have been proposed in the last years by the group of IMEM-CNR in Trento, the National Research Council Institute for

Materials for Electronics and Magnetism, where the SuMBD approach has been proposed, developed and applied to several topics. Several high level publications testify the suitability, feasibility and efficiency of SuMBD for materials science as well as setting the basis for new promising and challenging scientific problems.

1.3 Thesis structure

The potentialities of the SuMBD technique are so promising that some high level scientific problems have been recently addressed, but others not studied in details nor understood, some others have been only foreseen. The aim of this Thesis is to study these potentialities by understanding how it is possible to control surfaces and interfaces properties during the film growth and/or synthesis, by kinetically activated processes. Three different test cases will be addressed, investigating the SuMBD ability to control electronic properties in inorganic thin films, induce synthesis of nanostructured carbon-based materials, functionalize inorganic surfaces. Studies will be performed by using mainly surface electron spectroscopies in in-situ experiments at the IMEM-CNR labs in Trento.

The Thesis will initially present a comprehensive panorama of the physics ruling the SuMBD approach, putting attention on generation and properties of supersonic molecular beams and showing most relevant examples of materials synthesis and growth, which fundamental mechanisms will be described as well (Chapter 2). The experimental apparatus used for thin film deposition and in-situ analysis will be described in details, drawing attention to the complex data analysis procedure as well as to some ex-situ used characterization techniques (Chapter 3). The following of the Thesis will be divided in three parts, each of them presenting one of the mentioned test case, with a brief general description of the scientific problem introducing the specific experimental work and a final results summary. Chapter 4 will be devoted to the analysis of electronic properties of thin film of perylene on SiO_2 surface, a π-conjugated organic molecule used for the realization of n-type semiconductors in Organic Field Effect Transistors. The ability of SuMBD to improve the organic film electronic properties will be analyzed and correlated to the OFET electronics, putting in evidence the presence of specific chemical/physical process at the interface. The synthesis of carbon-based nanostructures, namely graphene single layer

films, will be studied in Chapter 5. This is a totally original approach to the field, based on previous studies of energetic impacts of supersonic fullerene on clean and reconstructed silicon. By using supersonic beams seeded by fullerene, the ability to induce the cage rupture on different copper surfaces (polycrystalline and single crystal) by means of the high precursor kinetic energy and of the substrate temperature will be investigated. Chapter 6 will be devoted to study the functionalization of silicon oxide based surfaces by means of partially fluorinated tetraphenylporphyrin with SuMBD approach. Having as a reference the functionalization of SiC/SiO_2 core/shell nanowires to be used for biomedical applications (i.e. as a photosensitizers for a Photodynamic Therapy induced by X-ray), the complex physical/chemical processes leading to the observed organic on inorganic anchoring will be studied also considering the same process on a similar but far simpler surface, that of native silicon oxide on silicon. Final conclusions and perspectives will be presented in the last Chapter 7.

Chapter 2
Supersonic Molecular Beams and thin films growth

2.1 Introduction

The advantage to use the supersonic beams in gas-surface dynamics is based on the possibility to work with molecules and aggregates in non-thermal equilibrium, controlling their kinetics parameter and properties. In fact, molecular scattering studies [1] have evidenced that kinetic properties of the molecular precursors are crucial parameters to study some physical and chemical processes at surfaces. For a proper understanding of the supersonic molecular beams generation and their applications, two books by G. Scoles [2] and P. Milani and S. Iannotta [3] can be considered as main references. This chapter is an introduction about the supersonic molecular beams technique and their employment in thin film growth. Nonetheless, basic principles of epitaxial growth will be examined, as well as gas-surface dynamics studies and a brief review on some of the most used growth methods in surface science, to better emphasize differences with respect to the approach with supersonic beams. More detailed information of film growth of specific organic molecules will be given in the following chapters.

2.2 Supersonic Molecular Beams: fundamentals

The earlier studies about the potentiality of supersonic beams in molecular and surface physics were carried out by Stern and Gerlach [4] in the 30's: for the first time they investigated a number of physical phenomena, ranging from the measurement of electric and magnetic moments of atoms and molecules by beam deflection in applied fields, to measurements of intermolecular forces in scattering experiments. In 1951, Kantrowitz and Grey [5] developed a design of an asymmetric converging-diverging nozzle, together with a cone shaped skimmer, in order to obtain a well defined molecular beam and to solve the so called problem of the "scattering cloud". The resulting molecular beam in fact showed intensities that could be considerably higher than those reached by conventional effusive sources. As a matter of fact, these studies can be considered as the foundations for the development of supersonic molecular beams. However, the basic vacuum requirement has long limited the use of supersonic beams, preventing the demonstration of the effectiveness of this method.

Becker and Bier [6] in 1956 were able to confirm the predictions of Kantrowitz, developing a system with a pumping speed high enough to produce and maintain a reliable supersonic beam. In a following work, Becker and co-workers [7] found the narrowed distribution of the velocity distribution of argon beam predicted in the previous paper. It was not possible to make a direct comparison between theoretical assumptions and experimental results, since at that time the skimmer interference on supersonic beam properties not was fully understood. These studies, which demonstrated the high intensity and narrow velocity spread of a supersonic beam, were the starting point in the development of supersonic beams knowledge. In fact Hagena in 1970 [8] showed the relaxation of internal degrees of freedom of carbon dioxide in a supersonic free jet, followed by Anderson [9] who studied the process of "running out of collisions" in the supersonic expansion.

To better understand which are the physical processes leading to supersonic molecular beams it is possible to start from the "classic" effusive source: the Knudsen cell. It is essentially an oven in a vacuum chamber, opened to the external environment through a small orifice (nozzle) where the desired material can be heated (see Figure 2.1). The evaporating material, characterized by a temperature T_0, is in thermal equilibrium with its vapors at a pressure P_0 ($P_0 \sim 10^{-3}$-10^{-1}torr, $T_0 \sim 10^2$-10^3K). The nozzle aperture is smaller than

the mean free path (λ) of the particles (usually some cm) so the outgoing flux is molecular and can be fully described by the classical gas kinetic theory as an effusive flux. Its internal degrees of freedom (the roto-vibrational energies) are typical of a gas in thermal equilibrium at the specific temperature, with a cosinusoidal spatial distribution of the particles and a Maxwellian energy distribution, centered at the energy corresponding to the temperature of the evaporated species T_0.

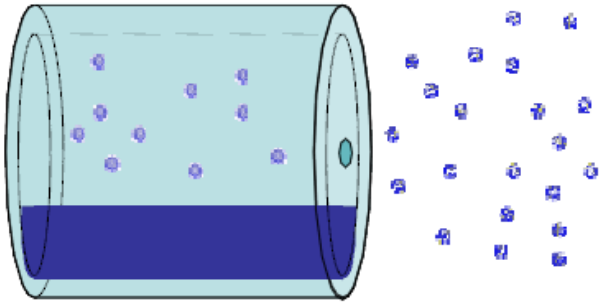

Figure 2.1: Schematic view of an effusive Knudsen cell.

From an experimental point of view, the oven is warmed up through an external heating element and thermally stabilized by a temperature sensor (usually a thermocouple), and a feedback system acting on the power supplier. In the following are reported some basic expressions to describe the characteristics of an effusive beam and necessary to introduce those of a supersonic one. The mean free path (λ), the intensity N, the average molecular velocity ($\bar{v}$) and the normal velocity distribution ($f(v)dv$) of the particles in the beam are given by the following relationship:

$$\lambda_{[cm]} = \frac{7.321 \times 10^{-20} T_0}{P_0 \sigma}$$

(σ is the collision cross-section in cm^2)

$$dN = \frac{d\omega}{4\pi} n_0 \bar{v} A \cos\theta$$

where n_0 is the number density in the source, in atoms/cm^3, A the orifice area and dω the solid angle;

$$\bar{v} = 1.4551 \times 10^4 \sqrt{\frac{T_0}{M}}$$

(in $cm \times s^{-1}$, M is the mass in atomic units)

$$f(v)dv = \frac{4}{\sqrt{\pi}} v^2 e^{-v^2} dv$$

In the classical effusive molecular regime, the particles leave the oven though the nozzle without encountering collisions with other particles, and the Knudsen number is $K=\lambda/d>1$ (d is the nozzle diameter). A supersonic beam is obtained by increasing the pressure P_0 so that the Knudsen number $K=l/d\ll1$, regime in which the particles will undergo a large number of collisions, giving rise to the free jet expansion driven by the pressure gradient between the source and the external vacuum. To maintain the pressure gradient also in presence of high gas loads, an adequate pumping speed is needed, much larger that for the typical classical molecular regime due to five order of magnitude larger P_0. From an experimental point of view, a supersonic beam source consists essentially of a closed heated cylinder, with a micrometric nozzle, inside of which is injected a high pressure gas. To give a description of the generation of a supersonic beam, the expansion process (and subsequent beam's extraction) for a short converging nozzle will be taken into account. We will see, in the following, how the nozzle's shape affects the beam formation.

Figure 2.2 shows a general scheme of the free jet expansion in steady-state conditions, assuming an isentropic expansion with negligible heat conduction and viscous effects. Within the oven, the physical parameters, P_0 and T_0, are representative of a chemical-physical state of the source, the so called *stagnation state*. It is a thermalized condition where the gas particles have a statistical thermal velocity distribution that depends on P_0 and T_0, but showing a quasi-static drift towards the nozzle. Because of the much lower outer pressure P_{out}, as they flow towards the throat, particles accelerate increasing their speed up to the sonic speed corresponding to a Mach number M=1, i.e. the ratio between the velocity of gas particles and the local velocity of sound propagation, M=v/vs.

The onset of the supersonic expansion depends on the pressure difference between the source and the outside, provided the latter is kept low enough to provide the expansion itself.

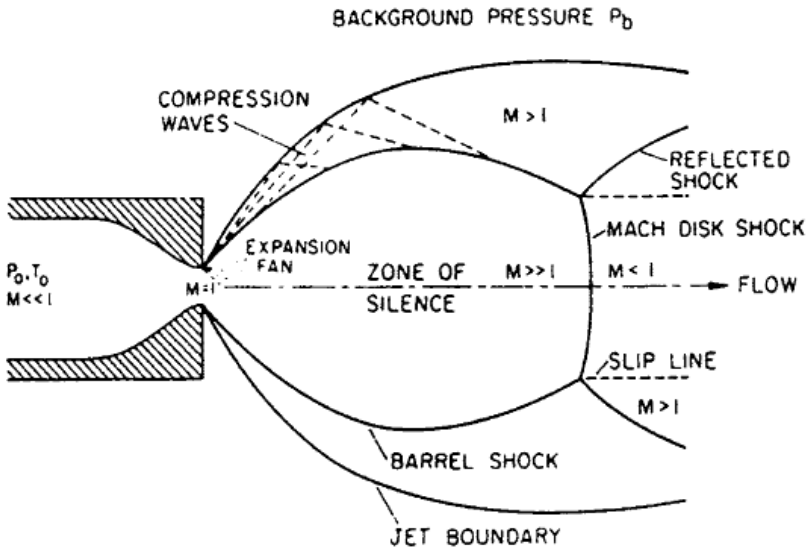

Figure 2.2: Diagram of the free jet expansion describing schematically the different region.

The critical P_{out} value can be calculated by the following expression:

$$\frac{P_0}{P_{out}} = \left(\frac{\gamma+1}{2}\right)^{\gamma/(\gamma-1)}$$

where $\gamma = c_p / c_v$ is the ratio between the specific heats at constant pressure and volume.

At the stationary state, the gas flow outside of the source will be characterized and confined by a matching between the expansion zone and the vacuum environment. The pressure just outside the nozzle is about $P_0/2$ (typical of an *underexpanded* flow), reaching M=1 at the nozzle exit and M>1 in the portion of beam just outside the nozzle. This region is the so called *sonic region*, while the following larger region is the *core of the expansion*, called the *zone of silence* just because the beam does not "feel" the presence of the external environment (Figure 2.2). The border of the supersonic beam's portion (*Mach disk*), in the forward direction, is outlined by shock waves outside of which the supersonic properties are strongly depleted and lost. Differently, on the side portions the flow loses the isoentropic, not viscous behavior with M>1 by means of compression waves. The distance between the Mach disk and the nozzle (x_M or δ_M) can be estimated in terms of nozzle diameter d, using an empirical, experimentally tested rule:

$$\delta_M = \frac{x_M}{d} = 0.67\left(\sqrt{\frac{P_0}{P_{out}}}\right)$$

In the zone of silence the particles are extracted by an interfering conical collimator (*skimmer*), in order to obtain a well defined supersonic molecular beam. To reduce as low as possible the interference of the skimmer in the zone of silence, a specific geometrical shape is necessary, i.e. a sharp edge skimmer with a hyperbolic profile. Moreover, the skimmer can grant decoupling of the vacuum pumping independence between the chamber where the beam is generated and the chamber where the beam itself will be used.

2.3 Supersonic Beam's properties

The thermodynamic approach to the beam properties can be simplified by assuming an isentropic flow, without any heat conduction effect (the unperturbed zone of silence satisfies these assumptions). The energy equation for such a flow can be written as

$$h_0 = h + \frac{v^2}{2} \tag{1}$$

where h_0 is the enthalpy per unit mass and is considered constant along any streamline. This relationship does not take into account the internal energy, that it's not relevant since the driving force for the particles acceleration is the pressure gradient. It shows that when the enthalpy decreases, because of expansion process, the mean velocity of the particles must increase. Taking into account that $dh = C_p dt$, for an ideal gas equation (1) gives:

$$v^2 = 2(h_0 - h) = 2\int_T^{T_0} C_p dt \tag{2}$$

Under the assumption that C_p is constant over the range of interest ($T_0 \rightarrow T$):

$$v = \sqrt{2C_p(T_0 - T)} \tag{3}$$

From which it is possible to calculate the limiting velocity:

$$v_\infty = \sqrt{\frac{2k}{m}}\left(\frac{\gamma}{\gamma-1}\right)T_0 \tag{4}$$

where the subscript ∞ means that we are considering the terminal or maximum beam's velocity, that is at the end of the free jet expansion. v_∞ can be obtained considering a large cooling, that is $T \ll T_0$, and using the relationship $C_p = k_B/m(\gamma/\gamma-1)$, that is the case of an ideal gas (k_B is the Boltzmann constant).

The supersonic expansion is characterized by its temperature, pressure and density. They can be written as a function of the Mach number M, defined as

$$M = \frac{v}{v_s} \tag{5}$$

where v is the speed of the particles in the beam and

$$v_s = \sqrt{\gamma KT/m} \tag{6}$$

is the speed of sound.

Taking in account these parameters, we obtain:

$$\frac{T}{T_0} = \left(1 + \frac{\gamma-1}{2} M^2\right)^{-1} \tag{7}$$

$$\frac{P}{P_0} = \left(\frac{T}{T_0}\right)^{\gamma/(\gamma-1)} = \left(1 + \frac{\gamma-1}{2} M^2\right)^{-\gamma/(\gamma-1)} \tag{8}$$

$$\frac{\rho}{\rho_0} = \frac{n}{n_0} = \left(\frac{T}{T_0}\right)^{1/(\gamma-1)} = \left(1 + \frac{\gamma-1}{2} M^2\right)^{-1/(\gamma-1)} \tag{9}$$

Therefore, once the value of M along the beam axis is known, equations (6), (7), (8) give a complete thermodynamic description of the beam. The exact solution of these equations is not simple for the supersonic region of the beam, due to the dependence of M versus the distance from the nozzle along the beam axis. However, by using a numerical method like the so-called Methods of Characteristic (MOC), the analytical expressions can be derived through a fitting procedure on the calculated values. The detailed description of this method [2] goes beyond the aim of the present thesis; however, its main result gives the following relationship:

$$M = A\left[\frac{x-x_0}{d}\right]^{\gamma-1} - \frac{\frac{1}{2}\left[\frac{\gamma+1}{\gamma-1}\right]}{A\left[\frac{x-x_0}{d}\right]^{(\gamma-1)}} \quad (10)$$

where A is the nozzle cross section.

The typical behavior of the thermodynamic variables, as a function of the distance and in terms of number of nozzle diameters, is shown in Figure 2.3, for the case of a gas with γ=5/3 and in regime of isentropic flow, ideal gas behavior, C_P constant, continuum flow. All the variables, except the terminal velocity v_∞, show a continuum decrease from their initial values. v_∞, on the other side, rapidly increases its initial value till it reaches the 98% of the asymptotic limit in a few nozzle diameters (x/d, see Figure 2.3).

The collision frequency decreases rapidly, so that the continuum flow regime cannot be maintained and there is the transition to free molecular flow (see Figure 2.3): this happens beyond reaching 98% of v_∞, so that the molecular velocity is not significantly affected by this transition. Its spread, on the other side, depends on T which is affected by this transition: this is at the origin of a change in the beam energy distribution that results proportional to the ratio T/v^2.

In the sonic and subsonic part of the beam, thermodynamics provides an approximation to calculate the beam's properties: the flow, in fact, can be treated as a quasi one-dimensional compressive flow, with M constant across any nozzle cross section. Using this approximation, we can calculate the mass flow rate $\dot{m}$ related to M, in particular regarding the nozzle's shape. For converging nozzles, in fact, the sonic and subsonic regions are characterized by viscous effects that generate boundary layers, but in the regime of fast flow rates and sonic nozzles (see section 2.4) the quasi one-dimensional approximation can be used. Therefore we have:

$$\dot{m} = \rho v A = P_0 A^* \left(\frac{m}{kT_0}\gamma\left[\frac{2}{\gamma+1}\right]^{\frac{\gamma+1}{\gamma-1}}\right)^{1/2} \quad (11)$$

where A^* is the nozzle cross section at the throat, thus at the minimum diameter.

Each other cross section area can be calculated by the following relation:

$$\frac{A}{A^*} = \frac{1}{M}\left[\frac{2}{\gamma+1}\left(1+\frac{\gamma-1}{2}M^2\right)\right]^{(\gamma+1)/2(\gamma-1)} \quad (12)$$

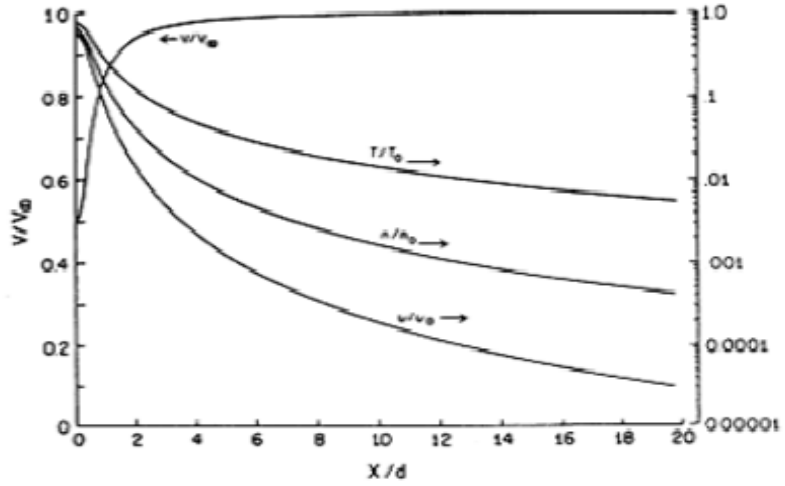

Figure 2.3: Evolution of velocity V, temperature T, density n and ν (collision rate for binary hard spheres) normalized to the corresponding values in the stagnation conditions (T_0 and n_0) and to the limit velocity (V_∞), plotted against the parameter x/d.

The intensity of a supersonic beam, in terms of molecules per radiant per second, can be evaluated to be

$I_0 = \kappa N/\pi$, where the molecule flow rate N at the nozzle is

$$N = n_0 F(\gamma) \left(\frac{\pi d^2}{4}\right) \sqrt{\frac{2kT_0}{m}} \tag{13}$$

and

$$F(\gamma) = \left(\frac{\gamma}{\gamma+1}\right)^{1/2} \left(\frac{2}{\gamma+1}\right)^{1/(\gamma-1)} \tag{14}$$

The parameter κ is the *peaking factor*, and its values can range from 1 to 2 as a function of γ (1 is referred to the ideal effusive source). The forward intensity of a supersonic beam is much higher than for a classical Knudsen source, mainly due to the higher values of *N* and of the peaking factor (κ >1).

Up to now, we have discussed the beam properties when the flow is in the continuum region, approximating it to an ideal gas, but it is necessary to take into account the non-equilibrium processes in a supersonic expansion, leading to fundamental kinetics effects.

Molecular collisions provide an efficient mechanism of cooling the internal energy states: after the expansion, the collision rates fall down rapidly and the internal states "freeze", so that the particles molecular flow extracted by the skimmer in this zone will remain in a "frozen" configuration. Assuming that the typical number of collision in free-jet expansion is $\approx 10^3$, it is clear that vibrational and rotational modes of large polyatomic molecule can be efficiently cooled down, considering that a molecule needs only about $10\text{-}10^2$ collision to relax. Energy is exchanged during the expansion and the molecule enters the collision-less flow zone in a "cooled" internal state.

The cooling of rotational (mainly) and vibrational modes can be particularly important for those molecules that have strong structural anisotropies. From the point of view of thin film growth of these kinds of molecules, as the Trento IMEM-CNR group has shown, the initial energy state of the molecular precursors can play an important role in the growth of thin film in terms of structural order and morphology [10-15]. In particular, the roto-vibrational cooling and the collisions in the free jet expansion could lead to the alignment of the backbone of strongly anisotropic molecules along the propagation axis of the beam [11]. As shown for oligothiophene molecules, the preferential orientation plays an important role in the growth processes that deserves more detailed studies [12], while for pentacene thin films [13-15] the kinetics have been proved to be a discriminating factor in achieving highly ordered structures, also over a large range of film thicknesses. In other words, the different film morphologies and characteristics can be controlled by the beam's parameters, including the precursor kinetics in terms of collision rates, particles' velocity and kinetic energy, momentum and internal energy.

Coming back to the properties of supersonic beams, other prediction can be made about the distribution of the final velocity. Its evaluation can be performed with sufficient accuracy in the continuum region, while in the non-continuum regime the solution of the Boltzmann equation have to be carried out via a model. The resulting distribution has a Gaussian profile function of the mean velocity and of its components in the two directions, perpendicular and parallel to the beam propagation axis.

$$f(v) = n\sqrt{\frac{m}{2\pi k T_{II}}}\left(\frac{m}{2\pi k T_{\perp}}\right) exp\left(-\frac{m}{2kT_{II}}(v_{II} - V)^2\right) - \frac{m}{2kT_{\perp}}v_{\perp}^2 \qquad (15)$$

It is useful to introduce another parameter to characterize the beam energy dispersion: the speed ratio S, defined as the ratio between the mean velocity V and the velocity thermal spread

$$S = \frac{V}{\sqrt{\frac{2kT}{m}}} = M\sqrt{\frac{\gamma}{2}} \tag{16}$$

High S values correspond to highly-monochromatic beams, a goal that can be achieved by means of a high degree of cooling in the supersonic beam. In a pure helium beam source, for example, the gas pressure can be increased to very high values without producing any condensation, the heat of which would deplete the supersonic expansion. The very high degree of cooling that can be obtained gives rise to values for S as high as 150 and the velocity spread $\Delta V/V<1\%$. As a matter of fact, a He supersonic beam is an ideal source to carry out scattering experiments on surfaces and atomic diffraction [16].

2.3.1 Supersonic expansion of a gas mixture

Let we consider the interesting case of the expansion of a gas mixture, particularly relevant for thin film deposition. *Seeded beams* are supersonic beams in which the main carrier gas is "seeded" by a small amount of an evaporating species, so that highly diluted beams are obtained. As far as gas mixtures are concerned, we have to consider that the heat capacity must take into account the weighted contribution of the different species constituting the flow; thus we have

$$\overline{C_p} = \sum_i X_i C_{pi} = \sum_i X_i \, k_B(\gamma/(\gamma-1))$$

where X_i is the molar fraction of the i-component. The average kinetic energy (KE) of the particles in the beam depends on $\overline{C_p}$ and T_0: each species will be characterized by an energy above or below the average, in dependence of their mass with respect to the weighted averaged beam's mass. More in detail, there is an inverse relationship between the molar or average molecular weight of the mixture and the mean velocity, thus the i-component, which is one of the "seeding" species in the beam, can increase or decrease its velocity if it is the heavier or lighter gas in the mixture. This process is usually denoted as

aerodynamical acceleration and the energy of the individual species (assuming $\overline{C_p}$ and T_0 constant over the range of expansion temperatures) can be roughly written as:

$$E_i \approx \left(\frac{m_i}{\bar{m}}\right) T_0 \tag{17}$$

here $\bar{m} = \sum_i X_i\, m_i$.

The dilution process is briefly called "seeding", while the difference in velocity between the carrier gas and the seeded gas is called *velocity slip*. Just to quantify the effect of the dilution, let's consider the case of a binary mixture (which is the case of the supersonic beams used in this work), in which the seeding particles are less than 1% of the mixture, while more than 99% is the carrier gas. Helium can be taken as the example of the light carrier gas while, as seeding particles we can consider a polyatomic molecule of large mass, about 700 amu for instance (i.e. the TetraPhenylPorphyrin H_2TPP): applying the relationship (17) the KE of beam particles increases up to about one hundred times (at a given temperature) with respect to the energies in classical molecular beams. This means, for examples, that the H_2TPP seeding particles in an Helium carrier gas can reach kinetic energies as high as some tens of eV. In this thesis it has been used also Hydrogen as gas carrier, lighter than Helium, for fullerene deposition on metals (see Chapter 5) in order to increase the KE of the beam up to 35eV. The H_2 flux was produced by a hydrogen generator as described in the Chapter 3.

In the case of cluster species, their KE depends on the ratio between clusters' mass, M_c, and carrier gas's mass, M_g, so that:

$$E_{kin} = \left(\frac{\gamma R T_0}{\gamma - 1}\right)\frac{M_c}{M_a}\ ,$$

where M_a is the average molecular weight. It is clear that the highest KE is achieved by employing hydrogen as a major component of the mixture (carrier gas), which gives rise to the higher $\gamma/(\gamma - 1)$.

Another important feature of highly diluted beams is the effect of confining of heavier and lighter species in different part of the molecular beam, after the skimmer selection. If we assume that the composition of the beam impinging on the skimmer is approximately the same of the gas mixture coming out from the nozzle, after the skimmer selection the heavier species will be concentrated on the centerline of the supersonic molecular beam flux, while the density of the lighter species increases at the border. Taking into account

that the perpendicular component of velocity, after the skimmer selection, depends on the factor S and can be written as:

$$S_{\perp} = \frac{V}{\sqrt{\frac{2kT_{\perp}}{m}}} \tag{18}$$

for given V and $T_{\perp}$, it is evident that the lighter species get a low $S_{\perp}$ and consequently a large perpendicular component of the velocity, leading to a centerline density of lighter species lower respect to that of heavier ones.

2.4 Clustering process in supersonic beams

Even if this is beyond the scope of this thesis, it must be mentioned the phenomenon leading to production of aggregates of particles, clusters that are due to the onset of nucleation processes in supersaturated regions by using supersonic beam sources. The formation of clusters requires that the heat of condensation is carried away from the forming aggregates efficiently enough to enable nucleation: to this extent, a cold buffer gas, usually a rare gas as He or Ar, is typically used. In fact, the very fast cooling rate in the free jet expansion represents an ideal environment to produce and control the cluster formation from vapors seeded in noble gases [17]. The average cluster size and their density in a supersonic beam depend on the initial state of the vapor into the source (partial pressure and temperature), on the pressure and the temperature of the carrier gas, and on the geometry of the nozzle (size and shape). Low source temperatures favor the onset of *supersaturation*, that is the higher T the smaller is clusters size and number.

Also carrier gas pressure can enhance clusters production: at a given source temperature, nozzle diameter and cross-section, the supersaturation region moves upstream as the carrier pressure increases, since the increased number of collisions increases cluster formation. The mass of the inert carrier gas and the seeding are other two parameters that determine the final mass distribution in a supersonic molecular beam. Cooling of the growing aggregates is due to the collisions between carrier gas particles and those of the seeding species, taking away the heat of condensation, a process that efficiently stabilizes large cluster.

The nozzle geometry and opening is a critical parameter to control some beam properties, for instance, cluster formation is pushed up by large nozzle diameters while smaller nozzles, at a given pressure, produce an expansion that runs out collisions rapidly, so that smaller and fewer clusters are produced. Moreover, a constrained expansion may lead to the production of larger clusters, since the outgoing particle experiences a higher number of collisions and the clusters have an increased opportunity to grow. Conical, cylindrical and converging/diverging nozzles are then suitable for clustering production, while sonic nozzles behave as the opposite. Basically, three different geometries can be defined (following the notation of Hagena and Obert [18]) to produce an axial symmetric free jet: the sonic nozzle, the conical nozzle and the Laval nozzle [18]. Among them, the first configuration (a circular hole opened in a wall much thinner than the diameter, see Figure 2.4) is designed in order to reduce clustering: in fact, the number of effective collisions, as well as the expansion time, here are reduced to a minimum.

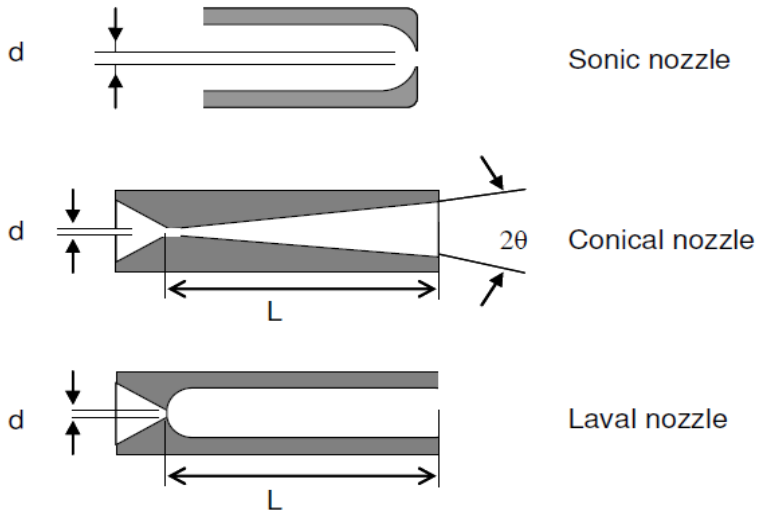

Figure 2.4: Schematic representation of three nozzle geometries, axially symmetric.

2.5 Supersonic and effusive molecular beams

The two kinds of molecular beams differ in several aspects, mainly velocity spread, spatial distribution and thermodynamic properties. The framework conditions for the two cases

are dramatically different: while Knudsen cells are characterized by processes at thermal equilibrium, supersonic beam sources are non-equilibrium systems.

Parameters like the Knudsen number K_n, the evolution of temperature (from T_0 to final value T_f) and pressures (from P_0 to the final P_f) show distinct behaviors:

- K_n is less than unity for supersonic beams: the gas is underexpanded and a large number of collisions occur during the expansion. For K_n larger than 1, as for Knudsen cells, the flow is molecular and effusive: in supersonic beam, this occurs over a distance of few nozzle diameters.
- T_f and P_f are considerably smaller with respect to initial values in supersonic beams. The expansion can be assumed isentropic. Knudsen cells, operating in thermal equilibrium, show no significant differences between initial and final temperatures.
- An isentropic expansion leads to final velocities in supersonic beams considerably larger than initial values, while the velocity distribution from Knudsen cells reflects that of the oven (Maxwell distribution).
- The free jet expansion produces the cooling down of the ro-vibrational modes, the efficiency of which depends from the energy spacing of the molecular states. Such effects are not present in Knudsen cells, where the state population is given by the standard distribution at the temperature of the source. Diluted or very diluted insemination (seeding) of the species under study in lighter non condensable gases can be used to improve control of the KE and of the ro-vibrational cooling.
- Clustering is promoted by the use of constrained nozzles and by seeding in carrier gases, while in Knudsen cells the process can be achieved only by external cooling and gas aggregation [3].
- As far as velocity spread is concerned, Figure 2.5 reports a comparison between the velocity distributions of the two types of sources: the supersonic source shows a narrower spread (it is proportional to$\left((2/\gamma)^{1/2}/M\right)$, while a Knudsen cell gives rise to a Maxwellian considerably larger velocity distribution.
- The angular distribution has a typical cosine-like angular intensity distribution in effusive molecular beams (Figure 2.6), while for supersonic molecular beams it has a very high forward intensity narrowly peaked along the beam axis.

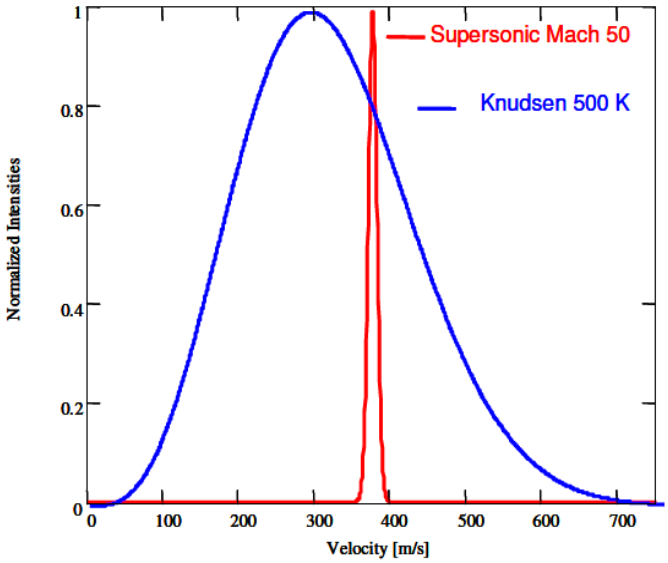

Figure 2.5: Velocity spread for a molecular beam produced by two sources (supersonic and effusive).

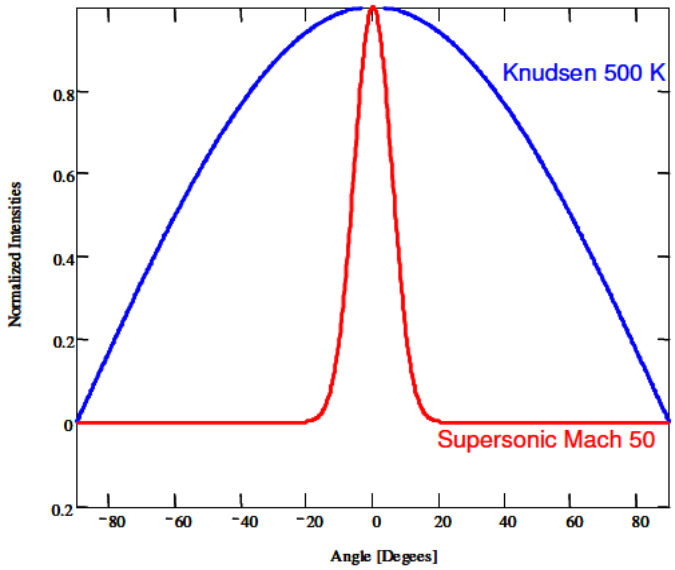

Figure 2.6: Angular distribution for a molecular beam produced by two sources (supersonic and effusive).

Effusive molecular beams are probably the main tool for thin film deposition in UHV conditions: the evolution of the technology of Knudsen cells has brought a very large diffusion of the Molecular Beam Epitaxy (MBE), as a matter of fact a standard in UHV growth [19].

The group of IMEM-CNR in Trento has shown that Supersonic Beams are a viable method to tailor thin film properties by controlling the precursor kinetics in terms of beam source parameters. In particular, it has been shown the ability to induce surface structural and morphological ordering in organic molecular films [12-15], as well as formation of chemical bonds and synthesis of materials [20,21]. These aspects will be analyzed in detail in the paragraph 2.9.

2.6 Gas-surface interaction and dynamics

2.6.1 General remarks and kinetic activated processes

Gas-surface dynamics is the subject of very wide and extensive studies exploring several different systems, regimes and processes, including adsorption, desorption, chemisorption, energy transfer, clustering and coalescence [22,23]. The basic concepts will be here recalled, in order to give the background for the work carried out for this thesis.

The interaction between a gas particle A and a solid surface B is an adsorption process that can be basically described by two main processes: physisorption and chemisorption. The one or the other occurrence depends on the interplay of the surface energy potential curves of the dissociated (A+B) and associated (AB) gas particle-surface system.

In the case of physisorption (showed in Figure 2.7), the particle approaching the surface experiences a weak attraction due to the weak dispersive forces generated by Van der Waals interaction at the gas-surface interface, with the typical laterally averaged z^{-3} dependence, but the well depth is not enough to produce a real stable bound state as it is the case of the associated AB case. Let us consider an atom, or a molecule that approaches the solid surface: we can define a laterally averaged potential energy curve which varies with the distance z between them (Figure 2.7-b, AB curve). As the particle comes closer to the surface, the attractive forces are dominant till a critical distance (z_c), located at the first shallow minimum (due to the weak dispersive forces giving rise to the physisorption states): at lower z values, repulsion forces dominate the interaction, as shown by the presence of a potential barrier that has to be overcome to reach the much deeper minimum connected to a real chemisorptions interaction.

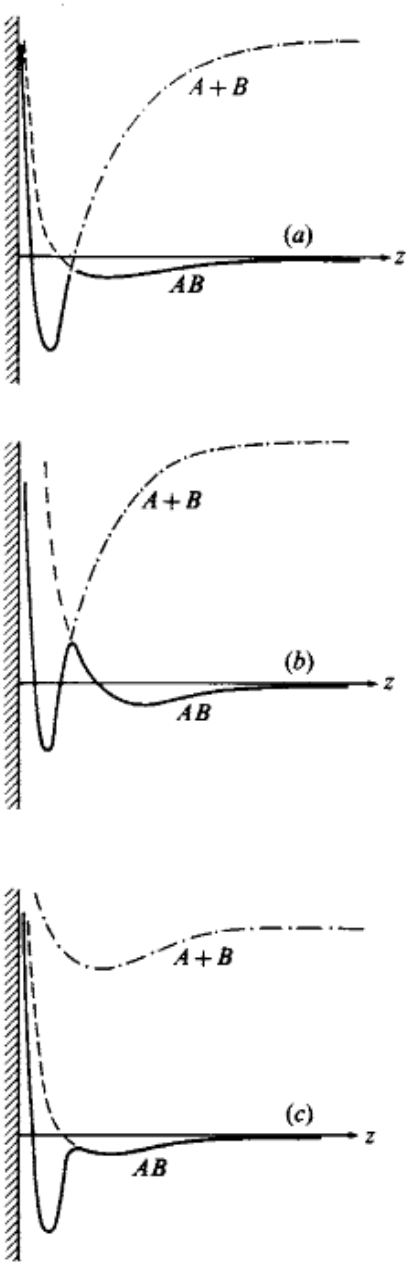

Figure 2.7: Schematic diagram of the potential energy for three adsorption processes for an adsorbate/substrate system: a-dissociative chemisorptions; b-physisorption and c-molecular chemisorptions.

The chemisorption process (Figure 2.7-c) is very complex and it is difficult to describe by a simplified potential energy model: in fact, the occurring of a chemical bond needs short distance range, strong interactions and is often an activated process requiring the overcoming of a "potential barrier".

The strong attractive forces characterizing a chemisorption event lead to a defined deep potential well, responsible for the stability and sometimes irreversibility of the process.

Physisorption presents often a reversible state, being characterized by a much shallower well (up to a few hundreds of meV): this process can often be considered as a "precursor" of chemisorption and, generally, of surface chemical reactions. The system stability is ensured if the dissociated A+B potential lies well above that of the formed adsorbate-substrate system. A variation to the simple chemisorption process is the occurring of molecule's dissociation after the adsorption step: if the crossing of the A+B and AB system occurs below the zero of energy, there is a spontaneous dissociation after a preliminary physisorption (Figure 2.7-a).

To better understand the adsorption mechanisms it is necessary to discuss in detail the concept of "energy barrier". Let us consider the path of a gas particle approaching a substrate (dashed lines in Figure 2.8), with a gas-surface interaction potential that is described as in Figure 2.8-a or -b, without or with an energy barrier respectively. In the former case, if the gas particle energy is much higher than the laterally averaged well depth, it will scatter back (upper dashed path). At lower incident energies, the particle can be trapped into the potential well: a stable bond with the surface can be formed via energy loss processes (transitions between electronic levels, vibrational or rotational states), phonon assisted processes and so on. The presence of an energy barrier to the adsorption process (see Figure 2.8-b) implies that only the particles having a sufficient amount of energy will be potentially chemisorbed on the solid surface: if the impinging molecules do not possess enough energy, the adsorption is not stable and desorption or backscattering will occur. The height of the energy barrier depends on the type of adsorption process: in the case of physisorption, this value is in the range of few meV, it can be easily overcome but leads to weak bonds (see Figure 2.8-a), mainly based on Van der Waals interactions. For chemisorption processes (Figure 2.8-b), the energy barrier is in the eV range and the potential minimum, where the bond is stable, cannot be reached if the total energy of the interacting system is not high enough.

The picture is somewhat more complex when we consider the whole synthesis process, taking into account the substrate as a reagent and the presence of a much more realistic potential energy surface. Other factors such as dissociation processes, molecules

breaking/dissociation or molecular distortions or conformational changes should be taken into account, together with the energy loss processes that have been described before.

Chemisorption can also occur when the gaseous precursors have a sufficiently high energy: this is the case of fast particles in a supersonic beam, where the appropriate energy content, in terms of KE and momentum, can lead to overcoming the potential energy barrier. In this case we will refer to "*kinetic activated processes*". It is interesting to note that the KE must not be too high, since this could increase the probability of back scattering from the surface (see Figure 2.8-a).

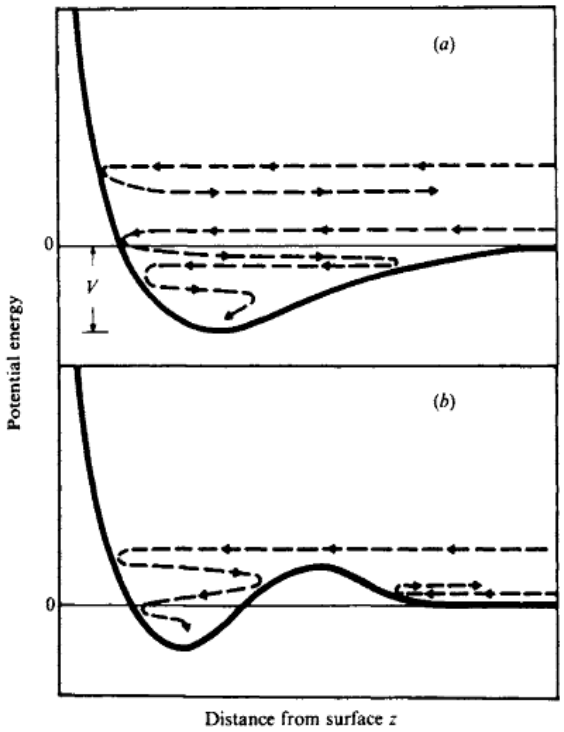

Figure 2.8: Schematic diagram of the processes occurring when a gas particles approach a surface with a given KE. A-simple adsorption well, b-potential well with an energy barrier.

From this point of view, a critical role is played by the energy transfers and rearrangements that occur during the collision, that are strongly affected by the intramolecular and molecule-surface potential interactions and the nature of the surface.

Another surface process characterized by an energy activation barrier is diffusion. Let's consider, for example, surface diffusion after adsorption, over an ordered monolayer. The adsorbate particle "feels" the periodic surface potential due to the regular array forming the

monolayer: the sites where the interaction will favor the absorption will be therefore separated by barriers, as sketched in Figure 2.9.

Depending on the available energy, the particle can have a finite probability of jumping from one site to another with a rate ν, determined by:

$$\nu = \frac{1}{z}\nu_0 e^{\left(-E_d/K_b T\right)}$$

where E_d is the height of the energy barrier to diffusion.

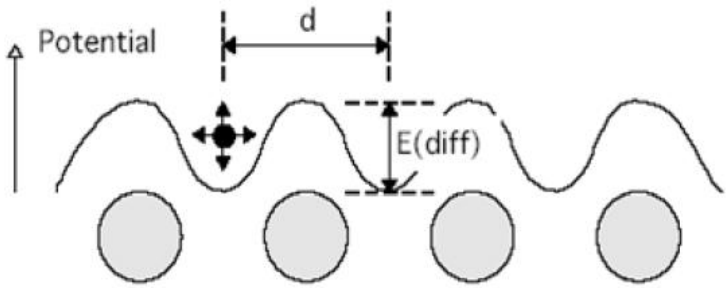

Figure 2.9: Mechanism for adsorbed particles on ordered monolayer.

In its simplest formulation, also the relationship between surface diffusion and energy has the typical form of an activated process (Arrhenius form):

$$D = D_0 exp\left(-\frac{E_a}{kT}\right),$$

where D_0 is a pre-exponential factor, and is known as diffusivity.

Hopping rate and diffusion are processes that can be thermally activated or enhanced: this leads to the presence of very different regimes, morphology and structures [12] in films growth, with a complex dependence of the surface mobility from the temperature.

2.7 Thin films growth and study

2.7.1 Growth processes

Growth of thin film is a very wide subject that includes several growth techniques as well as processes at interfaces. The use of supersonic beams seeded by organic precursor can

lead to the control on kinetics, opening the way to grow highly ordered films showing state of the art physical/chemical properties.

It was been widely demonstrated that the growth mode affects the film morphology, which gives the structural properties such as perfection, flatness and interface abruptness of the layers (see paragraph 2.9). As shown in Figure 2.10, different atomistic processes can occur during film growth: deposition, diffusion on terraces, nucleation on second-layer island, diffusion to a lower terrace, attachment to an island, diffusion along a step edge, detachment from an island, diffusion of dimers [24].

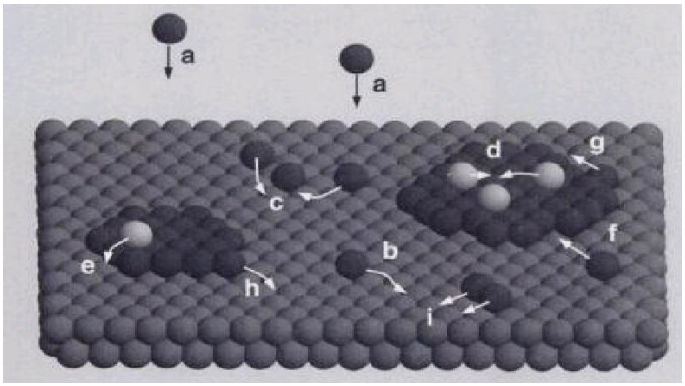

Figure 2.10: Atomistic processes during the growth: a) deposition, b) diffusion on terraces, c) nucleation on islands, d) nucleation on second-layer island, e) diffusion to a lower terrace, f) attachment to an island, g) diffusion along a step edge, h) detachment from an island, i) diffusion of dimers [24].

Experimentally, it's possible to classify three general growth modes, taking into account the different processes occurring at the interface and in the film itself: the layer by layer growth, islands formation and a situation where both occur (see Figure 2.11).

Frank van der Merwe (FV): The film grows layer by layer and a new layer is nucleated only after completion of the layer below, so that a bi-dimensional growth occurs, also over long distances in ideal case and it is due to the presence of an adsorbate-surface interaction that is stronger than adsorbate-adsorbate. The film completion has thus a linear dependence on the deposition time, provided the rate is constant.

Volmer Weber (VW): In this case, the adsorbate-adsorbate interaction is stronger than any other, so that the molecules do not tend to cover the surface, as previously observed, but

aggregate in a molecular structure commonly denominated “island”. Often, this three-dimensional growth does not lead to a complete substrate coverage.

Stranski Krastanov (SK): this mode is a considered as intermediate between the two former cases and can be found when a significant lattice misfit match from film and substrate occurs. Initially, we observe a two dimensional growth process (usually up to three monolayers), layer by layer, that will be followed by a three dimensional island growth, when the influence and the interaction with the underlying layer becomes weaker.

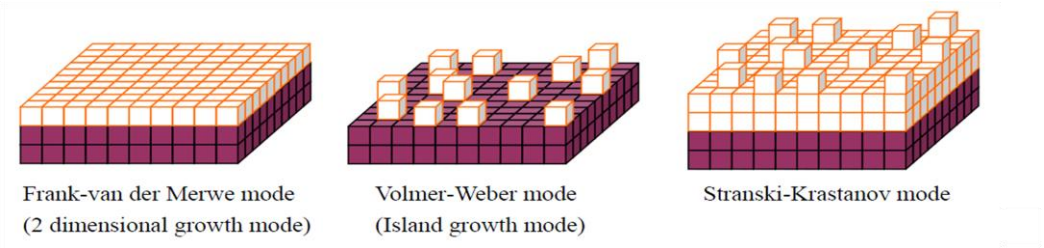

Figure 2.11: Schematic view of the three modes of thin film growth.

The number of layers prior of the island formation usually is no more than three: such a layered structure is also called a “wetting layer” and is often observed in molecular films. This term comes from chemistry where a surface giving origin to layer by layer growth is considered as “wet”.

2.7.2 Growth techniques

Improvements of growth techniques, as well as the development of processes that can tailor the growth from the microscopic scale down to the nanoscale, have made possible a careful control of the epitaxial processes and, on the other side, have projected all the device technology toward an increasing miniaturization. Among all the growth technique, Chemical Vapor Deposition (CVD), Physical Vapor Deposition (PVD) and Molecular Beam Epitaxy (MBE) are the reference tools for thin film growth. Supersonic Molecular Beam Epitaxy (SuMBE) is a novel technique that shares with MBE some features, and will be described in more details hereafter.

CVD involves the dissociation and/or chemical reaction of gaseous reactants in an activated environment (heat, light, plasma, etc.), followed by the formation of a stable solid

product. It is a versatile technique and it has become an established process for the deposition of amorphous and crystalline films for a wide range of applications, e.g. semiconductors for microelectronics and optoelectronics (Si, SiC, Ge, III-V semiconductors), dielectrics (SiO_2, AlN, Si_3N_4, etc..), metallic films, refractory ceramics and ceramic fibers.

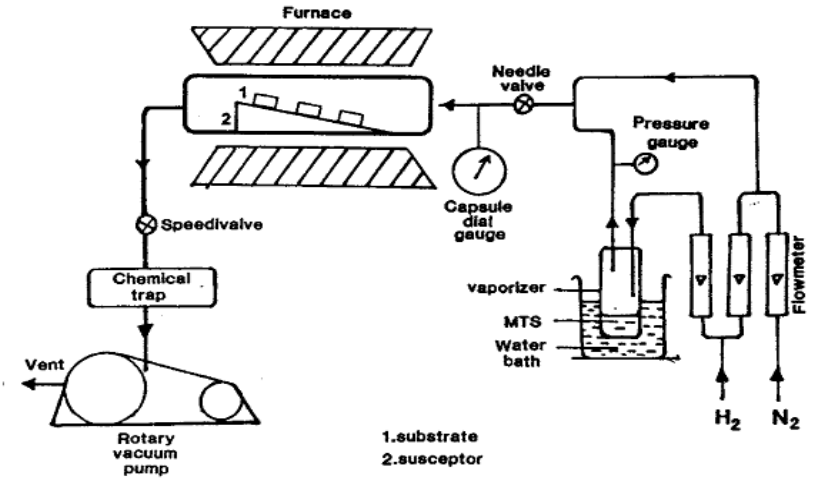

Figure 2.12: Schematic diagram of a typical CVD experimental set-up.

In general, a CVD set-up is composed of three main parts (Figure 2.12):

- the reactor, the main function of which is to heat the substrate at the required deposition temperature. Cold-wall and hot-wall reactors are the two common configurations for CVD: in the last case the whole chamber is heated and samples are brought to the desired temperature by indirect heating. In the other case, only the substrate is heated so that the walls of the reaction chamber are cold.
- The precursor supply system, that generates the chemical vapors from solids, liquids or gasses, and delivers them to the reactor, through a carrier gas.
- The effluent gas handling system, where the exhaust gasses are neutralized, and the vacuum system, that provides the necessary reduced pressure for the CVD process.

CVD growth itself includes several steps:

1. Generation of active gaseous precursors species,
2. Their transport into the reactor,
3. Formation of intermediate species by gas phase reaction,
4. Absorption of active species onto the heated substrate,

5. Heterogeneous reaction at the gas-solid interface,
6. Diffusion of the deposited species along the host surface and growth,
7. Removal of the by-products and not reacted precursors from the boundary layer by diffusion or convection.

The CVD system is quite complex, but it allows production of high purity and crystalline materials, with a good reproducibility, high adhesion at reasonably high deposition rates and control on surface morphology: this is why CVD is the technique of choice for thin film growth, especially when large growth areas are required.

However, some drawbacks have to be taken into account: the use of hazardous precursors, the difficulty to control the interface properties, as well as to deposit multicomponent materials with well controlled stoichiometries and homogeneity. This is mainly due to the complexity of chemical-physical processes occurring at the same time in the whole volume of a CVD reactor (high temperature, dissociation, chemical reaction, adsorption, diffusion, etc), making it a growth method limited in the control of film properties from the "ab-initio" control of process parameters. Moreover, the presence of contaminants cannot be easily reduced, either due to relative high pressures in a CVD apparatus (from 10^{-3} Torr up to few Torr) or to the precursors activation reaction.

The MBE approach [19] is a sophisticated technique that is widely employed, due to its ability to achieve a good control on interfaces. Basically, it consists on the use of particles in effusive molecular beam at thermal energies generated from Knudsen cells, impinging on a surface at controlled temperature. A very clean environment together with a fine control on process parameters are the key factors that makes this technique so important. MBE has solved several problems regarding the growth of materials like III-V semiconductors, e.g. GaAs, where a fine control of stoichiometry is critical and difficult to obtain, since the constituents have different vapor pressures.

Major peculiar characteristics of MBE with respect to other growth techniques are:

a) slow growth rate, that enables control on the interface and film thickness even in the low nm range,
b) reduced growth temperatures, reducing bulk diffusion at abrupt material interfaces,
c) possibility to perform in-situ analysis during deposition, in order to control and eventually change deposition parameters in real time.

A typical UHV MBE apparatus (Figure 2.13) is composed of one (or several) evaporation sources, a sample holder that intersects the molecular beam at a distance of few tens of cm, and a mechanical shutter, which allows interruption of the deposition process at the desired film's thickness.

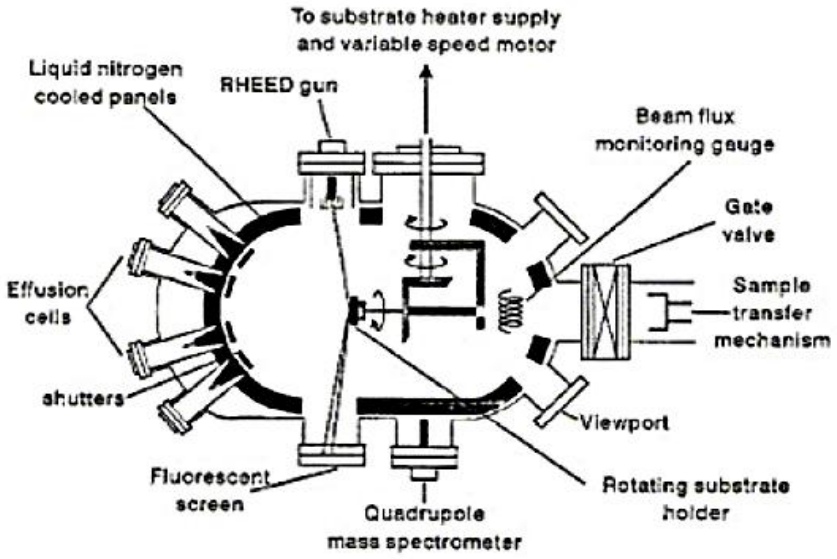

Figure 2.13: Schematic representation of a typical MBE growth chamber.

Usually RHEED (Reflection High-Energy Electron Diffraction) characterization technique is mounted in the growth chamber to monitor the growth in-situ and in real time.

The development of high quality molecular beam sources has been and is a key point in MBE growth. Knudsen cells are the prototype of effusion cell employed in such an apparatus, and must work in UHV conditions: they are heated ovens with a small orifice, in which collision-free thermal energy beams of the precursors are generated and directed towards the substrate (see paragraph 2.2). When the vapor pressure of the material heated in the cell is on the order of 10^{-3} Torr or higher, a molecular flow of particles occurs, with a mean free path larger than the orifice diameter. The flux of the molecular beam can be controlled by changing the source temperature in a wide range of values and can be used for a great variety of materials, including most metals and semiconductors.

A conventional MBE is typically employed to grow semiconductors, multilayer structures, semiconductor-metal-dielectric composites, as well as metastable materials. The growth of thin film from organic molecules has been also developed and is often called OMBE [25]. There are substantial differences between two methods: "standard" MBE must fulfill the

requirements for lattice matching in order to realize a real epitaxial growth, while, on the other hand, it has been demonstrated that organic molecules aggregate in ordered phases, even though the lattice matching is not as high. The materials that falls into this class are usually bonded by Van der Waals forces, and are called layered or VdW solids. Well-known examples are molecular crystals of pentacene, perylene and phthalocyanines.

2.8 SuMBD: a novel approach to film growth

Supersonic molecular beams have been originally developed to perform molecular scattering and spectroscopy studies. Recently, supersonic seeded beams have been proposed as a new approach as a film growth technique: a standard beam of a carrier gas seeded by vapors of the material precursor is used to grow or synthesize thin films. The idea on which this approach is based is that a large and controlled amount of energy can be delivered by the precursors in the beam, and then to a localized region of the surface, where it can stimulate chemical processes and surface diffusion. A Supersonic Molecular Beams Deposition (SuMBD) apparatus shows several differences with a standard MBE facility: while in the latter the sources are in the same UHV chamber where the characterization is carried out, for SuMBD the generation and control of the beam properties are obtained in a separate UHV or HV chamber connected to the growth chamber. This is mainly due to the requirement of larger pumping system to produce a supersonic beam with an appropriated gas throughput: supersonic molecular beams sources, in fact, lead to a large gas load which has to be efficiently pumped out in order to assure the vacuum conditions for the supersonic expansion and molecular beam propagation.

Figure 2.14 shows an example of an apparatus for SuMBD growth [26]: the supersonic beam is generated in a separate chamber by introducing into the source the carrier gas at a pressure in the range between few hundreds of mbar up to few bar. The vacuum system consists of a high pumping speed diffusion and primary pump, namely ≥2000 l/s and ≥30 m^3/h respectively, a solution that assures high and appropriate throughput. Similar solutions are adopted in other SuMBD set-up, eventually differentiated in the use of oil free pumping systems. A skimmer selects the molecular beam in the expansion zone, then the supersonic beam enters into the growth chamber: a valve separates the two chambers

and allows the generation of supersonic beam without breaking UHV in growth chamber. The possibility to control carrier gas pressure, together with source temperature allows operations in the low growth rate range, as well as with high flux and density.

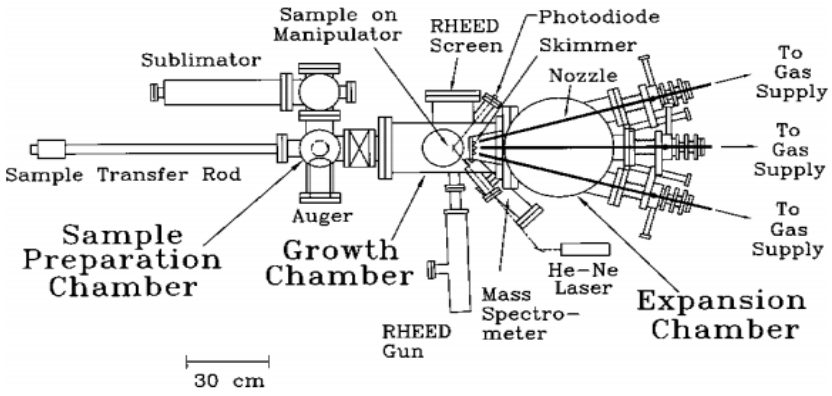

Figure 2.14: Scheme of a supersonic Beam Epitaxy apparatus [26].

The high directionality of the beam can be further increased by the insertion of a second pumping stage in the source chamber (and a second skimmer) with a further step towards ultra-high-vacuum systems compatibility. The example showed in Figure 2.14 refers to the experimental set-up developed by Ustin and co-workers, a group that has reported of SiC deposition by SuMBE, employing methylsilanes as precursor: this work was fundamental for the affirmation of the supersonic source as growth facility. They demonstrated [27] that carbide synthesis occurs at temperatures well below those related to CVD or standard MBE and that crystalline ordering can be achieved, as well. They have reported on the usefulness of a buffer SiC layer by carbonization of Si(111), a method that enables to further expose the substrate and reach highly ordered films.

It is worth mentioning also the work of Malik et al. [28] on the homoepitaxial growth of silicon from gas sources. This task presents some problematic features tied to the growth temperature. Silicon epitaxy, owing to technological needs, has to be carried out at temperatures as low as possible, in order to minimize the extent of diffusion of unwanted dopants and impurities. MBE is the technique of choice for such a growth and hydrogen containing chemical species are often used. Moreover, in order to minimize surface roughness, hydrogenated silicon surface are prepared, and heated in the growth chamber for H_2 desorption. The SuMBD approach could solve most of the problems inherent to the aim of carrying away hydrogen and in order to lower the substrate temperature. Supersonic

beams of Si have been employed to get collision-induced desorption of unwanted species and subsequent film growth in a kinetic activated process: the authors reported high crystal quality films at 300°C.

2.9 Processes activation by SuMBD

The IMEM-CNR group of Trento has shown that Supersonic Molecular Beam deposition (SuMBD) is a viable method to control thin film properties by changing the precursor kinetics in terms of beam source parameters. In particular, the ability to induce surface structural and morphological ordering in organic molecular films [12-15] was proved, together with the activation of physical/chemical processes by the unique kinetics properties of the precursors in supersonic beams [29,30].

In order to explain these properties of SuMBD approach, three peculiar examples of film growth will be presented:

- Growth of organic films using a molecular beam of pentacene and control of their morphology by changing the carrier gas and, consequently, the KE,
- Functionalization of a titanium oxide substrate by a supersonic beam of copper-phthalocyanines
- Synthesis of hybrid Erbium-Tetraphenylporphyrin system and silicon carbide at room temperature.

2.9.1 Organic materials: pentacene

Pentacene is a promising candidate for organic electron and optical applications (Figure 2.15), since it exhibits high hole mobility (up to 5.5 $cm^2/V\ s$) in OFET, organic thin film field effect transistors [31]. It is well known that the charge transport properties of conjugated molecules like pentacene depend on the π-orbitals overlap between the molecules, and they are correlated with their crystalline structure, the degree of orientation and grain size.

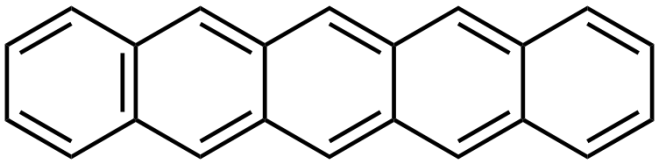

Figure 2.15: Molecular structure of pentacene.

The orientation of the pentacene molecules with respect to the substrate, especially for the first monolayer, is defined by the balance between the pentacene-substrate and pentacene-pentacene interactions [32]. As a general rule, pentacene molecules stay flat on highly interacting substrates, maximizing the interaction with the different molecular orbitals. On the contrary, in case of low interactions, molecules have a propensity to be vertical, forming an induced dipole structure that polarize the molecule along the vertical axes: this minimizes the interaction with the substrate and maximizes the interaction between molecules.

When the lateral pentacene-pentacene interactions are more important than either the pentacene-substrate or interlayer pentacene-pentacene, the molecules stand nearly vertical and pentacene will tend to form crystals with the (001) plane parallel to the substrate [32]. Indeed, when pentacene is grown on an inert substrate like oxide (SiO_2) or polymeric dielectrics [33], pentacene tends to self-assemble forming crystalline domains. Regardless of the crystallographic orientation of the substrate, the molecules are arranged nearly perpendicular to the substrate. In this condition it is possible to observe large size (up to 0.1mm) single crystal pentacene grains with "standing-up" molecules: this particular configuration is the only observed for pentacene on inert substrates. [15]. Considering the case in which the interaction with the substrate is very strong (Si or metals), with possible charge transfer at the interface, the molecules in the first layer grow parallel to the surface.

Highly ordered thin film have been obtained by SuMBD approach [13,14]: it has been found that a layer by layer growth occurs, with formation of large grains and few boundaries. The role of the KE in determining the growth process has been found to be crucial. As a matter of fact, it is possible to control the nucleation and the island density at different growth stages tuning the impinging molecules flux and energy, giving rise to films of much better quality.

As demonstrated by S. Iannotta and co-workers [12] in the case of pentacene, it is possible to work in a range of KE from less than 200meV, in a seeded Kr beam, to more than 10eV, using a seeded H_2 beam (Figure 2.16). The high carrier gas pressures are coherent with the equation

$$E_{kin} = \frac{5m_{or}}{2m_{av}} RT_{nozzle}$$

where m_{or} and m_{av} are the organic molecule molar mass and average molar mass (organic molecule and carrier gas), respectively.

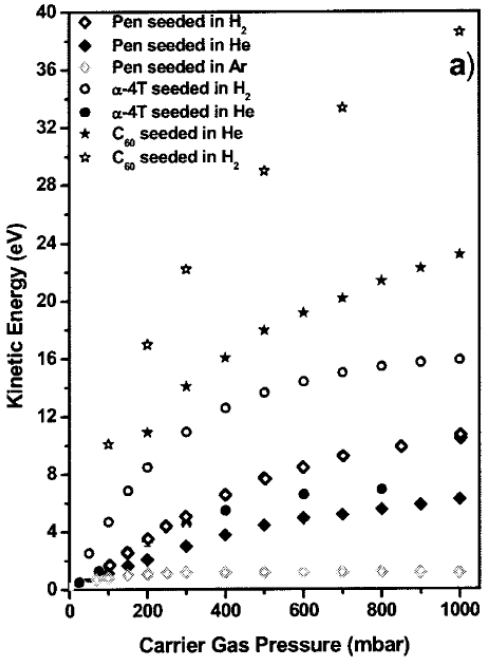

Figure 2.16: KE of several π-conjugated organic molecules as function of the carrier gases pressure [12].

The number of collisions between the heavy molecules and the atoms of the carrier gas affects the aerodynamic acceleration, causing a velocity slip between the two species that becomes zero when the pressure of the gas carrier is increased [12].

Studying pentacene deposition on a native SiO_x at different KE regimes (3eV up to 6eV), it was observed that for higher values a high order film can be obtained, with the typical island size decreased and the island density increased.

The initial KE of pentacene following the collision with the surface is converted, partially, into KE parallel to the surface through a mechanism which involves inelastic molecule-molecule and molecule-surface energy transfer processes. So it is possible to assume that molecules with high KE can diffuse on the surface for long distances before aggregating and forming molecular island. The resulting film will be characterized by a more uniformly dispersed pattern of small island. At high KE the samples showed a monolayer of better quality with a low defect density and islands quasi completely coalesced and sharper island edges. On the contrary, molecules with low KE move for shorter distances and have a lower probability to give rise to new islands by means of the collisions with other molecules, giving rise to smaller grains [14].

2.9.2 Surface Functionalization

Hybrid systems, nano-composite materials constituted by both inorganic and organic components, in the last years have acquired great importance for their possible application in energetic, gas sensing and optoelectronics. In particular, metal oxides for their capability to exchange charges with condensed materials are object of many studies.

SuMBD approach allows producing hybrid structures by means of the functionalization of inorganic material with organic molecules, as proposed by F. Detto in her PhD thesis [34]. This approach has the advantage to work with both organic molecules and inorganic aggregates, activating chemical and physical processes at the interface.

She studied the functionalization of nanostructured titanium dioxide (TiO_2) with copper-phthalocyanines (CuPc), demonstrating the possibility to create chemical bonds at interfaces by high KE activated processes.

Common technique to grow high crystalline quality TiO_2 consists in thermal treatments in order to activate the crystallization. For this reason it is necessary to carry out the functionalization in a subsequent step in order to avoid damage to the intermolecular structure of the organic. Supersonic beams by Pulsed Microplasma Clusters Sources (PMCS) allow instead to synthesize nanocrystalline TiO_2 (about 60 nm-thick film on Au) exploiting the high KE, without any thermal treatment. PMCS permits to obtain inorganic clusters by condensation of a plasma from high voltage discharge, while film growth is achieved by aggregation of single building blocks (clusters) on the substrate. The

description of the PMCS apparatus is beyond the purpose of this thesis, however a detailed explanation can be found in the Ref. 3.

The TiO_2 obtained by PMCS was characterized by a rough morphology, and an oxygen super-stoichiometric (O/Ti ≈ 2.20), in contrast with metal oxides obtained with other techniques which show oxygen vacancies due to the necessary heat treatments at high temperatures. After the TiO_2 growth, the organic material was deposited *in-situ* in the same chamber, avoiding any atmosphere contamination.

F. Detto in her work compared two hybrid systems constituted by the same components (CuPc on TiO_2) but grown at different organic KEs by means of SuMBD technique, i.e. more than 20eV and a quasi-effusive regime at about 0.5eV, achieved by using He and Kr as carrier gas respectively. The two systems have been analyzed by photoelectron spectroscopies (XPS and UPS) in order to assess the electronic properties and the chemical-physical process occurring at the hybrid interface.

The system obtained at higher KE showed a disordered organic decoration on the inorganic film, due probably to the high roughness of the $TiO_{2.2}$ surface. Moreover, the molecule stoichiometry calculated by XPS analysis ensured that CuPc molecules were not fragmented during deposition despite the high KE. This result demonstrated once more that supersonic beams deposition does not induce any degradation in the chemical structure of the organic molecules. Furthermore, XPS showed the presence of different components in C1s core level suggesting the presence of new chemical states. UPS also provided evidence of a strong interaction, with a shift of the CuPc HOMO band towards lower binding energy (BE) with the deposition time (Figure 2.17). This evidence can be explained by considering that the interaction at the organic/inorganic interface is characterized by a strong covalent rather than a Wan der Walls interaction.

Similar result has been obtained in a previous work carried out by our group in IMEM-CNR laboratories in Trento [35]. M. Nardi, indeed, demonstrated that the deposition of tetrakis(pentafluorophenyl)porphyrin ($H_2TPP(F)$) by quasi-effusive regime was characterized by a layer-by-layer growth ruled by Wan der Walls forces. Similarly to the previous experiment performed at high KE, C1s core level acquired by XPS showed a significantly weaker reactivity with respect to the high KE SuMBD case.

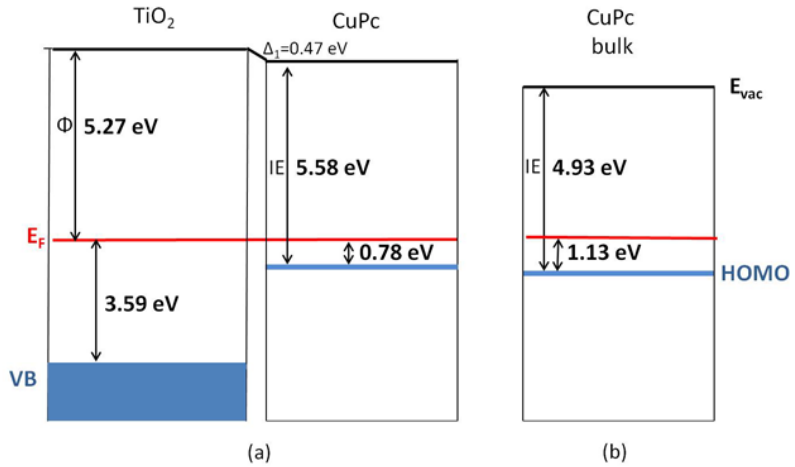

Figure 2.17: Energy level scheme of the CuPc/$TiO_{2.2}$ system (a) and CuPc thick film (b) [34].

Considering the film deposited at low KE, the growth on the inorganic substrate was faster with respect to the high KE case, more similar to a layer-by-layer growth (Figure 2.18).

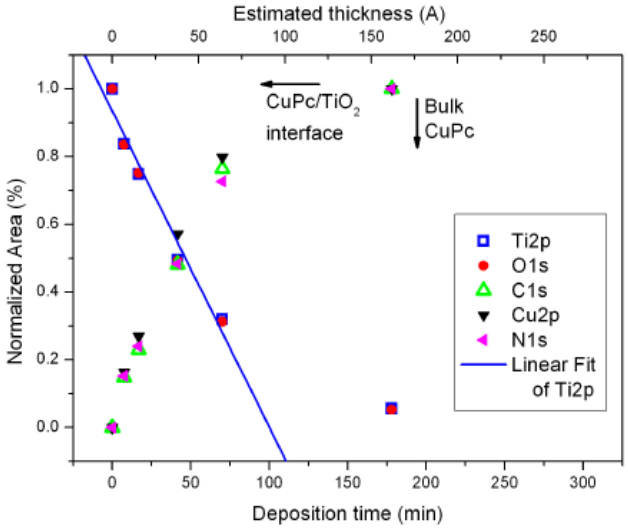

Figure 2.18: Normalized area by XPS as function of the deposition time (bottom *x*-scale) and the estimated CuPc thickness (top *x*-scale) [34].

Summarizing, the deposition performed at low energy leaded to a more efficient and quicker molecular coverage of the inorganic substrate, but surface chemical reactivity at high KE was improved of more than 100%.These results suggest the high potentialities of

SuMBD technique to activate chemical-physical processes at the interface, achieving an efficient functionalization of the inorganic surfaces by means of organic molecules.

2.9.3 Materials synthesis

- *Hybrid Er-Tetraphenylporphyrin (Er-TPP) synthesis by SuMBD*

Organolanthanide hybrid complexes are a class of compounds which attracted wide interest for their properties and possible application in optoelectronic devices. Indeed, the organic molecules could act as antenna in order to absorb light and transfer energy to the metal partner. The latter, in turn, decays by luminescence [36,37].

These hybrid systems are commonly synthesized by means of wet chemistry using precursors in liquid phase [38], obtaining a complex in which the lanthanide has the desired chemical coordination. However, this technique cannot be applied in microelectronics which requires vacuum conditions.

M. Nardi and co-workers demonstrated the possibility to synthesize organolanthanide hybrid complexes by means of co-deposition process in UHV combining SuMBD and MBE techniques for the deposition of the organic material and lanthanide, respectively. The precursors used in this work were tetraphenylporphyrin (H_2TPP) and Erbium (Er) which gave rise to a hybrid Er-Tetraphenylpoprhyrin (Er-TPP) complex [20]. The organic and inorganic materials were deposited simultaneously at room temperature on Si(100) with its own native oxide layer.

The Er-TPP film obtained was characterized by photoelectron XPS and UPS spectroscopy, comparing results with a the free base film . The molecular orbitals analysis through UPS showed interesting differences between the pure H_2TPP and the co-deposited Er-TPP films (Figure 2.19). As a matter of fact, the whole spectrum of the latter was shifted towards high binding energy probably due to the formation of a dipole at the underling interface, an effect already observed in organic molecules grown on metals [39]. Moreover the molecular orbitals' distribution of the porphyrin was characterized by a charge rearrangement related to the presence of Er in the center of the macrocycle, whereas the peripheral region was not involved in the interaction with metal.

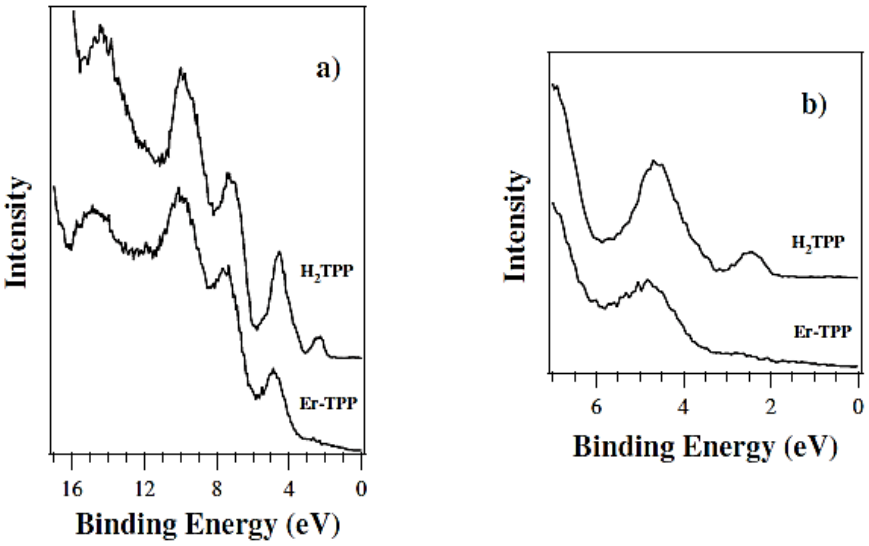

Figure 2.19: UPS valence bands spectra for H_2TPP and Er-TPP film (a). Magnification of the HOMO region [20].

Considering the XPS analysis, the Er-TPP N1s core level showed a completely different lineshape with respect to the free base H_2TPP (Figure 2.20).

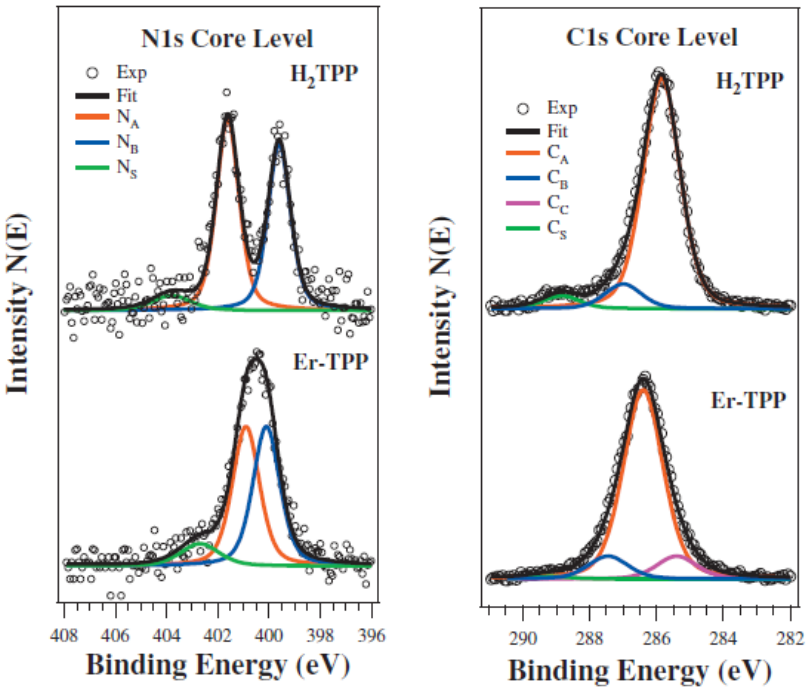

Figure 2.20: N1s (left) and C1s (right) core level for H_2TPP and Er-TPP film [20].

Keeping in mind that the porphyrin macrocycle is constituted by two different types of nitrogen atoms (hydrogenated and aza- nitrogen), the XPS results suggested a strong modification of their chemical properties, becoming chemically comparable one to the other after the co-deposition process, suggesting the lost the two hydrogen atoms. The experimental evidences confirmed the formation of a metal-porphyrin complex with Er located in the center of the macrocycle and bonded, coordinated to the four nitrogen atoms. This result is suggested also by the Er-TPP C1s core level analysis (Figure 2.20), which showed a new component at lower BE that can be associated to the carbon atoms rearrangement due to the interaction with Er.

All the observed effects by XPS and UPS characterization were coherent with the interaction of the lanthanide metal with the central macrocycle of the porphyrin, inducing its chemical modification. Finally, this work shows the high potential of SuMBD technique in the synthesis of complex hybrid systems.

- *Silicon Carbide (SiC) synthesis by SuMBD*

Silicon Carbide (SiC) is a wide gap semiconductor (2.2-3.3eV) greatly studied for its interesting properties such as thermal stability, high breakdown voltage and hardness [40-42]. SiC has two different crystallographic structures, hexagonal (α) and cubic (β) in a very large number of polytypes. Nevertheless, only the cubic polytype (3C-SiC) owns the best electrical properties and it can be grown directly on Si.

The standard technique used to grow a good quality SiC film is the Chemical Vapor Deposition CVD at high temperature (>1000°C), which leads, however, to the growth of a highly defected film [43]. The IMEM-CNR group in Trento demonstrated that it is possible to obtain SiC films with high crystallinity and quality by reducing the synthesis temperatures with a supersonic beam of fullerene (C_{60}), used as carbon precursor on Si substrate [29]. It was shown that fullerene has a strong and complex chemical interaction with the Si(111) surface [44], also at room temperature. Moreover, C_{60} has a large total mass and thus can be efficiently accelerated in the SuMBE experiments, reaching very high values of KE (see Figure 2.16) [29,30].

In the first step of this study, R. Verucchi and collaborators showed that the SiC bond formation on the Si(111)7x7 surface can be obtained by kinetic activation at a substrate

temperature of 750-800°C. They operated the C_{60} supersonic beams at two different KEs, 5eV and 20eV, using He and H_2 as carrier gas respectively. The analysis of the surface electronic properties of the two films (Figure 2.21) suggested that, in both cases, the Si-C covalent bond formation was strongly favored by a kinetic activation process, even at the low substrate temperature of 750°C.

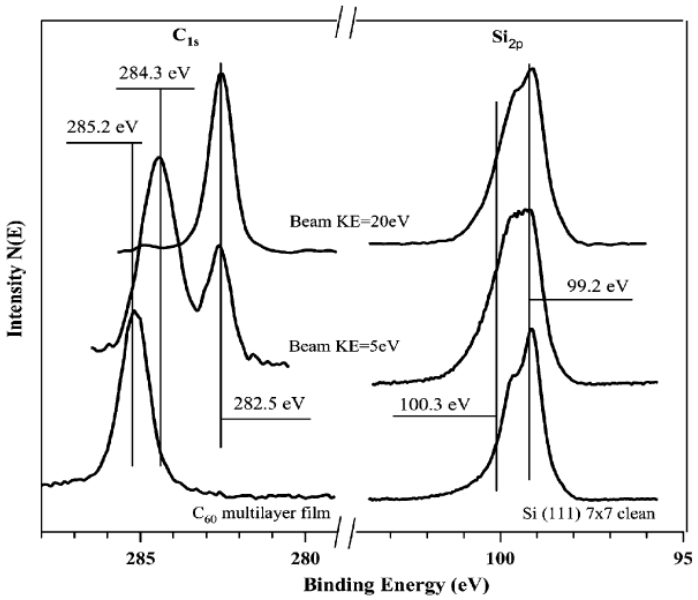

Figure 2.21: XPS C1s and Si2p core level. Si(111)7x7, C_{60} multilayer film, SiC films grown by supersonic beams at 5 and 20eV [30].

The films showed polycrystalline properties and the surface morphology was characterized by a granular structure: using the highest energy C_{60} supersonic beam largest grain size and higher rough film were obtained.

The presence of a surface order for the SiC film grown at a substrate temperature of 750°C and 20eV C_{60} is an evidence of the influence of the precursor KE on the structural properties, as this result has never been reported before.

In 2012 they demonstrated, furthermore, that it is possible to obtain nanocrystalline 3C-SiC on the Si(111)7x7 surface at room temperature (300K), through the chemical activation by a fullerene (C_{60}) supersonic beam. The C_{60} translational KE reaches values of 30-35eV by aerodynamic acceleration in vacuum, activating chemical processes on the Si surface, absolutely forbidden in conditions of thermodynamic equilibrium [29,30]. During this study, they deposited submonolayers C_{60} films with two different precursor KEs of 30eV

(0.30ML, 0.65ML) and 35eV (0.35ML, 0.70ML) [21]. The C1s core levels of 0.65 ML and 0.70 ML are shown in Figure 2.22, putting in evidence the presence of four components.

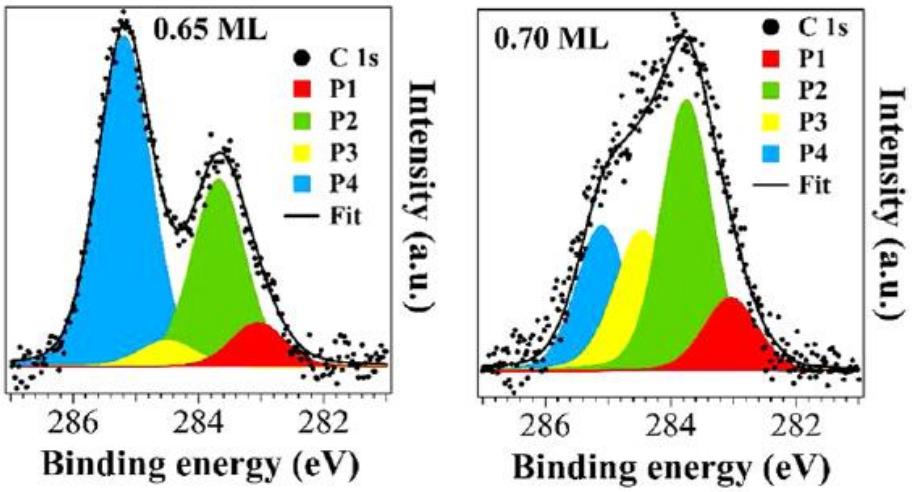

Figure 2.22: C1s core levels grown at 30 eV (0.65ML, on the left) and at 35eV (0.70ML, on the right) [21].

The peak at lower BE (named P1) is related to the amorphous/stoichiometric carbide whereas the P2 components represents the nonstoichiometric SiC compounds or hexagonal SiC polytypes. P3 and P4 instead are associated to the formation of C_{60}-Si bonds [21].

Comparing the chemical and structural properties of the films grown with the two different KEs regimes at room temperature, it has been demonstrated that the activation of physical-chemical processes at the film surface (first and foremost the cage breaking) occurs only when the precursor reaches an energy threshold of about 30eV. Moreover, it is expected the formation of only one or few layers on the silicon surface, due to the low Si and C mobility at room temperature. They found instead that, it is possible to observe ~10 nm wide 3C-SiC islands with a completely relaxed lattice, a very significant result if we consider the large lattice mismatch between 3C-SiC and Si(111).

In the light of experimental evidences, it can be assumed that part of the fullerene KE is used even to improve the surface mobility, in order to achieve the formation of SiC islands, and not only to support the covalent bond formation between the fullerene cage on the inorganic surface.

A very interesting result which confirms the formation of 3C-SiC at room temperature by SuMBD, is provided by LEED (Low Energy Electron Diffraction, see the paragraph 3.6.2.)

characterization (50eV). In Figure 2.23-a is shown the LEED pattern of the Si(111) surface with the typical Si 7x7 features. The 0.70 ML film at 35eV (Figure 2.23-b) displays the typical features of the Si 7x7 and further a set of hexagonal 1x1 extra-spots. Both the Si(111)7x7 and the new 1x1 pattern are well visible and identifiable following the subtraction of the Si pattern from the 0.70ML film (Figure 2.23-c). The lattice parameter calculated for the new 1x1 extra-spots correspond to a typical 3C-SiC(111) 1x1 structure [45]. To further highlight the achieved results, it is worth mentioning that in a common MBE experiment it is possible to obtain crystalline 3C-SiC only at temperatures above 1030°C [46], since at 830°C only amorphous islands are present [47].

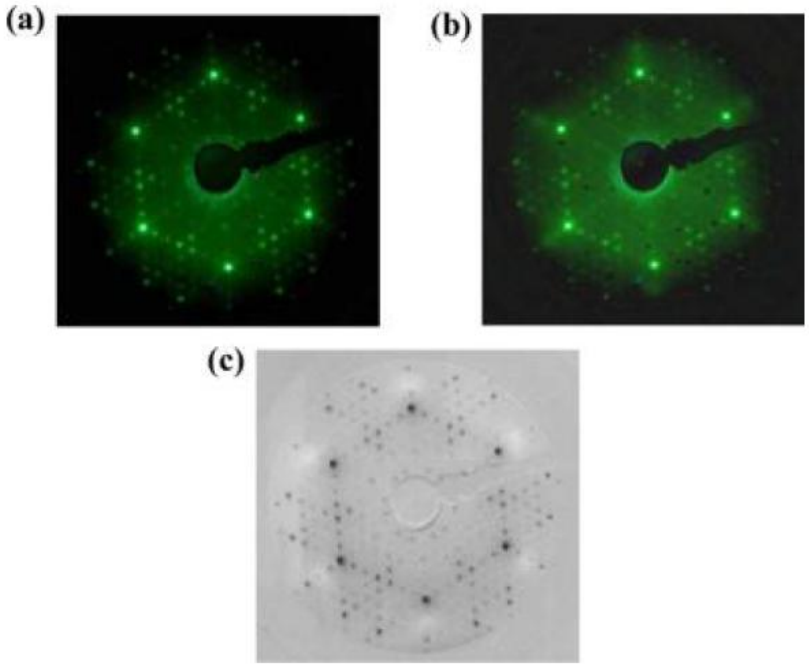

Figure 2.23: LEED patterns for (a) Si(111) 7x7 and (b) 0.70 ML C_{60}/Si(111) 7x7 grown at 0.35eV KE. (c) subtraction of (a) from (b) [21].

The first and most important process occurring at the organic-inorganic interface is the fullerene rupture, necessary to enable the observed synthesis of SiC. A theoretical analysis in order to obtain a possible mechanical explanation of the C_{60} cage fragmentation was developed by LISC group in Trento, performing simulations at different KE in the range 35eV to 450eV [48], using a non-adiabatic MD approach.

In this method, excited states of the system are employed to develop stochastic hope between adiabatic surface. The calculation of the excited states has been carried out by

using time-dependent density functional theory (TDDFT) in the Tamm-Dancoff approximation [49]. The computational results suggested that the fullerene cage opening at energies from 0.6eV per atoms is related to the variation in the force field to which the nuclei are subject. This process is associated to the production of excited electronic states of the fullerene molecules when they bump the surface [48]. The experimental results were finally confirmed by NA-DM studies, which approximate the C_{60}-Si collision dynamics by performing stochastic hops between adiabatic surfaces constructed with excited states of the system, developed for C_{20}-Si(100) system under similar collisional condition of experiments. In the Figure 2.24 is showed the trajectory of C_{20} impinging on the Si(100) surface up to the fragmentation of the cage [21]. The energy threshold where fullerene fragmentation occurs around 35eV, so close to the observed experimental value.

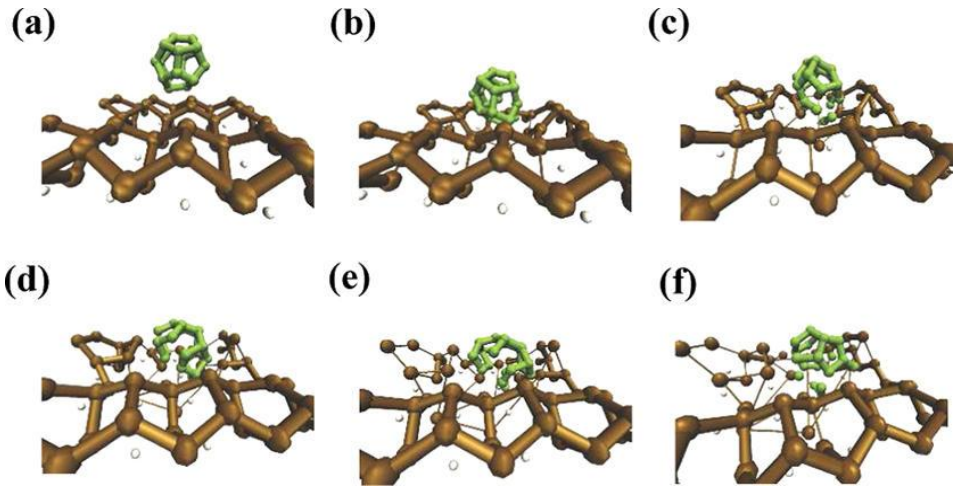

Figure 2.24: Sketch of a C_{20} molecule impinging on Si(100) 2x1 at 11.3eV from NA-MD calculations. Frames were taken every 22fs [21].

Chapter 3

Experimental

3.1 Apparatus description

Thin film deposition and characterization was performed in a UHV apparatus, mainly developed from an original project designed in the Trento IMEM-CNR Laboratory. The main feature of this system is the possibility to bind together a compact supersonic molecular beam source and an analysis chamber, in which it is possible to make in-situ characterizations of thin films grown in UHV by means of surface electron spectroscopy techniques. Figure 3.1 shows the devices by which the present work has been carried out.

The experimental set-up consists of three sections:

1. The supersonic beam source,
2. The UHV chamber for surface analysis,
3. The Fast Entry Load Lock chamber.

The latter has the aim to introduce the samples into the chamber analysis from air without breaking the vacuum in the main UHV apparatus. It is equipped with a transfer arm in order to insert a sample holder into the manipulator of the main chamber. The final pressure, reached without need of back-out procedure, is on the order of low 10^{-8} mbar, also by using a liquid nitrogen trap to pump most of water vapors: in this way, after less than one hour, the sample can be introduced in the UHV apparatus maintaining UHV conditions.

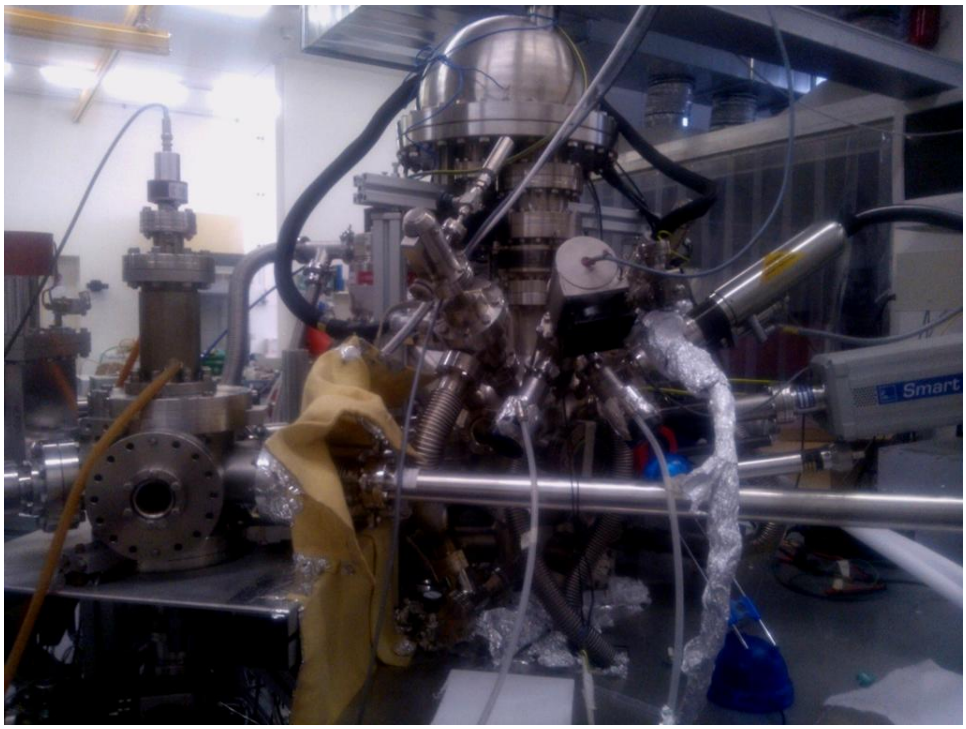

Figure 3.1: UHV apparatus in IMEM-CNR laboratory in Trento.

3.2 The analysis chamber

The analysis chamber (Figure 3.2) is made of μ-metal, a special steel alloy able to screen the earth magnetic field, as well significantly reduce the intrinsic magnetism of stainless steel.

This UHV chamber is pumped by a main system constituted by a dry primary pump (Edwards, Scroll type 15m3) connected with a magnetic-levitation turbomolecular pump (Edwards STP451 MAGLEV): the pumping system is totally dry and oil free. After the bake-out procedure (the whole system is heated up to 150°C after air exposure), this pumping system assures a base pressure of about $1x10^{-10}$ mbar. Moreover, in order to further improve the UHV conditions, down to $3x10^{-11}$ mbar, the main chamber can be pumped by a titanium-sublimation stage together with a liquid nitrogen (NL) cold wall.

The analysis chamber is a sphere so that the photons and electrons probing sources radially converge to the chamber focus point (i.e., the sphere center). The sample holder is a VG XL25 type, made by a sample carrier with an on-board heater and a cooling system (-

100/+1200°C temperature range), a thermocouple is present to monitor sample temperature.

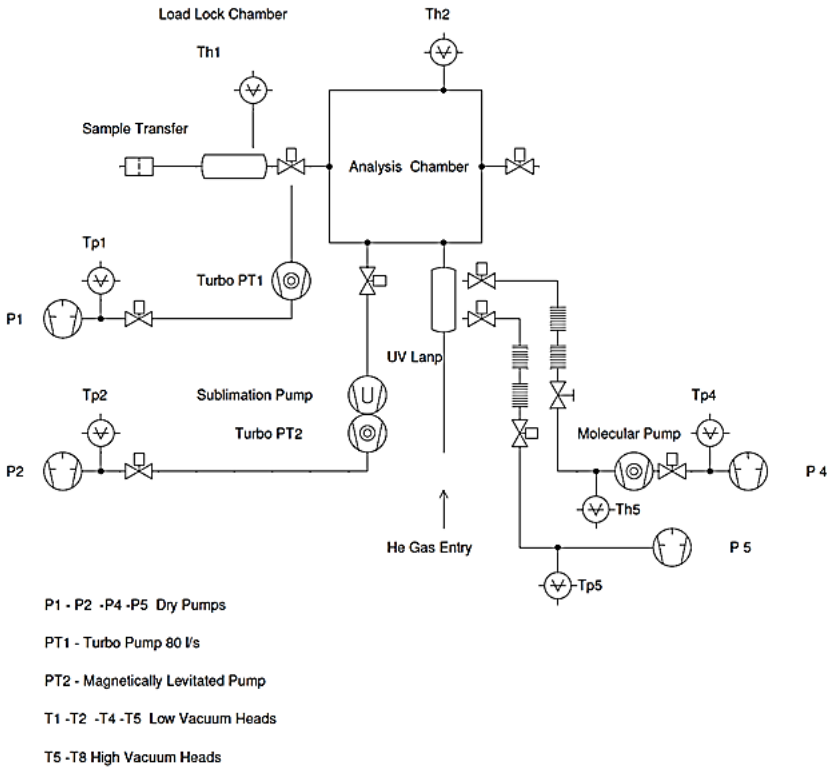

Figure 3.2. Sketch of the analysis chamber and the pumping system.

The sample is correctly positioned at the focus point by means of a 5 degrees of freedom manipulator, which besides assures the correct sample positioning for both surface analysis and film deposition. A VG type OMNIAX manipulator is used: it allows three translational degrees of freedom (x, y, z movements) and two rotational degrees (ϕ, azimuthal and θ, polar). Moreover, UHV electrical feedthroughs provide electrical contact to bias the sample surface, as well as the needed wiring to resistively heat the sample and measure its temperature. Annealing temperature can be monitored also from the outside of the UHV chamber by an optical infrared pyrometer, which operates in a range of temperatures from 300°C up to 1100°C.

The analysis chamber is connected by UHV lines with the Fast Entry system and to the SuMBD source chamber (see hereafter) by means of gate valves to assure UHV conditions and systems independency. This chamber is equipped with several facilities, that are discussed in the following.

3.2.1 Main electron energy analysis system

The electron energy analyzer is a hemispherical type (VS WHA100), with a spheres' radius of 100mm. This analyzer acts as a narrow energy pass filter, letting pass only the electrons that have a specific KE, and has three main components: the lenses system, to focalize and adjust initial electron energy, the analyzer, composed by two hemispherical and concentrical lenses, and five Channel Electron Multipliers (so called Channeltrons) to collect and reveal the electrons (Figure 3.3). Different surface electron techniques can be performed, namely X-ray and UV Photoelectron spectroscopies (XPS and UPS), Auger electron spectroscopy (AES), electron energy loss spectroscopy (EELS).

Using this analyzer, the maximum energy resolution achieved for XPS and UPS techniques is 0.78 and 0.1eV, respectively, while for AES is 0.5eV. The collection geometry is such that the sample surface is typically normal to the analyzer in XPS, UPS and AES spectroscopies, while excitation sources are positioned at different angles with respect to the sample's surface: Figure 3.4 is the scheme of the collection/excitation geometry.

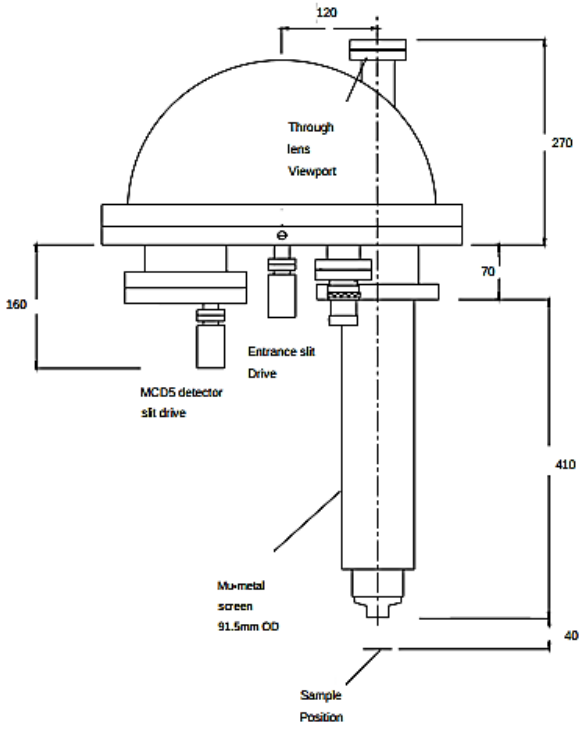

Figure 3.3: Scheme of the CLAM2 electron energy analyzer.

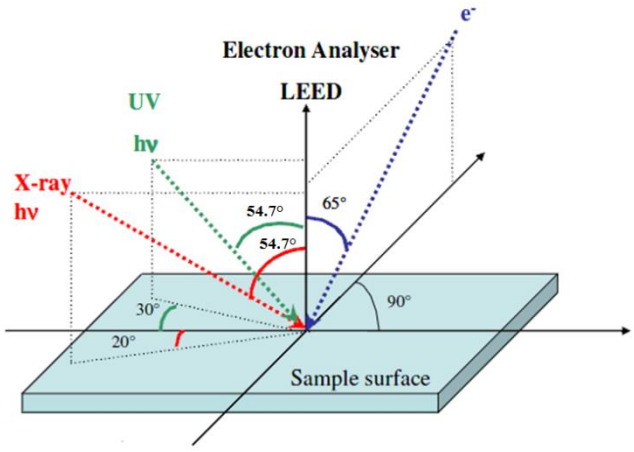

Figure 3.4: Excitation and collection geometry referred to sample's surface, for characterization techniques present on analysis chamber.

The analyzer is interfaced with a PSP RESOLVE power supply unit which receives signals from the analyzer and gives a digital output signal in terms of counts. Then, the acquisition software (PSP Collect) plots this output as a function of electrons KE (AES, UPS) or binding energy (XPS).

3.2.2 System for electrons spatial distribution analysis

The chamber is equipped with a reverse view type LEED (Low Energy Electron Diffraction), as shown in Figure 3.5.

It is provided with an electron beam gun that operates at energies ranging from 10 to 1000eV (typically at 20-200eV), with high brilliance and small spot thanks to the LaB_6 electron emitting filament. When in operation, the sample is positioned in front of a biased grid system that is constituted by five spherically shaped grids, which are concentric and critically aligned. The grids angular opening is about 100° to 120° and there is a central shadow angle of 10°, due to the presence of the coaxial electron beam gun. Pattern view occurs from the back of the grids, not in front of them, and it is collected, in a back view mode, by means of a photo or digital camera outside the UHV chamber. The overall system can be moved along the main axis of about 7cm in order to bring the optics out of the way when other analysis or thin film growth are carried out, as well as during normal sample transfer operations.

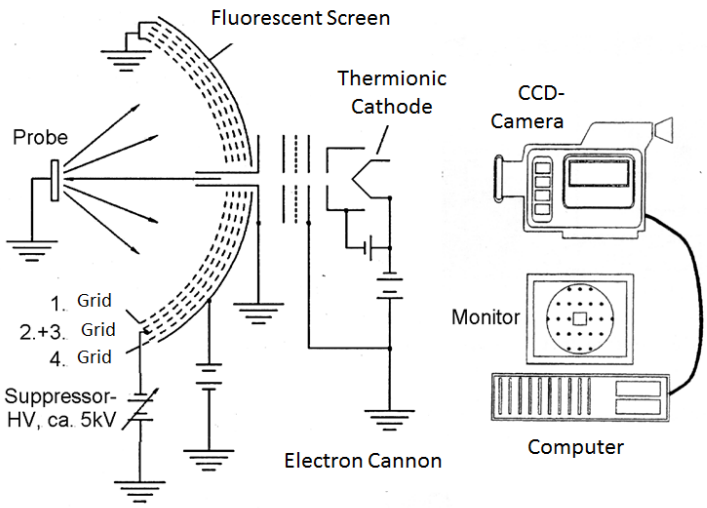

Figure 3.5: Outline of the LEED experiment's apparatus.

The excited emission is the line $K\alpha_{1,2}$ and the emission energy is 1253.6eV (phonon energy width ΔE=0.70eV). The continuum Bremsstrahlung spectrum is filtered by the insertion of a thin (1μm) aluminum foil in correspondence of the exit aperture, which also acts as shield to the high voltage of the anode for the sample surface.

The electron source (LEG62 ThermoVG electron gun), used as excitation source for AES, has a maximum beam energy of 5keV and a maximum current of 20μA: spot size can be as small as 5μm. The same source can be used to perform Scanning Electron Microscopy (SEM), which allows, by the monitoring of the secondary photons emitted in the Auger process, an image of the sample surface with a resolution as high as ~3μm.

Figure 3.6: The UV source lamp used in this work.

The UV source is a home-made He discharge lamp (see Figure 3.6), with a two-stages differential pumping (Alcatel 300 and primary stage pumping) employed to minimize gas load in the main chamber.

The ionization sources used in this thesis are HeI ($h\nu$ = 21.22eV) and HeII ($h\nu$ = 40.8eV). These lines are produced by a cold cathode capillary discharge and represent the resonance fluorescence produced when the gas is excited in the discharge and decays back to its ground state.

3.2.3 Ion Gun sputtering

Sputtering is both a cleaning and deposition process that allows to physically remove atoms from a surface by means of bombardment with ions at high pressure, in UHV conditions and at room temperature. The contaminants removal by sputtering with an inert gas is known as "etching". In this work the sputtering has been performed by an EX05 Ion Gun (Figure 3.7), constituted by the ion source, equipped with two tungsten filaments, an optical column and a scan plates.

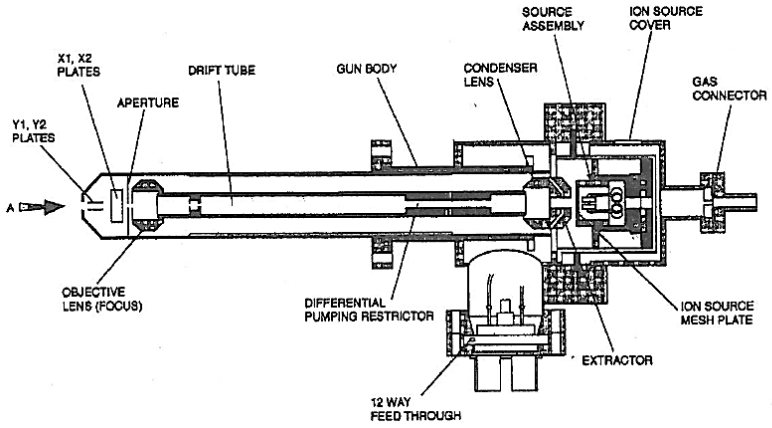

Figure 3.7: Schematic view of the EX05 Ion Gun.

The filaments are biased to a certain electron energy below the source potential causing the electrons emission. These electrons are then accelerated towards the source cage where interact with the high pressure gas (typically Ar) injected in the source. The mix of gas and ions thus produced, are then injected into the optical column of the gun by the potential on the extractor lens. The ions beam is collimated by the lenses present inside the optical

column, accelerated through the drift tube and then focused towards the sample by the focus lenses. At the end of the tube there is an aperture which defines the final beam diameter.

The pressure during normal gun operation is about $7x10^{-7}$ mbar, due to the high partial pressure on injected gas. During the preparation by sputtering of the samples described in this thesis, it has been used Argon as inert gas, an ion energy between 0.5 and 3KeV, with a raster of 3x3mm.

3.2.4 Tools for monitoring chamber status and supersonic beam flow

Residual gasses in main chamber can be monitored by means of a gas analyzer. It is a Smart-IQ+ model from VGgas and is based on a quadrupole mass spectrometer, covering the range 1-200amu and software controlled by means of the interface electronics.

3.2.5 Hydrogen Generator

The H_2 used as gas carrier in the supersonic beam was produced by a compact hydrogen generator, the Hydrogen Genius TH300-6 BAR (Figure 3.8). The device uses an electrolytic cell with Proton Exchange Membrane (PEM) which generates hydrogen from the electrolysis of deionized water.

Figure 3.8: Hydrogen generator used in this work.

The hydrogen produced is mixed with water that must be removed via a gas-liquid separator (GLS): the hydrogen is dried through a filter of silica gel commonly at a dew point less than -60°C. A further purification is ensured by a molecular sieve filter. It is possible to control the H_2 pressure in a range of 0.3-6 bar, as long as the internal pressure is maintained at 6.5 bar.

3.3 Supersonic beam apparatus

A supersonic beam apparatus is essentially composed of a two stage vacuum system, having as a basic requirement the possibility to manage high gas load. In the first chamber a maximum pressure in the 10^{-4} mbar range is maintained by two turbomolecular pumps (Varian TV1001 Navigator and Leybold MAG W830) of 700-1000 l/s. A pressure of 10^{-7} mbar is reached in the second chamber by a turbomolecular pump (Varian TV301 Navigator) of 300 l/s (see Figure 3.9 and Figure 3.10).

All the turbo pumps are connected to a dry primary pump (Edwards QDP80 (6kW) connected to a QMB500 Booster Rebuilt), composed of a rotary pump and a mechanical booster with pumping speed up to $150 m^3/h$.

The supersonic source is mounted in the first chamber while the second chamber acts as an interface between the beam chamber and the final UHV deposition chamber, working as a differential pumping stage. Two collimators define the beam geometry and axis. One is positioned between the first and the second chamber on the axis of the vacuum system, and the other between the second chamber and the analysis chamber. The first is the real skimmer used to extract the supersonic “molecular” beam out of the zone of silence of the supersonic expansion, it also works as a diaphragm between the two vacuum chambers.

The second collimator, shaped as the first skimmer, maintains a differential vacuum between the second and the analysis chamber and defines the size of the beam spot downstream of the generation apparatus.

The beam source has to be aligned on the axis defined by the two skimmers every time that the source itself is changed. To this end, it is usually mounted on X,Y,Z transition stage by means of which it is possible to optimize the beam performance.

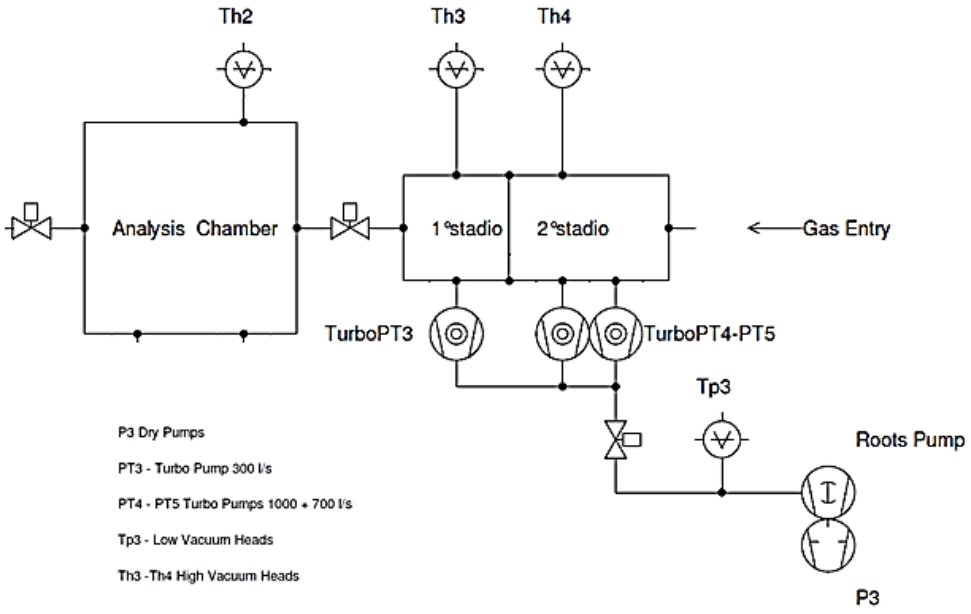

Figure 3.9. Scheme of the Supersonic Molecular Beam apparatus.

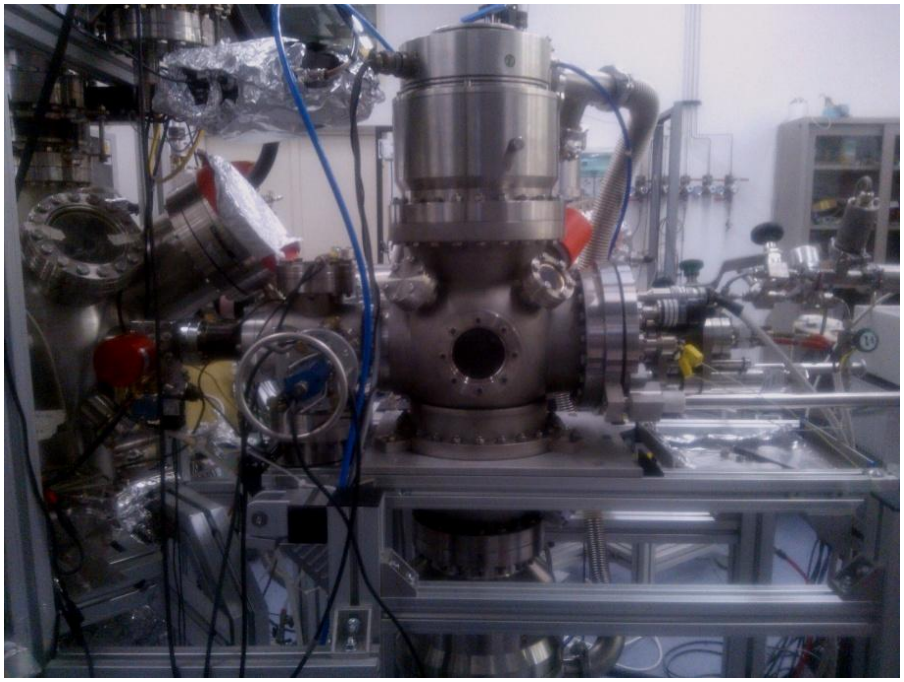

Figure 3.10: SuMBD apparatus connected with the analysis chamber.

3.4 Supersonic beam source

The details of the supersonic beam source are drawn in Figure 3.11. It is essentially a quartz tube, having internal and external diameters of 8 and 10mm, respectively and a length of about 12cm: the back end is used to inject the high pressure gas carrier, the front end is closed and a channelled opening forms the nozzle. The latter has typically a length that is 4-5 times the diameter the latter being about 60-100 μm The source is shielded by a thin Ta foil, which is resistively heated and can reach a maximum temperature of about 1000°C.

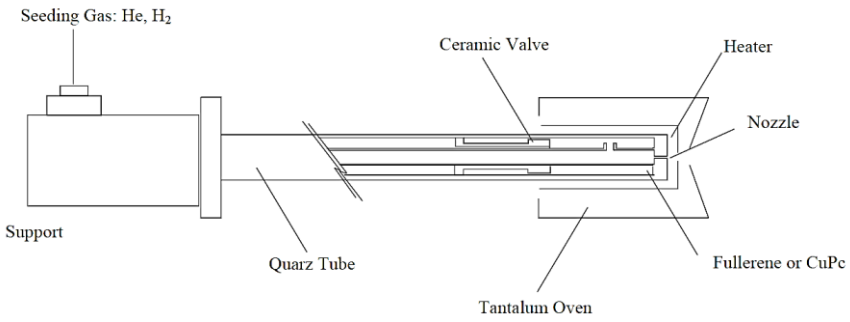

Figure 3.11: Schematic view of the supersonic beam's source.

A second heater is placed near the nozzle, so that the supersonic expansion can be controlled by setting the source temperature in two points: at the nozzle point we will refer to as the source "head" temperature, while a thermocouple positioned at the end of the Ta foil (near the ceramic valve) measures the source "body" temperature. The head value better defines the temperature before the supersonic expansion, while the body value is related to the sublimating process of the seeding material. The latter is placed in the region near the nozzle: the supersonic beam production proceeds via the introduction of the high-pressure gas (helium or hydrogen) in the quartz tube.

As stated before, the exiting molecular beam is selected by a sharp-edged conical collimator (the skimmer), the aperture of which was 0.5 mm for the first skimmer and 2 mm for the second during the performed experiments. The skimmer to source distance is a function of the beam's production conditions, so that in this work, taking into account that the nozzle aperture is about ~100 μm, the carrier gas pressure in the range of 1000-1300 mbar, the background pressure in the range of $1x10^{-4}$ - $3x10^{-4}$ mbar, the skimmer-to-nozzle distance is set at about 1cm, according to empirical rules. Distance between the source and

the sample surface is 54cm, and the deposition is carried out maintaining the surface normal to the beam axis; the deposition rate was monitored by placing a quartz microbalance in the second source chamber, at a distance of 15cm from the source.

The supersonic beam source is mounted on a three stages translational (x,y,z) manipulator: in this way it is possible to carefully align the source with the skimmer. Previous to this work, the used beam source has been characterized and calibrated in terms of the relationship between particles KE and buffer gas pressure. Since the supersonic beam source could not be characterized in-situ, in previous works it was inserted in a different apparatus [35,52], equipped with a time of flight mass spectrometer (TOF-MS) and laser photo-ionization spectroscopies, better described hereafter.

3.5 Time of Flight Mass Spectroscopy (TOF-MS)

TOF-MS technique combined with laser photo-ionization is an useful approach for the characterization of the Supersonic Beam in terms of beam composition-particles velocity versus carrier gas pressure. The basic principles governing a TOF experiment are simple: ions, having different masses, when accelerated to the same KE have different velocities so that, after traveling a defined distance, they can be separated by analyzing their arrival time. The typical configuration of a TOF mass spectrometer is that proposed by Wiley and McLaren [50]. If it can be assumed that all the ions have no initial velocity and are formed in a plane parallel to the accelerating electrodes, their flight time depends only on the charge/mass ratio. In the real case, one should take into account two main factors affecting this simple picture: the finite volume where the ions are formed and their velocity distribution. The first factor gives rise to a spatial spread, due to the finite dimension of the ionization source (in this work a laser source), so that ions formed at different points will fly through different paths and will reach the detectors at different times, even though they have the same mass and are isobaric. Obviously, also the second factor introduces a time spread, since isobaric ions that have different velocity components along the instrument axis (but are generated at the same point) will arrive at different flight times. In particular, for what concern spatial focusing, this is a critical parameter, and the designing and construction of such instrument was optimized in order to achieve a second-order spatial

focusing (a detailed analysis including all the construction parameters of the present TOF apparatus can be found in ref. [51]).

The overall resolution of a TOF-MS spectrometer depends on time and spatial spread, the compensation of which being a critical factor, affecting the performance of the instrument. Resolution is expressed as the ability of the instrument of separating ions with similar masses, and it is usually written as m/Δm, that is the highest mass that can be resolved by 1 amu. Masses analyzed by this technique include also isotopes, so that it is of interest to develop instruments with a resolution high enough to discriminate them. Typical commercial instruments used in surface science have resolution in the range of several thousands.

In the present work we took as reference the TOF characterization carried out by M.V. Nardi for H_2TPP and by L. Aversa for C_{60} in their PhD thesis. M.V. Nardi analyzed H_2TPP KEs versus the pressure and by using H_2, He and Ar, as shown in Figure 3.12.

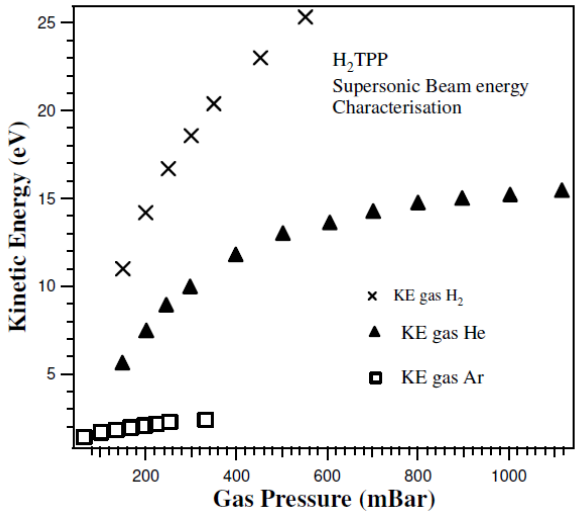

Figure 3.12: KE as a function of the pressure for the H_2TPP molecule seeding supersonic beams having H_2, He and Ar as a carrier gas [35].

He found that the KE constantly increases by increasing pressure until it reaches a plateau, where the velocity of the seeding particles and carrier gas molecules are substantially equal. The maximum KEs reached for H_2, He and Ar are respectively 25eV, 15eV and 1.5eV [35]. Considering the partially fluorinated tetraphenylporphyrin used in this thesis, $H_2TPP(F)$, due to the higher ionization potential with respect to the H_2TPP molecule it has

not been possible to perform TOF analysis. Taking into account the higher molecular mass, we can estimate that the maximum KEs for H_2, He and Ar are respectively 40eV, 25eV and 2.5eV [35].

Regarding fullerene, L. Aversa compared a fullerene beam in two different carrier gas, He and H_2. She demonstrated that the seeded molecules increase their velocity by increasing the pressure of the gas carrier (He) from 250 mbar to 1500 mbar (Figure 3.13-a), keeping a constant temperature at 700°C. As mentioned in the Chapter 2, this effect, aerodynamic acceleration, is due to the reduction of the slip in velocity between the light He carrier gas and the heavy seeded species when the dilution increases. She estimated, moreover, that fullerene molecules can reach a KE of 5eV in He gas carrier. Instead, when fullerene is seeded in hydrogen the maximum achievable KE is about 35-40eV (Figure 3.13-b) with our SuMBD apparatus [52].

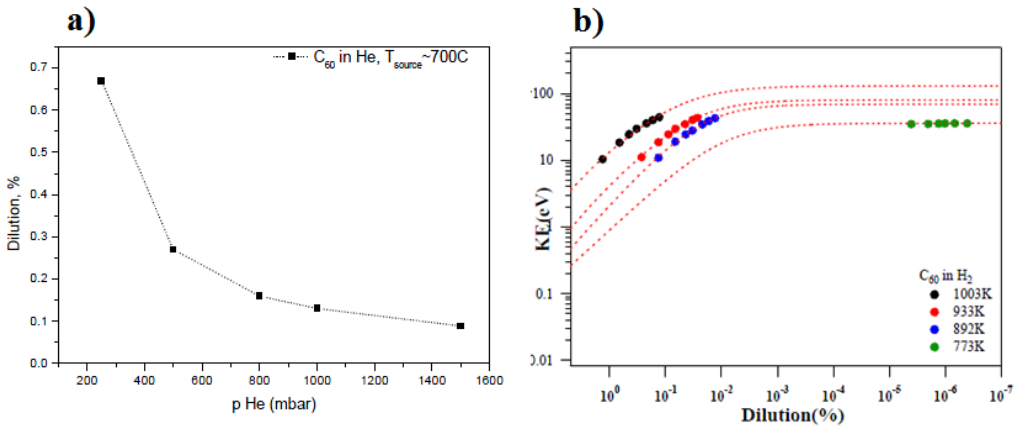

Figure 3.13: a) Dilution (in percentage) C_{60} seeded particles (gas carrier He, T~700°C); b) C_{60} KE versus dilution (seeding) when H_2 is the gas carrier , at different source temperatures [52].

3.6 Characterization method

Surface in-situ characterization experiments have been carried out at different stages of synthesis/deposition on samples. This work deals with electron spectroscopies that are carried out by using two kinds of probes, electrons and photons. The detection of the emitted electrons occurs in two ways: electron energy distributions (XPS, AES, UPS

techniques) are measured by means of the energy analyzer, the output of which is electrons KE, while their spatial distribution is determined by means of diffraction techniques, i.e. LEED in this work. Ex-situ studies have also been carried out, in particular by Atomic Force Microscopy, Raman Spectroscopy, TEM and Microfluorescence, as discussed in the next paragraphs.

3.6.1 A general introduction to surface electron spectroscopy

Several surface electron spectroscopies (SES) were used to characterize in-situ and ex-situ the synthesized and grown films, which will be briefly described in the following. SES are considered surface spectroscopies due to the nature of the electron-matter interaction and the regime they are operated.

Electrons that are emitted from a solid surface undergo several collision and interaction processes with matter before exiting the sample surface. In particular, electrons with a kinetic energy (KE_{el}) in the range of 10-1000eV undergo diffusion processes in the solid and their mean free path is of the order of about 10Å. Let's consider now the electron escape probability as a function of the creation's depth. If α is the take-off angle (i.e. the angle between the analyzer and the sample surface) this probability can be written as:

$P = exp(-d/\sin\alpha)$.

As is clear in Figure 3.14, the large majority of the electrons leaving the surfaces comes from a maximum depth of 4λ.

As can be seen, the escape depth is in the 5-20Å range: taking into account the previous considerations, only the upper surface contributes and the electrons signal comes from a maximum length 80Å. It is noteworthy that UHV conditions are mandatory for SES, and not only for the strong interaction of escaping electrons with surrounding atmosphere (that would lead to energy loss processes). In fact, assuming that the sticking coefficient for the most common residual gases in a vacuum chamber is 1, at a chamber pressure of 10^{-6} mbar it takes only 1sec to completely cover the whole surface, i.e. a coverage of 1 Monolayer (ML) on the surface.

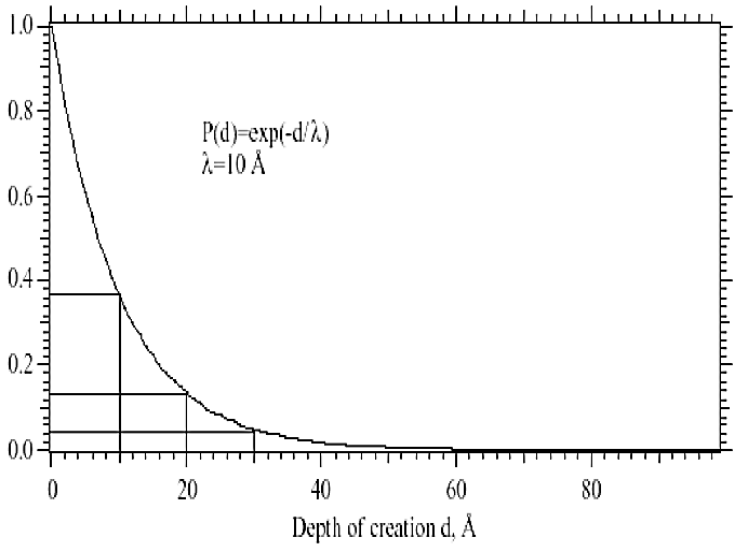

Figure 3.14: Probability of electrons escaping without loss as a function of their creation depth, for SES.

Figure 3.15 represents the electron escape depth as a function of their KE_{el} (this curve is known as the "universal curve").

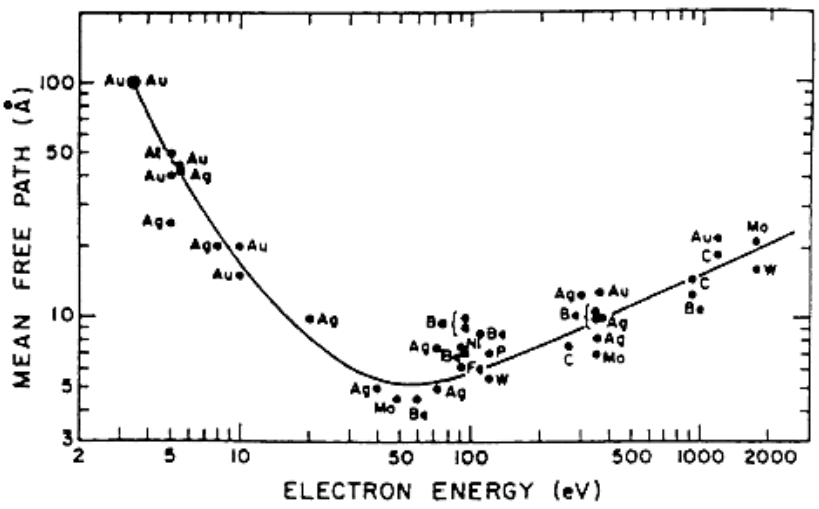

Figure 3.15: Electron escape depth as a function of their KE for various metals.

For pressures in the range of 10^{-9} mbar, it takes about 1000s to have the surface fully covered, so that pressures in the low 10^{-10} mbar range are necessary to perform a surface spectroscopy experiment for an extended period of time. Emitted electrons can be characterized in energy (see Figure 3.16-a for an example of a photoelectron spectrum) and

spatial distribution (see Figure 3.16-b). In the first case, instruments are generally based on electrostatic condenser (cylindrical or hemispherical), biased in such a way that only electrons having specific velocity (i.e. kinetic energy) will reach the final detector, while the others will hit the internal surface of the condenser. Energy analysis is thus achieved by using a voltage ramp applied to the condenser plates.

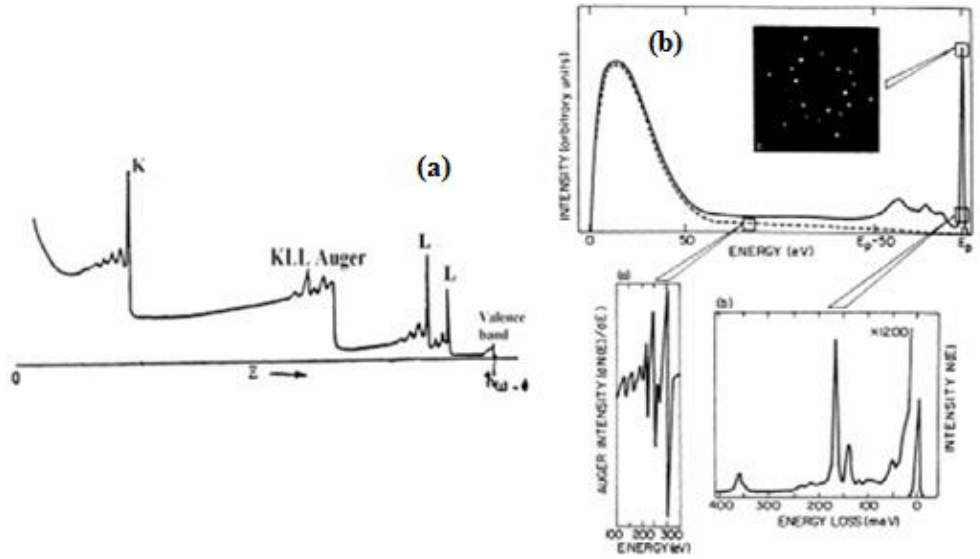

Figure 3.16: a) A photoelectron spectrum showing the several electrons emitted by the surface: core electrons (K and L shell), Auger electrons, VB valence band electrons. b) Energy distribution of scattered electrons: example of the Rh(111) surface covered by ethylene [53]. The elastic peak and together with the losses and Auger peaks are outlined in the panels.

3.6.1.1 X-Ray Photoelectron Spectroscopy (XPS)

This technique is based on the photoelectric effect, by means of which when a surface is hit by X-ray photons, their energy (from few hundreds of eV to thousands of eV) can be absorbed by an electron of a core level, thus escaping original parent atom, and from the surface sample.

Figure 3.17 is an outline of this process: electrons are generated from a core level and leave the surface with a KE_{el} that depends, in a first approximation, from the initial photon energy, the binding energy and the work function of the solid.

The fundamental relationship that describes the photoemission process traces that used for the first photoelectric experiments:

$$KE_p = h\nu - BE - \phi \quad (19)$$

where KE_{el} is the final electrons kinetic energy, BE the binding energy they had in the solid (i.e. the binding energy of core level from which they were ejected) and ϕ the work function of the system (considering the sample in electric contact with the analyzer, and at the same ground potential).

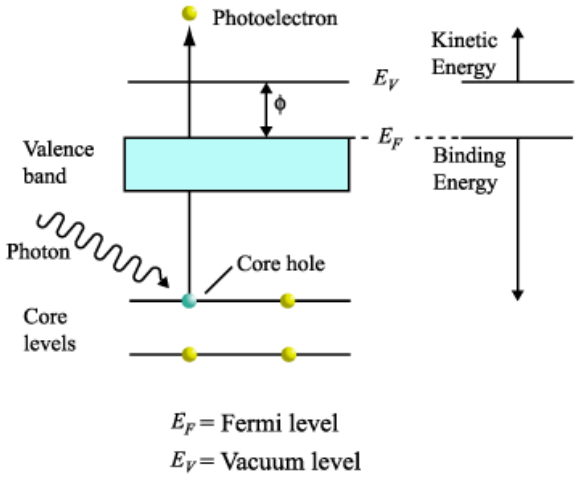

Figure 3.17: Scheme of the photoemission process.

This relationship is based on the so called *one-electron approximation.* A more accurate description of the processes involved in the photoelectron process requires to take into account:

1. the relaxation processes occurring in the excited parent atom that has N electrons at the beginning, while in the final state becomes an ion having N-1 electrons;
2. the energy loss processes that electrons experience while moving in the solid (electron-phonon coupling and plasmon losses).

These processes lead to a final energy distribution that is composed of main features, reflecting the core level density of states, and secondary peaks, due to transport processes. The photoemission process is so fast that is usually described under the so-called sudden approximation: the system cannot reach the equilibrium state prior to the photoemission, thus the final state can have two configurations. In the first configuration one electron lies

in one atomic excited state, while in the second an electron is ejected, leaving the atom double ionized. These processes decrease the KE_{el} of the photoemitted electrons and give rise to satellite peaks, such as the so-called shake-up and shake-off features. A detailed description of these processes is beyond the scope of this thesis, and can be found in Ref. [54].

The photoelectron spectrum is obtained by measuring the KE_{el} of photoemitted electrons and plotting the intensity (usually expressed as counts per seconds) versus the KE_{el}. It consists of several features: core-hole lines, shake-up and shake-off excitations, Auger peaks, valence band peaks and secondary peak due to minor physical processes.

XPS is a powerful technique in surface science since it allows the observer to get information about the chemical properties and the elemental composition of the studied surface (see sketch in Figure 3.18).

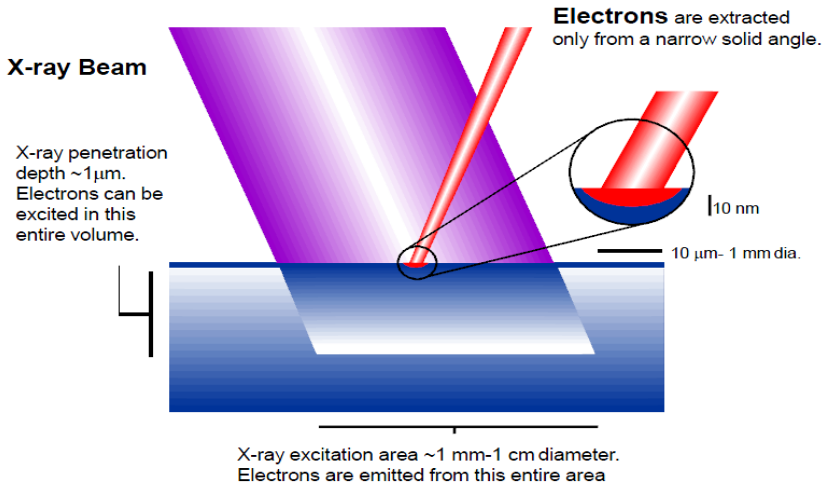

Figure 3.18: XPS small area detection.

Elemental characterization is possible due to the intrinsic uniqueness of each atom electronic configuration, just by evaluating the Binding Energy position.

Quantitative analysis can be performed measuring the peak area associated to an element, weighted by a sensitivity factor that takes into account the excitation efficiency of each element. For a homogeneous sample with an isotropic elastic diffusion of the photoemitted electrons, the photocurrent intensity can be expressed as:

$$I_i(KE_{el}, i) = I * N_i * \sigma_i(k) * \lambda(KE_{el}) * H \quad (20)$$

where I is the incident photon flux, N the atomic concentration of the i-species, σ_i the ionization cross section referred to the level i and to the incident photon, $\lambda(KE_{el})$ the escape depth length at the KE_{el}, H an instrumental factor. Since ab-initio calculation of some of the factors in equation (20) is quite difficult, the general procedure for this type of analysis is the use of calibrated quantities and of the atomic sensitivity factors (ASF), which take into account the excitation probability of the element i, for a certain impinging photon. In such a way the relative atomic concentration of the element i can be expressed as:

$$N_i = \frac{A_i}{ASF} \tag{21}$$

in which the peak intensity is its integrated area A_i. The ASFs, which are also defined for the AES peaks, are tabulated taking as a reference the element i in a standard state [55].

3.6.1.2 UV Photoelectron Spectroscopy (UPS)

As excitation sources UPS uses UV photons the energy of which ranges from few eV up to few hundreds of eV. The main difference from the XPS spectroscopy hence is that only the most external electronic levels of single atom, molecular bands (Highest Occupied Molecular Orbital, HOMO, for example) of aggregates and high-laying energy bands in the case of solids (valence band for semiconductors, for example) are involved in the process of photoelectron production. UPS has a probing depth of ~15Å and it is therefore used to extract important information about interaction processes involving the external electronic levels, [56].

The photoelectric effect generates free electrons with a KE_{el} which depends on the exciting photon energy *hv*, the work function of the sample (φ, that is the minimum amount of energy needed to remove an electron from the sample), the binding energy of the excited electron and the inelastic scattering events in the sample.

Figure 3.19 [57] represents a typical UPS spectrum, that can be divided in two regions:

- the left part is the low KE_{el} secondary-electron region, that represents the secondary electron cut-off (SECO). This cut-off, named photoemission onset, is associated to the vacuum level (E_{vac}), since electrons with less energy cannot come out from the

solid. This onset gives the position of E_{vac} with respect to other photoemission features such as the highest occupied molecular orbital (HOMO).

- the right part is the high KE_{el} valence band region, typically characterized by the presence of Fermi level (for metals) and VB offset, as well as HOMO (for molecules).

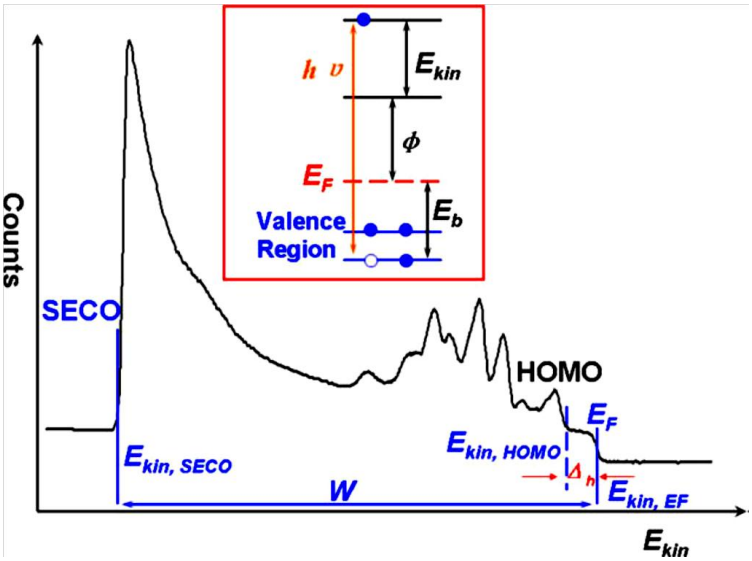

Figure 3.19: Typical UPS spectrum. The inset shows the photoelectron emission process in a PES experiment [57].

From the spectrum is possible to calculate the sample work function in according to the following equation (22):

$$\varphi_{sample} = h\nu - w = h\nu - \left(E_{Kin,EF} - E_{Kin,SECO}\right) \quad (22)$$

where $E_{Kin,EF}$ and $E_{Kin,SECO}$ are the KE_{el} of the sample Fermi level and the SECO respectively, and w is the spectrum width (the KE_{el} difference between E_{EF} and SECO).

In the case of a semiconductor, the Fermi level is located within the band gap (Figure 3.20), so that it is not possible to calculate the work function directly from the spectrum, but we have to consider the ionization potential (*IP*), calculated as the energy difference between the leading edge of the HOMO peak and the vacuum level.

In this case the work function can be calculated as difference between *IP* and the quantity ε, defined as the difference between Fermi level and HOMO:

$$\varphi_{sample} = IP - \varepsilon \quad (23)$$

Work function changes in the order of 1 eV are typical in metal and semiconductors depending on the surface conditions. These variations are generated by electric dipoles at the surface, which can change the amount of energy required for an electron to leave the sample.

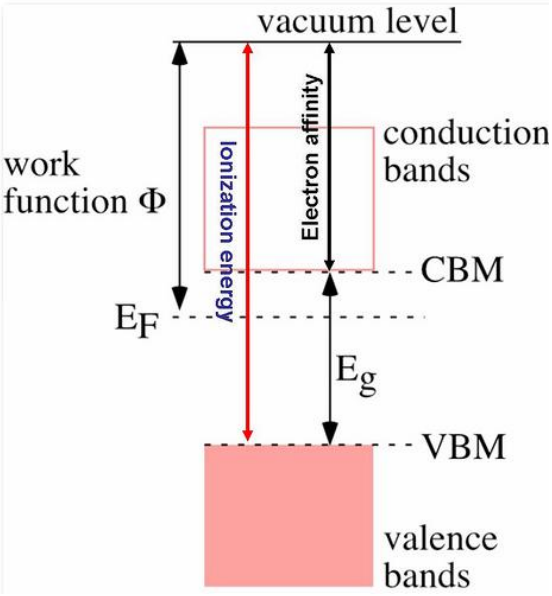

Figure 3.20: Scheme of the energy levels in a semiconductor.

For organic materials, which haven't a well-defined Fermi level, ionization potential (*IP*) is calculated from the UPS spectrum as the difference energy between the HOMO and the vacuum level. In a similar manner to the equation (22) *IP* is calculated by the relation:

$$P = h\nu - \left(E_{Kin,HOMO} - E_{Kin,SECO}\right) \quad (24)$$

where $E_{Kin,HOMO}$ is the linear extrapolation of the high-KE of the HOMO peak [58].

Irrespective of the nature of the sample analyzed, for a correct measurement of the SECO, it is necessary to take into account the secondary electrons of the analyzer as well, generating by the impact of the sample photoelectrons with the surface analyzer. These electrons are superimposed to the secondary edge of the sample spectrum and make difficult to determine the position of the secondary edge of the sample. To overcome this problem, an accelerating potential (Bias) is applied between sample and analyzer: electrons coming from sample are accelerated and the spectrum is shifted ahead respect to the

analyzer secondary electrons in order to distinguish sample and analyzer secondary edges. In this work, we applied for all the characterizations a bias of -7V.

3.6.1.3 Auger Electron Spectroscopy (AES)

Auger [59] is a three-particles process that leads to the emission of a secondary (Auger) electron after initial emission of an electron from a core level of an atom. The two processes (emission of an electron from a core level and the Auger emission) are independent from each other and are produced by the initial excitation induced by radiation or electron bombardment. Figure 3.21 summarizes the basic scheme of the Auger emission for an atom in a solid.

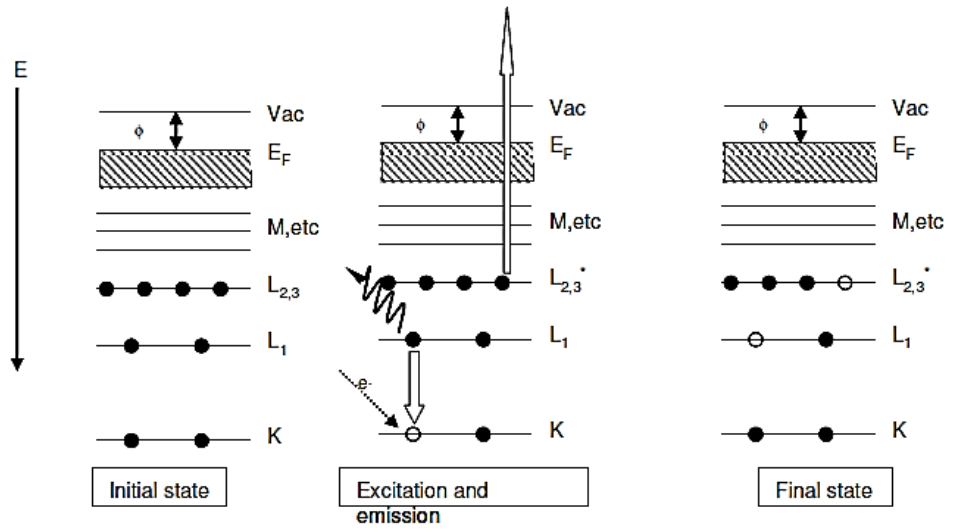

Figure 3.21: Schematic energy diagram of the Auger process in a solid.

On the left is represented the initial state, with the valence band filled up to the Fermi level, the core levels K,L,M fully occupied and the work function being ϕ. When a photon, or an electron having energy in the range of 3-10keV (that is larger than the binding energy of a core level), impinges on the sample it can create a hole in a core level (in this case the K shell).

This hole is immediately filled up by an electron coming from a shallower level (the L_1 shell) and the energy released (BE-EL_1) can be dissipated either by the emission of a photon (radioactive decay), or by energy transfer to a second electron, the so called Auger

electron. The KE_{el} with which the electron emerges from the surface is also a characteristic of the atom and can be represented in its final value by

$$E_{L1L2,3} = BE - E_{L1} - E_{L2,3}{}^{*} - \phi \quad (25)$$

being ϕ the sample's work function. It's worth that the binding energy of the level $L_{2,3}$ is not that of the unperturbed atom, because of the relaxation effects occurring after the first ionization step, which slightly changes after this process.

Notation used for labelling the Auger peaks reflects the three electron process, so that for a transition involving the deep level K and two shallow levels L, the transition's symbol will be KLL or better $KL_1L_{2,3}$, where:

K→(1s) location of core hole

L_1→(2s) origin of relaxing electron

$L_{2,3}$→(2p) Auger electron that leaves the ion

Radioactive and electron emission are competitive processes. In particular, for elements at high atomic numbers Z one of the commonly observed decay is the emission of photons (X-ray fluorescence), more likely for deep core holes (i.e. those at a higher binding energies). For low Z elements, on the other hand, Auger electron emission is more probable, as shown in Figure 3.22, AES is therefore a technique suited for species low atomic numbers.

A quantitative analysis based on Auger peaks gives information about the chemical composition at the surface. The emission electron current can be written as:

$$I_i = I_p * N_i * \sigma_i * \rho * \gamma * R * H \quad (26)$$

where I_i and I_p are the measured emission of electrons in the peak i and the incident electron currents, respectively; N_i the atomic concentration of the atom i; σ_i the ionization cross section for the level K; ρ the KLL auger transition probability; γ the electron escape depth; R the backscattering factor and H the instrumental factor (as discussed for XPS).

Among the parameters that appear in this formula, R, which is a complex function of material and incident energy, is not simple to predict and the whole ab-initio calculation,

with the same considerations made for the photoelectron current, isn't often performed. For practical analysis the same procedure applied to XPS peaks is defined. Usually relative sensitivity factors (RSF) are used and the electron current for an emitting atom is written as $I=I_{measured}/RSF$.

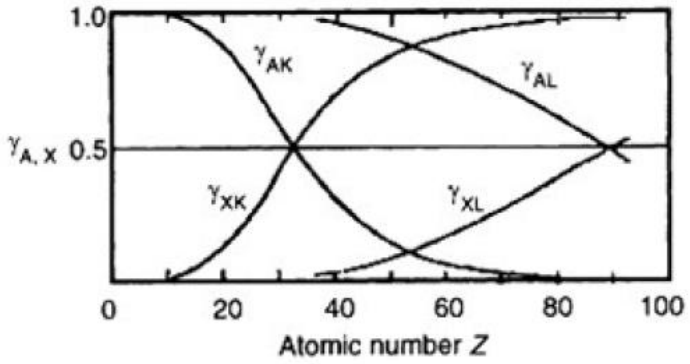

Figure 3.22: Emission probability (γ) of an Auger electron (A) and a photon X (X) as a function of the atomic number Z. The curves are related to the core level K and L.

3.6.2 Low Energy Electron Diffraction (LEED)

LEED is a convenient and widely used method to assess the presence of an ordered crystalline surface. The technique is based on the wave-particle duality of electrons in the 10-1000 eV range. In general, a LEED experiment is carried out directing a beam of low energy electrons (their energy is in the range from 10 up to 1000eV) towards a crystalline surface, and collecting the elastically back-scattered electrons. This technique, which works in a UHV environment and is one of the most used for surface structural investigations can be applied in two ways, qualitatively (looking at the position of the spots of the diffraction pattern, their brightness, size and rotational alignment) and quantitatively (recording the diffracted peak intensities as a function of the incident beam energy, and analyzing the corresponding curves).

According to the principles of waves-particles duality, the impinging beam of electrons can be regarded as a succession of electron waves with a wavelength given by the de Broglie relationship, incident normally on the sample. These waves are scattered by regions of high localized electron density, so that the surface atoms, responsible for these scattering events,

can be regarded as point scattered. If V is the potential by which the electrons are accelerated by the electron gun, their energy and impulsion are:

$$E = \frac{1}{2} m|\bar{v}|^2 = -eV \tag{27}$$

$$\bar{P} = m\bar{v} = \hbar\overline{k_0} \tag{28}$$

So that

$$E = \frac{\hbar^2}{2m} k_0^2 \tag{29}$$

The de Broglie wavelength associated with ψ_0 is

$$\lambda = \frac{2\pi}{k_0} = 2\pi \sqrt{\left(\frac{\hbar^2}{2m}\right)} / \sqrt{E} \tag{30}$$

The diffraction pattern is the result of an interference process induced by the two-dimensional periodicity of the crystal surface and gives a representation of the reciprocal lattice. For electrons having a KE in the 10-1000eV range, the de Broglie relationship gives a λ in the range of a few Angstroms, that matches the typical length-scale of lattice parameters of the crystalline structures of interest. Moreover, since the electron penetration depth is narrow, only the first 1-3 layers can be responsible for the diffraction process, so that LEED can be considered a truly surface sensitive technique.

In general, a highly ordered surface gives very bright and well defined spots, with low background intensity. The interpretation of LEEDs pattern should take into account that the diffraction image revealed by the screen is a picture of the reciprocal lattice. Therefore, for example, the Si(111) unit cell will lead to a hexagonal pattern, and hence the 7x7 reconstruction consists of a series of inner spots, the interpretation of which was given by McRae [60]. On the other hand, the analysis of the diffracted intensities requires a full understanding of the complicated multiscattering events that the electron undergoes during the collision [61].

3.6.3 Atomic Force Microscopy (AFM)

Atomic Force Microscopy is a technique of surface characterization based on the interatomic forces. The instrument uses a tiny "atomically" sharp probe (a tip), integrated to the end of a spring cantilever, to scan across the sample's surface in a raster pattern spawning an area of few nm^2 to some tenths of μm^2 large. The tip-sample interaction has a very low intensity with a force in the 10^{-9} N range: the detection system does not detect directly this force. By measuring the cantilever deflection, the topographic features of the surface can be estimated. According to the tip-sample interaction mode, it is possible to define three AFM methods: i) contact mode, the tip scans the surface in close contact (tip-sample separation of the order of Å) and the force on the tip is repulsive; ii) non-contact mode, using Van der Waals forces with a tip-sample separation of 10-100 nm; iii) tapping mode, suitable for soft samples, is gained by alternating placing the tip in contact with the surface and lifting it off to avoid dragging the tip across the surface.

AFM advantages such as high lateral resolution (few nm, limited by the tip dimensions), possibility of mapping several materials (conductive, insulating, biological samples as well as liquid samples) and operation in air or UHV, make it a technique of choice for a fast morphology characterization of surfaces.

The AFM characterization of the Si/SiO_2 planar surface functionalized with $H_2TPP(F)$ films was performed *ex-situ* by Prof. L. Cristofolini and his group at the Parma University. The sample morphology is studied by AFM in contact mode by a Thermomicroscope Autoprobe CP-R, acquiring the images on a 10x10 μm area with a 256x256 sampling points.

3.6.4 Raman

Raman spectra of C_{60} deposited on metal were taken ex-situ by DR. G. Speranza and DR. G. Baldi at the FBK Institute in Trento by a microprobe set-up (Horiba-Jobin-Yvon, model Aramis) using a He-Ne laser operating at 632.8 nm (power 10mW). This spectroscopy technique is based on inelastic scattering of monochromatic light, usually from a laser source. Photons of the laser light are absorbed by the sample and then reemitted with a frequency shifted up or down in comparison with original monochromatic frequency (ν_0). When the incident radiation is shifted to a lower frequency (lower energy), the scattered

light is called Stokes scattering. In this case the energy is transferred to the vibrational mode of the molecule which ends up in a higher vibrational energy state. Besides, when the incident radiation is shifted to a higher frequency (higher energy), in the so called anti-Stokes scattering, the energy is transferred from a vibrationally excited molecule, which ends up in a lower vibrational state after the scattering event. Moreover, a substantial number of the scattering photons are not shifted in frequency. These photons are generated in a process called Rayleigh scattering, where the excited molecule returns back to the same basic vibrational state and emits light with the same frequency ν_0 as an excitation source. Figure 3.23 displays the energy levels and transitions that are responsible for Rayleigh, Stokes, and anti-Stokes scattering [62].

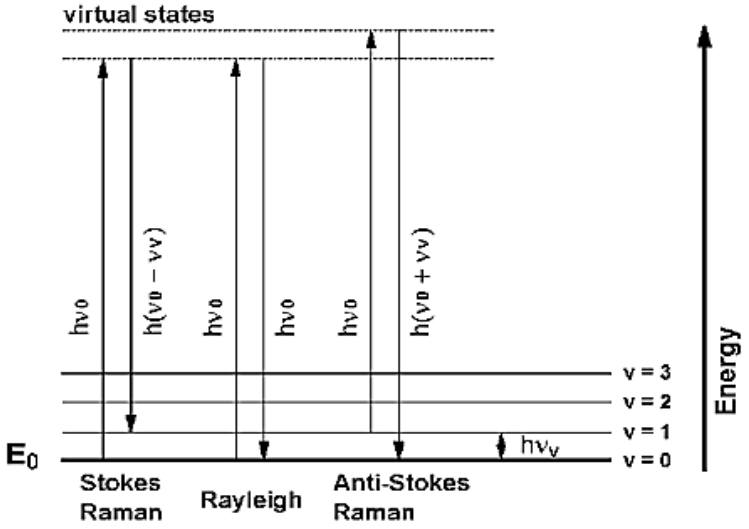

Figure 3.23: Energy-level diagram displaying Raman Scattering.

A Raman spectrum is obtained by exposure of a sample to a monochromatic source of exciting photons and measurement of the frequencies of the scattered light. It is necessary to consider that the intensity of the Raman scattered component is much lower than the Rayleigh scattered component, so that a highly selective monochromator and a very sensitive detector are required. A typical Raman apparatus consists of four major components: i) Excitation source (Laser); ii) Sample illumination system and light collection optics; iii) Wavelength selector (Filter or Spectrophotometer); iv) Signal processing system (detector, amplifier and output device).

The scattered light is collected with a lens and is sent through interference filter or spectrophotometer to the detector in order to obtain Raman spectrum of the sample.

3.6.5 Transmission Electron Microscopy (TEM)

Transmission Electron Microscopy is a technique widely used to get information about the sample morphology, crystallography and in some case also chemical properties. The high-resolution images result from the interaction between the sample and electrons at high energy in a vacuum chamber. A typical TEM apparatus consists of three components:

- the illumination system: it is composed by the gun and the condenser lenses which have to collect the electrons coming from the gun and transfer them to the specimen,
- the objective lens/specimen stage: the first are used to focus and magnify the image while the sample holder is inserted into those for imaging purpose.
- the imaging system: this uses several lenses (intermediate and projector lenses) to magnify the image coming from the objective lens and to project the image on to a phosphorescent screen.

To be analyzed by TEM, samples need to be thin enough to be crossed by electrons (electron transparency) and to hold out to vacuum conditions. For this purpose, before being inserted into the vacuum chamber, samples could be subjected to procedures such as dehydration, sputter coating of non-conductive material, cryofixation, sectioning and staining. TEM analysis of the samples described in this work have been performed by DR. G. Salviati group in IMEM-CNR institute in Parma by means of a JEOL 2200FS microscope operating in 200 kV.

3.6.6 Microfluorescence Spectroscopy

Fluorescence spectroscopy is a spectrochemical technique highly sensitive and selective, widely used in bio-molecular systems investigations. As shown in Figure 3.24, the fluorescence process is the result of the excitation of a sample from its ground state into a higher electronic one (S_1'), by absorbing an incident photon of energy $h\nu_{EX}$ (1). The excited state S_1' has a short lifetime (~10^{-9} sec) and its energy is partially dissipated giving

rise to a relaxed singlet excited state (S_1) (2). The fluorescence process originates from the state (S_1), following emission of a photon of energy $h\nu_{EM}$ (3). The energy of this photon is lower than the excitation photon $h\nu_{EX}$, so that the emitted light is observed at longer wavelengths than the excitation (i.e. absorption in UV region and emission in visible one). The difference in energy ($h\nu_{EX}$- $h\nu_{EM}$) is called the Stokes shift.

From an instrumental point of view, the fluorescence detection system is composed by an excitation source (xenon and mercury- vapor lamp), a wavelength filters to separate the emission photons from excitation photons and a detector that registers emission photons and produce an electrical signals or a photographic image.

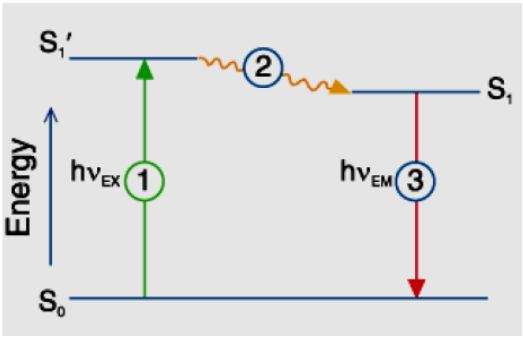

Figure 3.24: Fluorescence process illustrated by Jablonski diagram.

Fluorescence intensity is defined by the Lambert-Beer law and it is generally proportional to the concentration of the fluorophore, as described in the following equation:

$$I_F = \phi I_0(1 - 10^{-\epsilon_\lambda l C}),$$

where ϕ is the quantum efficiency, I_0 is the incident radiant power, ε_λ is the molar absorptivity, l is the path length and C is the molar concentration.

The microfluorescence spectra of the Si/SiO_2 planar surface functionalized with $H_2TPP(F)$ films was carried out *ex-situ* by Prof. L. Cristofolini and his group at the Parma University. The fluorescence spectra are acquired by an ad-hoc built microfluorescence setup around a TRIAX320 Horiba/Jobin-Ivon single pass monochromator. The integration times ranged from 1 to 30 seconds with maximum power density on the sample 1-2mW/μm^2.

3.7 Film synthesis: methods and processes

3.7.1 Substrate cleaning procedure

All the samples analyzed (silicon and metallic substrate, SiC-SiO_2 nanowires), before being introduced in the UHV chamber, are wet cleaned by employing a series of degrease solutions. This cleaning acts on the surface by a degrease cycle that removes the organic contamination.

More in details, the whole procedure follows these steps back to back:

- sonic bath of trichloroethylene [$ClCH=CCl_2$] at room temperature (RT) for 5 min,
- sonic bath of acetone at RT for 5 minutes,
- sonic bath of isopropyl alcohol at RT for 5 minutes,
- the samples were then outgassed at 350°C in UHV.

The mono- and poly-crystalline copper surfaces, when introduced in UHV chamber, undergo to further sputtering and annealing treatments. In particular, the sputtering process is necessary to remove sulfur inside the metal, using an Ar ion energy of 0.5KeV: during this treatment the sample gains a current of 900 nA and chamber pressure reaches a value of $7.5*10^{-7}$mbar due to Ar partial pressure.

After sputtering, the copper surfaces are recrystallized by a series of repeated flash annealing at 500°C for 15 minutes, necessary to recover the lattice damage induced by the sputtering. The quality and the purity of copper surface reconstruction is checked by AES and LEED.

3.8 General procedures for the analysis of the sample

The sample studied in this work were characterized both in-situ and ex-situ. AES, XPS, UPS and LEED were performed in-situ prior to the deposition to check the cleanliness and the reconstruction of the surface, as well as to have reference spectra for core levels and valence band photoemission. AES was used only for the C_{60} films characterization with an electron primary beam energy of 3KeV. XPS and UPS were carried out using the Mg Kα emission line at 1253.6eV, the HeI line at 21.22eV and HeII line at 40.8eV, respectively.

The final energy resolution of electron spectroscopies was 0.78eV for XPS, 0.1eV for UPS and 1eV for AES.

UPS and XPS were used for a quali-quantitative characterization. A quantitative analysis of the Porphyrin film evolution during and after deposition was carried out by collecting the main signals from surface sample at fixed pass energy of 20eV.

After thin film deposition and the mentioned in-situ characterizations, the samples were extracted to air. Ex-situ Raman analysis was carried out in air without any further surface treatment on C_{60}/Cu samples. Porphyrin deposited on Si/SiO_2 planar surface and on SiC/SiO_2 NWs was analyzed ex-situ with TEM spectroscopy, AFM and Microfluorescence spectroscopy.

3.9 Data analysis procedures

3.9.1 Background subtraction

AES spectra were background subtracted using an appropriate polynomial fitting curve: this procedure is reliable and not difficult, since AES peaks are small features superimposed to a continuum background. More complex is, on the other side, the background subtraction procedure for core level and valence band peaks. In general, background of core level photoemission peaks appears to be a "stepped" contribution to the whole spectrum, and depends on the extrinsic losses from electrons deep in the bulk Figure 3.25. In fact, only the electrons photoemitted from the surface can escape without undergoing loss, while the electrons deeper inside the surface escape with a reduced KE_{el} (and increased BE).

The procedure for fitting this background takes into account the Shirley's method: it is assumed that the background intensity at any point is proportional to the total spectral area at higher energy. This assumption implies then that for each photoelectron ejected at a particular KE_{el} there is a constant background to lower energies. Thus the true intensity at the energy E can be expresses as:

$$I_t(E) = I_{obs}(E) - k \int_0^E I_t(y)dy \quad (31)$$

where $I_{obs}(E)$ is the observed intensity at E (which includes the background).

The zero energy is assumed to be at the higher KE_{el} side of the peak where the background can be regarded as flat. The method for evaluating I_t is iterative and the constant K is determined by matching the calculated to the observed background, at some energy chosen below the peak.

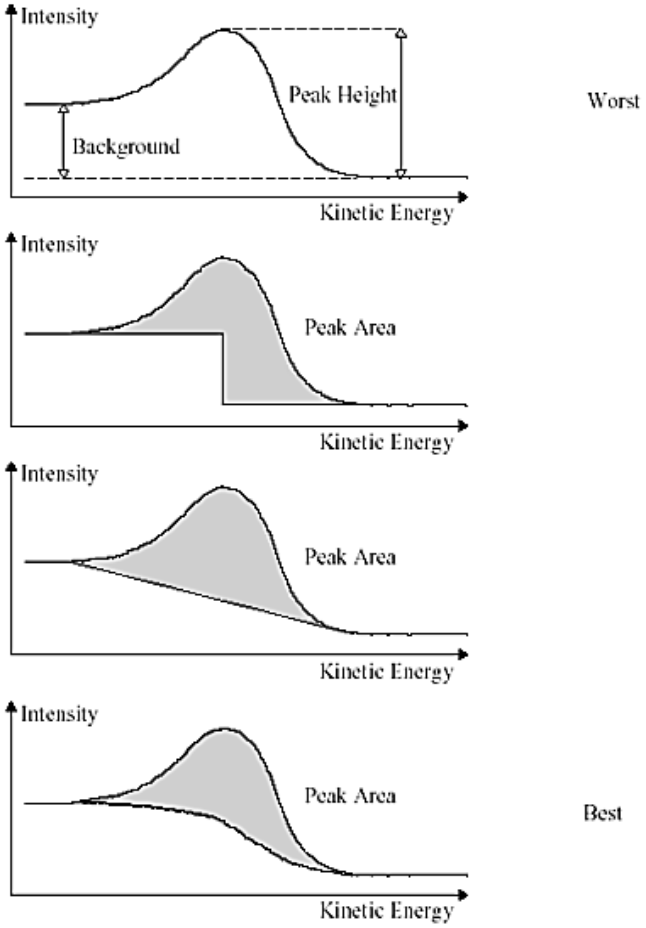

Figure 3.25: Examples of background subtraction in XPS line-shape analysis.

The BE determination in the XPS spectra can be simply calculated, taking into account the Koopmans' theorem, by subtracting the peak's KE_{el} to the photon's energy, and correcting this value by the work function. For a matter of convenience, the lines aligning is made by settling a reference line, in this case the emission from a gold clean surface, setting the Au $4f_{5/2}$ emission at a BE of 84eV.

UPS spectra (and ex-situ valence band photoemission spectra) were plotted against BE, which was calibrated taking into account the Fermi level edge of a clean gold sample, set at a BE of 0eV.

3.9.2 Core levels line-shape fitting and AES line shape analysis

The lineshape analysis of the core-level peak is commonly made by subtracting an appropriate background (taking into account the secondary electron emission) and fitting the peak's curve with a Voigt-like function [53]. For a metal core-level the line shape is not symmetric and is fully described by a Doniach Ŝunijć profile [53]. For semiconductors and insulators this profile resembles that of a Lorentzian that is then usually applied. This profile fits better to the photoemission peaks if it is convoluted to a Gaussian function, because it better simulates both the vibrational phonon broadening together with the instrumental resolution. The convolution is well described by a Voigt function:

$$V(X;Y) = Y/\pi \int_{-\infty}^{+\infty} dz \frac{e^{-z^2}}{Y^2+(X-z)^2} \quad (32)$$

which has to be generated, scaled and added to the analytical function describing the secondary electron background. Since the generation of the Voigt function involves a numerical integration, approximation methods were developed. In the present work the line-shape analysis is made using an algorithm based on the following asymmetric Gaussian-Lorentzian sum function [63]:

$$F(x,p,w,h,m,TS,TL) = h\{(1-m)e^{-ln(2)Q} + (m/1+Q) + TS[1-e^{-ln(2)Q}]e^{-6.9Q/TL}\}$$

where $Q = \left[\frac{2(x-p)}{w}\right]^2$ and m defines the % of Gaussian-Lorenztian (m=0 for 100% Gaussian).TL and TS are parameters for the asymmetric tail, so that TS=0 defines a symmetric G-L function. This function also includes the total FWHM, and the Lorentzian/Gaussian FHWMs. Spin-orbit splitting is also taken into account [53].

Similar to photoemitted electron, the Auger peaks show an amount of chemical shift that depends on the chemical environment experienced on the surface by the element. The

lineshape, however, cannot be treated in the same way, because the Auger emission contains multiple final state effects, that strongly complicate data interpretation: each one of the three electrons involved in this process is in fact associated with a multiple final state or relaxation effects. Auger peaks are then broader if compared to the photoemission ones. For this reason the AES peaks are numerically differentiated, and their recognition proceeds via comparison with known spectra [64].

Calculations based on the AES spectra include determination of the protective-oxide thickness. Considering I the intensity (area analytical integral) of the silicon AES peak in the oxidized sample, and I_0 its intensity in a clean silicon sample, the Si LVV line taken in the same AES conditions, the thickness x can be expressed as:

$$I = I_0 e^{\frac{-x}{\lambda}} \quad (33)$$

λ (escape depth for silicon electrons in silicon oxide) being 6±2Å.

Chapter 4
Thin film SuMBD controlled electronic properties

4.1 Introduction

In this Chapter we explore the potential of SuMBD approach to control and improve electronic properties of organic thin films suitable for application in organic electronics, in particular for the realization of organic field effect transistor, OFET. Besides the known ability of SuMBD to improve film morphology and structure, we will draw the attention to the analysis of chemical/physical processes at the organic/organic and organic/inorganic interfaces studying electronic properties with UPS spectroscopy. To better emphasize the potentiality of UPS to study the properties crucial for OFET performances, such as charge transfer and dipole formation at interfaces, the Sexithiophene (T6)/N,N-bis(n-octyl)-dicyanoperylenediimide (PDI-8CN_2) system will be first described. Afterwards, N,N'-1Hperfluorobutil dicyanoperylenediimide (PDIF-CN_2)/SiO_2-Si(100) system will be considered, investigating the enhancement of OFET performances achievable by the deposition of the organic material by SuMBD. An introduction to organic electronics is also given.

4.2 Field Effect (FET) and Organic Field Effect (OFET) Transistors

Originally, the first transistor was invented in 1947 by John–Bardeen and Walter Brattain at Bell Labs and it is composed of a block of germanium in contact with three gold wires [65]. A year later, in 1948, Shockley invented the bipolar junction transistor, which used alternating layers of *p*-type and *n*-type germanium to control the current flow. In 1954 germanium was replaced by silicon by Texas Instruments.

Junction transistors were used until 1961 when they were replaced by field effect transistors (FET), able to control the migration of electrons or holes into a conduction channel between source and drain electrodes. The field effect, that characterizes FET devices, is a phenomenon in which the conductivity of a semiconductor changes after the application of an electric field via a metallic gate normal to its surface [66].

Even though inorganic materials are still fundamental in modern electronics, nowadays organic semiconductors are materials of large interest in the development of electronic and optoelectronic devices, such as organic light-emitting diodes (OLEDs) and organic filed-effect transistors (OFETs). The latter, in particular, are promising for novel applications requiring large-area coverage flexible electronics, low-temperature processing and low cost [67].

In the last years organic semiconductors have been widely studied, in order to develop reliable devices that could overcome the limits of inorganic (as silicon, for example) in selected electronic applications. Indeed, it has been shown the deposition at room temperature of organic materials on plastic substrate by means of solution-based printing techniques [68], an approach widely extending the typical growth/deposition processes of the inorganic materials, occurring at higher temperatures. In the last 20 years the performance of the OFETs has improved enormously [69,70], reaching charge mobility values in the range of 0.1-10 $cm^2V^{-1}s^{-1}$ in the best OFETs [71-74].

An OFET is a device where an organic thin film semiconductor is deposited on top of a dielectric material, and an underlying gate (G) electrode, where the contacts are ensured by charge-injecting source-drain (S-D) electrodes (Figure 4.1). The current through the semiconductor is controlled by the gate voltage creating an electrical field through the dielectric [75].

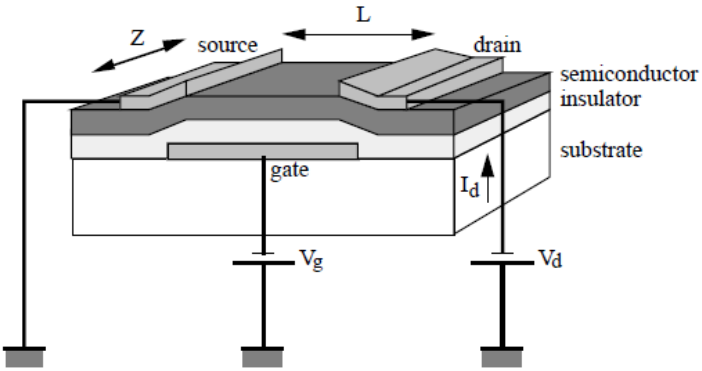

Figure 4.1: OFET three dimensional view [76].

On the basis of the electrodes-semiconductor positioning, it is possible to distinguish a *Top-contact configuration*, when the source and drain electrodes are evaporated on the top of the organic material, a *Bottom-contact configuration*, when source and drain are evaporated on the dielectric before depositing the organic semiconductor film (Figure 4.2) [77]

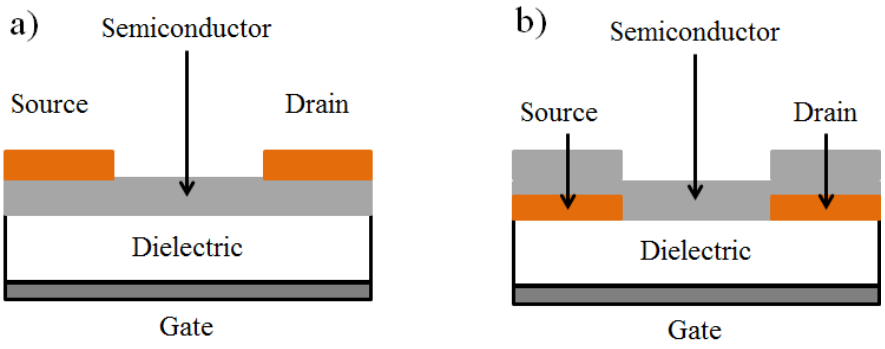

Figure 4.2: OFETs configurations: (a) Top contact. (b) Bottom contact [77].

When the voltage is applied to the gate (V_G) an electric field through the dielectric is created, leading to the formation of a charged layer at the interface of the semiconductor deposited above. Then, by applying a source-drain voltage (V_{SD}) one measures a current between the source and the drain (I_{SD}). Figure 4.3 shows the typical electric characteristics obtained in an OFET [77].

There are two regimes [77]: the linear regime, where the current is described by a parabola and is described by the relationship

$$I_{SD} = \frac{W}{L}\mu C V_{SD}\left(V_G - V_T - \frac{1}{2}V_{SD}\right) \quad (34)$$

and the saturation regime, where the source-drain current is independent of the source-drain voltage, described by

$$I_{SD} = \frac{W}{2L}\mu C(V_{SG} - V_T)^2 \quad (35)$$

where L is the length of the transistor from source to drain in the direction of the current flow, W is the width of the transistor, C is the capacitance per unit area of the insulating layer, V_T the threshold voltage, V_{SD} the source-drain voltage and V_{SG} the source-gate voltage. When V_{SD} and V_{SG} increase, at low drain voltage ($V_{SD} < V_{SG}$, equation 34) a linear current regime is observed, followed by a saturation regime (equation 35) when the drain voltage goes over the gate voltage.

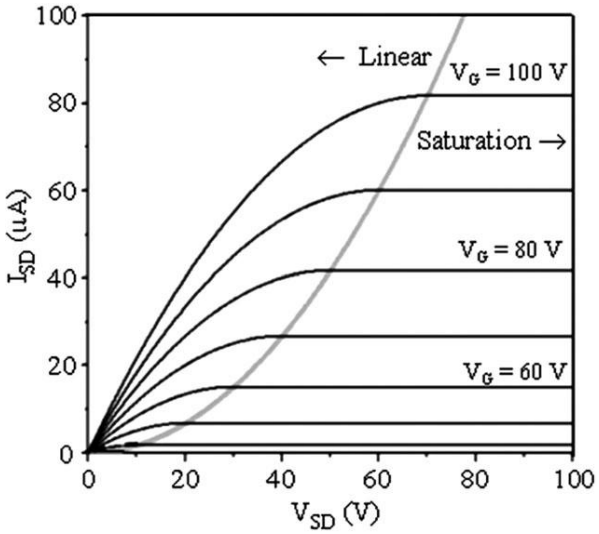

Figure 4.3: Typical electrical characteristics obtained in a field-effect transistor. The grey curve represents the boundary between linear and saturation regime [77].

Generally speaking, the application of a negative voltage between the gate and the source, greater than the threshold voltage of the semiconductor material, creates a *p*-type channel at the semiconductor-insulator interface, since the majority charge carriers is represented by holes. In fact, at the same time a negative voltage is applied between the drain and the source, determining a holes flow from the source to the drain. On the contrary, applying a positive V_{SD} and V_{SG}, a source-drain current is observed and the semiconductor is *n*-channel since the charge carriers are electrons (Figure 4.4) [75].

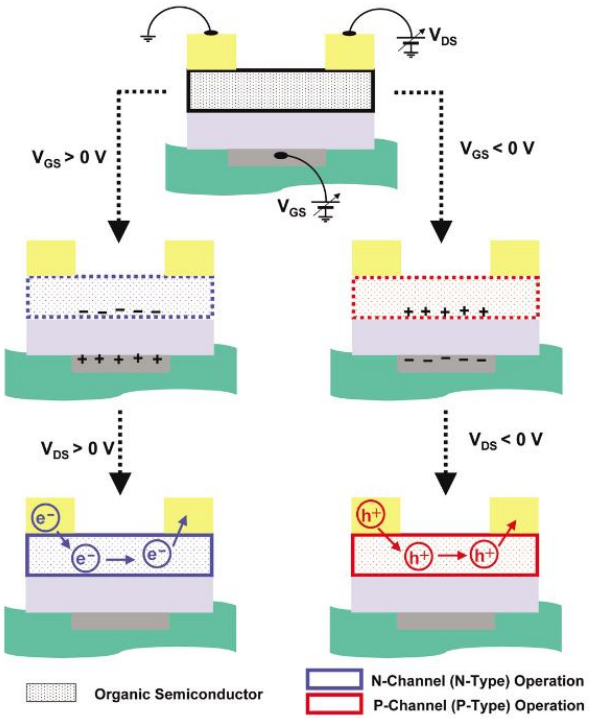

Figure 4.4: Scheme of *p*- and *n*-channel thin film transistor operation [75].

To better understand the *p*- and *n*-channel formation in case of organic semiconductors, we can consider the energy level diagram taking into account the Fermi level of source-drain metal electrodes and the HOMO-LUMO levels of the organic semiconductors, as shown in Figure 4.5 [77,78]. In this case, we are not dealing with energy bands but rather with single molecules showing π-conjugated molecular orbitals, giving rise to intramolecular charge transport and possibility of intermolecular charge transport.

We can consider three possible situations, depending on the V_G voltage applied to the gate.

a) V_G=0V, organic semiconductors intrinsically undoped in absence of gate voltage, so they will not show any charge carriers (Figure 4.5-a).

b) V_G<0V, the HOMO and LUMO orbitals of the semiconductor move upwards respect to the Fermi level of the metal, with the formation of positive charges at the organic semiconductor/organic insulator interface. If the HOMO level is close to the Fermi level, after the application of a voltage between drain and source (V_{SD}) a positive charges extraction by the electrodes occurs. In this case the material has a behavior typical of a *p-type semiconductor* (Figure 4.5-b).

c) V_G>0V, the HOMO and LUMO orbitals of the semiconductor shift down with respect to the Fermi level of the metal, with the formation of negative charges at the organic semiconductor/organic insulator interface. If the Fermi level of source/drain metal is close to the LUMO level of the organic semiconductor, by applying a voltage, V_{SD}, between drain and source electrons will flow from the metal to the LUMO. Organic semiconductors with the ability to conduct only negative charge carriers will behave as a *n-type semiconductors* (Figure 4.5-c).

Differently from the conventional silicon metaloxyde-semiconductor FET, the conducting channel does not correspond to the formation of an inversion channel, but rather to an accumulation layer at the insulator-semiconductor interface. In practice, the drain current voltage characteristic presents a linear behavior at low drain voltages V_d, and tends to saturate as the drain voltage approaches the gate voltage [76].

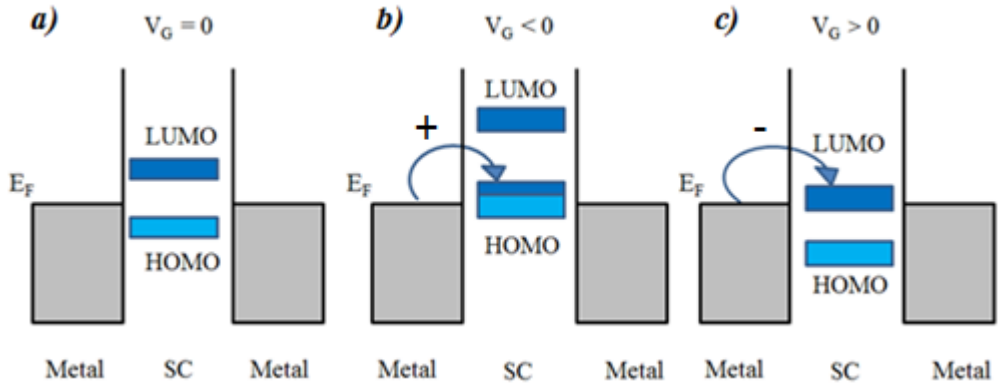

Figure 4.5: Schematic explanation of a working principle of an OFET with respect to applied voltage V_{SD}. (a) No charges injected. (b) Negative voltage applied to the gate and positive charges at the organic semiconductor/organic insulator interface. (c) Positive voltage applied to the gate and negative charges at the organic semiconductor/organic insulator interface [78].

4.3 Organic Semiconductors

The binding forces in semiconductors play an important role determining the different charge transport regimes. In inorganic semiconductors, the atoms are held together by strong covalent bonds, while in organics the molecules are kept together by weak Van der

Waal's forces. The organic semiconductors employed in OFETs devices are typically constituted by a high density of aromatic rings, characterized by electron delocalization in the aromatic structures. In aromatic rings, the overlapping of p_z orbitals lead to the formation of π-bonds, in which the electrons are delocalized and shared between the atoms on the ring's backbone (Figure 4.6). These delocalized π electrons in organic compounds are characterized by a freedom of movement which makes the organic molecules able to conduct electricity and behave as semiconductors.

Nowadays, π-conjugated organic oligomers and polymers are subject of great interest for OFET application, inasmuch they can function both as *p*-type, the most widely present, and *n*-type semiconductors. Whereas in the *p*-type the majority carriers are holes and they are characterized by high electron affinity, in the *n*-type most carriers are electrons and they show a low ionization potential.

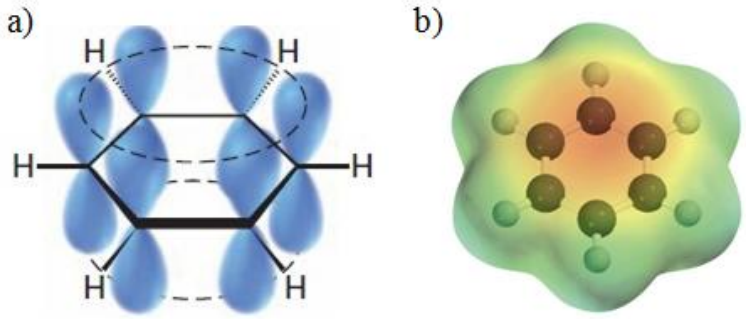

Figure 4.6: p-orbitals in a benzene ring (a) characterized by electron delocalization (b).

4.3.1 *p*-type and *n*-type semiconductors

Most of the organic semiconductors studied so far are *p*-type, stable in air and having high mobility when used in OFETs. Common *p*-type semiconductors used to develop organic transistors are acenes, thiophene and phthalocyanines, as shown in Figure 4.7 (left).

Pentacene and tetracene, linear fused chains of benzene rings, are the most studied organic semiconductors for OFETs for their high carrier mobility. In particular pentacene, thanks to the extended π-system, shows a high hole mobility (1.5 $cm^2\ V^{-1}\ s^{-1}$, on/off current ratio > 10^8), near-zero threshold voltage as reported by Lin *et al*. [79]. A high rate of charge

transfer is reached when pentacene molecules are oriented perpendicular to the substrate surface. On the contrary, if the molecules are oriented flat on the dielectric surface, the carriers will be transported perpendicular to the π- orbital overlap with a consequently mobility reduction [80]. The principal limitations of this class of compounds are the low solubility in the common organic solvents and the low stability in air. Compared to pentacene, tetracene has better solubility and stability and it was found that its single crystal has a field-effect mobility of 1.3 $cm^2 V^{-1} s^{-1}$ [81]. Giri and co-workers [71,72] demonstrated the possibility to achieve mobility of about 11 $cm^2 V^{-1} s^{-1}$ growing, by blade coating technique, a derivative of pentacene obtained inserting triisopropyl-silylethynyl (TIPS) groups in the central 6- and 13-position of a pentacene core.

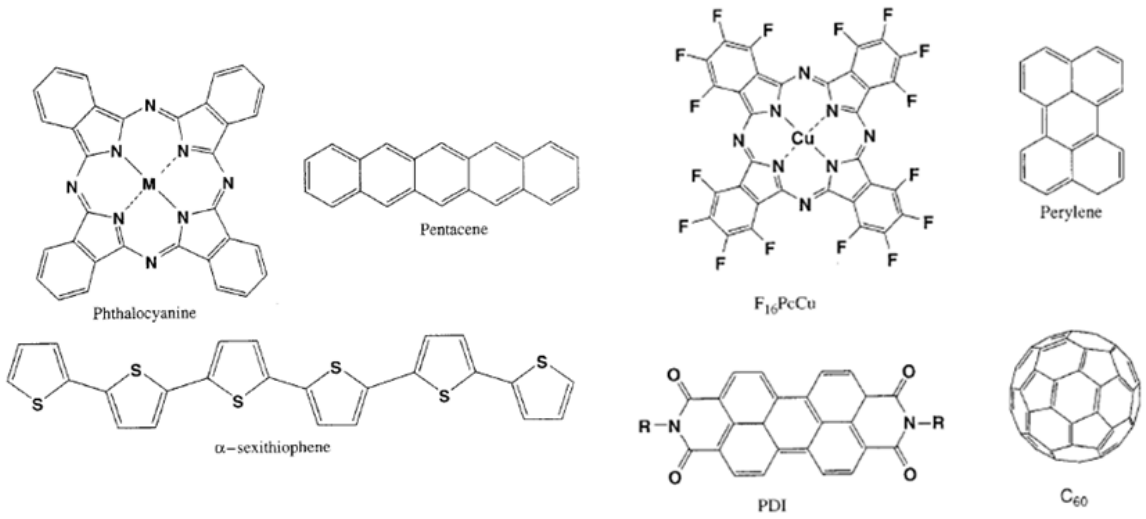

Figure 4.7: Chemical structures of several common *p*-type (left panel) and *n*-type (right panel)organic semiconductors [78].

Another interesting class of organic semiconductors exhibiting high carrier mobility is based on an electron-rich heterocycle such as thiophene and its derivatives, sexithiophene and hexyl-substituted thiophene oligomers. Nevertheless, these oligo-thiophene compounds can be easily oxidized in air, because of their high HOMO energies. To overcome this problem is possible to replace some thiophene with phenyl rings, in order to lower the HOMO energy [75]. Minemawari and collaborators [74] developed highest performance solution-processed OFETs, using benzothienobenzothiophene (C_8-BTBT), able to reach a maximum mobilities of 31.3 $cm^2 V^{-1} s^{-1}$.

Phthalocyanines as well have arisen great interest for their excellent photoelectric characteristics: they are thermally and chemically stable so that the devices can resist in air for months. However, they have a very low charge mobility that can be up to 0.11 $cm^2 V^{-1} s^{-1}$ [80].

Compared to *p*-type semiconductors, *n*-type with high mobility are very rare because of the low stability of these materials in air Figure 4.7 (right panel).

A viable approach to obtain *n*-type semiconductors with high performance and high environmental stability consists in the conversion of known *p*-type materials by introducing electronegative substituents such as –F, -CN, -Cl, $-NO_2$, -C=O, *etc*. In this way, the LUMO energy levels of materials is lowered with consequent increasing of the electron affinity, reaching efficient electron injection and transport. An example of this strategy was proposed by Marks *et al.* [82,83] who produced some fluoroarene-thiophene oligomers by functionalization with perfluorinated substituents. The presence of these end-fluoroarene groups confers to these oligomers an *n*-type activity and a high resistance to environmental electron traps (O_2 and H_2O).

Another approach to produce *n*-type organic semiconductors consists in combining proper substituents with electron-deficient π-systems, such as perylene diimides. The imide N atoms or π-system cores can be easily functionalized in order to improve the charge transport properties [84].

4.4 Controlling morphology

The carrier mobility in OFET devices is related to the molecular ordering and to the π-π stacking of the organic materials. It is known in fact that it is possible to improve OFETs performance controlling the morphology and the microstructure crystallinity of the organic semiconductors [85,86].

In order to reach high carrier mobilities, an efficient π-π intermolecular overlapping is necessary and the stacking direction of the organic molecules has to be in the plane of current-flowing direction. This means that different factors can influence mobility, such as the electrodes position and architecture (top, bottom contacts), the orientation of the molecules in the film, the different organic film growths on metal and oxide substrates. K.

Xiao and co-workers [87] have demonstrated, for example, that when phthalocyanines (CuPc) are arranged perpendicular on the dielectric, as shown in the Figure 4.8, the mobility increases.

The molecules orientation depends on the preparation conditions of the thin film, as for example the substrate temperature (T_{sub}), the type of substrate used (mono- or poly-crystalline) and the deposition rate. Therefore, the deposition conditions are a crucial point to obtain an ordered thin film with suitable electronic properties. [88,89].

K. Xiao *at al.* [87] showed how the copper phthalocyanine films morphology changes at different temperature of the Si/SiO_2substrate. At room temperature, the film is made of homogeneous small crystal grains, while at higher temperatures the films morphology changes from grains to rod-like and flat crystal. On one hand, a flat crystal favors the carrier flow but, on the other, the nucleation process at high temperature is not so easy resulting in the formation of a discontinuous film which has a negative effect on the mobility of OFET devices.

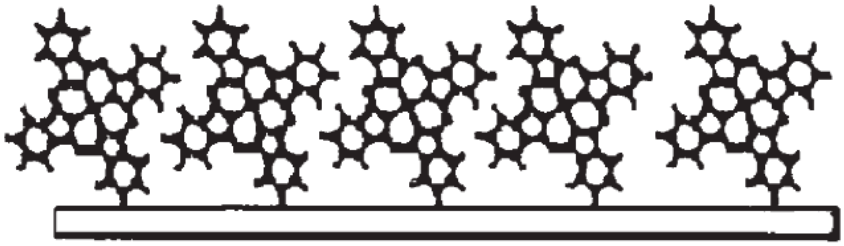

Figure 4.8: Organic molecules, in this case phthalocyanines, oriented perpendicular to the substrate surface [80].

In pentacene films, it was observed that the substrate temperature can affect grain size and shape and the crystal quality. The grains of a film grown at room temperature are smaller than those of a film grown at 80°C. Moreover, on 80°C film, when the film becomes thicker, the interaction between the impinging molecules and the surface gets weaker: at increasing film thickness, the grain sizes grows [90].

The molecular orientation is also affected by the surface chemical structure of the dielectric, in fact the growth of molecules is driven by the molecules-surface and molecule-molecule interaction [91-96].

4.5 OFETs fabrication techniques

As mentioned above, being a typical OFETs constituted by different layers of thin films, the interfaces between layers play an important role in the transistor characteristics. It is well known that the optimization of the semiconductor deposition conditions, as well as the substrate temperature and the control of the surface chemical structure of the insulator, allow improving the performances of the devices. Thus, the major step in the OFET fabrication is the deposition of the organic semiconductor. Nowadays, the common fabrication techniques used include Langmuir-Blodgett [97], solution-processes deposition [98,99] and stamping or microcontact printing (μCP) techniques [80], vacuum evaporation *etc*.

Growth of high quality organic thin film can be achieved using the Organic Molecular Beam Epitaxy (OMBE) technique working in ultra-high vacuum atmosphere. This approach consists in the deposition on a substrate of molecules coming from a sublimation source. The growth process is schematically shown in the Figure 4.9 [100]. When the first layer of molecules A is completed, a beam of molecules B is directed towards the substrate so that the new molecules can react with the first monolayer. The process is repeated till to obtain the desired structure and thickness.

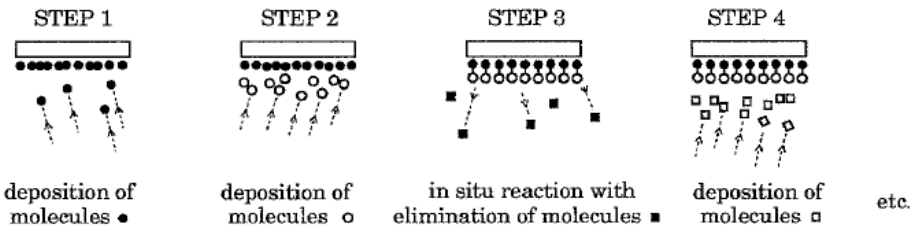

Figure 4.9: Scheme of the OMBE process [100].

The film growth occurs in a chamber in which a vacuum ranging from 10^{-7} to 10^{-11} mbar and where the organic source material is sublimated by a temperature-controlled oven or Knudsen cell. Parameters that affect the quality of the film are the source and substrate temperatures (generally between 80 to 400K), improving film reproducibility with respect to LB and spin-coating [101]. Using OMBE it is possible to characterize *in situ* the film grown in UHV provided the deposition chambers is equipped with different analitical tools (RHEED, LEED). Using this technique it is possible to obtain highly ordered thin films

with different thickness, keeping under control the substrate temperature and the deposition rate. The mobility of OFETs produced by this technique can be one or two orders of magnitude higher than those formed from solution-processed deposition technique [80].

Finally, the use of Supersonic seeded molecular beams is one of the most viable and promising approach for growth organic films suitable for OFET realization, since it allows control of critical parameters, such as kinetic energy and momentum, that is not easily feasible with other methods. The technique has been better presented in the previous Chapter, with deposition occurring in vacuum or UHV and possibility to analyze in-situ the grown films, as happens for OMBE. The efficiency in controlling film morphology, structure, surface order and thus OFET final electronic properties during the film growth has been widely described. Most important achievements are shown in paragraph 4.5.1.

4.5.1 OFETs by SuMBD

As described in the Chapter 2, the SuMBD technique allows a better control of the growth process through a control of the KE of the impinging molecules, showing to be very promising in the realization of OFET devices. The structure and morphology control of the organic films play an important role in the fabrication of high quality OFET. Tuning these parameters, together with a better comprehension of the processes at the interface, it is possible to improve the performances of these devices. S. Iannotta and his group [13], indeed, have shown the possibility to control the organic films (such as oligothiophene [11], phthalocyanines [102] and pentacene [15]) growth by SuMBD approach. Furthermore, they demonstrated that it is possible to strongly increase the performance of pentacene-based OFET tuning the KE of the organic molecules during the growth. They analyzed an OFET device (Figure 4.10) constituted by a pentacene film deposited of about 35-40 nm on the gate electrode at room temperature at several KEs (3.5eV, 5.5eV and 6.5eV) using He as carrier gas. The organic films showed different morphology, in fact, at lower KE (3.5eV) the film appears polycrystalline and characterized by terraced structures and the grains size increases with the KE (5.5eV). At higher KE (6.5eV), instead, the surface is quite flat over a very extended area, as shown by the AFM analysis (Figure 4.11).

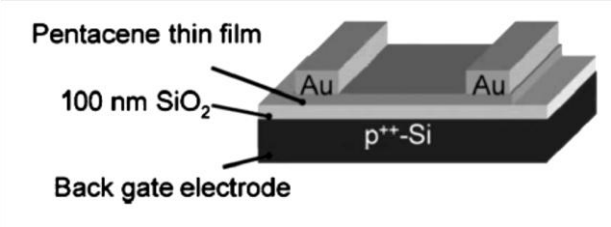

Figure 4.10: Sketch of the OFET device [13]

The different structure of the organic films affects the electrical characteristics of the organic devices, in particular by the carrier mobility point of view. The field effect mobility depends strongly on the pentacene KE increasing at higher KE: passing from a KE of 3.5eV (0.22 cm^2 V^{-1} s^{-1}) to 6.5eV (1.00 cm^2 V^{-1} s^{-1}), the mobility increases of a factor of 5. Moreover, all the parameters, such as the sub-threshold slope, the threshold voltage and the I_{on}/I_{off} ratio, are affected by the KE effect.

These results give a clear evidence of the potentiality of the SuMBD technique to control the film morphology and consequently to improve the OFETs performance, simply tuning the KE of the organic precursor in the supersonic beam.

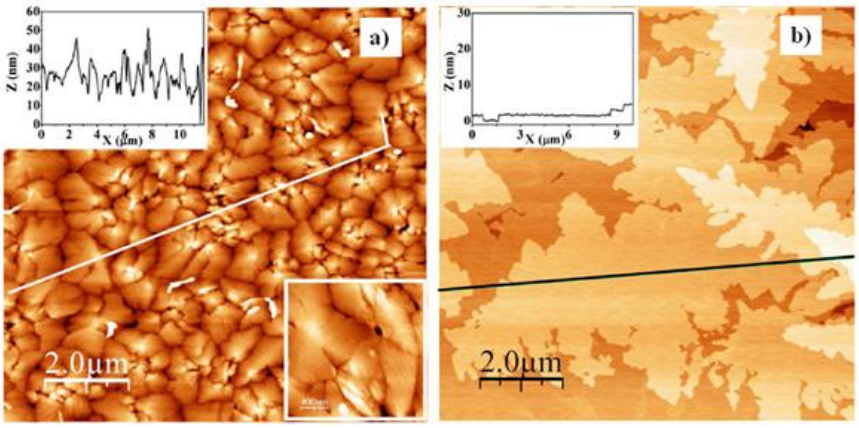

Figure 4.11: AFM micrographs of pentacene films grown by SuMBD at 3.5eV (a) and 6.5eV (b). The inset shows the height profile [13].

4.6 Electronic properties of interfaces

To better understand how to improve performances in OFET devices, it is necessary to control the electronic properties at the organic/inorganic interfaces. As previously

described, in OFET we observe the formation of an accumulation layer at the organic-inorganic interface characterized by a carrier distribution *n* that can be estimated by:

$$n = n_0 \left(1 + \frac{y}{\lambda_D \sqrt{2}}\right)^{-2}$$

where n_0 is the density at the insulator-semiconductor interface and λ_D the Debye length, defined by the equation:

$$\lambda_D = d_i \frac{kT\sqrt{2}}{qV_g}$$

The parameter d_i is the thickness of the insulator, k the Boltzmann constant, T the absolute temperature and q the electron charge. It is interesting to note that the Debye length decreases as the gate voltage increase and the width of a layer is therefore almost equal to the length of a molecule. This means that, working in accumulation regime, all the charges are concentrated in the first layer, explaining the dependence of device performance on the molecular film features at the insulator-semiconductor interface [103].

Among the different processes occurring at the organic-inorganic interface, two are by far the most important: doping/charge transfer processes and formation of electric dipole.

4.6.1 Surface transfer doping

Doping is a key process used to improve the semiconductor-based electronic devices performance, manipulating their charge carrier density and conductivity. For inorganics, this approach consists in incorporating atoms (dopants) with specific properties into the host lattice of the semiconductor bulk [104]. Depending on their valence number , the dopants can act both as *donors* and as *acceptors*. In the first case, the dopants donate excess electrons as negative free charge carriers to the semiconductor conduction band and the Fermi level shifts towards the conduction band of the semiconductor (*n*-type doping, Figure 4.12-a).

In the second one, the dopants accept electrons from surrounding atoms, in order to complete a covalent chemical bonding, giving rise to formation of positively charged carriers, holes, in the semiconductor valence band (*p*-type doping, Figure 4.12-b) and to a Fermi level shifts towards the valence band. Semiconductors can also be doped by an

electron exchange with a doping species located on its surface, without the introduction of atoms into the lattice: this process is known as *surface transfer doping*.

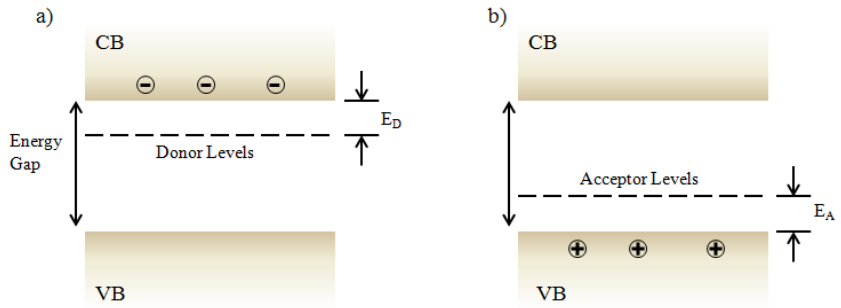

Figure 4.12: Schematic view of the valence and conduction bands of a *n*-type semiconductor (a) and a *p*-type semiconductor (b). E_D and E_A indicate the electron band energy in a donor and in an acceptor atom, respectively.

This effect can be schematically represents as shown in Figure 4.13, where it is reported the comparison between the classical doping process (on the left) and the surface doping (on the right) [105].

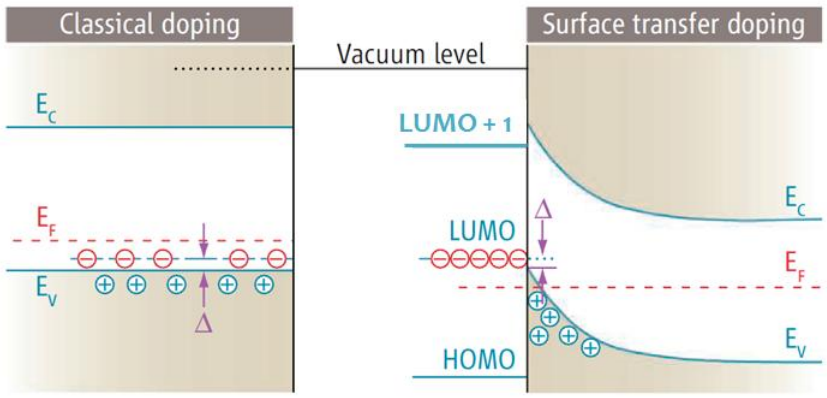

Figure 4.13: Comparison between classical *p*-type doping (left) in inorganics and surface transfer doping (right) with organics. E_C and E_V are the energies of the conduction band and the valence band, respectively, and E_F the Fermi energy [105].

Considering the case of a *p*-type doping, where an intrinsic semiconductor is in contact with an organic acceptor dopant, electrons move from the valence band of the semiconductor to the empty LUMO level of the surface adsorbate.

This interfacial charge transfer will induce a localization of negative charge on the surface acceptors and the formation of compensating holes in the semiconductor valence band. After the electron transfer, in thermal equilibrium, the Fermi level of substrate and dopant are aligned and an upward band bending occurs [106,107].

This charge separation will determine the formation of an electrostatic potential that forces the holes to stay in a direction perpendicular to the surface but they are free to move parallel to that [105].

At thermodynamic equilibrium, the effective surface doping efficiency η gives the relationship between the surface electron density (n) and the surface density of the dopants (n_A) [107]:

$$\eta = \frac{n}{n_A} = \frac{1}{1 + e^{((E_{LUMO} - E_F)/kT)}}$$

Typical surface doping molecules are tetracyanoquinodimethane (TCNQ), tetrafluoro-tetracyanoquinodimethane (F4-TCNQ), 3,4,9,10-perylene tetracarboxylic acid dianhydride (PTCDA), used as electron acceptors and copper phthalocyanine (CuPc) that acts as electron donor (Figure 4.14).

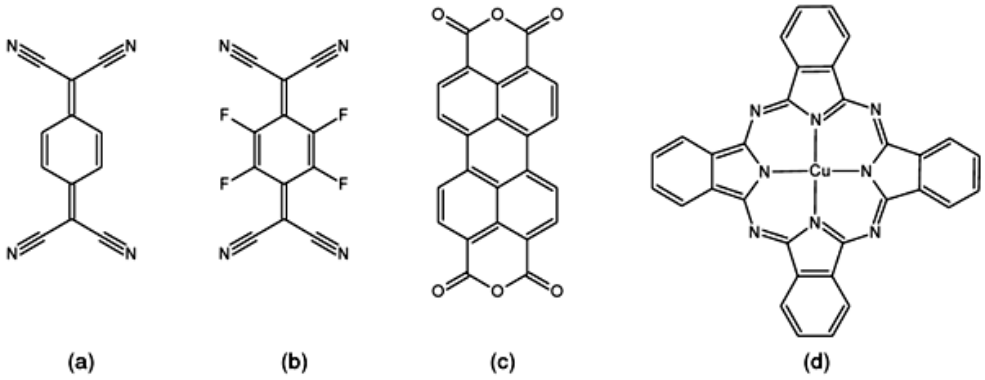

Figure 4.14: Molecular structures of TCNQ (a), F4-TCNQ (b), PTCDA (c) and CuPc (d) [106].

Based on the previous considerations, in p-type doping case, the LUMO of the surface adsorbates must be located near or below to the semiconductor valence band. In n-type doping, instead, the HOMO of the surface adsorbate must be close or above to the conduction band of the semiconductor. Moreover, the holes and electrons generated in

semiconductor, must be delocalized in proximity of interface region with the surface to act as effective charge carriers [108,109].

This technique has been successfully used for the doping of hydrogenated diamond, silicon carbide, graphene and carbon nanotubes [105,106,108,110].

4.6.2 Dipole formation at interfaces

When a semiconductor is put in contact with another material two aspects must be considered: the energy level alignment at the interface and the possible formation of interfacial dipoles. Let we consider a general case of metal/organic semiconductor interface, for which the energy levels of the system without (a) and with (b) an interface dipole are showed in the Figure 4.15 [111].

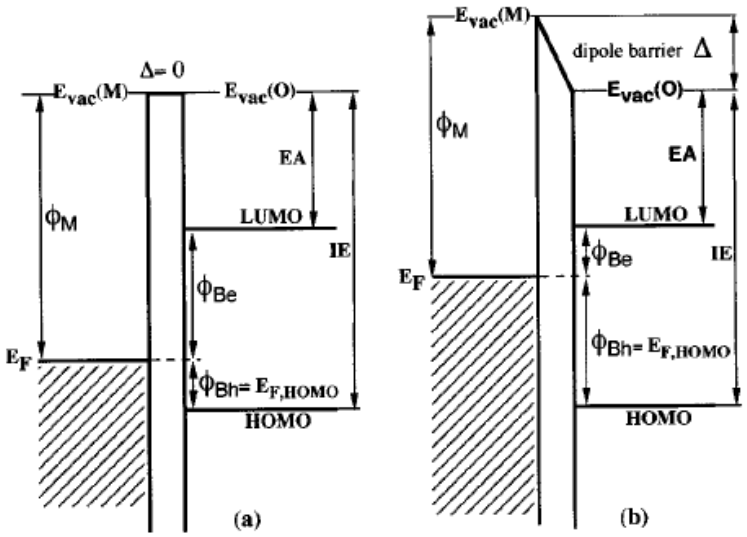

Figure 4.15: Energy levels scheme of a system without (a) and with (b) an interface dipole [111].

We can define ϕ_M as the metal work function and ϕ_{Bh} and ϕ_{Be} as the hole and electron barriers which depend on the position of HOMO and LUMO orbitals with respect to the Fermi level (E_F). If the vacuum levels of metal and semiconductor are aligned (Figure 4.15, a), it is possible to calculate:

- $\phi_{Bh} = E_{F,HOMO} = IE - \phi_M$, *IE* being the ionization energy of the organic film,
- $\phi_{Be} = \phi_M - EA$, EA being the electron affinity of the organic film,

In the case of finite dipole formation (Figure 4.15, b), the dipole barrier (Δ) is related to the difference between the work function of the two materials, representing a charge developed on the organic side of the interface balanced by an opposite charge on the metal [111].

The presence of the dipole at the interface has the effect to change the metal work function and the HOMO/LUMO positions, as showed in Figure 4.16 [112], leading to a possible hole injection (when charge is transferred *from* the substrate to the HOMO) or electron injection (when charge is transferred *to* the substrate from the LUMO).

The interface dipole results from two effects. The first is the alteration of the metal work function because of the presence of the organic molecules (chemisorbed or physisorbed). The second effect comes from the molecules strong interaction (i.e., chemisorption) on the metal surface, with bond formation that produces an electron density flow through the atoms involved in the bond itself, resulting in a partial charge transfer between metal and adsorbate [112].

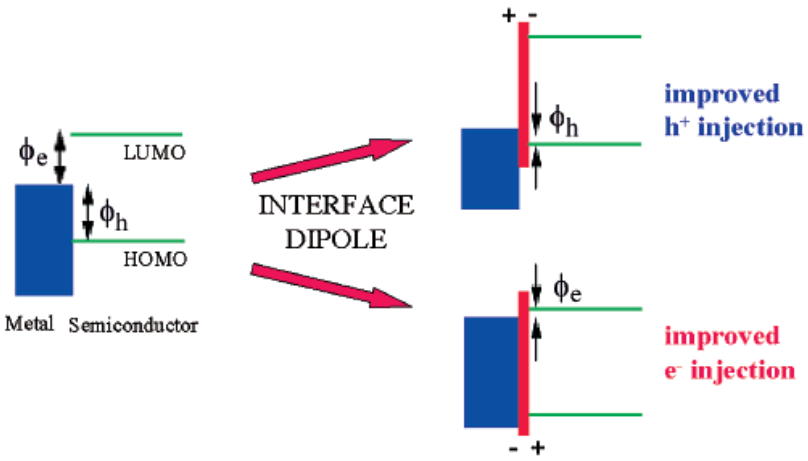

Figure 4.16: Effect of the interface dipole on the electronic levels at an organic semiconductor/metal interface [112].

Electronic dipole layers can be found also at organic/organic interfaces, as in the case of organic semiconductor heterojunctions employed in ambipolar OFETs. In organic devices indeed it has been observed an energy level alignment and the formation of an interfacial dipole due to the charge transfer at the heterojunction [113,114].

In these devices an electron transfer from HOMO of the *p*-type organic material to LUMO of the *n*-type material gives rise to a charge transfer accumulation on both side (Figure

4.17). This conductive channel could be regulated by an external gate voltage [58]. Keeping in mind the diagram in Figure 4.15, the formation of an interface dipole between the organic materials can occur if the *IE* of one organic semiconductor is lower than the *EA* of another. This charge transfer will cause the formation of the interface dipole that realigns the energy levels on both sides so that electronic equilibrium is established, with an intensity depending on type of interactions leading to the observed dipole.

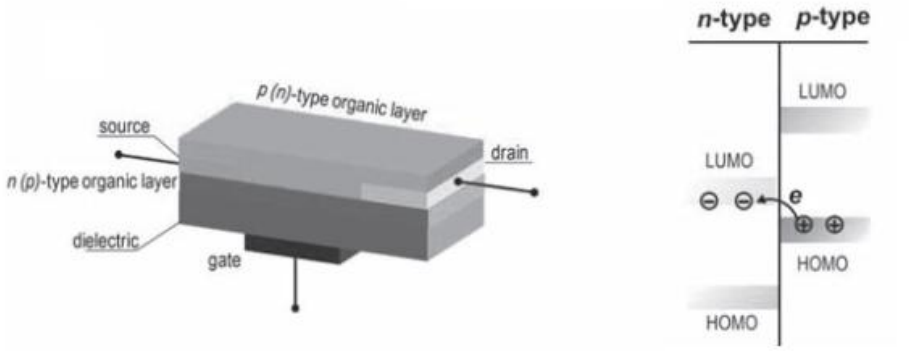

Figure 4.17: On the left an ambipolar OFET device with a *p*-*n* organic-organic heterojunction; on the right the charge transfer in the ambipolar OFET from the HOMO of the *p*-type organic material to the LUMO of the *n*-type organic material [62].

Another important aspect to take into account is the dependence of the interfacial energy level alignment and dipole formation from the molecular orientation [115-117]. In organic-organic heterojunction it depends on the interfacial (interaction between two different molecular species) and intermolecular (interaction within the same type of molecular specie) interaction. In particular, it was demonstrated the correlation between the ionization potentials *IEs* and the orientation in organic thin films, originating from the surface dipoles created into the ordered molecular layers [118,117]. N. Koch group has showed, for example, the variation of *IE* for α,ω-dihexyl-sexithiphene (DH6T) and α-sexithiphene (6T) on Ag(111) as the molecules are lying flat on the substrate or stay upright. They found an increase of *IE* values for flat-lying thin film DH6T and 6T, attributing this trend to the formation of intrinsic surface dipole. When the molecules are oriented upward no such dipoles are present on the surface [118].

4.7 Evaluation of the electronic properties by UPS

The analysis of the electronic performances of OFET devices is typically achieved by measuring current-voltage characteristics at different gate voltage values. However, to better understand and the physical/chemical processes at the different involved interfaces leading to the observed OFET performances, it is advisable to properly study the electronic properties and energy levels alignment of layers and materials forming the device itself. From this point of view, the UPS technique is one of the most used and useful approach to achieve the required information on electronic materials properties. To better emphasize the suitability of UPS, before moving to the case of organic film deposited by SuMBD, we analyzed in detail a complex organic/organic heterojunction composed of molecules similar to that used in the SuMBD experiment.

4.7.1 Characterization of the T6/PDI-8CN$_2$ system

The electronic properties of organic/organic interfaces are of great interest for application in optoelectronics and electronics. Sexithiophene (T6) and N,N-bis(n-octyl)-dicyanoperylenediimide **(**PDI-8CN$_2$) (Figure 4.18), as described in paragraph 4.3, are respectively common *p* and *n* type semiconductors studied for their application in ambipolar field-effect transistors.

The peculiarity of these organic semiconductors is associated to the values of the molecular energy levels, which allows the transfer of electrons from the HOMO level of the *p*-type semiconductor to the LUMO level of the *n*-type compound. Furthermore, considering a possible T6/PDI-8CN$_2$ double-layered heterostructure (Figure 4.19-a) [119], these organic materials could act as hole and electron carriers for OFETs.

This behavior can be enhanced if a good match is achieved between the work function of the metal and the HOMO level of the hole transporting T6 layer [120], the LUMO level of electron transporting PDI-8CN$_2$ layer [121] (Figure 4.19-b). To this end, gold could be a good candidate.

F.V Di Girolamo and the group of Prof. A. Cassinese at the University of Napoli, Physics Department [119], demonstrated an accumulation of charge carriers at the T6/PDI-8CN$_2$

interface, and the dependence of the electronic characteristics of these devices with physical processes occurring at the organic layers interface.

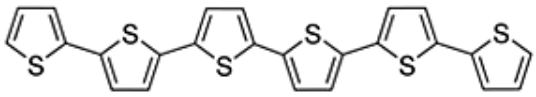

Sexythiophene

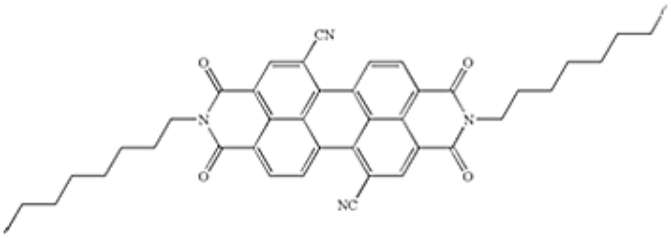

$PDI\text{-}8CN_2$

Figure 4.18: Molecular structure of Sexithiophene (T6) and N,N-bis(n-octyl)-dicyanoperylenediimide **(**$PDI\text{-}8CN_2$).

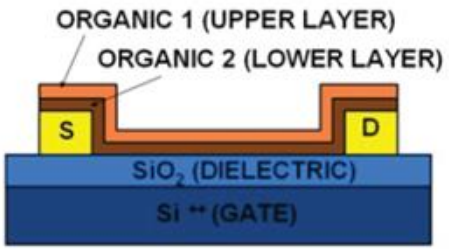

(a)

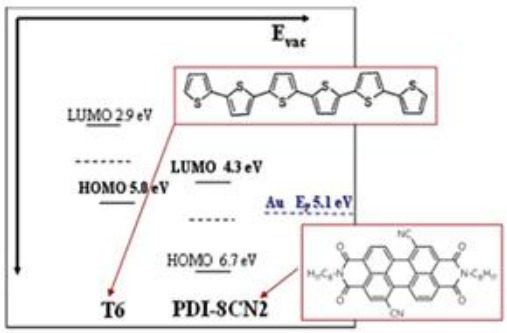

(b)

Figure 4.19: a) The double-layered configuration device, b) energy levels of the two semiconductors [119].

They evaluated the output and transfer characteristics of T6/PDI-8CN_2 heterojunction as a function of the T6 thickness, keeping the PDI-8CN_2 thickness fixed at 24 nm:

- when T6 thickness is ≤ 1 nm these devices behave as *n*-type transistors showing only electron accumulation and not supporting hole current.
- when T6 thickness is > 1 nm, these devices are able to transfer holes from source to drain. The enhancement of mobile hole conductivity causes a current increase: this feature can be associated to the presence of T6/PDI-8CN_2 interface.
- when T6 thickness is 2-4.5 nm, the T6/ PDI-8CN_2 device displays the *negative transconductance* (NTC) effect. This electrical feature consists in the decrease of the current due to the hole contribution, which gives rise to a peak and it is related to T6 film thickness.
- with a T6 layer of 7.5-15 nm, T6/ PDI-8CN_2 heterostructures show a hole-accumulation regions: this can occur as a consequence of the trap filling due to the accumulation of the charge [122].

In order to explain such complex electronic properties of these devices, they proposed an energy levels model where an electron from the HOMO level of the *p*-type semiconductor (T6) is transferred to the LUMO level of the *n*-type semiconductor (PDI-8CN_2). This charge transfer could cause the formation of a built-in local electric filed which bend the electron and hole band at the organic/organic interface.

In view of a tight collaboration between the IMEM-CNR group in Trento and that of Prof. A. Cassinese, at University of Napoli, aiming at the realization of OFET devices based on p-n heterojunction by using suitable *p* and *n* organic molecules and exploiting the ability of the SuMBD approach to improve film morphology and structure, the IMEM team was involved in the evaluation of the electronic properties of these systems by means of UPS analysis, to experimentally reveal and confirm the surface transfer doping effect and the band bending at the interface between T6 and PDI-8CN_2, as previously proposed by [119]. The results developed within this thesis are presented in the following and have been the subject of a specific publication on the journal Applied Physics Letters [123].

4.7.2 UPS studies

The electronic properties of the T6/PDI-8CN_2 system have been evaluated by UPS spectroscopy, as a matter of fact confirming the high potential of this technique to study complex processes such as charge transfer, band bending and dipole formation.

The organic field-effect transistors were fabricated (by group in Napoli) by in-situ sequential deposition of each organic layer on Si^{++}(500 μm)/SiO_2(200 nm) substrates, provided of gold source-drain interdigitated electrodes (bottom-contact, bottom-gate configuration). The organic films were deposited in a high vacuum evaporation system equipped with independent Knudsen-cells filled with commercial T6 and PDI-8CN_2 powders. UPS analysis have been performed ex-situ directly on OFETs. Due to the intrinsic low dimension of the electrodes in the devices, comparable to the spot diameter of the UV lamp used for photoelectron analysis, the results for valence band can be considered representative of organics covering both metal contacts and oxide region. A complete set of UPS analysis have been performed on different devices, as described previously in paragraph 3.6.1.2, to have access on all information regarding work function (WF), ionization potentials (IP) and BE of main molecular bands, such as HOMO. The films have been studied by AFM, while OFET performances have been thoroughly characterized. Briefly, T6 thick layer exhibits mainly the classical three-dimensional island morphology based on the coalescence of disk-shaped crystallites. PDI-8CN_2 4 nm thick film are very smooth, but changes when deposition occurs on T6 film, suggesting that at 1 nm thickness molecules fill the spaces between T6 islands, and an almost complete molecular film is achieved only at 4 nm. Drain-source I-V measurements show an increase of the current proportional to the PDI-8CN_2 thickness, related only to an increase of the hole flux. Mobility increases from $5x10^{-3}$ to $2x10^{-2}$ cm^2/Vs, considering T6 film. Weak evidences of ambipolar behavior have been found only for the 4 nm perylene film on T6.

In order to better understand the processes occurring at such a complex interface, analysis has been performed on bilayer as well as single species systems. Figure 4.20 shows the valence band (VB) spectra (a), with close-up of the HOMO (c) and SECO (b) energy regions for PDI-8CN_2 thick film (4 and 20 nm), T6 thick film (15 nm) and the bilayer films (4 nm PDI-8CN_2/15 nm T6, 1 nm PDI-8CN_2/15 nm T6). VB from a clean Au surface is also shown in all figures (yellow curves): it is characterized by the presence of well

defined Fermi edge at 0eV BE, emission from 5d band in the 2-8eV range and a WF of 5.1eV, typical of polycrystalline gold.

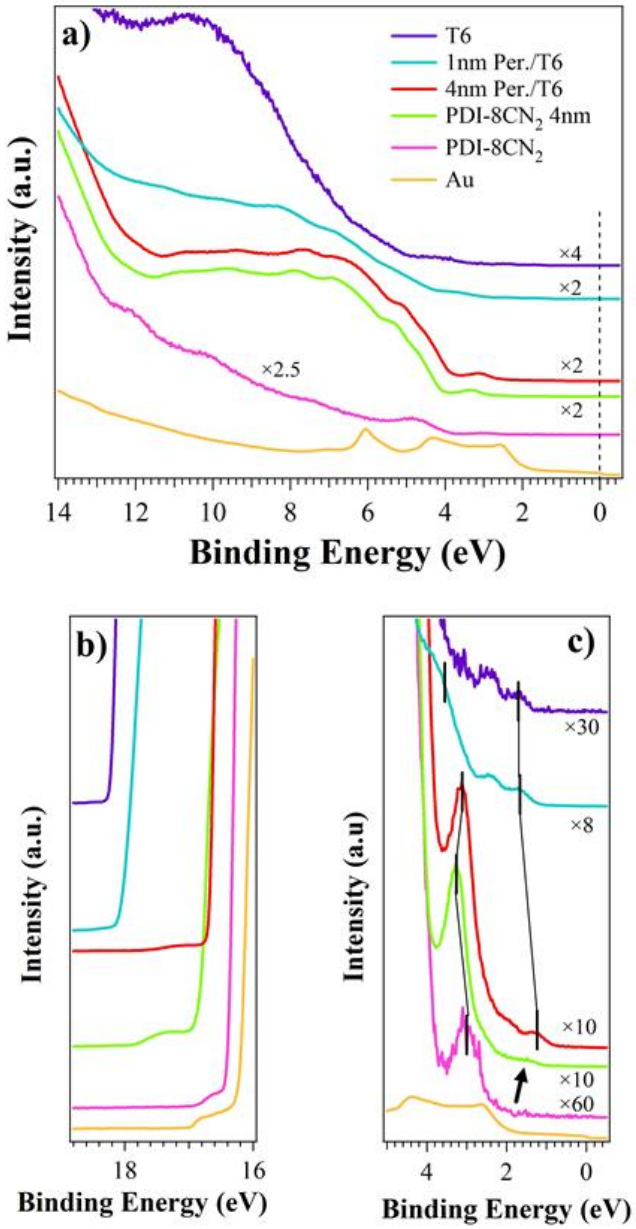

Figure 4.20: UPS analysis of T6/ PDI-8CN_2 OFET devices in comparison with thick film of T6, perylene (4 and 20 nm) and Au where: a) valence band, b) SECO and c) 0-5eV range. The arrow indicates the gap state [123].

PDI-8CN_2 20 nm film VB is characterized by several structures in the 4-12eV region, with HOMO located at 2.9eV, IP of 7.1eV and WF of 4.8eV. At the reduced PDI-8CN_2 film thickness of 4 nm, VB shows a +0.3eV BE shift, while IP is the same but WF is lower (-

0.3eV) (Figure 4.20). T6 VB shows HOMO and HOMO-1 positioned at 1.7eV and 2.4eV, and is characterized by a very low intensity, suggesting an island growth in organic films with high aspect ratio, as observed by AFM analysis as well.

The HOMO BE is in agreement with T6 films grown on Au substrate, as demonstrated by Y. Ge and J.E. Whitten [124], while similar WFs have been found for T6 films deposited on SiO_2 [125]. On the contrary, IP is significantly lower [126,127]. The variation of these parameters can be attributed to specific molecular packing, which leads to greater π conjugation and polarizability [125].

In presence of PDI-8CN_2, T6 valence band significantly changes. With respect to the T6 thick layer, for both the PDI-8CN_2 films thicknesses (1 and 4 nm), the intensity of HOMO T6 (located at 1.7 (1 nm) and 1.3eV (4 nm)) and perylene features (located at 3.5 (1 nm) and 3.1eV (4 nm)) enhances (Figure 4.20-c). At higher perylene film thickness, the intensity of T6 features decrease. Moreover, the shift of the SECO position (Figure 4.20-a) indicates IP and WF increasing with perylene thickness.

Starting from the parameters calculated from UPS spectra (WF, IP, Δ, HOMO centroid and leading edge energy, expected LUMO position), it was developed a scheme of the energy levels for all analyzed films and Au (Figure 4.21). The energy gap values employed for PDI-8CN_2 (2.4eV) and T6 (2.1eV) are the commonly occupied values found also in literature [121,128].

Regarding metal VB, it is evident the absence of any Au related feature for all organic films, with a significant shift of the SECO position suggesting presence of dipole at organic/inorganic interface.

Let’s consider the perylene/Au films of 4 and 20 nm, both show a LUMO position close to the Fermi level, and the HOMO position of the 4 nm thickness is shifted of -0.3eV BE with respect to the thick film, suggesting the presence of band bending. The most important evidence is the presence of a new peak in the HOMO-LUMO gap of PDI-8CN_2 4 nm. Such a feature can be originated only from a charge transfer process from the inorganic surface to the organic film. It is known that the charge transfer from the SiO_2 surface is unlikely [129], so the electrons transport involved the organic/Au interface. This process induces a rearrangements of the HOMO-LUMO molecular orbitals, with appearance of the new filled LUMO' band close to the Fermi edge and of a corresponding HOMO' structure,

located at lower BEs with respect to the original HOMO feature due to the new electronic configuration.

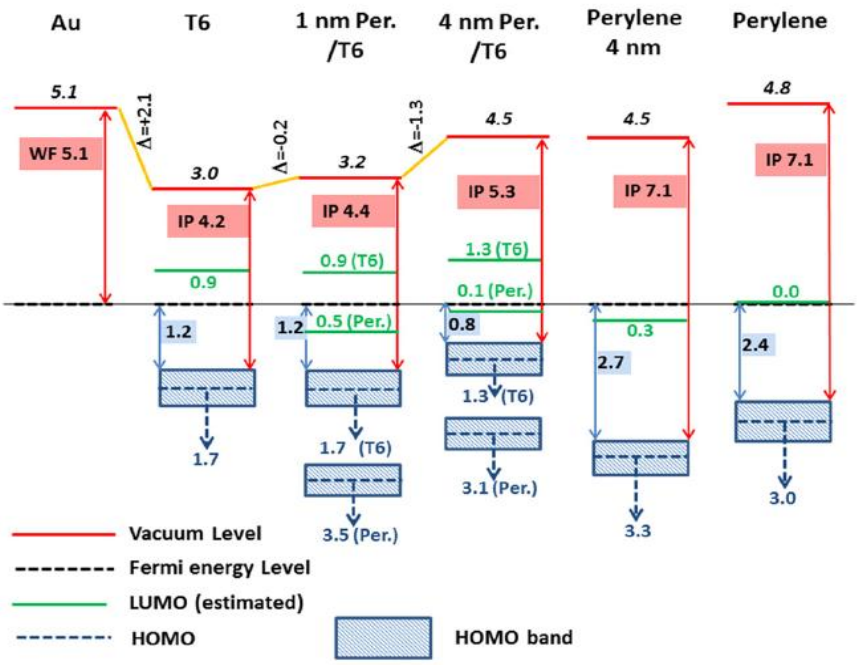

Figure 4.21: Energy level scheme of T6/ PDI-8CN$_2$ system, Au substrate, T6 thick film and PDI-8CN$_2$ (4 and 20 nm). There are shown WF, IP and extrapolated LUMO position. HOMO band and the centroid position are also shown. All values are in eV [123].

In T6 thick film, the reduction of organic IP and inorganic WF are in agreement with the formation of a dipole at the interface but without involvement of charge transfer. Moreover, HOMO BE and WF are similar to those found in literature for T6/Au [124], suggesting that the metal/organic interface plays a fundamental role in the final T6 film electronic properties.

After deposition of 1nm PDI-8CN$_2$ layer IP and WF increase (+0.2eV), while T6 HOMO (and LUMO) is located at the same position, according to the absence of band bending and the presence of a $\Delta\phi$ = -0.2eV surface dipole. Increasing the PDI-8CN$_2$ thickness to 4 nm, the vacuum level position shifts of Δ = -1.3eV, so that the IP is similar to T6 and WF is similar to perylene. T6 and PDI-8CN$_2$ HOMOs shift towards lower BE (-0.5eV) and perylene LUMO is located 0.1eV below Fermi level, suggesting the presence of both band bending and interface dipole ($\Delta\phi$ = -0.8eV). This configuration suggests that the charge

transfer involves the PDI-8CN_2 LUMO that could receive electrons from the T6 HOMO or the metal. Furthermore, the T6 HOMO BE shift is an evidence of the organic role in the charge transfer process and it is an indication that the electronic behavior observed in output and transfer curves is indeed due to the surface doping of T6 by PDI-8CN_2.

Experimental results suggest that charge transfer is much more efficient in 4 nm PDI-8CN_2/Au with respect to the thin layer. This characteristic can be associated to the surface morphology of the T6 film: the first 1 nm of perylene probably covers the zones between T6 islands and the subsequent 3nm lead to the formation of a (almost) complete perylene layer, inducing the observed charge transfer.

4.8 Perylene thin film transistors by SuMBD

As previously described in this chapter, the standard technique used to grow semiconducting organic films is the Organic Molecular Beam Deposition, which uses a Knudsen cells as effusive source, reaching KE of few tenth of eV.

Our group in Trento, in collaboration with Napoli University, has investigated the efficacy of SuMBD approach to grow organic films displaying dominant electron-transporting *n*-type character, showing the correlation between the electrical properties with the structural and morphological quality of the film and the properties at the organic/inorganic interface.

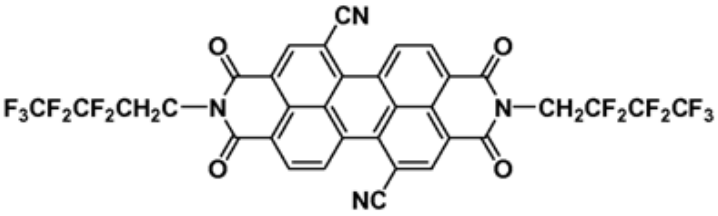

PDIF-CN_2

Figure 4.22: Molecular structure of N,N'-1H,1H-perfluorobutil dicyanoperylenediimide (PDIF-CN_2).

The system under investigation was a N,N'-1H,1H-perfluorobutil dicyanoperylenediimide (PDIF-CN_2) (Figure 4.22) film deposited on silicon dioxide (SiO_2) surfaces by SuMBD at

room temperature. The results that will be presented hereafter have been subject of a specific publication on Applied Physics Letters [130].

Bottom-contact, bottom-gate transistors were fabricated using multilayered structures consisting of a 500 nm thick highly doped Silicon (Si^{++}) substrate, a 200 nm thin SiO_2 dielectric barrier, and source/drain gold electrodes with interdigitated layout. Organic films have been grown at substrate room temperature using both OMBD and SuMBD, at growing rate of 5 and 1 Å/min respectively. Perylene KE with SuMBD of about 18eV gave the best OFET electrical performances. Devices have been characterized from electrical point of view, while AFM, X-ray diffraction (XRD) and UPS analysis have been performed ex-situ on organic thin films.

The structural properties of a 30 nm thick film PDIF-CN_2 deposited at room temperature both by SuMBD and OMBD approachs are shown in Figure 4.23 (a) and (b).

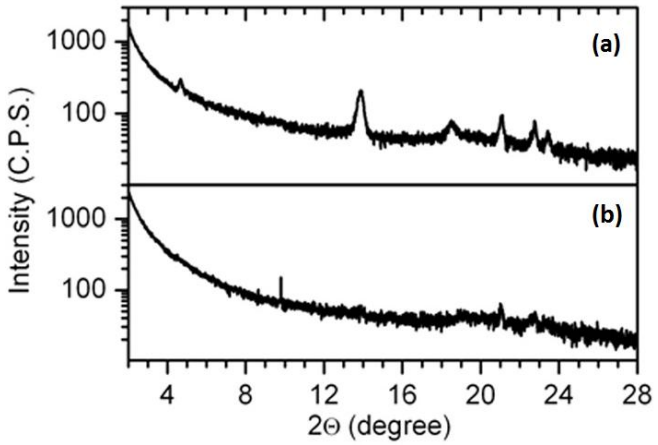

Figure 4.23: X-ray diffraction spectra of a PDIF-CN_2 thick film (30 nm) grown by a) SuMBD and b) OMBD [130].

The XRD results demonstrates that the SuMBD-deposited film is characterized by a long-range ordering while the film grown by OMBD does not show any diffraction peaks. In both cases, films exhibit a dominant granular morphology without the clear presence of flat crystalline islands showing molecular terraces. OMBD-deposited film appears basically amorphous, with a surface overall roughness (σ_{rms}) around 2 nm.

PDIF-CN_2 films grown by SuMBD result to be formed through the coalescence of columnar structures protruding the surface, with base diameters between 100 and 200nm (see the height profiles in Figure 4.24), with a three-dimensional character and σ_{rms}

increased up to 4 nm. Interestingly, the SuMBD film height profile resembles very closely that of PDIF-CN_2 films grown by OMBD at T_{sub}=120°C [131].

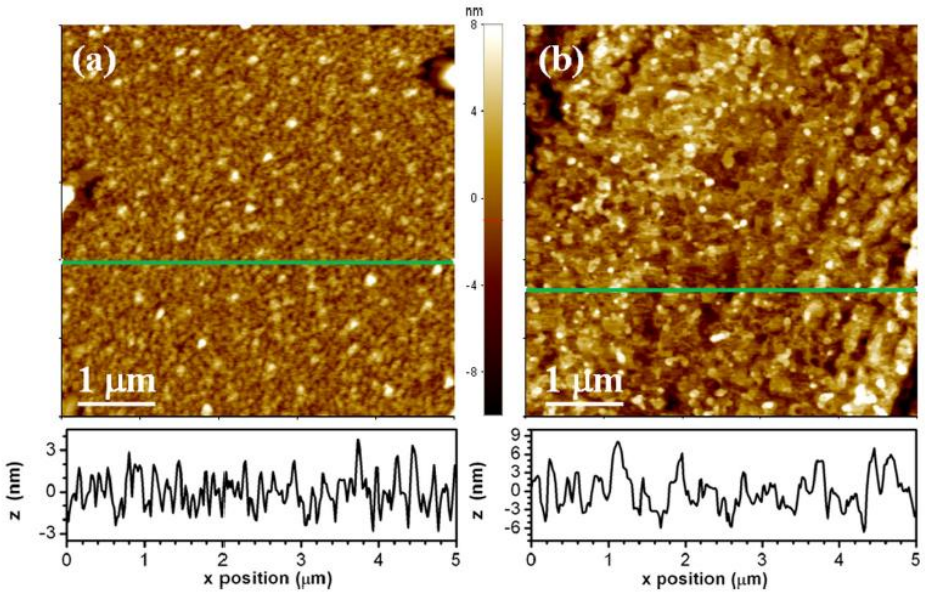

Figure 4.24: AFM analysis of a PDIF-CN_2 thick film (30 nm) grown by a) OMBD and b) SuMBD. Panels below report the height profiles recorded at the positions indicated by the green lines.

We have concluded that, the increase of the impinging molecules KE in SuMBD deposition has an effect on the morphology and structure of the organic film similar to that of the substrate temperature in the OMBD process. The organic molecules, because of the KE or T_{sub} increase, can diffuse over longer distance before their aggregation into forming islands, supporting the growth of films with reduced structural disorder [32]. However, while in the latter case the process is ruled by a thermodynamic process, by exploiting the KE excess given by SuMBD we are dealing with an energy transfer in conditions far from thermodynamic equilibrium.

Differences between films obtained by SuMBD and OMBD are evident also in the electrical performances of the transistors. As displayed in Figure 4.25, the devices constituted by PDIF-CN_2 grown by SuMBD shows currents that are typically three order of magnitude higher than for OMBD, while the best carrier mobilities are respectively 0.2 and $3x10^{-4}$ cm^2/Vs. Indeed, to improve the performance of PDIF-CN_2 thin-film devices by OMBD deposition, the films needs thermal treatments during or after their growth. In

particular μ increases growing the T_{sub} from 70°C to 130°C where it reaches maximum value of 0.6 cm^2/V s [121].

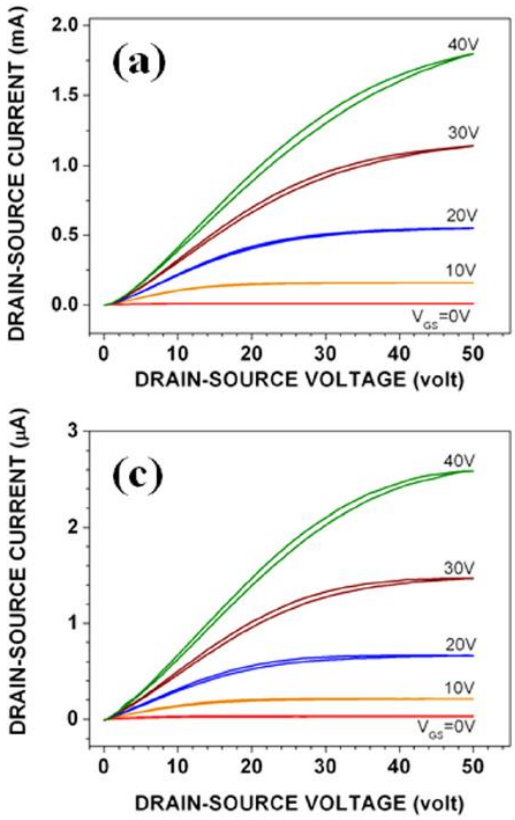

Figure 4.25: Output curves in the saturation regime for PDIF-CN_2 transistors fabricate by a) SuMBD and b) OMBD [130].

The interesting electrical properties of the PDIF-CN_2 film by SuMBD are once more comparable only to films deposited by OMBD at higher substrate temperatures.

The PDIF-CN_2 layer deposited on the Si(100) substrate with native oxide have been characterized by UPS spectrometry in order to better understand the electronic properties at the organic/inorganic interface. A thick SiO_2 substrate (typical of OFET devices) has been avoided because of formation of strong charging effects due to the UV photons beam.

VB of native silicon oxide on Si(100) is characterized by a large energy gap of about 8eV and a WF of 4.3eV. As shown in Figure 4.26-b (Figure 4.26-a displays the SECO region), the density of state distribution shows the typical features related to O2p level hybridization in the 6-10eV region.

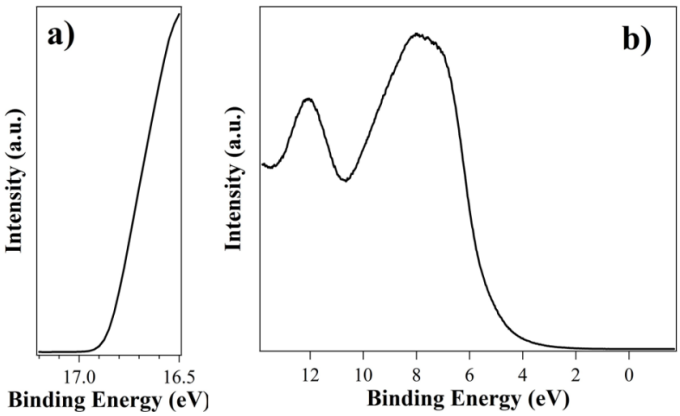

Figure 4.26: UPS spectrum of the Si(100) substrate

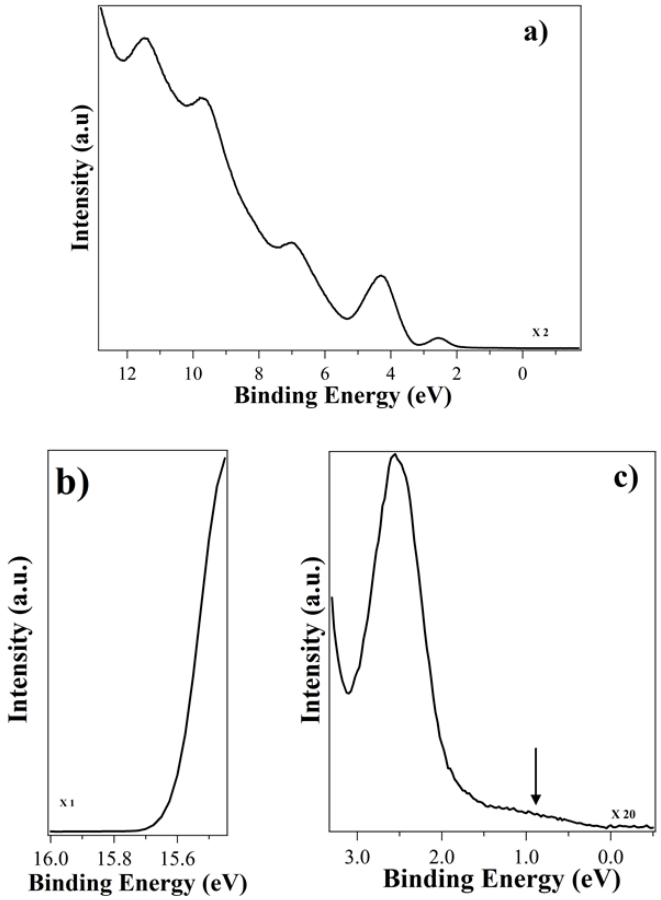

Figure 4.27: (a) Valence band of a PDIF-CN_2, film deposited on SiO_2/Si(100); (b) SECO and (c) HOMO region. The arrow points indicates the broad band related to the charge transfer [130].

Figure 4.27 shows the VB spectrum (a), with the close-up of the HOMO (c) and SECO (b) energy regions. The valence band region between 2-12eV is characterized by σ and π

molecular orbitals, with the peak of the HOMO level located at 2.5eV. In Figure 4.27-c is illustrated the 0-3eV BE region, where the arrow indicates a broad feature at about 1eV in the middle of the forbidden HOMO-LUMO energy gap. This structure is not related to replica in the UPS spectrum due to the HeI_{β} photon at 26.8eV, thus it can be associated to a charge transfer from the inorganic surface to the PDIF-CN_2, as better shown in the energy level scheme (Figure 4.28), assuming a molecule energy gap of 2.1eV.

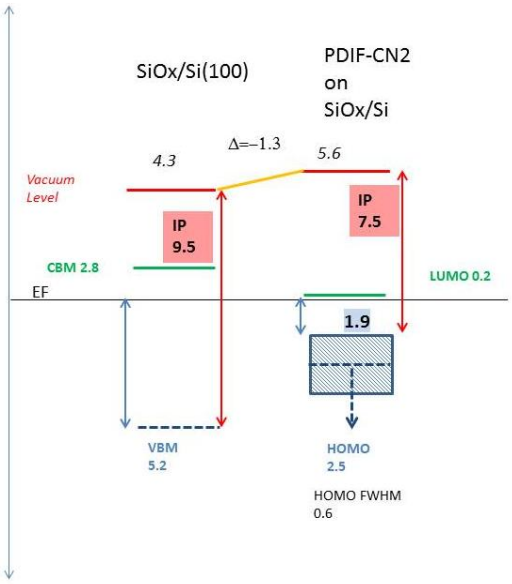

Figure 4.28: Energy level scheme of the PDIF-CN_2/SiO_2 interface [130] in comparison with the isolated systems. HOMO band and the centroid position are also shown. WF are shown on top of vacuum level lines, all energy levels values are calculated from the Fermi energy (EF) at 0 eV. All values are in eV.

The graph in Figure 4.28 displays the SECO shift versus the value of the substrate, suggesting the presence of a dipole of about Δ = -1.3eV. Comparing to the isolated organic film, HOMO and LUMO levels are shifted towards 0eV, a possible evidence of the injection of carriers in the LUMO from the inorganic substrate. Even though we are dealing with a strong insulator, the Fermi energy level positioning of SiO_2 close to conduction band, typical of a *n*-type insulator/semiconductor, suggests presence of a donor level close to the Fermi energy. Such a level could be responsible of an injection of electrons in the perylene LUMO, with following shift of HOMO-LUMO levels, dipole formation at interface and appearance of a band in the energy gap related to the new

HOMO'-LUMO' orbitals electronic rearrangement. The shift of the LUMO level towards the Fermi level and the band bending at the inorganic surface due to positive charge accumulation are at the origin of the negative onset voltages observed for these OFET, that has been hypothesized to be related to presence of positive charges at the organic/inorganic interface. Interestingly, this property has been found for both OMBD and SuMBD OFETs, even if for the latter the involved current are higher, possibly suggesting a more efficient charge transfer process.

Even though UPS studies of OMBD deposited films has not been realized, the lower electrical OFET performances, as well as better structural and morphological features put in evidence the ability of SuMBD to improve the interface electronic properties, with charge transfer process that have been hardly evidenced on insulating materials.

4.9 Summary

We have investigated the electronic properties of perylene derivatives, very promising organic material for organic electronics applications. We exploited the SuMBD approach to improve the chemical/physical, morphological and structural properties of organic films and, as a consequence, the performances of OFET devices based on them.

To check potentialities of the UPS spectroscopy to analyze electronic properties of interfaces, we studied the T6/PDI8-CN_2 interface, a layered structure that is suitable for the realization of p-n heterojunctions. The system is very complex, presenting both organic/organic and organic/inorganic interfaces. The perylene layer has shown to improve the T6 OFET performances, with the presence of a charge transfer between T6 HOMO to PDI8-CN_2 LUMO giving rise to the doping of the organic film, with accumulation of holes in the T6 layer and of electrons in the perylene LUMO at the interface layer. Such a behavior is evidenced by the presence of a peak in the HOMO-LUMO gap associated to the new perylene HOMO'-LUMO' rearranged electronic levels after charge transfer.

Exploiting the competences acquired in the analysis of electronic properties by UPS, the PDIF-CN_2/SiO_2 organic/inorganic interface has been studied for films deposited by SuMBD, with substrate at room temperature. OFET have been realized with SuMBD but also OMBD grown films, comparing the different performances. The experimental results

show that the SuMBD approach improves morphology and structural order of the film, a result achievable by OMBD technique only at substrate temperatures over 100°C. Moreover, the electrical performances of the OFET devices realized by SuMBD are significantly better, with a mobility three orders of magnitude higher than for film realized with OMBD mainly due to a higher structural order. Some performances are probably related also to the possibility of the perylene film to receive electrons from the donor levels in the insulating surface as shown by UPS analysis, creating a strong dipole at the interface and accumulation of positive charges (holes) in the inorganic surface, a process that has never shown before but only hypothesized, being very unlikely in strong insulating materials.

Chapter 5
Synthesis of carbon-based inorganic materials

5.1 Introduction

The supersonic molecular seeded beam approach has long shown its ability in the synthesis of inorganic material, namely SiC on Si from fullerene precursors. In the following we will explore the possibility to synthesize carbon-based nanostructured materials using the aforementioned supersonic beams of C_{60} impinging on surface having different chemical properties with respect to silicon, in particular showing lower intrinsic chemical reactivity. To this end, copper has been chosen with different surface structural order. The basic idea is to induce the opening of the fullerene cage due to the collision with the metal surface, studying also the influence of substrate temperature, precursor kinetic energy (KE). The aim is to define the threshold energy conditions to break the molecule, analyzing the chemical/physical properties of the interface as well as those of the new carbon based synthesized material. Different experimental conditions have been investigated, mostly by using in-situ surface electron spectroscopies but also ex-situ Raman technique. The final aim is to synthesize carbon-based nanostructured materials, namely graphene, by exploiting the unique SuMBD approach properties in inducing physical/chemical processes at the organic/inorganic interface, in particular the fullerene rupture. A brief introduction to materials object of this study will be presented.

5.2 Carbon allotropes

Carbon is an element of the VI A group of the periodic system with an electron configuration $1s^2\ 2s^2\ 1p^2$. It shows a tetravalent structure owing four electrons available to give rise to strong covalent chemical bonds. Up to 1980, only two natural allotropic forms of carbon, diamond and graphite, were isolated and characterized. In 1985 a new allotrope of carbon, Fullerene (C_{60}), consisting in a hollow cage of sp^2-bonded carbon atoms, was discovered by Kroto and coworkers [132], laying the foundations for the development of synthetic carbon allotropes.

Indeed, soon after fullerene discovery carbon nanotubes have been produced, characterized by a single layer of carbon atoms rolled in a cylindrical structure [133]. In this system carbon atoms are hybridized sp^2 and the σ bonds between carbons give rise to a honeycomb-like structure. Already in 1990 R. Smalley [134] hypothesized that these structures can be obtained by polymerization and elongation of fullerene.

In 2004 another carbon-based nanomaterial, a single layer of graphite called graphene, though being already known, gained a lot of renewed attention because of its magnificent and promising properties [135]. In graphene, each carbon atom is sp^2-hybridized giving rise to a strong covalent bonds which confer to the structure particular strength and stability, so that it can exists as a single "free-standing" layer [136]. The graphene discovery is extraordinarily important due to its two-dimensional atomic crystal structure and to its stability in ambient condition, up to this moment considered impossible [137]. Furthermore, we can imagine to achieve synthesis of all these carbon based materials starting from each one of the different dimensions represented by fullerene (0D), nanotubes (1D), graphene (2D) to graphite (3D). It is suggested that moving from one carbon state to the other could be just a matter of wrapping, unwrapping, rolling, unrolling, stacking and unstacking single layers or small portion of sp^2 coordinated carbon atoms [138]. In particular, it has been envisaged the possibility to obtain graphene by opening the fullerene cage, as described by M.S. Dresselhaus [139].

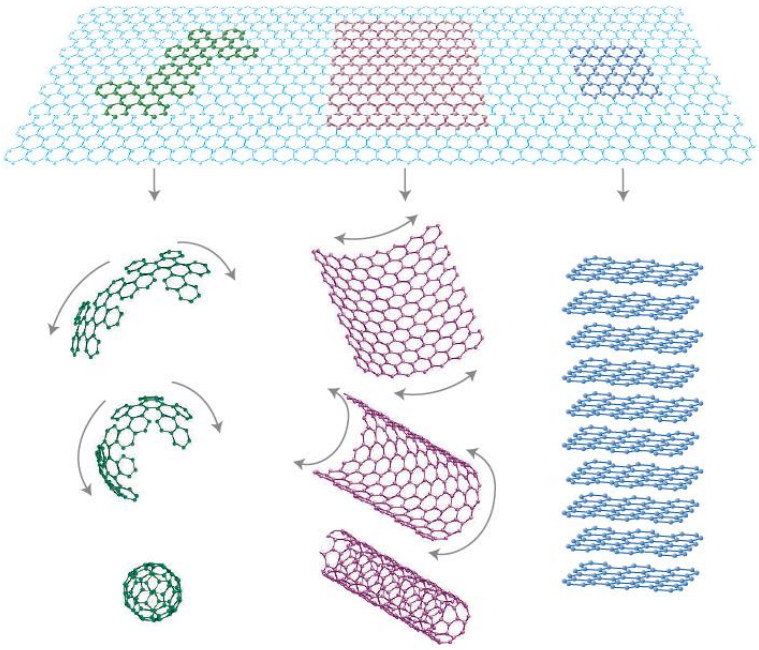

Figure 5.1: Sketch of carbon-based materials obtained by wrapping up (0D C_{60}), rolling (1D nanotubes) and stacking (3D graphite) graphene [138].

5.3 Graphene properties

Graphene shows peculiar electronic properties, with respect to the other carbon nanostructures, due to its unique crystal structure. The graphene lattice has two atoms for unit cell, A and B, which forms two equivalent sub-lattices shown in green and red in Figure 5.2-a [140]. In reciprocal space, the points at the corners, K and K', in the corresponding Brillouin zone (Figure 5.2-b) are fundamental for graphene physical properties and its band structure.

The remaining electros in p_z orbital give rise to a π-band system that is responsible for its very high electron conductivity. The structure of this band can be described by tight-binding calculation [141,142], as illustrate in Figure 5.3.

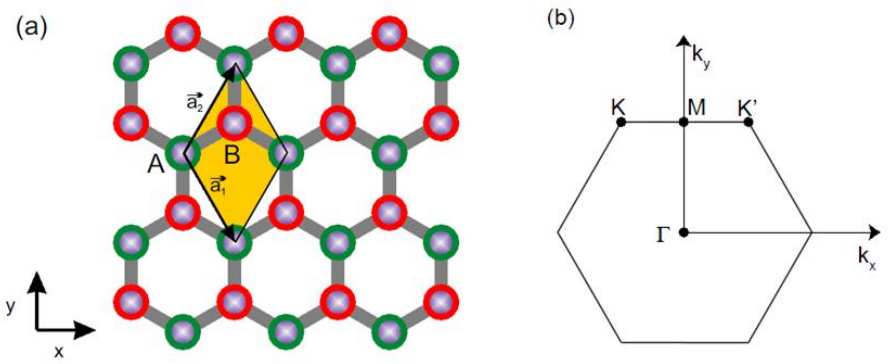

Figure 5.2: (a) Graphene honeycomb lattice structure; (b) Graphene Brillouin zone in reciprocal space[140].

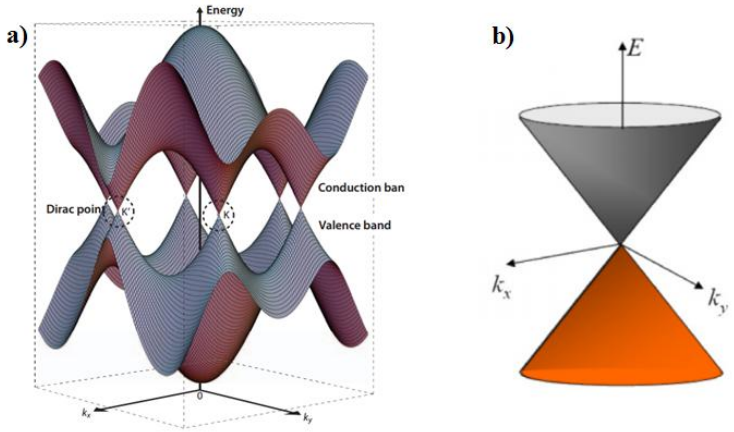

Figure 5.3: (a) Graphene π-band dispersion; (b) electron-hole cone structure at the K Dirac's point [143].

The valence band (π) and the conduction band (π*) cross in the K and K' points: these points, named Dirac points, are located at an energy which corresponds to the Fermi level. The two bands are neither separated by an energy gap nor overlapping, so that the electron dispersion around the Dirac point is linear and not parabolic as in the case of a semiconductor [141]. The charge carriers in graphene are described by the relativistic Dirac equation (Dirac particles) and not by the classical Schrödinger equation [144]. The relativistic description implies that the electrons act as if they were massless, as a consequence of the interaction with the periodic honeycomb lattice [145], moving at constant speed equal to the Fermi velocity of $v_F = 1x10^6$ m/s [136].

Figure 5.4 highlights the difference between the dispersion curves of charges carriers ruled by Schrödinger equation (A) and the Dirac particles in graphene, having zero mass (B and C) [136].

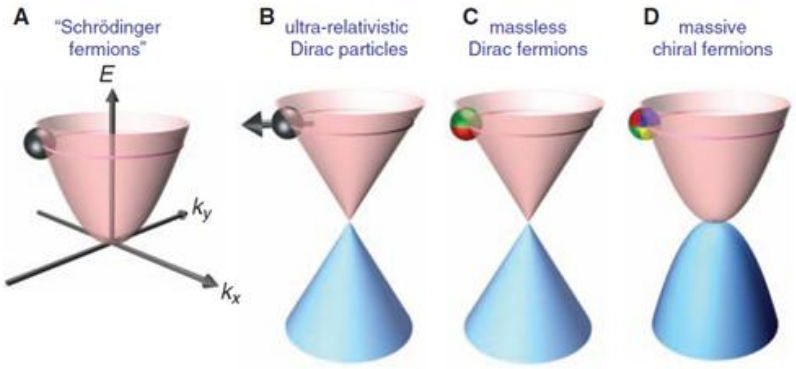

Figure 5.4: (A) Charge carriers having effective mass m* different from free electron mass described by Schrödinger equation; (B) Relativistic particles massless described by Dirac equation; (C) charge carriers in graphene, called Dirac fermions: (D) Bilayer graphene described by a combination of Schrödinger and Dirac equation [136].

The graphene bilayer shows another behavior as illustrate in Figure 5.4-D, and it is represented by a parabolic spectrum, that results from the combination of both Dirac and Schrödinger equations [136]. The presence of dopants or the alteration of the lattice symmetry can induce the formation of a gap between π and π* states [146].

The singular charge carriers behavior in graphene leads to other relativistic quantum effects, such as the Quantum Hall effect (QHE). Geim and co-workers [138] observed that for graphene at room temperature it is possible to quantize the Hall resistivity in discrete values of h/ne^2 (h is the Planck's constant, n a positive integer and e the electron charge). This phenomenon is generally observed in metals at very low temperatures and it depends on the thickness of the sample, as shown in Figure 5.5 [138].

In the graphene mono-layer (a) the Hall conductivity is represented by an uninterrupted series of steps which carries on even through the Dirac point. In the bilayer system (b) the spectrum shows a lack of symmetry maintaining, in any case, the metallic properties at the neutrality point [147]. Applying an electric field an asymmetry between the two layers

occurs, resulting in the formation of a semiconducting gap (Figure 5.5-c) which can be tuned changing the gate voltage intensity [148].

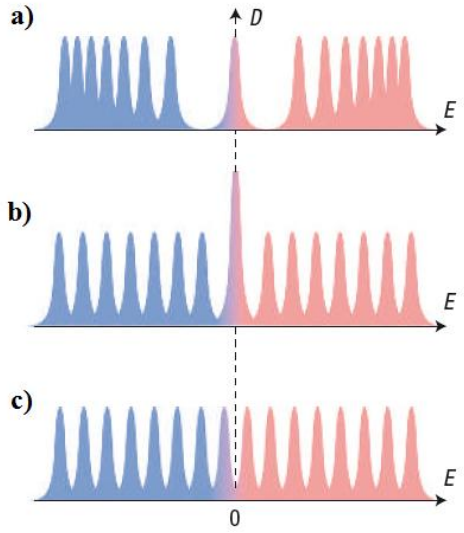

Figure 5.5: Different types of graphene Landau quantization in the case of (a) graphene single layer and (b) bilayer. (c) Formation of a semiconducting gap following electric filed application [138].

5.4 Fullerene (C_{60}) and its reactivity

C_{60} fullerene is a hollow spherical structure of sixty carbon atoms having a diameter of 7.1 Å [149] consisting of 12 pentagons and 20 hexagons, plus 30 π bonds and 90 σ bonds, with a truncated icosahedral symmetry (I_h) [150]. In this structure all the carbon atoms are equivalent and bonded to three neighbors with a sp^2 hybridization. The C-C bonds placed at the pentagon-hexagon border are single bond with a length of a_5 = 1.46 Å, whereas the C-C bonds along the hexagonal-hexagonal edge have double bonds with a length of a_6 = 1.40 Å (Figure 5.6) [151].

Each pentagon is surrounded by five hexagons so that there are not pentagonal rings adjacent to each other in an energetically unfavorable conformation, in agreement with the so called *isolated pentagonal rule* (IPR) [150]. To ensure this condition, the structure undergoes to a local curvature giving rise to the typical fullerene cage with a consequently excess of strain [152].

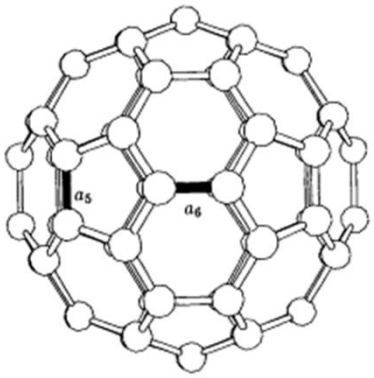

Figure 5.6: C_{60} Spherical structure. a_5 and a_6 represent the C-C bonds pentagon-hexagon (1.46 Å) and hexagon-hexagon (1.40 Å), respectively [152].

This surplus is responsible for C_{60} chemical reactivity associated to the spherical framework of the carbon atoms hybridized sp^2 and it gives rise to a pyramidalization of these hybridized atoms [153]. This effect consists in the conversion of the trigonal planar structure of the sp^2-hybridized carbon atoms into a tetrahedral molecular geometry (sp^3-hybridized), allowing the spherical system to release the strain in excess. The pyramidalization angle (θ_p), defined as the angle of the conjugated carbon subject to the curvature, in C_{60} (θ_p = 11.64°) is comparable to the ideal tetrahedral angle (θ_p = 19.47°) rather than to the trigonal one (θ_p = 0°) (Figure 5.7) [154].

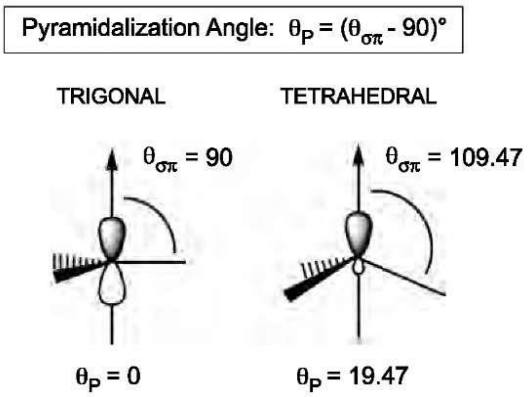

Figure 5.7: .Pyramidalization angle of sp^2 (left) and sp^3 (right) carbon atoms.

Fullerene acts as an electron-deficient olefin reacting readily with electron rich species and giving rise to a wide variety of chemical reaction (nucleophilic addition, Diel's Alder reaction, reductions, oxidation, cycloadditions, Friedel-Craft alkylations) [153,155].

5.4.1 Fullerene on metals

The interaction between C_{60} and metal substrates has been widely analyzed in the '90s by means of photoemission studies, in order to examine in detail the type on interaction between the metal surface and the C_{60} molecules. In general, when fullerene is deposited on metals, the alignment of its molecular orbitals with the Fermi level occurs in a charge transfer which fills partially the LUMO band and shifts the Fermi level [156]. The so called Pauli push-back effect has not been widely observed, probably due to formation of chemical activity and charge transfer at the organic/metal interface. In fact, this phenomenon is related to a compression of the electron density tail outside a surface and typically lead to strong decrease of the system work function [157,158], indeed not observed in the case of C_{60} on metals.

In Figure 5.8 is displayed the energy-level diagram proposed by J.H. Weaver [159] for a fullerene monolayer and a thick film adsorbed on a metal.

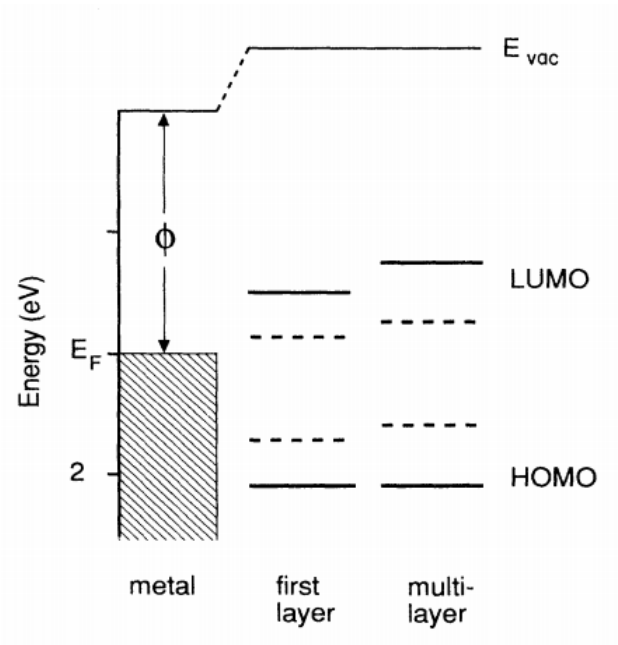

Figure 5.8: Energy levels diagram for the C_{60} first layer and multilayer on metal having work function ϕ. HOMO and LUMO ground-states are indicated by dashed lines, whereas the solid lines represent the measured energy by photoemission (N-1 system) and inverse photoemission (N+1 system) [159].

HOMO and LUMO ground-state are indicated by dashed lines, while the solid lines represent the energies measured by photoemission (N-1 system) and inverse photoemission

(N+1 system). For a mono-layer, the LUMO is placed closer to the Fermi level with respect to the bulk, because partially occupied. The strong interaction at low coverage gives rise to a combination of the LUMO ground-state with the metal levels creating a dipole that aligns the Fermi level and shifts the LUMO towards the Fermi level.

These processes at the interface depends on the involved chemical species and it have been measured using different metals as substrates, such as Au [160,161], Ag [162], Rh [163], Pt [164], In [165], Ta [166], Si [167,168], but we will focus our attention in particular towards Ni and Cu.

Regarding C_{60} deposited on Ni(110), as described by Rudolf and co-workers [164], in the case of thin films in the sub up to 1ML coverage the bands associated to HOMO (2.0eV) and HOMO-1 (3.5eV) undergo a shift. In particular, the C_{60} multilayer whole VB spectrum, with respect to the single layer, undergoes a rigid shift towards lower binding energies of about 0.4eV. The HOMO and HOMO-1 peaks of 1ML are instead shifted in the opposite direction and result to be broader than for the multilayer. This is the fingerprint of hybridization of the fullerene molecular orbitals between the substrate and the deposited layer, found also for other substrates [169].

Cu properties make it an ideal surface for fullerene deposition, taking into account the small lattice mismatch between the bulk C_{60} crystal and Cu(111) [170]. When fullerene is deposited on Cu(111) a shift of about 0.1eV towards higher binding energy of the HOMO is visible just with respect to the second layer. [156]. Tsang and collaborators [156], furthermore, have analyzed the photoemission spectra after annealing of a 2ML C_{60} film, putting in evidence the presence of two new contributions at 0.9eV and 0.15eV below the Fermi energy. The latter is associated to the charge transfer which derives from the partially occupied LUMO. The other contribution, instead, has been related to the changes undergone by the substrate as consequence of the well-ordered (4x4) C_{60} growth. Ten years later, A. Tami *et al*. [171] demonstrated that this peak is actually due to a strong hybridization between the fullerene carbon atoms and the first few layers of metal.

5.4.2 Fullerene film morphology

The properties of fullerene films depend on the interactions with the substrate on which they are grown. Generally, highly ordered films can be obtained only if the deposition is

carried out at high temperatures [172], inasmuch at room temperature imperfections can be occur. Let's consider the interaction of fullerenes with semiconductors and metals. In the first case, the presence of dangling bonds on the surface reduces the molecules mobility because of strong covalent bonds which occur between fullerene and substrate. As described by C.R. Wang *et al*. [173], fullerenes are distributed disorderly in the first layer and only in the second layer the mobility increases allowing the structure to be much more crystalline [173]. However, no ordered overlayer at long-range has been observed, since the disorder in the first layer does not allows the formation of a ordered growth. Yao and co-workers [174,175] described the fullerene adsorbed on Si(100) at room temperature as physisorbed molecules. Following annealing the molecules mobility increases and the post-annealed adsorbates size are smaller than before heat treatment. The annealing, furthermore, provides the necessary energy to convert the physisorbed in chemisorbed state.

As described in the previous paragraph, the interaction of fullerene with metals is very strong because of the charge transfer from the substrate to this molecule [176]. Considering a Cu(111) surface, during the first stage of adsorption at room temperature fullerene is very mobile and gives rise to two dimensional islands. Moreover, after annealing at 250°C to desorb the multi-layer, the first layer shows an ordered 4x4 structure stable up to 380°C [177]. Ordered structures have been observed also for fullerene grown on Au(111) [178] and Ag(111) [178].

5.4.3 Fullerene fragmentation

It was observed that fullerene film fragmentation can be achieved by thermal treatments. It is known that a temperature of about 1430°C is necessary to fragment isolated fullerene molecules [179], whereas for a solid C_{60} the temperature drops to 630°C [180].

S. Modesti and co-workers in 1996 [181] analyzed in detail by means of Auger spectroscopy the fullerene decomposition on Ni(110) substrate as a function of temperature. They found that fullerene fragmentation takes places above 490°C, whereas at about 530° graphitic domains are present on the surface. In particular, a fullerene film deposited at 430°C and afterwards heated at 490°C has been examined by AES, putting in evidence a shift towards high BE of the carbon *KVV* peak. This contribution undergoes a

reduction of the intensity with the further increase of the temperature up to 580°C, at which its signal is not detectable. Moreover, over 490°C, the C-*KVV* Auger peak changes shape, becoming similar to that of graphitic carbon on Ni(110). These results have been confirmed in 2001 by V. Saltas and collaborators [182] through LEED.

The fragmentation process of fullerene is closely related to the substrate nature, which can act as a catalyst in the decomposition. An important role is probably played also by the metal capability to form carbides, as it has been suggested by S. Modesti and collaborators [181]. Indeed, if on Rh(111) the decomposition temperatures are similar to those found for Ni(110) [163], on silicon the required temperatures are higher (about 730°C for Si(100) [183] and lower than 850°C for Si(111) [184], respectively).

A similar detailed analysis for the fullerene fragmentation on Cu is not available in literature. Nevertheless M.T. Lin [185], studying the superstructure transition of C_{60}/Cu(001), proposed a temperature of decomposition for fullerene at 610-690°C.

The fullerene decomposition on metal surface after thermal treatments can be exploited to obtain carbon-based nanostructured materials, such as graphene [186] exploiting the strong chemical interaction of C_{60} with Ni and solubility of carbon in Ni at a temperature of about 760°C. One of the common techniques used to grow graphene consists indeed in the direct deposition of carbon and hydrocarbons on metals [187]. This approach, however, requires high temperatures (above 700°C) in order to ensure the synthesis of highly ordered graphene layer [188].

Finally, it must be mentioned the study of J. Lu [189] of C_{60}/Ru(111), where formation of a complete graphene layer after fullerene decomposition has been achieved at 1200K, while graphene quantum dots regularly shaped can be synthesized at very low coverages (<0.2ML) around 650K. These results are achieved by exploiting the fullerene-rutenium strong chemical affinity, and formation of larger graphene domain is competitive with C_{60} and carbon diffusion on the metal surface, as well as with the tendency to sublimate.

5.4.4 Graphene synthesis on metal

The most common technique used for the synthesis of high quality graphene is the deposition on transition metal (such as Ni, Pd, Ru, Ir and Cu) by CVD. The formation of

graphene on metal surface has been observed for the first time during the preparation of Pt(111) and Ru(0001) single crystal surface. The metals were annealed at high temperatures giving rise to the segregation of the carbon impurities from the bulk to the surface and to the formation of graphitic layers. Moreover, graphene interacts very weakly with most metals, being the graphene' out-of-plain bonds saturated, on the van der Waals interaction order [190]. There are two common methods to prepare graphene layers on metals: by segregation of carbon (as impurities or dopant) dissolved in the bulk up to the metal surface (commonly Ni), and by decomposition of carbon precursors (as ethylene, propene, methane, CO and hydrocarbon molecules). Both these approaches require temperature above 700°C to grow graphene [191], inasmuch amorphous structures are obtained at lower temperatures.

A common metal used for graphene growth is Cu(111) that allows to obtain single layer graphene by CVD at ambient pressure [192]. Copper has the advantage to be fairly non-reactive and to have low carbon solubility so that it is possible to obtain graphene even at high temperature without dissolution of carbon in the bulk. Generally the graphene growth on Cu(111) is carried out in a UHV chamber using ethylene as carbon precursor at temperature up to 1000°C, very close to the Cu melting point [144]. At these temperatures, copper has a pressure of about 10^{-4} Torr and the graphene growth happens in a dynamic surface that is very close to being a liquid. The growth conditions and the carbon solubility in the metal strongly affect the graphene quality in terms of morphology and thickness.

Recently it has been demonstrated the possibility to grow graphene on Cu foil by CVD of methane at high temperature. The resulting film was mainly monolayer with small zone of bi- and multilayer and a not negligible presence of structural defects. Moreover, the graphene thickness was independent of copper thickness: the same graphene dimensions were been observed for foils with a thickness between 12.5 and 50 mm [193].

X. Li and co-workers [194] proposed an interesting study of the single layer graphene growth at different deposition times and studied by SEM spectroscopy. At the beginning (1min) graphene in finite size with a flake shape is visible: the small circle in Figure 5.9-a indicates a nucleation site whereas the larger circle a graphene domain. Increasing the deposition time (2.5min) the graphene domains increase giving rise to a uniform layer. The region indicates in Figure 5.9-b shows a void where the graphene domains connect to form a complete layer. Moreover, nucleated graphene flakes with various shape have been

observed on different Cu grains indicating that the growth is favoured on preferred Cu crystallographic direction. The growth mechanism is surface related and copper acts as a catalyst thanks to the mentioned low carbon solubility on it due to the closed d shells and free-electron-like surface state, properties common to noble metal [193].

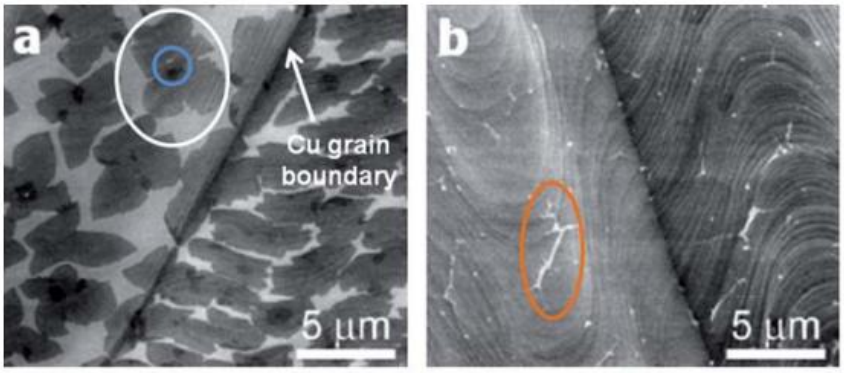

Figure 5.9: SEM images of graphene on Cu at different growth time. (a) small circle indicates a nucleation site and the larger one a graphene domain. (b) the circle puts in evidence a void where the graphene domains join to form a continuous layer [193].

5.5 Synthesis of carbon-based nanostructured materials by SuMBD

As already described in the paragraph 2.9.3, the IMEM-CNR group in Trento was able to break the fullerene cage at room temperature in the organic/silicon surface collision, exploiting the high KE of the C_{60} supersonic beams by SuMBD [21]. In this way they synthesized high quality nanocrystalline 3C-SiC islands using a fullerene supersonic beam as precursor on a Si(111) substrate. They demonstrated the possibility to open the fullerene cage, the first and foremost process in order to achieve synthesis of ordered carbide with a relaxed structure. Furthermore, the precursor KE necessary to induce the opening of the cage was estimated to be about 30-35eV. This value was moreover confirmed by non-adiabatic MD theoretical analysis carried out by LISC-FBK (Laboratorio Interdisciplinare di Scienza Computazionale-Fondazione Bruno Kessler) group in Trento [48] (see paragraph 2.9.3 for more details).

In the light of the excellent results obtained in these studies we have investigated the interaction of a fullerene supersonic beam on a metal surface, in particular Copper (Cu).

The purpose of this work was to break the fullerene cage in order to obtain carbon-based nanostructured materials at low temperatures, namely low dimensional materials like graphene, taking in mind that standard technique as CVD require far more extreme conditions (about 1000°C) for its synthesis. Theoretical studies carried out by LISC-FBK group in Trento by Non-Adiabatic Molecular Dynamics calculations have indeed demonstrated the possibility to open the cage employing a fullerene beam KE of about 35-40eV (Figure 5.10-a). As a matter of fact, the Kinetic Monte Carlo simulation for a 0.5 ML coverage shows the formation of hexagonal fragments on Cu following the fullerene opening, as displayed in Figure 5.10-b. The idea is to break the fullerene cage, open it and obtain a single layer of carbon atoms linked by sp^2 bonds, arranged in hexagons and pentagons laying on the Cu surface, i.e. a graphene layer showing specific defect related to presence of pentagons. Copper is an ideal candidate for this purpose, as formation of carbides is not allowed (like for many other metals), carbon solubility in its lattice is low and C_{60}/Cu interaction is a well known and widely studied system.

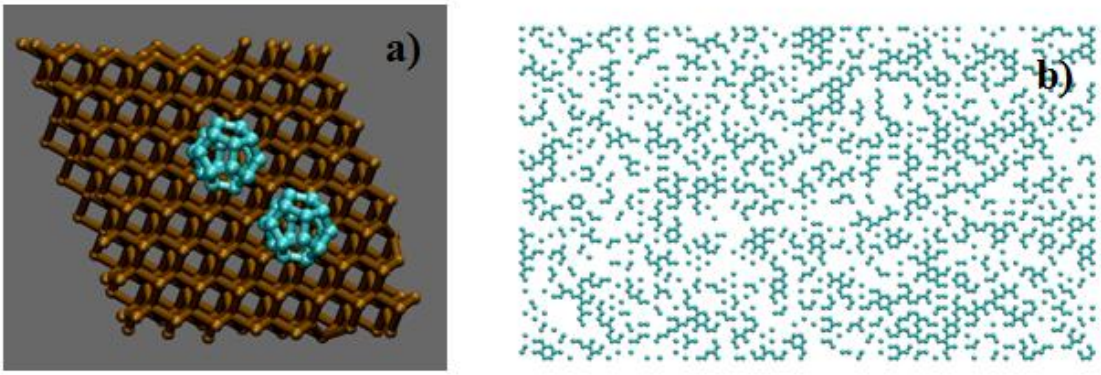

Figure 5.10: Theoretical models proposed by LISC-FBK group in Trento. (a) NA Molecular Dynamics approach shows the interaction at the interface C_{60}-Cu(111) confirming the possibility to open the cage applying a KE of 35-40eV. (b) Kinetic Monte Carlo simulation displays the formation of hexagonal fragments following the fullerene molecule opening.

Comparing to the C_{60}/Si(111) collision, where a theoretical energy threshold for cage breaking slightly higher than those observed in experimental evidences was found, the

foreseen values of 35-40eV is very high and present some experimental and practical difficulties to be overcome, however the presence of a metal and non interacting surface is significantly different from the semiconductor and interacting surface of silicon and it must be expected a process that do not develop in the same way.

The results that will be presented in the following are the subject of a paper that is currently under writing and will be soon submitted to Physical Chemistry Chemical Physics [195].

5.5.1 Metal substrate and fullerene precursor

Polycrystalline copper and single crystal Cu(111) (from Sigma-Aldrich) have been employed as substrate, in order to define the role of the ordered structure of the substrate in the C_{60} growth process. The single crystal Cu is mostly used in the graphene synthesis because of all the characteristics described in the previous section of this chapter, but the polycrystalline Cu could represent an interesting alternative from the applicative point of view, being cheaper than the monocrystalline copper and available in form of thin foil for synthesis on flexible substrates, so that the opportunity to grow graphene on it could pave the way for challenging perspectives. Before introduction in the analysis chamber, samples have been cleaned by wet chemicals and then they undergo the sputter/annealing procedure in UHV as described in the paragraph 2.1.6. To restore the crystallinity lost during the sputter processes, the surface has been annealed with a flash thermal treatment of 15 minutes at about 500°C. Such a treatment typically induce segregation of contaminants from the bulk, in case of copper the main one is sulphur. The sputtering-annealing procedure has been repeated until the total disappearance of the sulphur contamination. However, in order to perform experiments of fullerene deposition or post-deposition thermal treatments at temperature up to 800°C, in that case specific (and long time requiring) sputter-annealing procedure have been performed to avoid sulphur surface segregation also at these temperatures higher than the standard 500°C.

The organic molecule used as carbon precursor was C_{60} fullerene purchased by Sigma-Aldrich. We used two different carrier gas, He and H_2, in order to operate, respectively, at low (10-15eV) and high (30-35eV) translational KEs for C_{60} in the supersonic beam. The pressure of the He in the beam was of about 1200 mbar with a pressure in the analysis

chamber of $4.2x10^{-7}$ mbar. In H_2 case, instead, the gas carrier pressure was of 1100 mbar and a background pressure of $4.2x10^{-8}$ mbar in the main UHV chamber.

All the fullerene films have been characterized *in-situ* through photoelectron spectroscopies (XPS, UPS, AES) to analyse their chemical-physical properties and by LEED electron diffraction to study the surface order. The UPS analysis have been carried out by means of a He UV lamp, using the HeI, hv = 21.22eV, and HeII, hv = 40.80eV, photon emissions.

The films deposited on copper have been analyzed also *ex-situ* by Raman spectroscopy. The characterizations have been performed by DR. G. Speranza of the PAM_SE group of the CMM-FBK (Centro Materiali e Microsistemi-Fondazione Bruno Kessler) in Trento (see paragraph 3.6.4) and DR. G. Baldi of the IMEM-CNR institute in Parma.

5.5.2 Standard preparation and characterization

5.5.2.1 Copper substrate core level

The Cu2p core levels for polycrystalline and single crystal state are shown in Figure 5.11. The 2p orbitals give rise to a spin-orbital splitting characterized by a doublet with the two possible states located at different BEs. The peak at lower BE (932.60eV) is related to the Cu2p 3/2 while the other contribution to Cu2p ½ at 952.40eV, with a distance between the two peaks of 19.8eV, as reported in literature [55]. These two components are characterized by an asymmetry of the peak towards high binding energy that is typical for transition metal [196]. The lineshape is furthermore constituted by other four components (red lines in Figure 5.11) related to shake-up energy loss structures [197].

The analysis of the valence bands is displayed in Figure 5.12 where the comparison between polycrystalline Cu, single crystal and polycrystalline Cu thermal treated at 560°C is shown. All substrate are characterized by the Fermi edge located at 0eV (Figure 5.13), intense features in the 2-5eV region related to the 3d electronic levels/bands and a work function (WF) of 4.7-4.8eV, 4.94eV and 5.43eV respectively for the three mentioned metal surfaces, in total agreement with previous results [198,199].

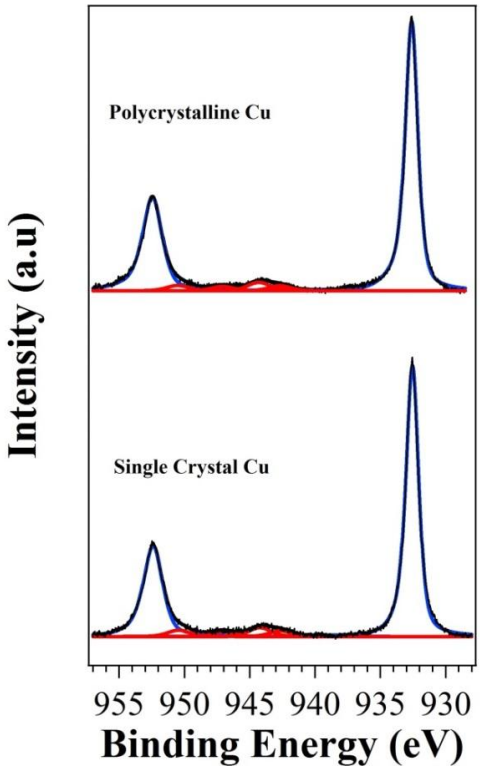

Figure 5.11: Cu2p core levels for poly and single crystal Cu.

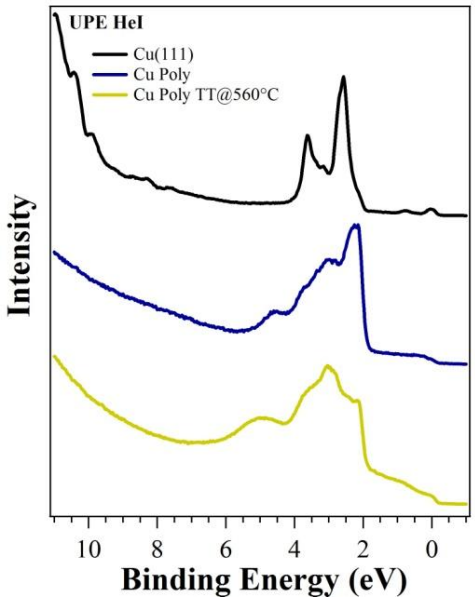

Figure 5.12: UPS valence bands of Cu(111), polycrystalline Cu and polycrystalline Cu annealed at 560°C.

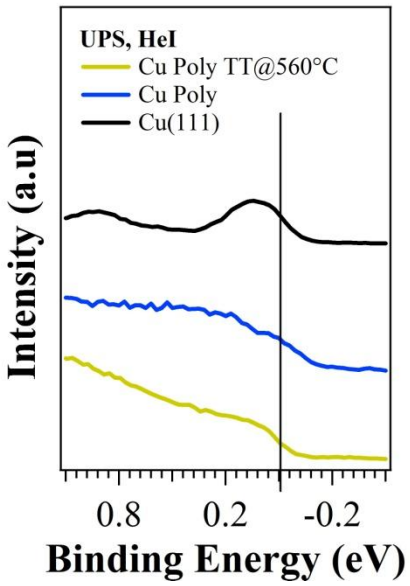

Figure 5.13: Fermi edge region for the different Cu substrates.

The single crystal presents weak bands at about 1eV related to the metal surface states, i.e. associated to electronic states on the metal surface and due to the surface rearrangement following the annealing processes. Treating the polycrystalline Cu at high temperatures (560°C, yellow line in Figure 5.12) without performing sputtering, the valence band undergoes changes in the 3-6eV region due to the sulphur segregation from metal bulk, forming sulphides, and the WF significantly increase up to 5.4eV.

5.5.2.2 HOPG, Graphene, Fullerene thick film core levels

Standard samples (single layer graphene, highly oriented pyrolytic graphite HOPG and a fullerene very thick film) have been characterized by XPS and UPS analysis. This is necessary to better identify single chemical species in the following analysis. The graphite HOPG and graphene single layer on polycrystalline copper foil were bought from Sigma Aldrich and from Graphenea (Spain). The fullerene thick film was deposited on polycrystalline copper by SuMBD at room temperature with a final nominal thickness of about 5 nm. In Figure 5.14 the graphene (a), HOPG (b) and C_{60} bulk (c) C1s core levels are shown, while their main features (BE, full width at half maximum FWHM, percentage on total C1s area) are summarized in Table 5.1.

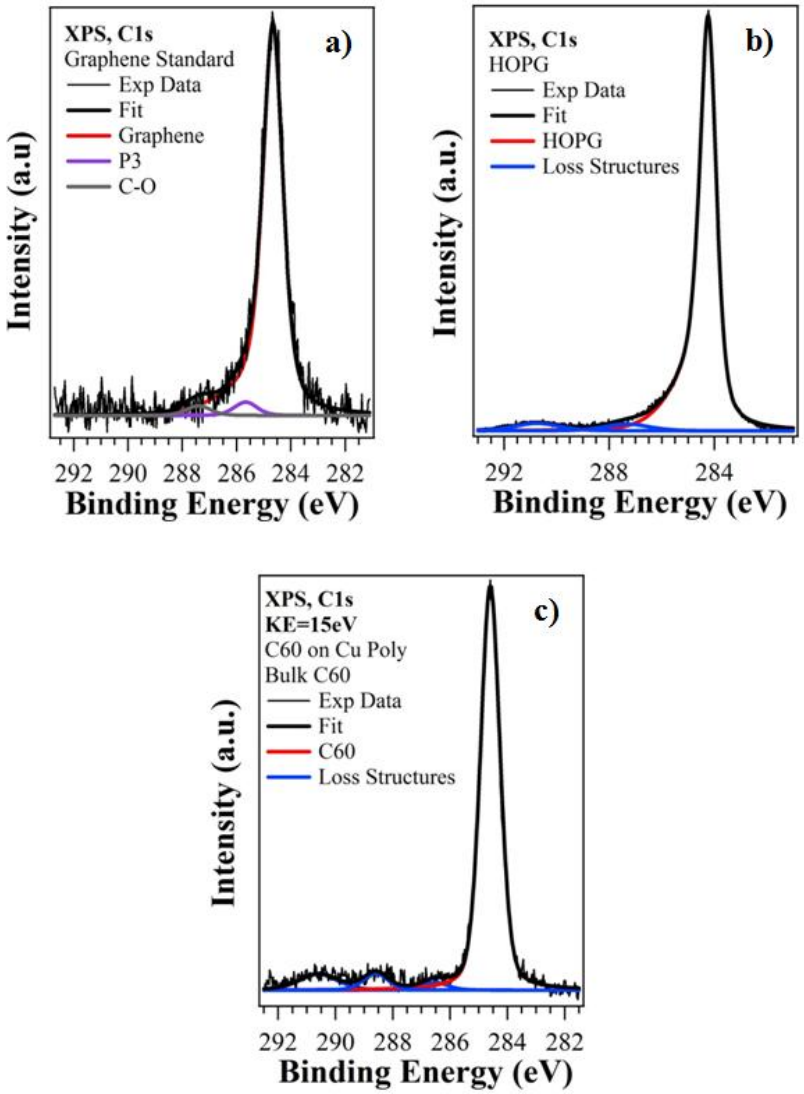

Figure 5.14: C1s core level of (a) standard graphene, (b) HOPG and (c) fullerene thick film.

Graphene				HOPG				C_{60} Bulk			
BE [eV]	**FWHM [eV]**	**%**	**Note**	**BE [eV]**	**FWHM [eV]**	**%**	**Note**	**BE [eV]**	**FWHM [eV]**	**%**	**Note**
284.66	0.88	95.1	sp^2 C-C	284.24	0.78	93.9	sp^2 C-C	284.60	0.80	86.6	sp^2 C-C
285.66	1.00	2.7	P3	287.33	1.00	3.3	Loss	286.50	1.00	2.0	Loss
287.40	1.30	2.2	C-O	290.75	1.30	2.8	Loss	288.60	1.30	4.6	Loss
								290.60	1.50	6.8	Loss

Table 5.1: C1s core levels main features from surfaces of graphene, HOPG and thick C_{60} film.

The main peak in the graphene C1s core level is located at 284.66eV, it is related to the sp^2-hybridized C-C bonds and it is characterized by a peculiar asymmetric shape due to the neutralization of the holes generated during the photoionization process by conduction electrons.

The dissymmetric shape is so defined by the band structure and is much more marked when the Fermi level density of states is high [200]. In materials such as graphite and graphene the electron-hole pairs can be easily formed inducing the characteristic asymmetry of the C1s line [201]. This lineshape is well described by the so called Doniach-Sunjic formula, a complex function characterized by the presence of an asymmetry factor (becoming typical for each material) but also by the low level of integrability and thus high difficulty in using it for peak lineshape fitting. Moreover, in some cases it can be hardly applied, as in the case of C1s emission from a C_{60} single monolayer (see paragraph 5.5.3). For these reasons, often different approaches based on double Lorentzian or other functions are preferably used, perfectly reproducing the asymmetric lineshape of core levels, and so we did.

The spectrum presents, moreover, two further contributions at higher BE, at 285.66eV and 287.40eV, related to sp^3 defects (named P3) and oxidized C-O species [202].

In graphite, the main peak is asymmetric but narrower and shifted at lower BE (284.24eV) with respect to graphene. The asymmetry is different from that of graphene, while the lineshape is characterized also by loss structures at high BE (287.33 and 290.75eV). As described by Filippi and Calliari [203] the loss structures in HOPG at lower BE are related to excitations which involve the π electrons and are defined as π plasmon. The second contribution at 290.75eV instead involves all the valence electrons (π and σ) and it is named as $\pi + \sigma$ plasmon. These structures are typically correlated to the energy loss which occurs when the photoelectron interacts with other electrons on the sample surface, a phenomenon particularly evident in metals [55].

The fullerene thick film (bulk phase) shows a main peak at 284.60eV and it is symmetric. Important loss structures are present, much more intense compared to HOPG and related also in this case to π and $(\pi + \sigma)$ resonances. A detailed description of C_{60} thick film loss energy satellites is proposed by Ref. [204].

It is evident that the three carbon chemical species show C1s core levels that are characterized by very similar binding energies, graphene shows a slightly larger FHWM

and they differs clearly only for the loss structures, that are however very weak structures. Thus, their identification in the following experiments and C1s analysis has required great attention and acquisition of signal with the highest signal-to-noise ratio.

Concerning valence bands, the comparison of all materials is shown in Figure 5.15-a where it is also illustrated the Cu substrate as reference. Fullerene thick film is characterized by a WF of 4.8eV and a ionization potential (IP) of 6.5eV [205] and intense features, i.e. the HOMO at about 2eV and the other π and σ structures at higher BEs, whereas the HOPG has very broad bands and a WF of 4.5eV [206]. Graphene single layer has weak features in the 0-6 eV region where the Cu bands are predominant, and a WF of 4.3eV, slightly lower with respect to the 4.5eV reported in literature [207] but probably related to presence of defects in the layer, as revealed by the C1s peak analysis.

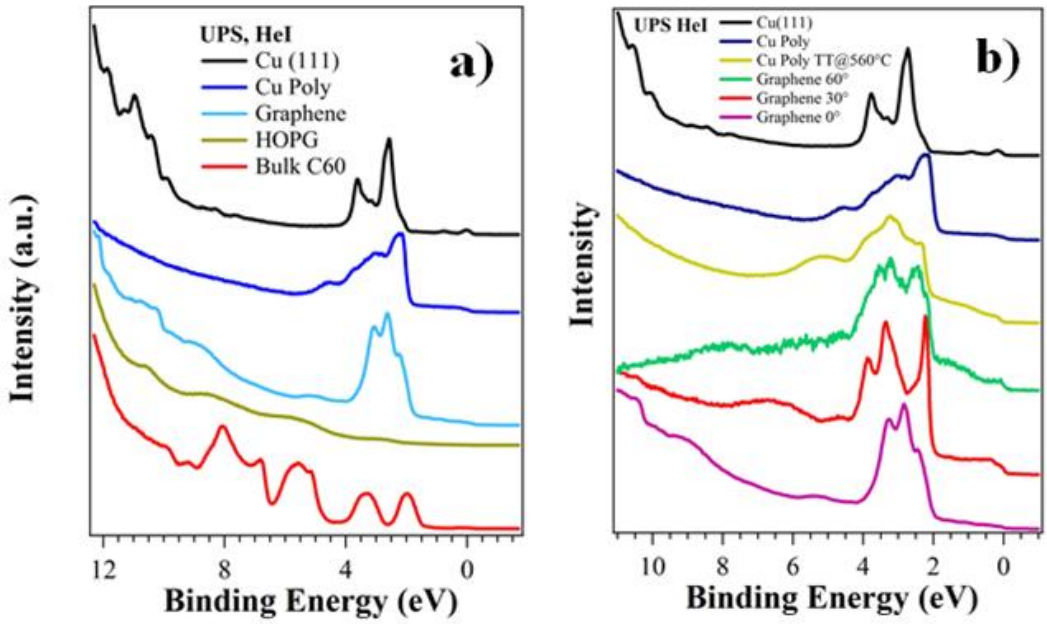

Figure 5.15: (a) UPS valence bands (HeI, *hv*=21.22eV) for the different materials; (b) UPS valence bands (HeI, *hv*=21.22eV) of graphene on polycrystalline Cu acquired at different acceptance angles. The spectra of single crystal Cu and poly-crystalline and the polycrystalline Cu treated at 560°C are displayed as reference.

It is possible to emphasize the graphene components performing the analysis in grazing angle electron acceptance, in order to improve the signal coming from by upper most surface layers and reduce that coming from the deeper metal layers. Graphene valence

band on polycrystalline Cu measured at three different acceptance angles (0°, 30° and 60°) is shown in Figure 5.15-b. In particular the spectrum acquired at 30° puts in evidence a peculiar structure located at about 6eV and related to the graphene σ bands. It is noteworthy the differences with respect to other reported graphene VB are mainly related to the large acceptance geometry of our electron energy analyzers.

5.5.3 C_{60} monolayer on Cu

A strong chemical interaction between the first fullerene layer and Cu surface has been widely reported, as previously stated. We have evaluated the properties of a fullerene thin film of about 1 monolayer (ML) grown by three different approach, in order to study the interaction at the organic/inorganic interface. In a first case, a thick film of fullerene has been deposited on a Cu polycrystalline surface by SuMBD at 15eV and room temperature. The deposit has been then heated at 445°C for 100 minutes to eliminate the physisorbed molecules and leave only the first C_{60} highly interacting layer. Having this standard amount of organic material as a reference, we deposited 1 ML fullerene film on a polycrystalline Cu at room temperature by supersonic beam at 15eV and on a single crystal Cu(111) by supersonic beam at 35eV. The C1s core levels relative to the three samples are presented in Figure 5.16. The main peaks related to the sp^2-hybridized C-C are located at the same BE and they are characterized by very comparable FWHM, as summarized in the Table 5.2. The C1s core levels in the three case have very similar lineshapes, with differences that are within errors typical of this type of analysis. This suggests that the different growth techniques do not affect the overall characteristics of the film in the form of 1ML, so the three approaches to achieve formation of a single fullerene monolayer are equivalent.

Moreover, these results demonstrate that the fullerene-metal interaction plays an important role in the interface formation, as the same results have been achieved independently by the surface crystallinity, the growth temperature and the different KE of the molecular beam impinging on the surface.

With respect to the C1s emission from the thick film previously described, the 1ML case shows several differences. The main peak is characterized by a 0.4-0.5eV lower BE,

+0.1eV FWHM and an evident asymmetry that, by the way, is completely different from that of graphene and HOPG.

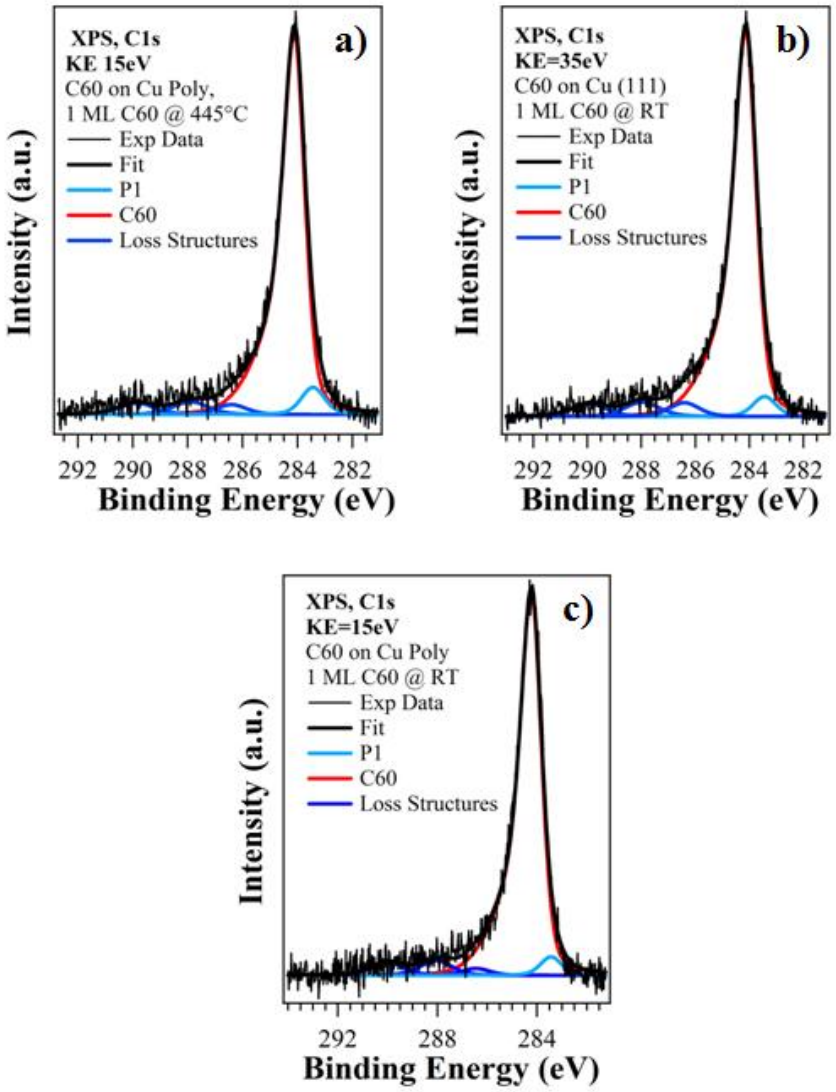

Figure 5.16: C1s core level of 1ML C_{60} on Cu surface. The fullerene single layer has been obtained by thermal treatment at 445°C of a thick film (a), C_{60} deposition at room temperature by SuMBD at 35eV (b) and at 15eV (c).

As explained by K.D. Tsuei and co-workers [208], the peculiar C1s asymmetry of 1ML C_{60} can be associated only to the "metallic" character of the fullerene film, showing strong chemical interaction and charge exchange phenomena at the metal interface. Even though the latter processes are somehow still a matter of debate, the screening effects due to the

metallicity of the fullerene single monolayer on copper are accepted and at the origin of the observed peak asymmetry.

The peak shift towards lower BEs as well as its broadening can be interpreted also in terms of screening effects, due to the metallic character of the first fullerene layer with respect to the thick C_{60} film, that is typically insulating. Loss structures show a shift towards lower Bes too, that it is different for the three peaks and their weight is significantly reduced.

	1ML, Poly Cu, KE=15eV, 445°C Bulk			**1ML, Cu(111), KE=35eV, RT**			**1ML, Poly Cu, KE=15eV, RT**		
	BE [eV]	**FWHM [eV]**	**%**	**BE [eV]**	**FWHM [eV]**	**%**	**BE [eV]**	**FWHM [eV]**	**%**
sp^2 C-C	284.12	0.90	86.9	284.14	0.92	87.6	284.23	0.95	89.0
P1	283.44	1.00	4.5	283.44	1.00	3.1	283.44	1.00	2.9
Loss	286.41	1.30	2.1	286.41	1.30	2.8	286.46	1.30	1.4
Loss	287.95	1.50	3.5	287.97	1.50	1.6	288.06	1.50	3.5
Loss	289.90	1.50	3.0	289.92	1.50	2.9	290.01	1.50	3.2

Table 5.2: Principal features of C1s core level for three different film of 1ML C_{60} obtained at different experimental conditions.

These phenomena are definitely related once more to the strong chemical interaction and possible charge transfer occurring at the interface. The differences between the bulk phase and the single layer on a metal surface are furthermore related to the corresponding insulating and metallic behaviours [209].

In addition to the main peak and the corresponding loss structures, the spectra show a further component at 283.44eV, named P1. This peak is only characteristic of the first layer, since it is absent in the bulk phase and cannot be associated to the presence of carbides on the surface. It represents 3-5% of the total emission signal of the carbon C1s. We suppose that it could be related to the rearrangement of the fullerene on the Cu surface. Recently, M.A. Hove and co-workers [210,211] demonstrated that heating a fullerene film (>1ML) grown on a Cu(111) surface at 330°C, a single monolayer fullerene film showing a (4x4) rearrangement has been obtained. This is related to the nearest-neighbour distance of Cu atoms on Cu(111) of 2.56 Å, thus being 1/4 of the C_{60} intermolecular distance of 10.02 Å, with a lattice mismatch of 2.5% leading to the formation of the observed (4x4) reconstruction.

After the reorganization in a well-ordered structure of the organic material, C_{60} molecules cause the deformation of the inorganic substrate. As a matter of fact, C_{60} is positioned in a sort of cup created as a result of the removal of 7 Cu atoms from the first layer, so 15 fullerene atoms give rise to a stable bonds with 9 Cu atoms of the first metal layer and 3 with the second one (Figure 5.17). This strong interaction induces a considerable charge transfer from the metal to the organic, that is evaluated in 3 electrons for molecule [203,210]. Taking in mind that the structural parameter of fullerene lattice is about 4 times that of Cu(111), the reorganization on the metal surface gives rise to a structure very stable and with a reticular position energetically favourable.

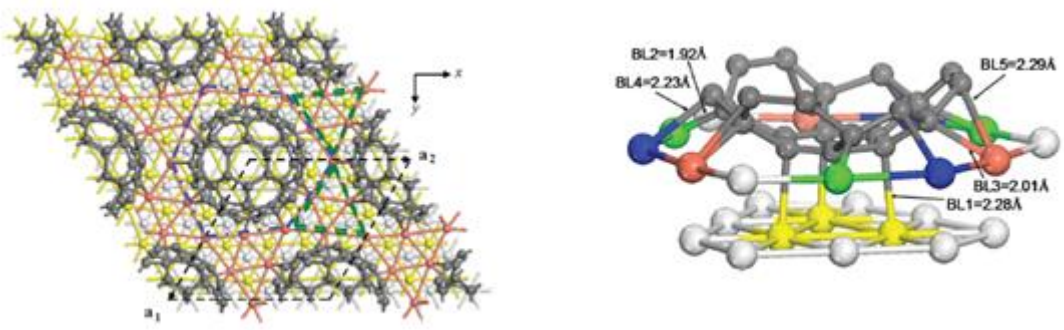

Figure 5.17: (a) Sketch of Cu(111) + (4x4)-C_{60}. The grey balls are C atoms; red, yellow and light gray balls are Cu atoms in the first, second and third Cu layers. (b) View of the interaction at the C_{60}-Cu interface, displaying the C-Cu bonds lengths [210].

We have reproduced the experiment carried out by Hove's group, heating 1ML C_{60} on Cu at 430°C in order to highlight if our samples possess the same properties. In Figure 5.18 the LEED pattern of these surfaces acquired at 70 (a) and 80eV (c) are shown and compared with the cleaned Cu(111) surface (b and d). It is evident the presence of a (4x4) reconstruction extended over the surface, visible in a wide range of energies from 30eV up to 200eV, so a reconstruction having the same characteristics of the mentioned studies.

The fullerene film achieved in these conditions shows a C1s lineshape similar to that of a 1ML C_{60} with the peculiar peak P1. LEED characterizations for 1ML C_{60} deposited on Cu at room temperature did not show similar results, while on the Cu polycrystalline no diffraction was evident.

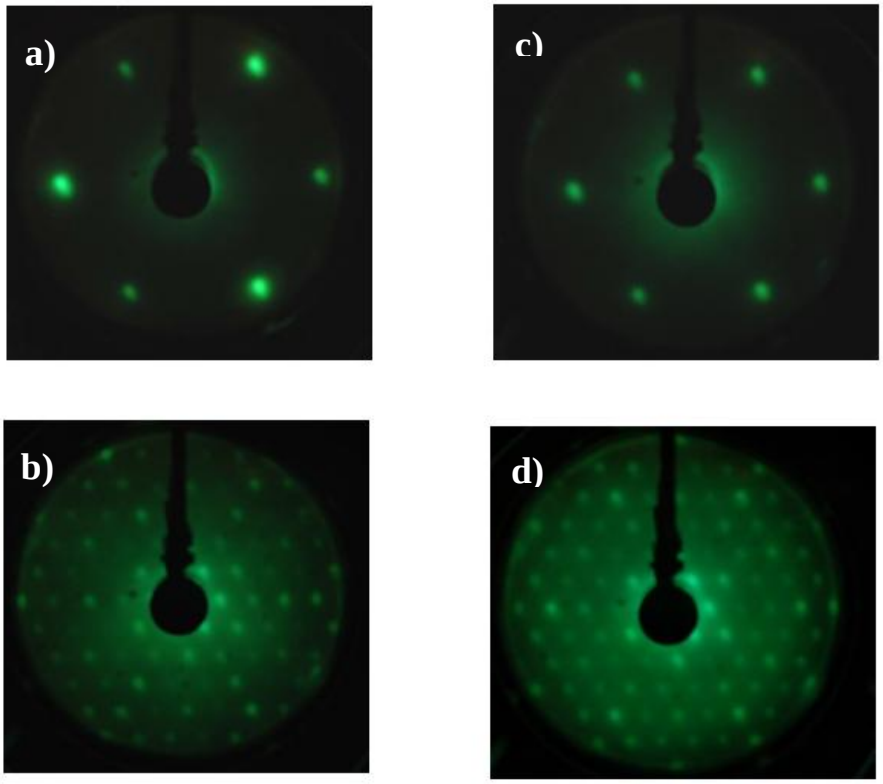

Figure 5.18: LEED pattern acquired at incident electron energy of 70eV (on the left) and 80eV (on the right). (a,c) Cu(111), (b,d) 1ML C_{60} on Cu(111) thermal treated at 430°C.

Considering the interaction mechanism proposed by Hove's group, the P1 component could be associated to the fullerene cage atoms which form strong bonds with the surface. These atoms are affected by the charge transfer from metal resulting further shifted at lower BE. Considering the P1 intensity (3-5% of C1s emission), it is possible to assume that it represents about 2-3 fullerene carbon atoms which could be really the 3 atoms of the hexagon located inside the hole in the copper surface, and chemically bonded to the Cu(111) atoms of the second metal lattice layer. The P1 peak is present also in the fullerene ML grown at room temperature, so that we can suppose that the (4x4) rearrangement occurs even without heat treatment (at 20°C room temperature), probably not with long range order but at the nanoscale. These experimental evidences could be an indication that the KE supplied by the SuMBD approach is used, in part or totally, to the surface rearrangement of the organic molecules. Finally, the presence of the P1 peak also for the C_{60} 1ML on the polycrystalline Cu surface suggests that the metal surface reconstruction is possible also for surfaces showing order at lower range. In fact,

polycrystalline Cu is characterized by the presence of micrometric domains with different rotation (making them undetectable by LEED analysis), whose extension depends on the temperature used in thermal treatments but that are nevertheless present. At the nanoscale this surface is comparable to that of a single crystal, making possible the first metal layer modification in a way similar to what observed for Cu(111), but not detectable by LEED due to the variability of domains rotation.

Another possible attribution of P1 peak could be the formation of carbon nanostructures as graphene free-standing islands, formed during the fullerene impact on the metal surface. Its position at lower BE can be associated to the decoupling of these nanostructures from the copper surface. However, we have not found differences in the P1 intensity between the deposition at the two different KE regimes at lower (15eV) and higher (35eV), as would be expected if the synthesis of these nanoislands of graphene occurs during the first C_{60}/Cu surface collision. So, such an interpretation seems unlikely.

The comparison between the UPS spectra of the fullerene thin films grown at room temperature on polycrystalline Cu by supersonic beam at 15eV, on single crystal Cu by supersonic beam at 35eV and thermal treatment at 430°C (showing the C_{60} (4x4) reconstruction) and the bulk valence band is illustrated in Figure 5.19. Similarly to what observed in the C1s core levels the 1ML C_{60} valence bands are both shifted of 0.5eV towards lower BE with respect to the bulk film.

The fullerene molecular orbitals bands in the single layer appear as slightly broadened and less defined with respect to the thick film (especially for the film at precursor KE of 15eV), suggesting an hybridization between fullerene and the metal electronic states [209], but no significant differences between the reconstructed and not reconstructed C_{60} film on the two different underlying Cu surfaces (single crystal and poly). Nevertheless, for the reconstructed C_{60} (4x4) film the spectrum is somewhat different than expected just summing the valence band of Cu(111) and that (shifted and enlarged) of fullerene, and could be related to different features from the copper surface. This once more would suggests that a structural rearrangement occurs on the copper surface and could be related to the fullerene KE. Due to the complex lineshape in the 1-5eV region, more specific investigations (that are far from the topic of this work) are necessary and will be performed in the future.

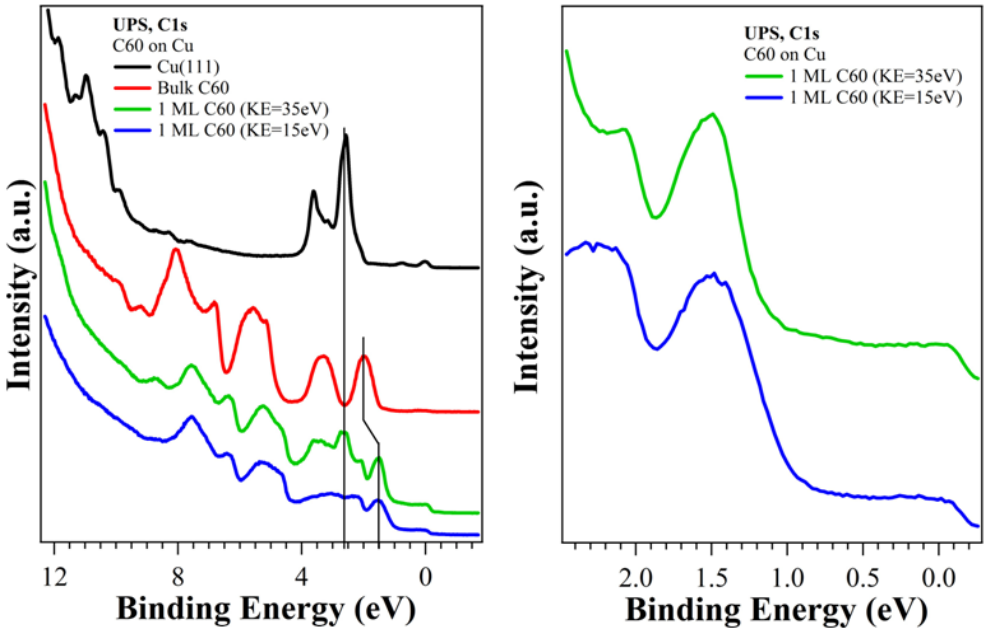

Figure 5.19: Valence bands (HeI, *hv*=21.22eV) of 1ML C_{60} deposited at room temperature on poly- and single-crystal Cu by supersonic beams at 15eV (blue line) and 35eV (green line). On the right magnification of the HOMO region.

Differently from what observed in MBE experiments, we did not find the feature at 1.0eV attributed to hybridization of the fullerene molecular orbitals to the Cu sp orbitals of the topper most metal lattice layers [171], as well as any evidence of LUMO presence near the Fermi edge [212], even though most of these analysis have been performed using a substrate temperature of 10K, not achievable in our experimental set up. Moreover, the WF shows a +0.27 and +0.07eV difference with respect to the original poly and (111) clean surfaces, while a small decrease (about -0.1eV) has always been reported [156]. These evidences suggest that the film growth by SuMBD lead to differences in the electronic properties of the final C_{60} single layer with respect to MBE approach, pointing to a role of the precursor kinetic energy in differently defining the chemical activity at the interface.

In summary, both XPS and UPS analysis indicate a strong chemical interaction and probable charge transfer at the fullerene-copper interface, with the formation of a metallic first C_{60} ML while the other layers in the thick fullerene film are characterized only by weak intermolecular forces, that can be easily broken with temperature inducing the organic sublimation.

5.5.4 Sub-Monolayer fullerene on copper

In the previous paragraph we have highlighted the strong interaction at the 1ML coverage of fullerene and the metal interface, with presence of new ordered phase that suggests both a high chemical affinity between Cu an C_{60} as well as a marked tendency of the latter to move on the metal surface, also inducing surface modifications. Having in mind our final aim to induce the C_{60} cage rupture, the results for 1 ML growth do not clearly show if this process can be enhanced or not in the physical/chemical condition occurring in a SuMBD experiment. What is comprehensible is that such an event can be achieved only at fullerene coverages lower than 1ML, where the C_{60}/Cu(111) collision has its maximum probability to occur, probability obviously decreasing at higher coverages where, moreover, different scattering and diffusion processes could be present. In this case, it is more appropriate to use terms like partial covering and not thickness, as we are dealing with a single layer being partially completed, but it is a common and accepted way to define also submonolayers using the equivalent thickness value.

We analyzed films of 0.3 and 0.6 ML of C_{60} grown on polycrystalline Cu by SuMBD at 15eV and on Cu(111) by SuMBD at 35eV at room temperature. In Figure 5.20 are shown the C1s core levels from the four films. The lineshapes have been deconvolved using the same model applied for the 1ML C_{60} in terms of BE position, FWHM and peak asymmetry of the main component (see Table 5.3).

	0.3ML, KE=15eV Poly Cu			**0.3ML, KE=35eV Cu(111)**			**0.6ML, KE=15eV Poly Cu**			**0.6ML, KE=35eV Cu(111)**		
	BE [eV]	**FWHM [eV]**	**%**	**BE [eV]**	**FWHM [eV]**	**% on C1s area**	**BE [eV]**	**FWHM [eV]**	**%**	**BE [eV]**	**FWHM [eV]**	**%**
C-C	284.15	0.92	73.8	284.11	0.92	84.1	284.15	0.93	80.1	284.11	0.92	85.1
P1	283.44	1.00	5.3	283.44	1.00	4.5	283.44	1.00	3.7	283.44	1.00	3.9
Loss	286.41	1.30	7.3	286.42	1.30	5.1	286.41	1.30	4.9	286.41	1.30	4.6
Loss	287.98	1.50	8.6	287.94	1.50	3.4	287.98	1.50	8.4	287.97	1.50	3.4
Loss	289.93	1.50	4.8	289.89	1.50	2.9	289.93	1.50	2.9	289.92	1.50	3.0

Table 5.3: Principal features of C_{60} sub-monolayers deposited on Cu poly by supersonic beams at 15eV and Cu(111) at 35eV.

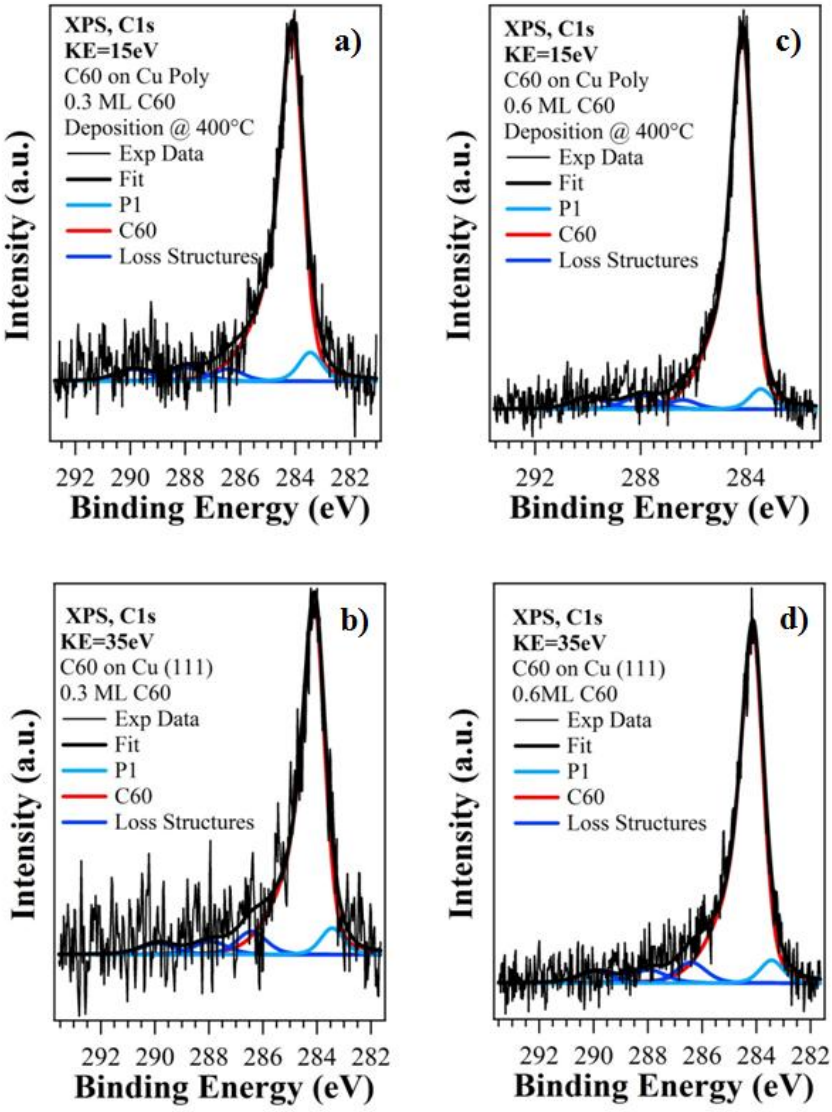

Figure 5.20: C1s core levels of C_{60} sub-monolayers deposited at substrate room temperature on poly Cu by supersonic beams at 15eV (a,c) and Cu(111) at 35eV (b,d).

As can be seen, the C1s peak fitting is achieved using the same components in terms of BEs and FWHM for all films, being the same also for the corresponding 1 ML film, suggesting that the great part of the cages show the same kind of interaction up to the completion of the monolayer. It is noteworthy the loss structures intensity that is higher than in the 1ML case, in particular for the growth at low KE (see Table 5.3).

Probably it is not related to the different substrate surfaces, as the corresponding monolayers did not show any difference. Moreover, the intensity of loss structures decreases with the thickness of the film (see the difference between 0.3 and 0.6 ML) up to

1ML which loss structures intensity are comparable to those of the thick film. The P1 peak is still present and its intensity is almost constant with the coverage, suggesting and confirming that it may be correlated to a carbon chemical species present at the interface which continues to be formed until the complete growth of the first monolayer.

The valence bands of the C_{60} 0.3 and 0.6 ML sub-monolayers on the two surfaces are shown in Figure 5.21. The main differences are related to the two underlying contribution from polycrystalline and single crystal copper, especially features in the region between 2-4eV. Cu(111) surface states are still visible for the 0.3 ML film, disappearing for the 0.6 ML thickness.

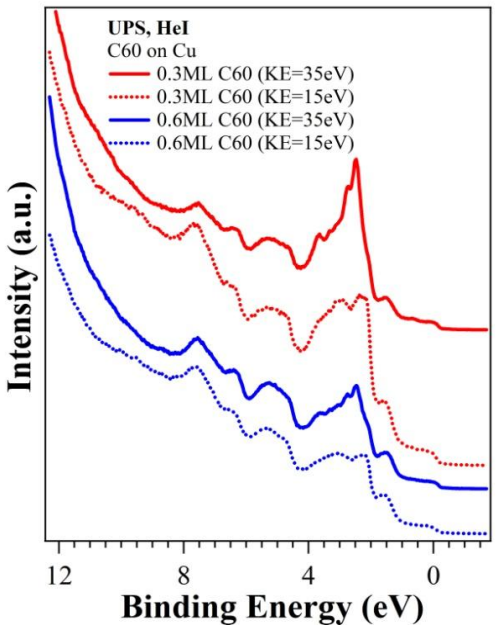

Figure 5.21: UPS valence bands of C_{60} sub-monolayers deposited on poly Cu by supersonic beams at 15eV (dashed line) and Cu(111) at 35eV (solid line).

The typical fullerene bands are visible in all the spectra, similarly to the C_{60} 1ML, showing the same 0.5eV shift in BE with an intensity increasing with the coverage, as expected. WFs have same values for the 0.3 and 0.6 ML films, 4.70eV for the poly Cu and 4.88eV for the Cu(111), being slightly lower than for the 1 ML case (4.98 and 5.01eV) but still larger than the clean metal surfaces.

In order to further prevent the influence of the thickness of the organic film in hindering the cage rupture in the first organic/metal collision, we have studied a very thin film of C_{60},

about 0.1 ML, grown by means of fullerene supersonic beam at 35eV on a Cu(111) surface. The idea is to work in the best condition for the C_{60}/Cu surface collision, i.e. higher KE and lower probability to interact with other deposited molecules, further avoiding any possible diffusion and reordering processes, as shown also in other similar experiments of C_{60} on Ru(111) [189]. The C1s core level and valence band of this film are displayed in Figure 5.22.

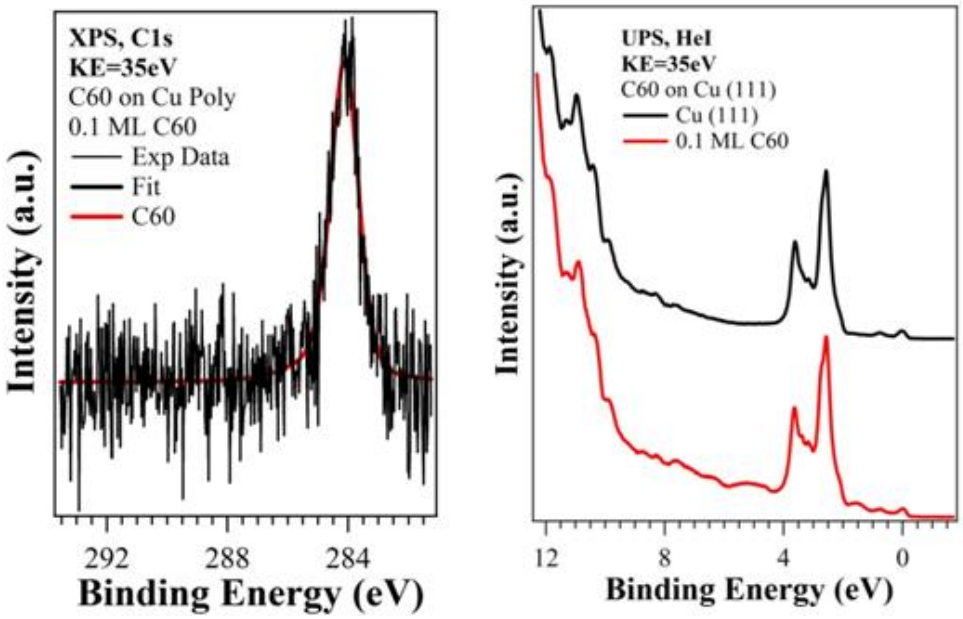

Figure 5.22: XPS (on the left) and UPS (on the right) of a 0.1ML C_{60} film on Cu(111) deposited at RT by supersonic beam at 35eV.

Regarding the XPS analysis, even though the signal to noise ratio is very low, the lineshape can be deconvolved by a single component at 284.12eV characterized by a different asymmetry with respect to the C_{60} 1ML, HOPG and graphene. The peak is larger compared to the other examples above (FWHM 1.10eV instead of about 0.9eV), indicating the presence of other possible components that cannot be introduced due to the low S/N ratio. The valence bands show the typical features of fullerene, even if very weak, with a predominant signal coming from the Cu3d, also for what concern the presence of surface states. We can conclude that the analysis does not highlight the presence of nanostructured materials or other chemical species different by fullerene.

5.5.5 Heat treatments of C_{60} films on Cu

The fullerene depositions at room temperature on copper, regardless of the beam KE, do not show evidence of the cage opening. The main physical/chemical processes at the interface seems to be once more the strong C_{60}/Cu interaction and the KE provided by SuMBD seems to further enable the rearrangement of the molecules on the substrate, increasing the fullerene mobility. Probably the KE excess is also transferred to the surface due to the high overlapping of molecular orbitals and copper 3d states and bands, instead of remaining located in the molecule during organic/inorganic collision, avoiding the foreseen rupture of the cage due to the presence of different de-excitation channels.

Fullerene fragmentation induced by thermal treatment has been reported. On Pt(111), formation of a disordered graphitic carbon layer has been achieved at 1150 K, while on Ni(100) cage rupture occurs at 760 K and followed by total desorption at 850 K [181]. C_{60} deposited on Mo(110) has shown great chemical interaction during thermal treatments, with full fragmentation at 585 K driven by the formation of chemical bonds [209], as already observed for the fullerene on silicon case. On the Cu(001) surface, decomposition and thermal desorption has been observed around 880-960 K, depending on the fullerene organization on the surface [185].

Thus, we investigated the influence of temperature in promoting the fullerene breaking in order to define a threshold value. A series of heat treatments have been carried out with two different approaches: keeping the substrate at high temperature during the deposition or treating the film after the deposition at room temperature.

5.5.5.1 0.3 and 0.6 ML deposited on Cu poly kept at 400°C (KE=15eV)

Two films of 0.3 and 0.6 ML have been deposited on a polycrystalline Cu kept at 400°C by C_{60} supersonic beams at 15eV. This temperature is sufficient to induce desorption of the physisorbed species but not affecting the fullerene bonded at the organic/inorganic interface.

Interestingly, by using the same deposition times used for the preparation of 0.3 and 0.6 ML films with substrates held at room temperature, the same final film thicknesses have

been achieved. This result suggests that the fullerene-copper interaction before the formation of the first monolayer is so strong that the sticking coefficient is not altered, not regarding if the substrate is kept at room temperature or at high temperature.

The C1s core level lineshapes for 0.3 and 0.6 ML deposited on the substrate at 400°C (Figure 5.23 and Table 5.4) are coherent with those observed for the deposition at room temperature (see Figure 5.22 and Table 5.3). The P1 peak is also present and its intensity slightly decrease with the coverage, whereas the loss structures are somewhat less intense.

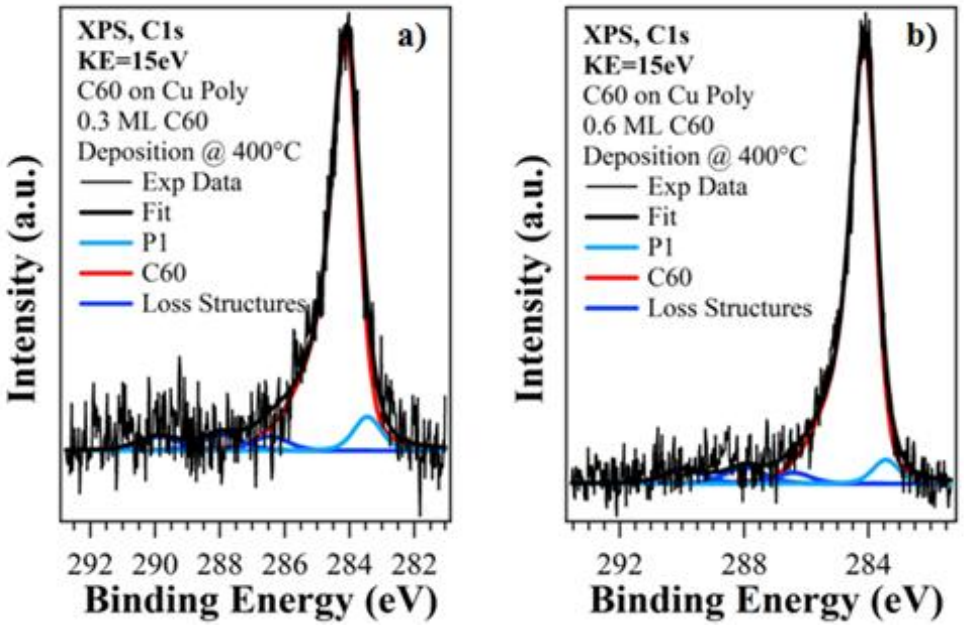

Figure 5.23: C1s core levels of 0.3 and 0.6 ML C_{60} films grown on polycrystalline Cu at 400°C by supersonic beams at 15eV.

	Poly Cu @ 400°C, KE=15eV					
	0.3ML			0.6ML		
	BE [eV]	FWHM [eV]	% on C1s area	BE [eV]	FWHM [eV]	% on C1s area
C-C.	284.11	0.95	86.0	284.14	0.92	87.9
P1	283.45	1.00	4.8	283.44	1.00	3.4
Loss	286.45	1.30	2.7	286.41	1.30	2.1
Loss	287.94	1.50	3.5	287.97	1.50	3.5
Loss	289.89	1.50	3.0	289.92	1.50	3.0

Table 5.4: C1s features of C_{60} sub-monolayers C1s core levels deposited on polycrystalline Cu at 400°C by SuMBD at 15eV.

The valence bands have been also analyzed, showing once more the overlapping of the Cu and fullerene contributions and the same characteristics (and WF), as observed for the deposition at room temperature (Figure 5.24). We can conclude that the deposition of C_{60} at 15eV KE on a hot polycrystalline Cu surface lead to the formation of film (in the submonolayer regime) that have the same chemical/physical characteristics of those deposited with substrate at room temperature, again suggesting the leading role of the C_{60}/Cu interaction in determining the film synthesis.

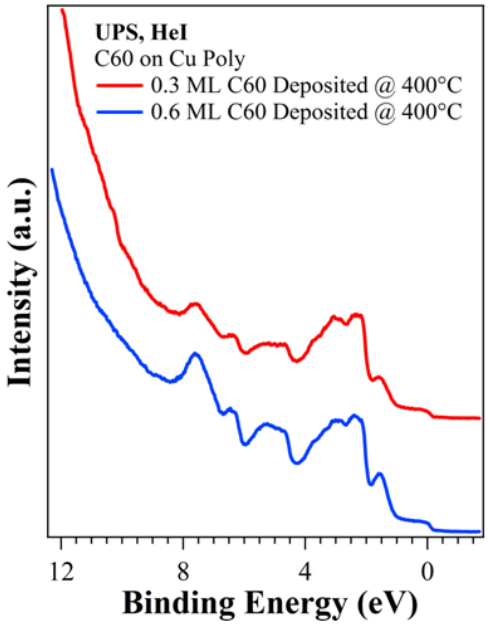

Figure 5.24: Valence band of 0.3 and 0.6 ML C_{60} films grown on polycrystalline Cu at 400°C by supersonic beams at 15eV.

5.5.5.2 C_{60} thick film on Cu poly annealed at 560°C (KE=15eV)

A thick film of fullerene deposited on polycrystalline Cu at room temperature by supersonic beam at 15eV has been annealed at 560°C. Differently from the previous experiments and also from the thermal treatment of a thick C_{60} at 460°C, the amount of carbon that is still present on the metal surface corresponds to a film of about 0.3ML, and not 1ML as can be evaluated from the C1s intensity (see Figure 5.25-a). It is more evident by analysing the valence band spectrum (Figure 5.25-b), characterized by the absence of the typical fullerene features, such as the HOMO band.

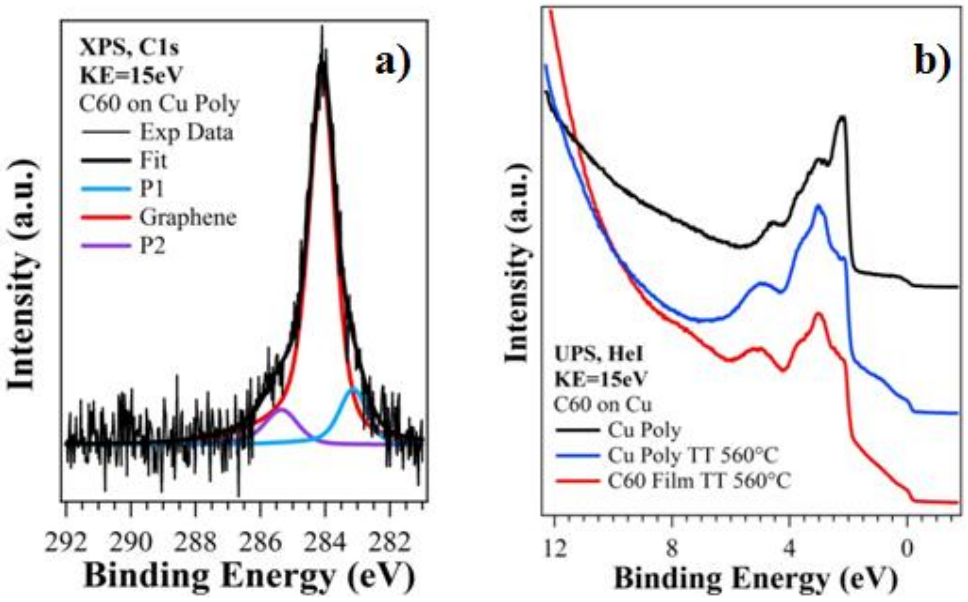

Figure 5.25: Core level (a) and valence band (b) of a film obtained treating a C_{60} thick film grown at RT on polycrystalline Cu at 550°C by supersonic beam at 15eV.

It is worth noting that, the high temperatures have brought sulphur to the surface (as shown by AES analysis, not presented here), thus affecting the original Cu3d levels shape. Moreover, a broad band is present in the range between 6-8eV, certainly associated to the carbon-based film on the surface. In fact, comparing the valence band of the Cu treated at 560°C (as reported in Figure 5.25-b), it is clear that structures in the 4-6eV range are due to sulphur while no features are present in the 6-8eV range. In addition, the C1s core level (Figure 5.25-a) has characteristics which differ from those typical of fullerene film of 1 ML and sub-monolayers, as summarized in Table 5.5.

The main peak asymmetry and FWHM are not those of thick, 1ML or sub-ML C_{60} layer, but are comparable to that of graphene, suggesting the presence of fullerene fragments after the cage opening and formation of nanoislands of this carbon-based material. The loss structures completely disappeared, again suggesting the absence of fullerene but presence of a new different carbon species. The P1 component is still present even if at BE about 0.2 eV with respect to the single layer. Considering the proposed origin of this peak, related to the more strongly interacting part of the fullerene cage with copper surface, if C_{60} fragmentation occurred we can suppose a mechanisms similar to that identified for the rupture of C_{60} on Ru(111) [189,213].

	C_{60}, bulk on Poly Cu			1ML, Poly Cu, 445°C bulk			0.3ML after TT@560°C			
	BE [eV]	**FWHM [eV]**	**% on C1s area**	**BE [eV]**	**FWHM [eV]**	**% on C1s area**		**BE [eV]**	**FWHM [eV]**	**% on C1s area**
C-C	284.60	0.80	86.6	284.12	0.90	86.9	**C-C**	284.09	0.98	79.9
P1	286.50	1.00	2.0	283.44	1.00	4.5	**P1**	283.23	1.00	11.5
Loss	288.60	1.30	4.6	286.41	1.30	2.1	**P2**	285.35	1.20	8.6
Loss	290.60	1.50	6.8	287.95	1.50	3.5				
Loss	284.60	0.80	86.6	289.90	1.50	3.0				

Table 5.5: C1s features of a film obtained treating a C_{60} thick film grown at RT on polycrystalline Cu at 560°C by supersonic beam at 15eV. The parameters of bulk C_{60} and single layer are reported as reference.

As shown in Figure 5.26, the rupture region when the molecule is in deep contact with the metal surface is located on those carbon atoms lying just outside the metal deformed site. This is because while carbon atoms in the cup show short bonds with metal atoms, those in the cage bonded to them experience an elongation of original bonds, with formation of a weaker zone in the cage where rupture can start.

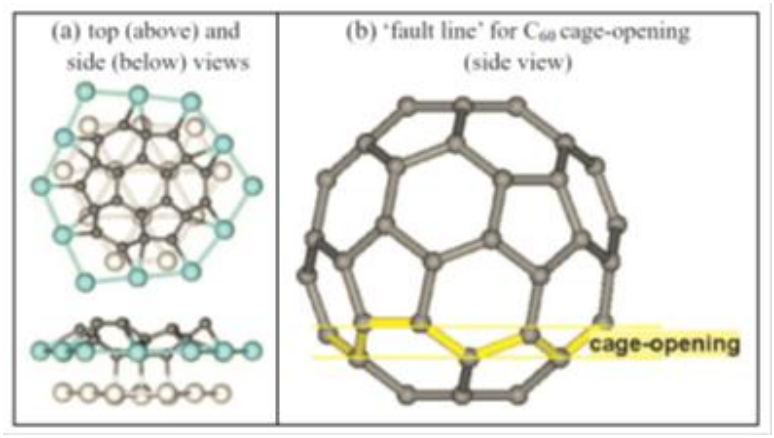

Figure 5.26: Assumed local adsorption geometry of Ru(0001)-(4 × 4)-C_{60} with a 7-atom hole; and (b) the "fault line" (yellow/light gray lines and bonds) for cage-opening of C_{60} on Ru(0001) (the Ru surface at bottom is not shown) [213].

So, due to the strong chemical interaction in the deep of the cup, it can be assumed that the cage will open on the surface, creating a graphene-like nanoisland with most of the original cage atoms, while the cage portion in the cup remains there, but being more electronically isolated than before. Thus, the observed energy shift can be associated to the stronger

interaction of the fullerene fragments with the copper surface compared to the intact molecule. A new component located at 285.35eV is present, labelled P2, that cannot be related to any kind of fullerene loss structure but rather to defects, similarly to the P3 peak in the graphene core level, due for example to the presence of pentagonal structures and to the incompleteness of the layer [190,214]. For sure, we can exclude that P2 is related to C-S bonds, since this contribution is expected at about 287eV [55].

The formation of graphene-like materials has been also demonstrated by *ex-situ* Raman spectroscopy as shown in Figure 5.27-a, where a reference spectrum of good quality graphene on quartz is also shown.

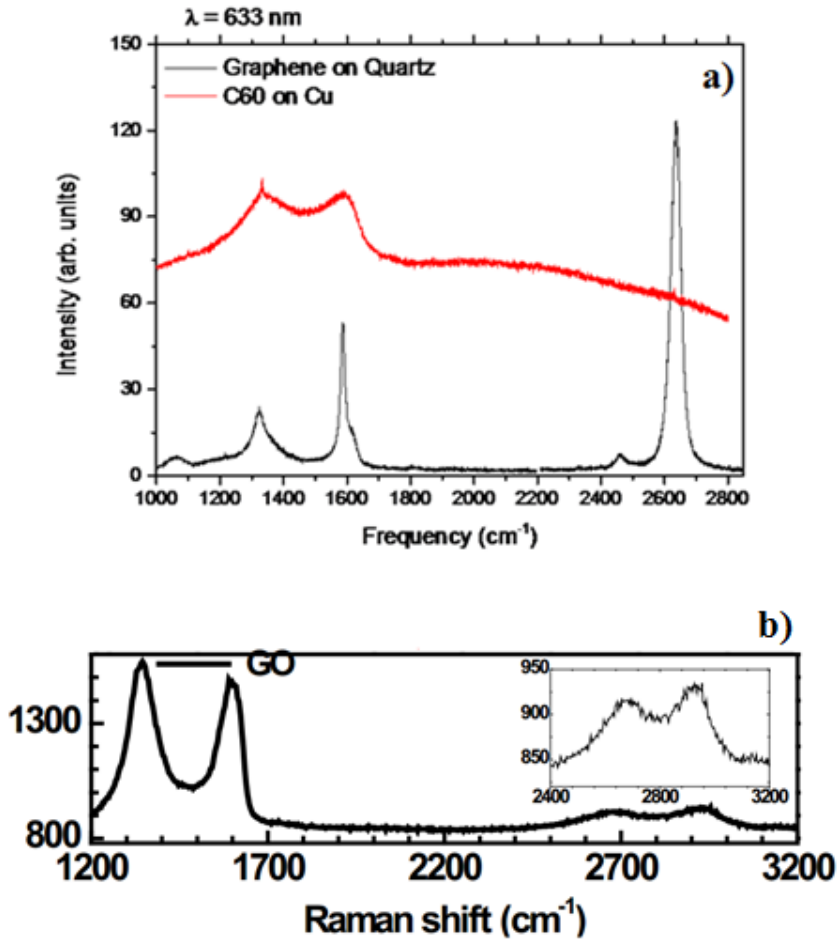

Figure 5.27: (a) *EX-situ* Raman spectrum of film obtained treating a C_{60} thick film grown by supersonic beam at 15eV at RT on polycrystalline Cu at 560°C. (b) Raman spectrum of graphene oxide (red line) [217].

The analysis put in evidence the presence of two bands at about 1600 (the G band) and 1300 (the D band) cm^{-1} whereas the main peak at 2700 cm^{-1} is absent (2D band). The latter is the second order of the D-band and it is the result of a two phonons lattice vibrational process. This contribution is very strong in graphene and it is present even when the D-band is absent. The G band is associated to an in-plane vibrational mode which involve sp^2 hybridized carbon atoms that form the graphene sheet. Its position is related to the number of layers present in the sample, giving accurate indications about the film thickness. The D band, instead, represents a mode from sp^3 bonded carbon and it is associated to defects in the material. Our film corresponds to the typical spectrum of a graphene oxide, as widely reported in literature [215,216] and shown in Figure 5.27-b [217]. This result is quite surprising, since by in-situ analysis no presence of oxygen has been found, but indeed repeating XPS analysis after the Raman studies, we found an highly oxidized surface, with both C-O and Cu-O species. While the latter was expected, the former was not if we are dealing with graphene nanoislands, as oxidation of graphene does not occur at room temperature so easily [218]. However, the possible graphene nanoislands are for sure small and with several defects, making their reactivity versus oxygen probably higher than usual.

Considering the promising results obtained treating at 560°C a fullerene bulk phase grown by SuMBD at 15eV, a deposition of about 0.8 ML on polycrystalline Cu (a thin sheet 25 μm thick) by supersonic beam at 35eV keeping the substrate at 565°C has been studied. In order to avoid presence of sulphur, specific thermal treatments have been performed achieving the desired result.

Surprisingly, the C1s core level and UPS valence band show the typical features of the fullerene single layer or submonolayer (see Table 5.6), as displayed in Figure 5.28, with no evidence of cage opening despite the greater amount of KE supplied. Also the carbon signal intensity is higher and confirmed by both XPS and UPS analysis. This result once more suggests that the process more energetically probable during the film growth is the molecular mobility and diffusion on the metal surface, that seems to be further enhanced by the higher precursor KE.

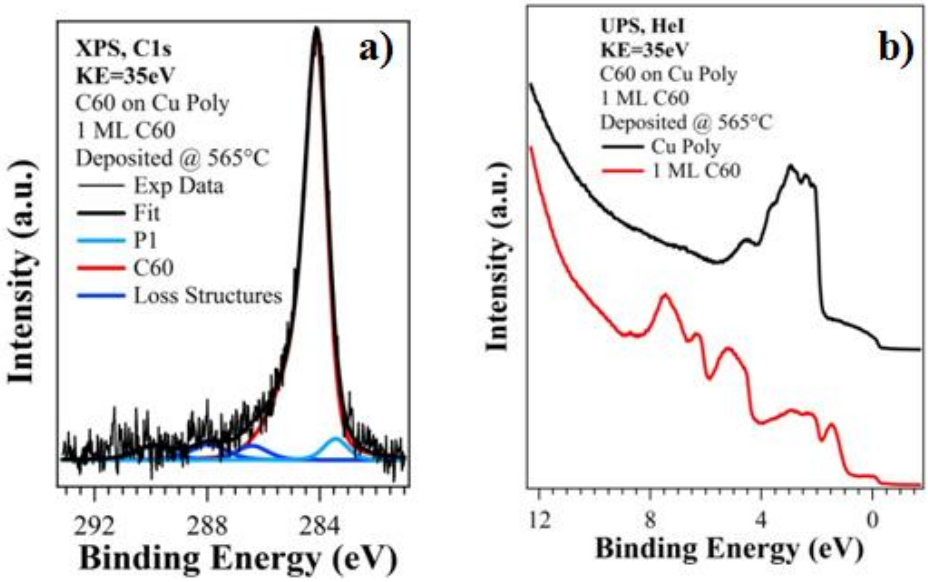

Figure 5.28: XPS (left) and UPS (right) analysis of a 0.8ML C_{60} film grown on polycrystalline Cu by supersonic beam at 35eV and then annealed at 565°C.

	C_{60}, O.8 ML on Poly Cu (KE=35eV), 565°C			1ML, Poly Cu, 445°C bulk		
	BE [eV]	**FWHM [eV]**	**% on C1s area**	**BE [eV]**	**FWHM [eV]**	**% on C1s area**
C-C	284.12	0.90	87.5	284.12	0.90	86.9
P1	283.44	1.00	3.2	283.44	1.00	4.5
Loss	286.41	1.30	2.8	286.41	1.30	2.1
Loss	287.95	1.50	3.5	287.95	1.50	3.5
Loss	289.90	1.50	3.0	289.90	1.50	3.0

Table 5.6: C1s features from a film obtained treating at 560°C a C_{60} thick film, grown at RT on polycrystalline Cu by supersonic beam at 15eV. The parameters of C_{60} single layer are reported as reference.

Another possible explanation could be found in the fullerene interaction with the sulfur present in the surface [219], not present in the second experiment at higher C_{60} KE, giving rise to defects which could catalyze and induce the breaking of molecules. Nevertheless, cage rupture has been achieved by thermal treatments but seems to be still not induced nor related to the quality of the first C_{60}/Cu surface collision, that indeed seems to improve molecular diffusion.

5.5.5.3 Treatments of 1ML C_{60} on Cu(111) at increasing temperatures

In order to shed light on the hypothesis previously suggested and to determine the threshold temperature for the cage opening, 1ML of C_{60} deposited on Cu(111) at room temperature by SuMBD at 35eV has been treated at increasing temperatures (107°C, 165°C, 255°C, 326°C, 380°C, 425°C, 498°C, 547°C, 598°C, 645°C, 695°C, 745°C, 795°C). The single crystal has been previously treated in order to avoid the presence of any sulfur contamination up to 800°C. The AES analysis has demonstrated that the C (KVV) intensity signal, compared to that of the Cu at about 60eV, does not show significant changes at all temperatures investigated, suggesting that no loss of material occurred. However, at temperature >600°C, chemical-physical processes have taken place strongly affecting the material characteristics. In Figure 5.29 is shown the valence band relative to the annealing at temperatures lower and higher than 645°C.

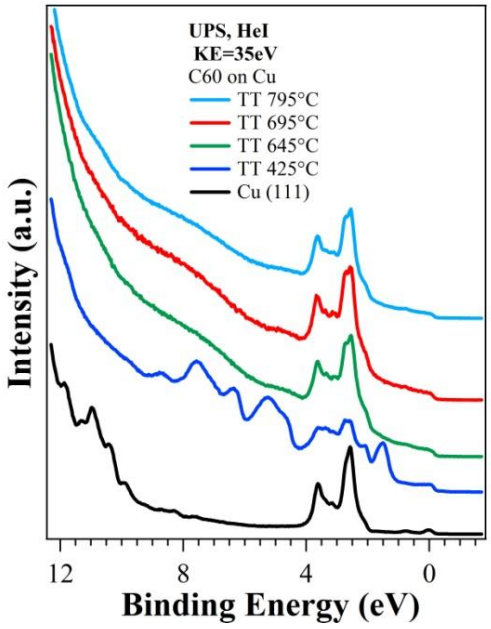

Figure 5.29: Valence bands of 1ML C_{60} grown on Cu(111) at room temperature by SuMBD at 35eV and treated at increasing temperatures (425°C, 645°C, 695°C and 795°C).

The typical fullerene features are completely disappeared, as just previously observed for the C_{60} film annealed at 560°C (beam KE=15eV). The valence band shape remains

unchanged after the subsequent heat treatments, up to the maximum temperature of 795°C. WF decreases from the 1 ML value of 5.01eV at 495°C to 4.84eV at 645°C, remaining almost unchanged at higher temperatures.

At the same time, the C1s core level (Figure 5.30) lineshape is that typical of a 1ML fullerene up to 600°C, whereas at 645°C an important variation occurs in particular regarding the main peak asymmetry and width. These parameters in fact become comparable with those observed in the previous experiment at 550°C, suggesting the cage opening and the formation of graphene-like material.

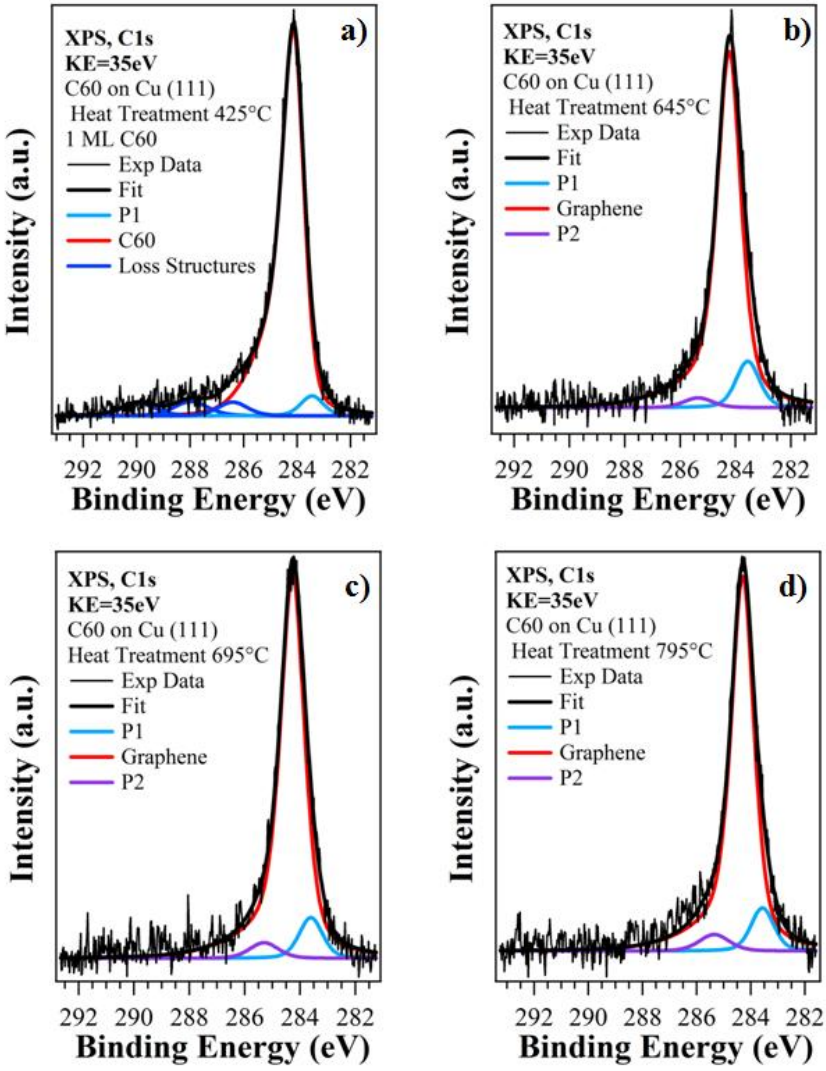

Figure 5.30: XPS core levels of 1ML C_{60} grown on Cu(111) at room temperature by SuMBD at 35eV and treated at increasing temperatures (425°C, 645°C, 695°C and 795°C).

In Table 5.7 are reported the details of the lineshape core level analysis.

	TT @ 425°C				TT @ 645°C			TT @ 695°C			TT @ 795°C		
	BE [eV]	**FWHM [eV]**	**% on C1s area**		**BE [eV]**	**FWHM [eV]**	**% on C1s area**	**BE [eV]**	**FWHM [eV]**	**% on C1s area**	**BE [eV]**	**FWHM [eV]**	**% on C1s area**
C-C	284.14	0.92	87.6	**C-C**	284.23	1.03	88.8	284.27	1.03	89.3	284.30	1.00	88.1
P1	283.44	1.00	3.1	**P1**	283.56	1.00	8.9	283.61	1.00	7.3	283.57	1.00	7.9
Loss	286.41	1.30	2.8	**P2**	285.35	1.22	2.3	285.30	1.22	3.4	285.35	1.30	4.0
Loss	287.97	1.50	1.6										
Loss	289.92	1.50	2.9										

Table 5.7: Principal features of 1ML C_{60} grown on Cu(111) at room temperature by SuMBD at 35eV and treated at increasing temperatures (425°C, 645°C, 695°C and 795°C).

Interestingly, the P1 and P2 peaks are present even if their intensity is higher with respect to the experiment described in the previous paragraph 5.5.5.2. In particular, P2 intensity enhances at increasing temperatures, so taking into account the peak origin, the amount of graphene defects grows with the thermal treatments. Furthermore, these components do not show energy variation with respect to the main peak as the treatment temperature increases. Another indication about the nature of the films obtained at high temperature is also supplied by the analysis of the XPS C1s loss structures for different carbon forms as illustrated in Figure 5.31.

The fullerene, both as thick film and single layer, and HOPG are characterized by intense and well defined structures, as described in paragraph 5.5.2.2. Graphene, on the contrary, does not show these components and the same is found on the films in which there is the evidence of cage opening, obtained at 550°C and 645°C by SuMBD at 15eV and 35eV, respectively.

The experimental results suggest, moreover, that the surface order and/or the presence of contaminants as sulphur play an important role in the activation of the chemical-physical processes at the organic/metal interface. Indeed, a higher temperature is necessary to induce the fullerene cage breaking on a crystalline metal surface and free from contaminations.

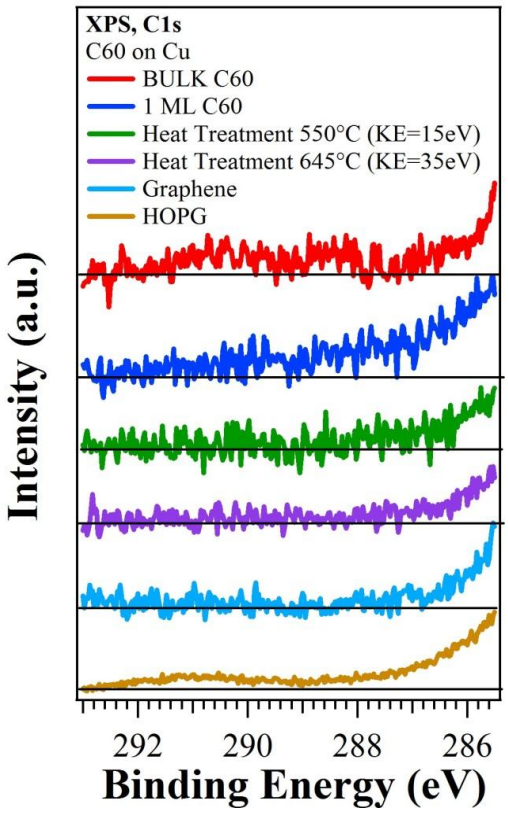

Figure 5.31: Loss structures region of HOPG, C_{60} single layer, C_{60} thick film, C_{60} films obtained at 550°C by supersonic beam at 15eV and at 645°C by supersonic beams at 35eV.

The film treated at 645°C has been also characterized *ex-situ* by Raman spectroscopy (Figure 5.32), providing a further confirmation of the graphene synthesis. Indeed, the 2D band at about 2700 cm^{-1} is present and the ratio between the 2D and G band is higher than 2, evidencing the presence of single layered graphene, while the intense G band suggests also this graphene is highly defected. As reference is reported a standard graphene on Cu(111) (red line). No evidence of any kind of carbon film oxidation has been found after exposure to atmosphere. The Raman spectrum of C_{60} is shown in Figure 5.33 for comparison, definitely proving the C_{60} rupture.

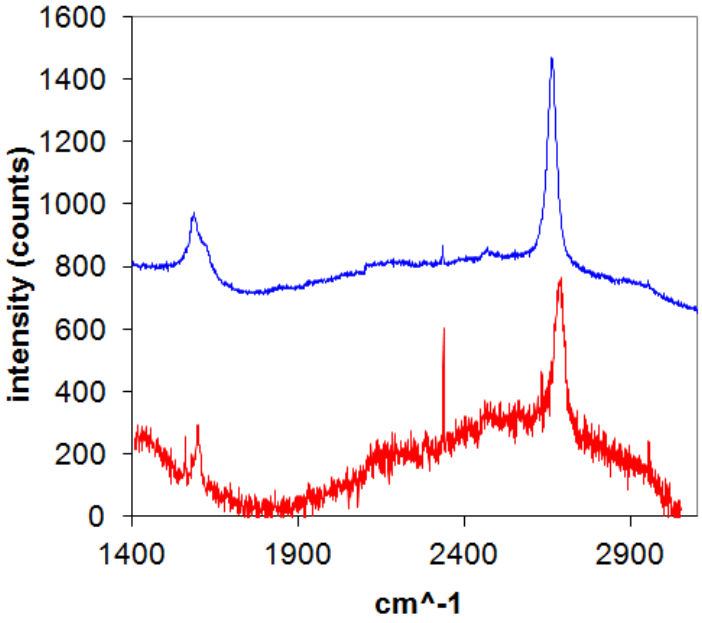

Figure 5.32: Raman spectra of 1ML C_{60} grown on Cu(111) at room temperature by SuMBD at 35eV and treated at 645°C (blue line) and of a standard graphene on Cu(111) (red line). The sharp peak at about 2300 cm^{-1} is an artifact due to the experimental apparatus.

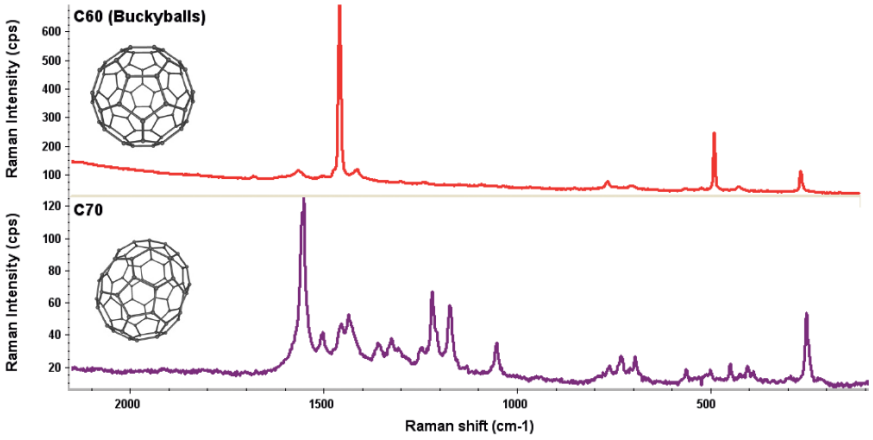

Figure 5.33: Raman spectra of two fullerenes C_{60} and C_{70} [220].

5.6 Summary

The aim of this work was to synthesize carbon-based nanostructured materials by supersonic beams of fullerene at low (15eV) and high KE (35eV) on polycrystalline and single crystal copper surfaces, in order to define the threshold for the fullerene cage opening and/or breaking. Cu(111) is typically used in the graphene synthesis having a low carbon solubility and not giving rise to carbide formation. The choice of polycrystalline Cu is instead innovative and the better comprehension of the processes at the interface with C_{60} could pave the way for the graphene synthesis on a with lower costs than for a single crystal and on a flexible substrate. The first step of this work has been the evaluation of the reference standards (graphene, HOPG and C_{60} thick film) in order to define their electronic properties by XPS and UPS analysis. These characterizations have been used to evaluate the nature of the films growth at different conditions and define the role played by the different parameters (such as C_{60} beam KE, substrate temperature and heat treatment after deposition).

We have obtained totally equivalent 1ML C_{60} by three different approaches: i) removal of the physisorbed molecules by heat treatment at 445°C, ii) film deposition at room temperature on Cu(111) by supersonic beam at 35eV and iii) film deposition at room temperature on polycrystalline Cu by supersonic beam at 15eV. As described by G. Xu [211], this interaction leads to (4x4) reorganization of the organic and to a copper surface reconstruction so that the cage is sited in a sort of hole, cup, with formation of few Cu-C strong chemical bonds and charge transfer. We have achieved the (4x4) rearrangement for 1ML C_{60} annealed at 430°C, a process that could be probably favored by the precursor KE in the supersonic beam. In fact, for all analyzed C_{60} 1 ML films, the XPS analysis has put in evidence the presence of a C1s component at low BE that can be associated to the proposed strong interaction between fullerene and Cu following to the substrate deformation. Interestingly, C_{60} sub-monolayers films have shown the same characteristics of the single layer, whatever are the KE of the C_{60} supersonic beam and substrate temperature, suggesting that the strong interaction between organic and inorganic plays the leading role in the film growth process. As a matter of fact, the experimental evidences suggest that the C_{60} exploits the excess of energy supplied by the supersonic beam to rearrange itself on the metal surface in a conformation energetically favorable, rather than break. Our intention will be to further push towards this direction studying study the

activation of the C_{60} (4x4) reconstruction process even at room temperature exploiting the kinetic activation by SuMBD.

There are not evidences of cage opening neither at room temperature nor keeping the substrate at higher temperature (up to 560°C) during the deposition even at high supersonic beam KE. The reason for this is probably that in the C_{60}/Cu surface collisions, several de-excitation channels are present due to the favorable overlapping of organic molecular orbitals and metal 3d surface states. This indeed leads to a strong chemical interaction at the organic/inorganic interface but not high enough to induce the cage breaking (as occurs for silicon), but rather diffusion processes to let fullerene find the lowest energy surface sites.

The thermal treatments have provided instead significant information, defining two thermal thresholds for cage opening at 560°C and 645°C for a C_{60} film on polycrystalline Cu and Cu(111) deposited by C_{60} at 15 and 35eV, respectively. The differences in the activation temperature could be associated to defects present on the surface, such as the presence of contaminants (sulfur) for Cu poly, which could act as catalysts for the cage opening. In this framework, the role of SuMBD lies on the possibility to let the C_{60} molecules go towards the lattice sites that could favor cage opening at lower temperatures, even lower than that experienced in this work during the thermal treatments. In fact, it seems that the C_{60} location on the Cu reconstructed surface sites is a prerequisite for cage breaking and a kinetic activation of these processes would act in a similar way with respect to the presence of sulfur, helping the molecules to reach the most favorable surface state and break other than reorganize on the surface towards the (4x4) scheme.

Both the materials obtained after the annealing at 560°C and 645°C are graphene-like, as demonstrated by XPS and Raman characterizations, even if defected. However, while the film synthesized at 645°C has shown characteristics of a graphene single layer with presence of defects, that achieved at 560°C has shown features of oxidized graphene indeed experiencing a strong oxidation once exposed to air. Influence of substrate is not fully clear, as we achieved graphene formation on both polycrystalline and single crystal copper. Nevertheless, these results are very promising considering that the standard technique, CVD, still requires temperatures up to 1000°C to synthesize graphene from hydrocarbons.

Our perspective is to further define the KE role in the fullerene cage opening, studying the effect of heat treatments at increasing temperatures of a 1ML C_{60} by supersonic beam at 15eV, other than the carried out experiment at 35eV. Given the impossibility to break the fullerene cage during the C_{60}/Cu surface collision, we think different scenario could be possible, also being counterintuitive such as use lower precursor KE and less ordered substrate in order to tune the organic KE de-excitation channels towards copper surface. The aim will be to control, keeping in mind the promising theoretical calculations for the kinetic thresholds for cage opening around 35-40eV, the balance between the thermal effects, that help to form graphene-like structures only in certain experimental conditions, and the kinetic activation of different processes, like the organic diffusion and reorganization preliminary and necessary for cage opening.

Chapter 6
Functionalization processes at organic/inorganic interfaces

6.1 Introduction

The activation of chemical bonds at organic/inorganic interfaces by exploiting the unique properties of SuMBD approach has been successfully used to achieve functionalization of specific inorganic surfaces. This process is particularly interesting towards the realization of materials showing multifunctional properties, suitable for sensing devices or to achieve an inorganic biocompatibility through the functionalization with specific organic molecules. This Chapter is devoted to the study of the functionalization of SiC/SiO_2 core-shell nanowires with partially fluorinated phenylporphyrin by SuMBD. This system is a viable nanohybrid photosensitizer suitable for photodynamic therapy (PDT) induced by X-ray irradiation [221]. These functionalized inorganics have attracted great attention for producing locally singlet oxygen as well as for the possibility to be injected in the bloodstream thanks to the nanometric dimensions, similarly to other chemical species used for PDT. Here we will focus on the physical/chemical properties of the molecular thin films and of interfaces to qualify the growth mechanisms and identify the chemical species involved in the organic/inorganic interactions. To this end, the surface functionalization has been studied using SiC/SiO_2 core-shell nanowires but also a flat surface showing similar chemical/physical properties but simplest from an experimental point of view. Thus, a $Si(100)/SiO_2$ planar surface functionalized by partially fluorinated phenylporphyrin has been chosen as possible model for the nanowires case and analyzed in detail. The two

systems will be separately discussed beginning from the basic properties of a thick film, followed by the analysis of the growth mechanism to end up with kinetically activated reactivity and surface processes.

6.2 Porphyrins

Porphyrins are an ubiquitous class of molecules involved in a wide variety of biological processes in nature: oxygen transport and storage (hemoglobin and myoglobin), electron and energy transfer (cytochromes and chlorophylls), biocatalysis (vitamin B12, cytochrome P450).

These molecules are basically conjugated macrocycle composed by four pyrrole subunits linked together by four methylene bridges (=CH-, *meso* carbons), in the α positions with respect to the N atoms (Figure 6.1-a).

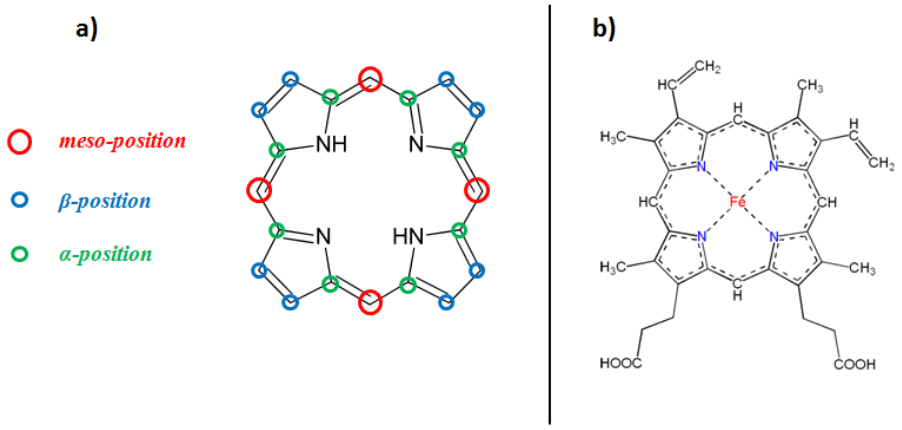

Figure 6.1: Scheme of the free-base porphyrin (a) and of the Haemoglobin molecule (b).

This tetrapyrrole ring structure is called porphin and its derivatives are named porphyrins. The macrocycle is an aromatic system with 22 π electrons, but only 18 of them are delocalized and involved in conjugated bonds. In the "free-base configuration", porphyrins do not show any central atoms, so that the four N atoms of the pyrrole macrocycle are not equivalent: two of them are bonded to H atoms (pyrrolic nitrogens) and the other two have a lone electron pair (aza nitrogens). The size of the pyrrole macrocycle allows insertion of

a metal ion in its center, forming metalloporphyrins, as in the case of the Haemoglobin molecule (Figure 6.1-b).

The π-electrons on porphyrin ring are responsible of the characteristic optical absorption spectra, which are perturbed by variations on the basic structure. In a similar way to other aromatic molecules such as benzene, porphyrins UV-Vis spectra consist of two absorptions in two different regions: in the near-ultraviolet and in the visible regions. The most intense band, called B- or Soret band, is placed at 390-450 nm and it is related to optical transitions localized on the nitrogen atoms of the central macrocycle. The bands at low energy (480-700 nm) are the Q-bands, involving the transitions from delocalized orbitals in the molecule.

Free-base porphyrins display four Q-bands (IV, III, II and I, Figure 6.2-a) , whose intensity depend on the substituents in *β*-pyrrol and *meso*-carbons positions. After macrocycle metallation, the spectra show only two Q-bands, denoted as α- (at low energy) and β- (Figure 6.2-b) [222].

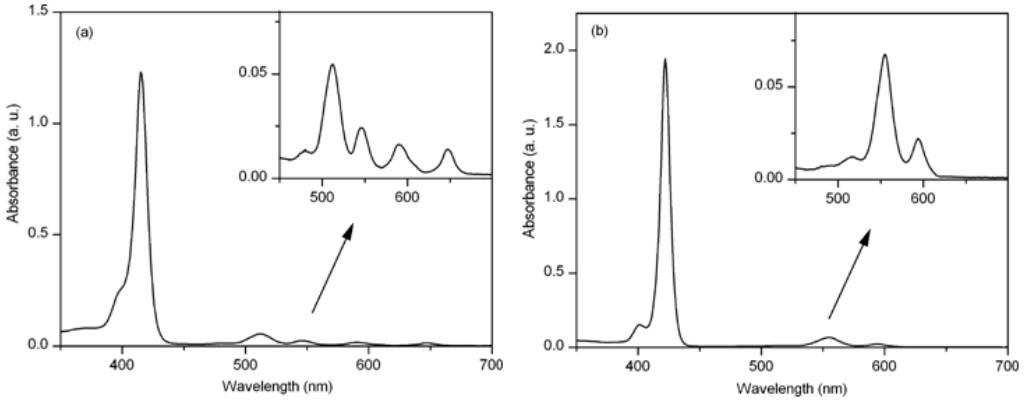

Figure 6.2: UV-vis spectra for (a) free-base porphyrin and (b) its metalloderivative [222].

Here we focus on the tetrakis(pentafluorophenyl)porphyrin ($C_{44}H_{10}F_{20}N_4$), a free-based molecule in the following denoted as $H_2TPP(F)$ and with a molecular weight of 974.57 amu (Figure 6.3). The molecule has a large steric volume, due to the presence of the four phenyl rings in the 5, 10, 15 and 20 positions rotated of about 45° with respect to the main pyrrole plane.

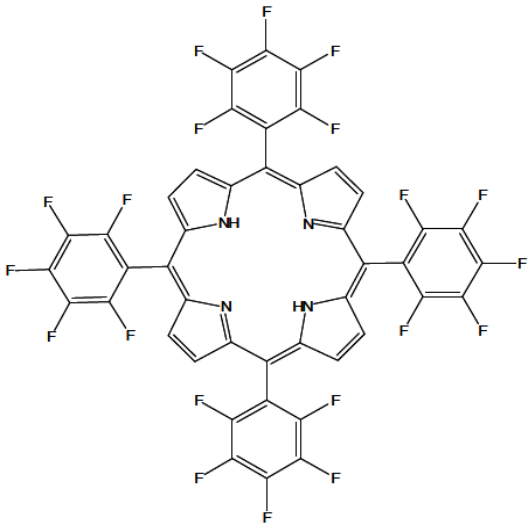

Figure 6.3: Sketch of $H_2TPP(F)$ structure.

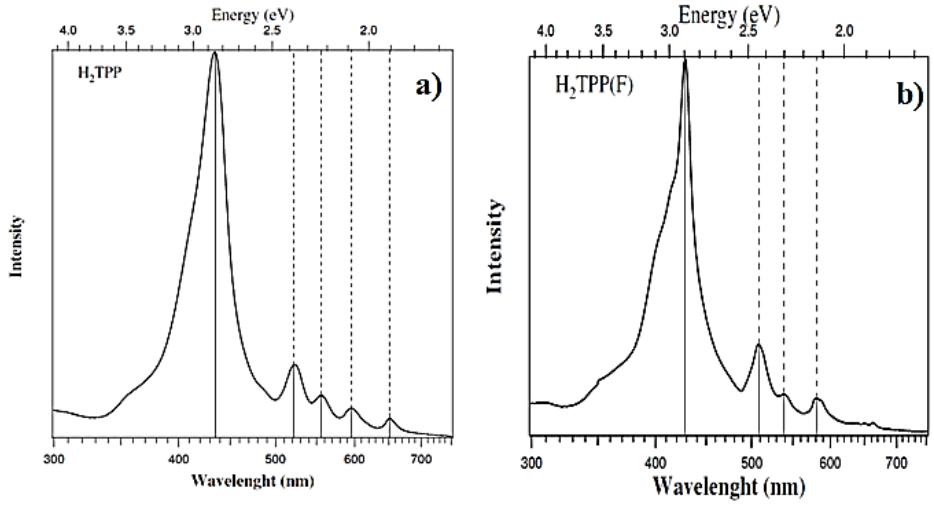

Figure 6.4: Absorbance spectra of a H_2TPP (a) and $H_2TPP(F)$ thin films on quartz [35].

M.V. Nardi compared the optical absorbance of thin films (40-50 nm) of TetraPhenilPorphyrin H_2TPP and $H_2TPP(F)$, grown in UHV conditions on high purity quartz by means of supersonic seeded beam (Figure 6.4) [35]. With respect to the not-halogenated form, the $H_2TPP(F)$ bands appear shifted towards the UV region, probably due an increase of the HOMO-LUMO gap energy associated to the presence of the fluorine atoms.

6.3 Porphyrins as Photosensitizer in Photodynamic Therapy

For their optical properties, porphyrins can be classified as photosensitizer (PS), namely chromophores that, in aqueous environment, generate reactive oxygen species (ROS) upon light radiation and absorption, so they can be applied to induce therapeutic effects by killing or damaging malignant cells. A common cancer treatment based on the dye-sensitizer photooxidation is the Photodynamic Therapy (PDT), which consists of 3 essential components: photosensitizer (PS), light and oxygen. The action mechanism of PDT is displayed in Figure 6.5 [223].

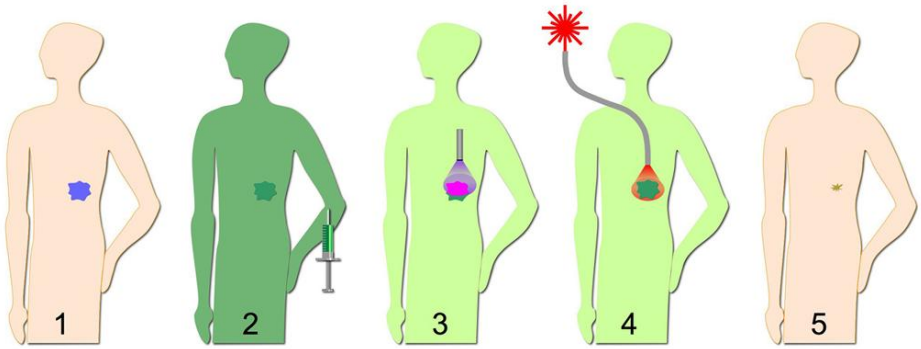

Figure 6.5: Typical PDT medical procedure. 1) patient with a solid tumor, 2) photosensitizer (PS) is administrated to the patient, 3) fluorescence can be used for PS quantification, 4) the tumor is irradiated by visible light, 5) the tumor regresses [223].

After the administration of a light-sensitive PS, the latter will reach every part of the patient body by bloodstream, hence also the tumor loci that will be then irradiated with a light of appropriate wavelength in order to generate highly reactive products, in particular, singlet oxygen ($^1O_2$). The latter can cause a cytotoxic activity leading to cell death via apoptosis or necrosis.

6.3.1 Singlet oxygen production in PDT and light sources

The photocytotoxic effects exploited in PDT take place after the absorption of visible light by the PS. In this way the PS is excited from its ground state (S_0) to a very unstable singlet excited state (S_1), which emits this energy excess as fluorescence or it may undergo an

intersystem crossing, generating a sensitizer triplet state (T_1). The lifetime of the T_1 state is longer (μs) than that of the S_1 state (ns), allowing this excited state to react in two different ways: Type I and Type II mechanisms. A Type I mechanism involves hydrogen-atom abstraction or electron-transfer between the excited sensitizer and a substrate, yielding free radicals. These radicals can react with oxygen to form active oxygen species such as superoxide radicals. In a Type II mechanism, singlet oxygen ($^1O_2$) is generated by an energy transfer process to molecular oxygen (O_2) in its triplet ground state (Figure 6.6) [224]. It is believed that most PSs operate via a Type II mechanism being it mechanistically much simpler [225].

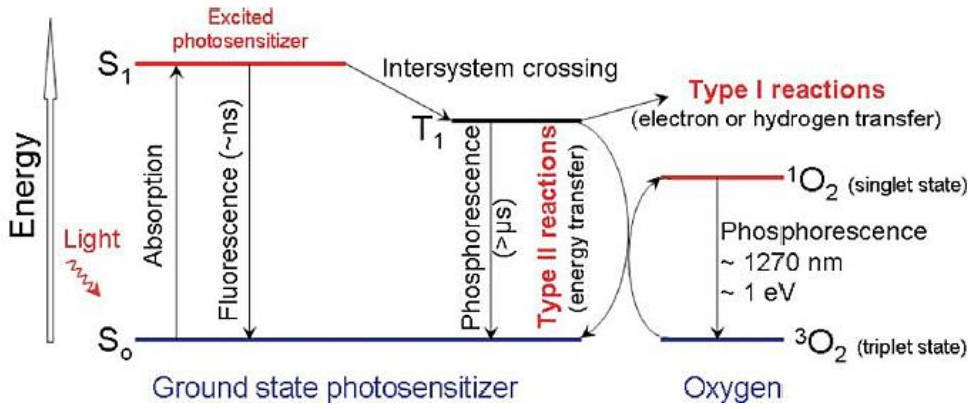

Figure 6.6: Modified Jablonski diagram of the photosensitization processes [224].

Each photosensitizer molecule can typically produce 10^3-10^5 molecules of $^1O_2$ before being degraded through photobleaching by $^3O_2$ or by some other process. The lifetime of $^1O_2$ is very short (10-320 nanoseconds), limiting its diffusion to only 10 nm to 55 nm in cells and aqueous solution. Thus, photodynamic damage will occur very close to the intracellular location of the PS primary photoexcitation [224]. PS can be activated by different types of light, typically in the ultraviolet (UV) and visible part of the spectrum. The choice of light source depends on PS absorption properties (fluorescence excitation and action spectra), disease to be cured (location, size of lesions, accessibility and tissue characteristics), cost and size. Conventional light sources can cover the entire visible spectrum and include laser, intense pulsed light (IPL), light emitting diodes (LEDs), red light, blue light and incandescent lamps. One of the main issue of this approach is that only a small part of the light will penetrate into tissue: MacDonald and Dougherty demonstrated that only about 37% of the light shorter than 800 nm can penetrate for 1-3 mm [226].

6.3.2 Photosensitizer in PDT

A large number of photosensitizing molecules have been tested in the last ten years. Depending on their chemical structures, they can be classified in three main families:

- Porphyrin (hematoporphyrin and benzoporphyrin and their derivatives, 5-aminolevulinic acid (ALA), texaphyrins);
- Chlorophyll (chlorins, purpurins and bacteriochlorins),
- Dye (phthalocyanine and naphthalocyanine).

Their structures are illustrated in Figure 6.7 [227].

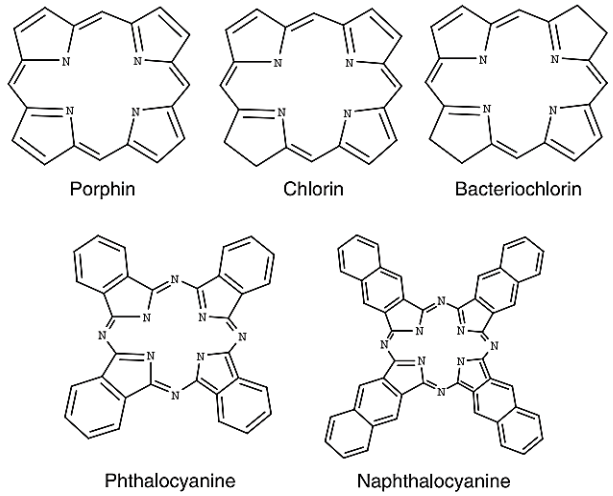

Figure 6.7: Basic structures of common PSs [227].

An ideal PS should have low levels of dark toxicity and it should be water soluble or soluble in aqueous solvent mixture in order to be administered intravenously and to be transported by the bloodstream to the target tissue.

In view of the above, PS should have a high absorption coefficient in the spectral region of the excitation light (visible light), generally between 600 and 800 nm. This region is the so called *Therapeutic Window* of tissue and represents the best compromise between light highest action depth in the tissues and best singlet oxygen production. Lights at shorter wavelength (blue) are characterized by a weak tissue penetration and they can be absorbed by endogenous molecules as hemoglobin [228]. On the contrary, lights with high wavelengths do not have sufficient energy to excite the PS and to form a sufficient yield of reactive oxygen species [229,224].

All porphyrin-derived compounds (chlorine and bacteriochlorin) have a strong absorption band at 400nm (Soret band), but the activation of PS through the absorption in this region is not useful because, as it has been said previously, blue light has only minimal penetration in the tissue. For this reason the absorption Q-bands between 600 and 700 nm are those used in PDT. The typical penetration depth at 630 nm is 2-3 mm and it rises up to 5-6 mm increasing the wavelength (Figure 6.8) [228,224].

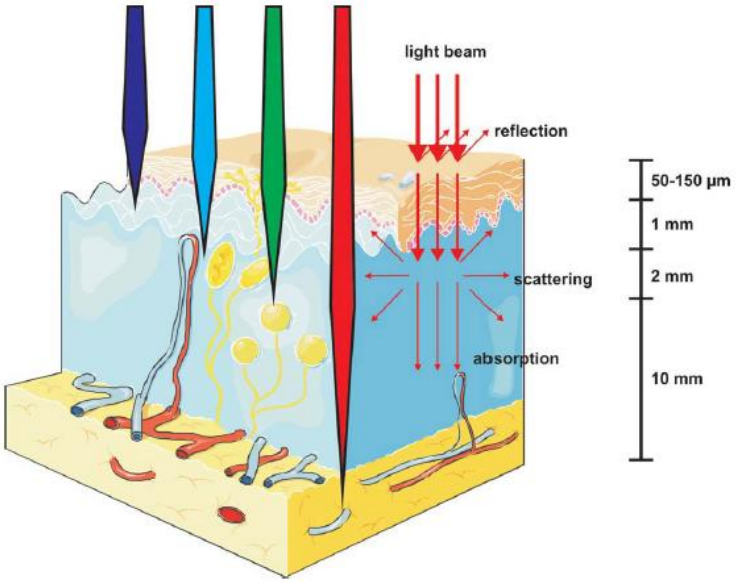

Figure 6.8: Light propagation thorough the tissue [224].

At the moment, no photosensitizer studied so far satisfies completely all these requirements. In particular, the depth limitation of the irradiation process allows to apply the PDT approach efficiently only to subcutaneous tumors or superficial lesions of the internal organs, reachable only by optical fibers illumination after surgical operations.

6.3.3 Nanomaterials as PS carriers for PDT

The PDT success is related to the properties of PS, i.e. chemical composition, absorption properties besides from the amount of PS in the treated tissue and the light doses. The main limitation of PS used so far is their low absorbance in the optical window for excitation, reducing in this way the $^1O_2$ production. Many efforts have been made to overcome these restrictions, studying new possible photosensitizers based on nanoparticles (NPs).

Nanomaterials represent a great promise in PDT applications because of their properties (Figure 6.9) [230]:

- they can be made hydrophilic,
- they possess a wide surface area that can be decorated with different functional groups for tumor specific targeting, giving rise to PS-loaded nanoparticles,
- they can penetrate deep into tissues thanks to their sub-cellular and sub-micron size.

The PS-loaded nanoparticles have been prepared using different nanomaterials, such as inorganic oxides, metal and organic compounds [231]. These systems can be divided in two families: biodegradable and non-biodegradable nanoparticles [232]. Biodegradable nanoparticles have received attention as possible drug-delivering agents, in particular those constituted by polymers whose composition and morphology can be optimized in order to improve their biocompatibility.

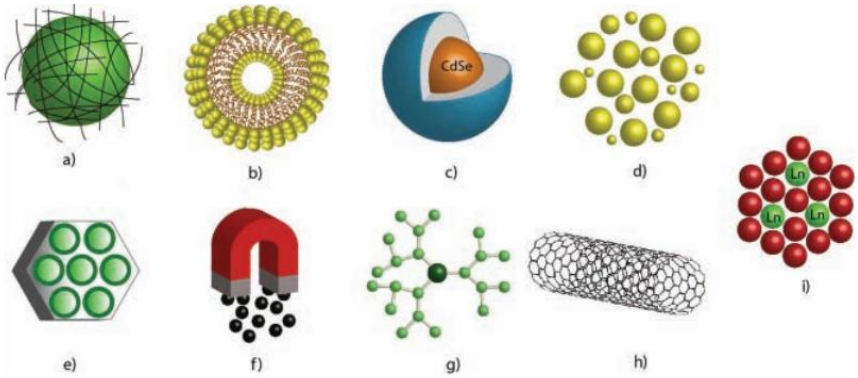

Figure 6.9: NPs used in cancer treatment. a) polymeric nanoparticles, b) liposomes, c) Quantum Dots with a CdSe core, d) Gold nanoparticles, e) zeolite L, f) magnetic NPs (iron oxide), g) dendrimers, h) nanotubes, i) upconverting nanophosphors [230].

Forasmuch as natural polymers (proteins or polysaccharides) often require crosslinking causing the denaturation of the embedded drugs, it is recommended to use synthetic polymers such as poly(lactic acid) (PLA), poly(glycolic acid) (PGA) and poly(lactide-co-glycolide) (PLGA), approved by USA FDA (Food and drug Administration) for therapeutic use in humans [233] and for drug delivery applications.

In order to release the PS, the polymer are degraded in the biological environment through a hydrolytic process that depends on the sizes of the particles micrometric being preferable (diameter less than 300 μm) [234], and using mixtures of polymer showing different hydrophilicity.

In non-biodegradable nanoparticles, instead, oxygen can diffuse in and out, so that it is not necessary to release the photosensitizers from the nanoparticles carrier, which can serve only as platform. Hydrated ceramic-based nanoparticles, doped with photosensitive drugs, have many advantages with respect to the common organic carriers. They can be easily prepared by means of a sol-gel process [235], tuning their size, shape and porosity, are chemically stable, so that they do not release the biomolecules encapsulated even in the blood extreme conditions of pH and temperature [236]. Prasad and co-workers [237] developed ceramic-based nanoparticles for PDT applications characterized by porous ceramic matrixes allowing diffusion of the molecular oxygen through the pores towards the embedded PS, leading to the formation of singlet oxygen that diffuse out, ensuring the cytotoxic effect towards the tumor cells. As demonstrated by Russell and collaborators [238], gold nanoparticles can carry a PS (phthalocyanine) and induce the generation of singlet oxygen, using a phase transfer reagent (tetraoctylammonium bromide, TOAB) linked to the gold nanoparticles by Van der Waals interactions. With respect to the ceramic-based nanoparticles, metallic nanoparticles have the advantage to have a very small size (from 1 to few nanometers) and a huge specific surface area. Another class of nanomaterials which represents a great promise in PDT applications, are semiconductor quantum dots (QDs), nanocrystals of a semiconducting material with a core-shell structure and a diameter in the range of 2-10 nm (10-50 atoms). Their optical properties are characterized by the *quantum confinement effect*, that occurs when the semiconductor crystal size is comparable to Bohr radius (average distance between the electron in the conduction band and the hole left in the valence band after excitation). Increasing or decreasing QDs size, the energy gap between the valence and conducting bands decrease or increase, respectively, changing the electron-hole distance: this variation affects their absorption spectra causing a shift of their emission wavelength towards the blue or red region [239].

As a matter of fact, more energy is required to excite the system, more energy is released when the crystal returns to its ground state, bringing about to a shift from red to blue in the

emitted light. This feature is very important for PDT application, since the emission properties can be tuned in order to emit in the near-IR region [240], where light penetrates tissue up to several centimeters. QDs conjugated with PS, with respect to the common PS used in PDT, are non-toxic in absence of light and have a strong absorption and photostability, while their surface can be modified to achieve water solubility and biocompatibility [241]. Samia and co-workers [242] demonstrated that CdSe QDs linked to a silicon phthalocyanine (Pc4) are suitable for PDT. Pc4 photosensitizer is excited indirectly by QDs through a fluorescence resonance energy transfer (FRET) mechanism and, in turn, interacts with the oxygen in the environment generating reactive $^1O_2$.

6.3.4 Self-Lighting Photodynamic Therapy

The most difficult challenge in PDT is to improve the light penetration in the tissues. To solve this problem, new PDT agent systems have been developed to exploit the combination of scintillation luminescent nanoparticles with the common PS, such as porphyrins. The therapeutic approach arising from the use of these new systems has been defined *Self-Lighting Photodynamic-Therapy* (SLPDT) by Chen and Zhang [243]. In the SLPDT, nanoparticles are excited by ionizing radiation such as X-rays, generating light which induce singlet oxygen generation in the PS. This approach has the advantage to combine together two techniques, ionizing radiation and photodynamic therapies, which can be activated by the same photon source [243]. In order to satisfy the characteristics of the two therapeutic methods, scintillating nanoparticles has to be a high-density material to ensure a higher probability of radiation absorption. Furthermore, the Stokes shift value of these nanoparticles, defined as the distance between the position of band maxima in the PS absorption and nanoparticle emission spectra, should be smaller enough to enhance the luminescence efficiency [244].

The luminescent nanoparticles and the PS are bonded together so that the energy transfer occurs by FRET mechanism, similarly to the QDs case, from the excited donor (scintillation nanoparticles) to an acceptor (photosensitizer) (Figure 6.10) [245]. In order to have an efficient energy transfer the distance between the two species should be less than 10 nm. [243].

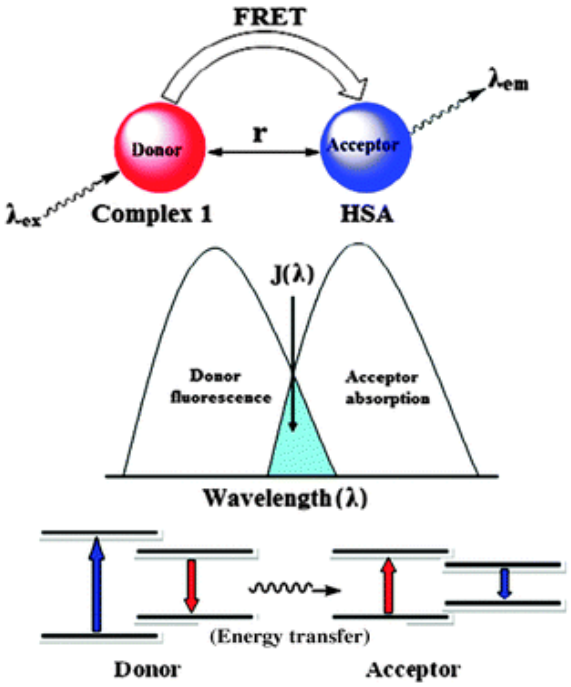

Figure 6.10: Fluorescence resonance energy transfer mechanism [245].

In Figure 6.11 is shown the nanoparticle-photosensitizer conjugated system proposed by Chen and Zhang [243], constituted by nanoparticles of cadmium sulfide bonded to tetrakis (*o*-aminophenyl) porphyrin (TOAP) through cysteine.

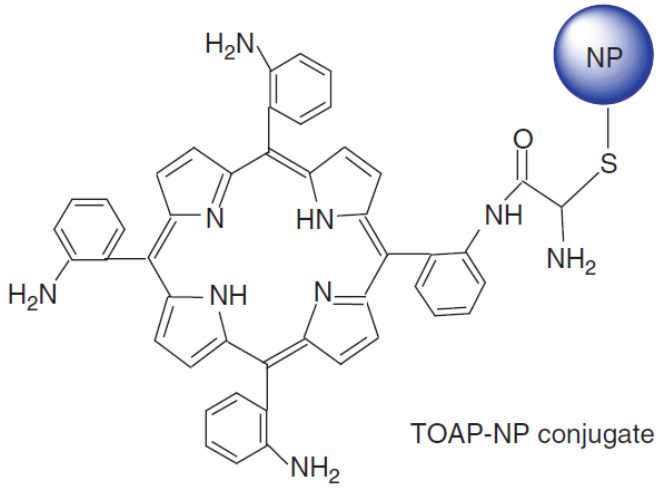

Figure 6.11: PS constituted by nanoparticles of cadmium sulfide bonded to tetrakis (*o*-aminophenyl) porphyrin (TOAP) through cysteine proposed by W. Chen and J. Zhang [243].

The action mechanism of the nanoparticles-X-ray-induced PDT was proposed by Christensen and co-workers [221], as displayed in Figure 6.12. Under ionizing radiation the scintillation nanoparticle transfers its energy to the porphyrin, generating the singlet oxygen necessary to activate the photosensitizing effect. Compared to the usual photodynamic therapy, thanks to the high penetration of X-rays into organic tissues SLPDT can be applied for deep tumor treatment, enhancing the efficiency of the tumor killing and reducing the total radiation dose.

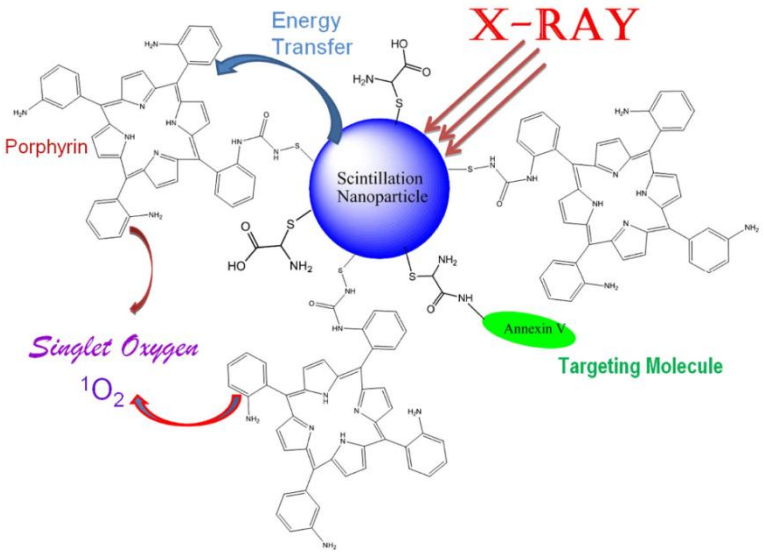

Figure 6.12: Scheme of X-ray induced PDT by scintillation nanoparticles proposed by Christensen and co-workers [221].

Starting from this innovative idea, our group in Trento, in collaboration with IMEM-CNR Institute in Parma, developed a new PS for a X-Ray induced PDT based on SiC/SiO_2 core/shell nanowires functionalized with porphyrin $H_2TPP(F)$ (Figure 6.13), as it will be described in the following paragraphs.

6.4 Why Silicon carbide-Silicon oxide core/shell NanoWires functionalized with H_2TPP(F)?

Silicon carbide (SiC) is a wide band-gap semiconductor characterized by a strong covalent bond between Si and C, that for its chemical-physical properties is well suitable for electronic, optoelectronic and sensing devices [246]. It has been demonstrated that SiC, in addition to being chemically inert, oxidation and corrosion resistant and mechanically robust, is not toxic and biocompatible [247]. In particular, the SiC polytype known as cubic silicon carbide (3C-SiC) is both bio- and hemo-compatibility [248], and hence is an excellent candidate for biomedical enforcements [249,250].

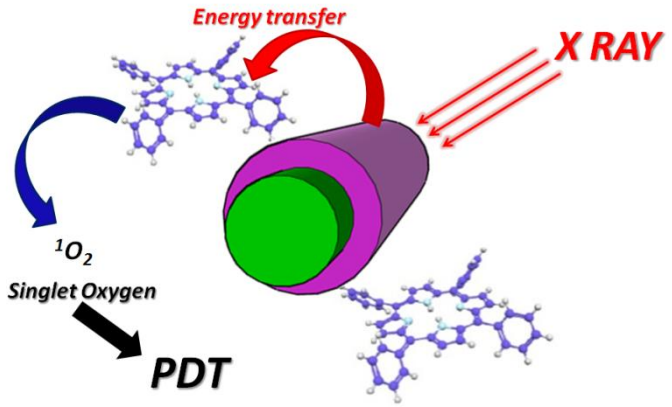

Figure 6.13: Action Mechanism of SiC/SiO_2 core/shell nanowires decorated with porphyrin H_2TPP(F) in X-ray induced PDT, developed by IMEM-CNR group.

In particular, 3C-SiC in its 1D structure as nanowire (NWs), thanks to its dimensions and intrinsic properties (electronic and optical features), has attracted a great interest for applications in nanoelectronic devices (nano field-effect transistors) and nano-sensors for biological systems [251,252].

Perriat and co-workers [253] have demonstrated that a promising strategy to improve the emission efficiency of nanomaterials is to cover them with a silicon dioxide shell. Besides, the inorganic coverage protects the core making the system water soluble and it acts as a platform to anchor specific biomolecules, getting rid of the known SiC low chemical reactivity. They reported an enhancement of luminescence that correlates to an energy

transfer from the shell to the core: the shell acts as an antenna absorbing the light and transferring excitation to the core, increasing the optical response.

F. Fabbri *et al*. [254] proved that this physical process also occurs in the case of 3C-SiC NWs covered by a native SiO_2 shell. By means of cathodoluminescence spectroscopy (CL), they proved that the increase of the 3C-SiC near-band-edge luminescence depends on the thickness of the amorphous SiO_2 layer. In order to highlight this correlation, they evaluated how the NW luminescence changes after a SiO_2 shell etching treatment. A typical CL spectrum acquired at room temperature for an untreated single NW is shown in Figure 6.14: the SiC/SiO_2 core/shell NWs hybrid-system gives rise to a very complex band due to the superposition of all the contributions coming from core and shell portions. The main peak centered at 2.41eV is associated to the near-band-edge emission (NBE) of the 3C-SiC core, which results blue-shifted with respect to the value at room temperature reported in literature (2.36eV) [255].

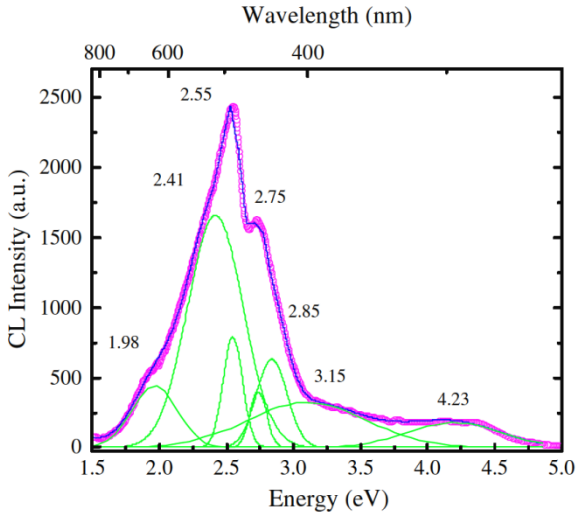

Figure 6.14: Single nanowire CL spectrum at room temperature [254].

The other bands can be associated to oxygen-deficiency center ODC(II) in the SiO_2 shell (2.75 and 4.23eV) [256]; to silicon oxycarbide [257,258] or carbon aggregates in the interface (2.55 and 2.85eV) as demonstrated by XPS core level analysis; hexagonal SiC polytypes (3.15eV) [259]. As a consequence of the etching treatment, the whole CL emission decreases, as shown in the Figure 6.15-a. SiO_2 emission bands decrease after the

HF treatment, while the reduction of SiC-related emission is linked only to the removal of the shell, being the SiC chemically inert (Figure 6.15-b).

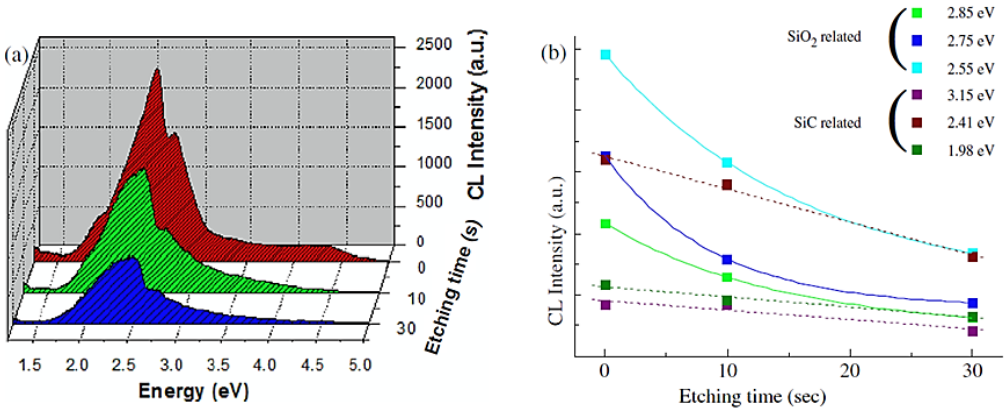

Figure 6.15: (a) CL spectra as function of the etching time and (b) evolution of CL bands coming from the SiO_2 shell and SiC core [254].

According to Sekiguchi and co-workers [254], the enhancement of the silicon carbide CL emission related to the SiO_2 shell is due to a specific band alignment between the core and the shell. The type of band alignment depends on the core sizes and shell regions, giving rise to three different regimes characterized by unlike electronic structure (Figure 6.16).

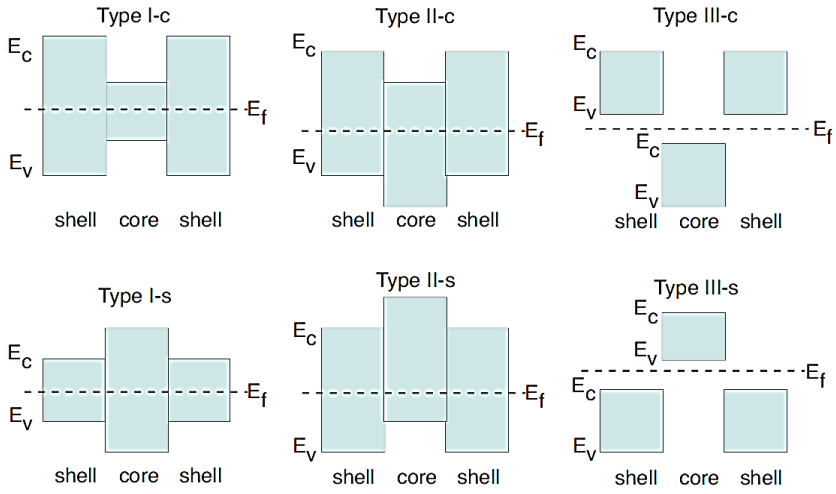

Figure 6.16: Different types of band alignments [260].

The type-I structure is a common quantum well where both electrons and holes are bound to the core. In the type-II structure only one of the two species (electrons or holes) are confined to the core. In the type-III or broken gap structure, the VB band of one material is placed at higher energy than the CB of the other material, so that electrons can move between materials [260].

In the specific case of SiC/SiO_2 core/shell NWs it has been proposed that a type-I alignment occurs, as displayed in Figure 6.17, where the VB and CB values are indicated, allowing the carriers diffusion generating by the electron beam from the shell into the core [254]. In this type-I conformation, an appreciable quantum confinement effect arises, depending on the SiC core size.

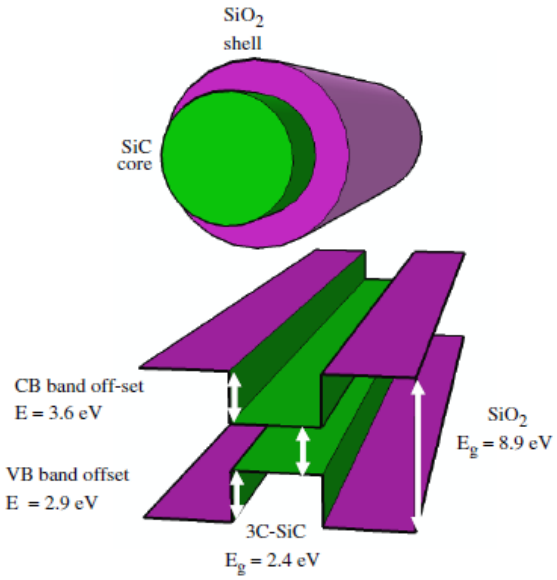

Figure 6.17: Illustration of the type-I band alignment between 3C-SiC and SiO_2.

Interestingly, it has been experimentally demonstrated that SiC/SiO_2 core/shell NWs emit visible light if irradiated by X-ray just as shown by Y. Zhang through X-ray Excited Optical Luminescence (XEOL) analysis (Figure 6.18) [261]. This means that SiC/SiO_2 core/shell NWs can produce the same luminescence if irradiated by both electrons (CL) and X-ray (XEOL) photons. The light emission, centered at ~460 nm, is due to the oxygen vacancy in the SiO_2 shell with a contribution coming from the SiC core leading to the tail at higher wavelengths.

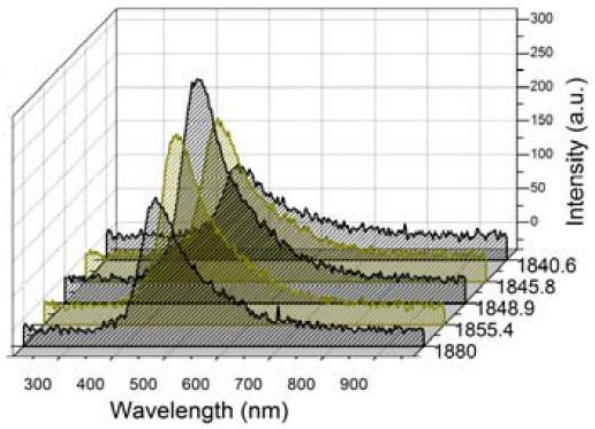

Figure 6.18: XEOL spectra of SiC NWs [261].

In the light of the above, SiC/SiO_2 core/shell NWs represent a promising nanohybrid-system for an efficient X-ray induced PDT being them, what's more, biocompatible and hydrophilic with respect to the system proposed by Christensen [221]. Thus, the envisaged scheme of Figure 6.14 proposed by the IMEM groups is viable and suitable to be used as basis for a PS. In fact, the system can be functionalized with organic molecules and, exploiting the energy transfer from the NWs to the organic molecules, it will de-excite transferring the energy to the surrounding environment in order to produce singlet oxygen.

The NWs functionalization has been pursued by two different approaches (in collaboration with Prof. F. Bigi, Chemical Department, University of Parma). By using specific linkers and wet chemical processes, the porphyrin has been anchored to NWs: the latter have been functionalized with azide groups by condensation reaction between the SiO_2 shell and alkoxysilyl groups. The porphyrin are synthesized with final C-C triple bonds which can react with the azide group in the NW surface [262].

In our laboratories in Trento, the NWs have been functionalized by SuMBD technique with partially fluorinated tetraphenylporphyrin (H_2TPPF), a molecule whose typical porphyrin absorption Q band matches the 3C-SiC near-band-edge optical emission at 2.34eV (Figure 6.19). After several analysis, the second functionalization approach has shown to be the reliable, producing more stable and reproducible organic/inorganic systems under electron irradiation. This once more suggests that SuMBD is a viable approach to the functionalization of inorganic surfaces, these promising results being indeed at the basis of the work presented in the following.

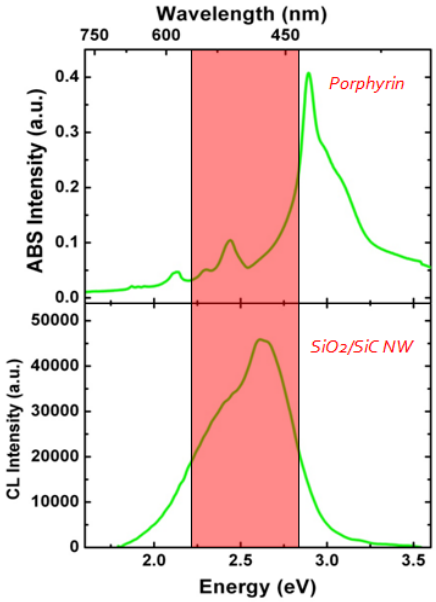

Figure 6.19: Match between porphyrin absorption and SiC/SiO_2 NWs emission bands.

6.5 Preliminary NWs characterization

SiC/SiO_2 core/shell NWs were grown on silicon substrates at IMEM-CNR in Parma by DR. M. Bosi and G. Attolini through a low-cost carbothermal mechanism [263,264]. The dimensions of this system has been evaluated by TEM analysis carried out by the DR. G. Salviati group in IMEM-CNR institute in Parma, putting in evidence that each NW has a diameter of about 60 nm, as shown in Figure 6.20 [254]. The SiC core has a diameter of 20 nm and has a cubic structure, while the shell is amorphous silicon oxide.

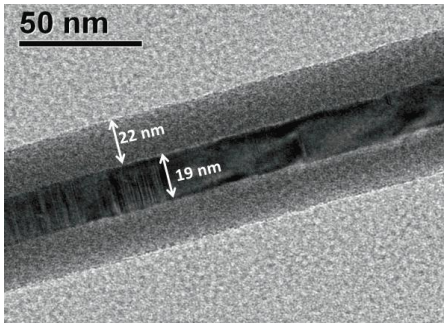

Figure 6.20: TEM image of a SiC/SiO_2 core/shell NWs [254].

The NWs functionalization was carried out in our laboratories in Trento by tetrakis(pentafluorophenyl)porphyrin ($C_{44}H_{10}F_{20}N_4$) $H_2TPP(F)$ supersonic seeded beam, using He as gas carrier and reaching a maximum KE of ~25eV. The typical organic arrival rate on the substrate was about 1Å/min, as evaluated from a quartz microbalance and has been kept constant during all experiments. The NWs samples (still on the silicon substrate) were cleaned before their insertion in the analysis chamber as described in the paragraph 2.6.1, and then annealed in UHV at ~300°C in order to remove any traces of solvent and water.

Characterizations on the SiC/SiO_2 core/shell NWs functionalized with $H_2TPP(F)$ were conducted by G. Salviati and collaborators through CL spectroscopy. The results are very promising and significant, as it is shown in Figure 6.21. In the bottom panel the CL emissions coming from the isolated components (NWs and organic molecules) are displayed and the signal of the whole system NWs-porphyrin is shown in the top panel.

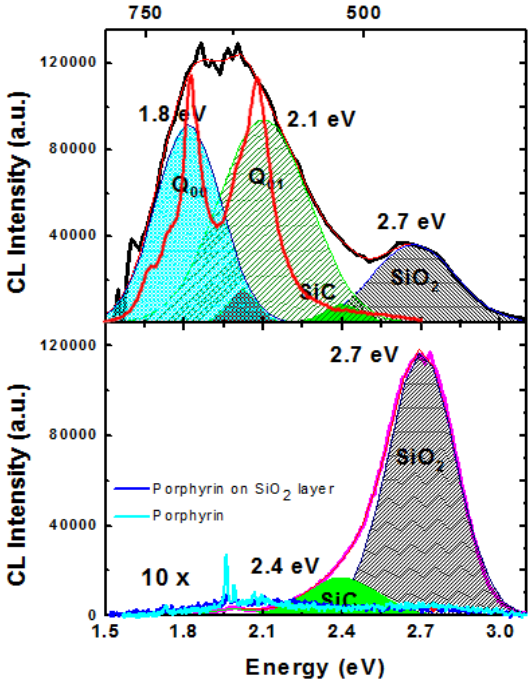

Figure 6.21: CL emission from the single components (panel in the bottom) and in the whole system (panel in the top). It is evident the enhancement of the signal in the NWs-porphyrin system due to an energy transfer process internal to the system. CL from a $H_2TPP(F)$ layer is shown for comparison.

After functionalization, SiC and SiO_2 signals associated to the core-shell NWs decrease, whereas that of porphyrin greatly increases, with an intensity being higher if compared to luminescence from a thick H_2TTP(F) layer deposited on silicon or from the organic powders.

The mechanism associated to this energy transfer has not been identified yet, but we can assume two possible ways:

- a process, where the photon excites the NW that, in turn, transfers its energy excess to the porphyrin which decays producing luminescence,
- an internal process, where the energy transfer takes place through hybrid electronic states at the interface.

It appears that the CL from the functionalized NWs is not merely the sum of the two contributions originated from NWs and H_2TPPF, suggesting that porphyrin is chemisorbed on the SiO_2 shell of the NWs and we are dealing with a new chemical species, at least for what concerns the interface layer. The functionalized SiC/SiO_2 core/shell NWs can be definitely considered a nano-hybrid-system.

These experimental evidences represent the starting points of this study inasmuch they suggest a chemical interaction at the interface between SiC/SiO_2 NWs and the H_2TPP(F). The following of this work is focused on the study of the interaction mechanisms between the chemical species of the hybrid system.

To this end, before the detailed analysis of the complex system of SiC/SiO_2 core/shell NWs decorated with H_2TPP(F), a SiO_2/Si(100) planar surface functionalized with H_2TPP(F) has been studied. This system can be considered as a simplified reference model considering that the NWs have an outer shell of highly defected silicon oxide. The main difficulties encountered during the NWs analysis dealt with the formation of strong charging effects that produce a significative enlargement, broadening and energy shift of the XPS photoemission peaks, while UPS analysis is not possible because of an intrinsic low reliability of the measured spectra. These phenomena are typical in highly insulating systems, but became almost uncontrollable for the analyzed SiC/SiO_2 core/shell NWs. Thus, in order to achieve a more reliable and comprehensive interpretation of the chemical/physical processes occurring at the organic/inorganic interface, we decided to study in detail the functionalization of the SiO_2/Si(100) planar surface.

6.6 H_2TPP(F) fundamental electronic properties

Our group in Trento has longstanding experience in the analysis of porphyrin by photoelectron spectroscopy, in-situ at Trento labs and at the BEAR Beamline of Elettra synchrotron (Trieste), installing the same supersonic source on the beam line. Indeed, M.V. Nardi has studied the valence bands and core levels of three types of porphyrin, including H_2TPP(F), deposited on a SiO_2/Si(100) native oxide surface by SuMBD approach [35]. Moreover, in collaboration with Padova University, theoretical models have been developed in order to achieve a detailed comprehension of the XPS core levels of C1s, N1s and F1s for very thick film, so that the molecule analyzed can be considered equivalent to those in the gas phase, i.e. isolated molecules as it occurs for any theoretical study [265]. The electronic properties of H_2TPP(F), to be considered as a reference, will be briefly described in the following.

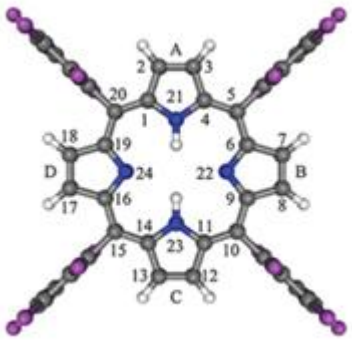

Figure 6.22: **:** Atom numbering recommended by IUPAC.

Tetraphenilporphyrin partially fluorinated is composed by a macrocycle with four pyrrol rings linked in *meso* position to four phenyl rings. These, tilted with respect to the macrocycle plane, are characterized by five C-F bonds (see Figure 6.22), for a total amount of 20 for the whole molecule.

We have taken as reference the theoretical model proposed by M. Nardi to deconvolve the C1s H_2TPP(F) core levels, based on five main components (Figure 6.23-b). The model proposed to fit this lineshape is supported by theoretical calculations carried out by means of DFT-ZORA (two-component relativistic zeroth-order regular approximation), that has been applied also to calculate the N1s and F1s contributions to lineshape as well.

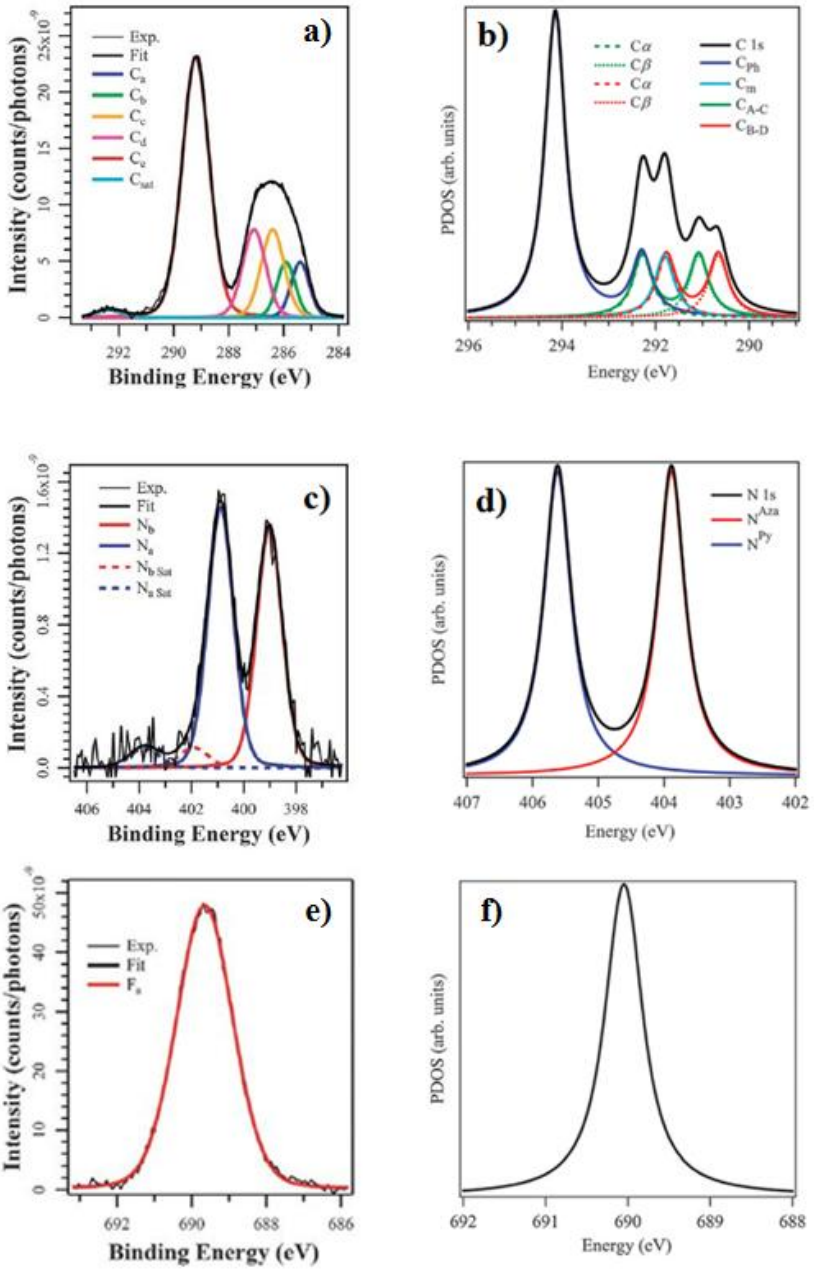

Figure 6.23: Theoretical (b, d, f) and experimental (a, c, e) analysis of $H_2TPP(F)$ core levels: C1s (a, b), N1s (c, d) and F1s (e, f) by M. Nardi and co-workers [265].

The main C1s feature at higher BE can be straightforwardly assigned to C-F bonds, while the entanglement of the different contributions to the carbon core level makes the deconvolution rather complex. The DFT-ZORA calculations solved this puzzle and let the fit proceed via the attribution of specific peaks, properly weighted, to the different carbons

in the molecule. Thus the contributions to C1s lineshape are here listed in order of decreasing BE:

- a peak at high BE related to the C-F bonds in the phenyl rings (C_e in Figure 6.23-a),
- a peak related to the bonds between C in α positions and pyrrolic N in the rings labeled as A and C in the macrocycle (1, 4, 11 ,14 positions in Figure 6.23-a) and the C atoms in the phenyls not involved in C-F bonds (C_d in Figure 6.23-a),
- a peak related to the bonds between C in α positions and aza-N in the rings labeled as B and D in the macrocycle (6, 9, 16 and 19 positions) and the C atoms in *meso* positions (5, 10, 15, 20) (C_c in Figure 6.23-a),
- a peak related to the C atoms in β positions involved in the C-C bonds in the A and C rings (C_b in Figure 6.23-a),
- a peak related to the C atoms in β positions involved in the C-C bonds in the B and D rings (C_a in Figure 6.23-a).

The Table 6.1 gives the complete picture of the model together with the results of the experimental deconvolution.

	Experimental analysis					Theoretical analysis				
Core level	Component	eV	ΔE	FWHM	%	Component	eV	ΔE	%	Molecule atoms
C 1s	C_a	285.80	0	0.78	7.60	C^{β}_{B-D}	290.66	0	9	C(7), C(8), C(17), C(18)
	C_b	286.30	0.50	0.78	7.60	C^{β}_{A-C}	291.08	0.42	9	C(2), C(3), C(12), C(13)
	C_c	286.80	1.00	0.98	15.1	$C^{\alpha}_{B-D} + C_m$	291.77	1.11	18	C(6), C(9), C(16), C(19); C(5), C(10), C(15), C(20)
	C_d	287.50	1.70	0.98	15.1	$C^{\alpha}_{A-C} + C_{Ph}$	292.28	1.64	18	C(1), C(4), C(11), C(14); C atoms in phenyls not showing the C–F bond
	C_e	289.60	3.80	1.17	53.0	C^{F}_{Ph}	294.14	3.48	45	C atoms in phenyls showing the C–F bond
	C_s	292.75	6.95	1.10	1.60					
N 1s	N_b	399.00	0	1.18	46.7	N^{Aza}	403.89	0	50	N(22), N(24)
	N_a	400.90	+1.90	1.16	44.9	N^{Py}	405.62	1.73	50	N(21), N(23)
	N^{sat}_b	401.80	+2.80	1.27	4.2					
	N^{sat}_a	403.70	+4.70	1.27	4.2					
F 1s	F_a	689.60	0	1.78	100	F_a	690.05	0	100	Fluorine atoms

Table 6.1: Analysis of C1s , N1s and F1s core levels for both theoretical and experimental studies, as Ref. [265].

It is evident that the experimental (Figure 6.23-a) fit, carried out on the basis of the theoretical model, shows a good match with calculations, demonstrating the effectiveness of the proposed approach. The differences in the BE of the core levels components from experimental and theoretical analysis are related to the assumption, for the latter case, of an isolated molecule, showing no interaction with anything else. The thick H_2TTP(F) film well resembles this condition, as only weak Van der Walls intermolecular forces are present and very unlikely can modify core level (but also external molecular orbitals)

distribution and energies, nevertheless solid state effects must be considered and absent for the theoretical study, e.g. the system work function, giving rise to the observed BE differences.

From the point of view of the nitrogen core level, previously it is important to correctly identify the chemically different atoms in the macrocycle: the pyrrolic nitrogen atoms (N^{Py}), having two N-C and one N-H bond (in position 21 and 23 in Figure 6.22) and the aza-nitrogens (N^{Aza}) owning a free electrons lone pair (in position 22 and 24 in Figure 6.23). The theoretical model for N1s properly accounts for two components related to the nitrogen atoms in the macrocycle, as displayed in Figure 6.23-d, separated by 1.90eV. Again the lineshape fit based on this model is in agreement.

The experimental fit, moreover, introduced for C1s and N1s other components at higher BEs that are representative of shake-up processes, often found in the photoemission of π-conjugated organic molecules: one peak (Cs) at about 3.15eV from the C-F contribution in C1s and two peaks (N_a^{sat} and N_b^{sat}) for N1s.

F1s core level, on the other hand, is represented only by a single component, related to the C-F bond in the phenyl rings, as illustrated in Figure 6.23 (e, f).

The VB photoemission was analyzed experimentally and theoretically as well. The experimental characterization is shown in Figure 6.24-a, where the same film has been analyzed at two photon energies (21.22eV and 90eV), and highlights the same VB features with different intensity due to molecular orbital cross sections. The first feature at low BE is the highest occupied molecular orbital (HOMO), while a band at about 11eV is usually correlated with F2p states.

There is a shift of the SECO threshold of about -0.7eV with respect to the substrate, a clear indication of dipole formation at the interface. The 2p PDOS (Figure 6.24-b), calculated taking into account the role of each atomic photoionization cross-section, has figure out the role of fluorine in influencing the valence band at the different photon energy explored, in particular the band at ~7eV.

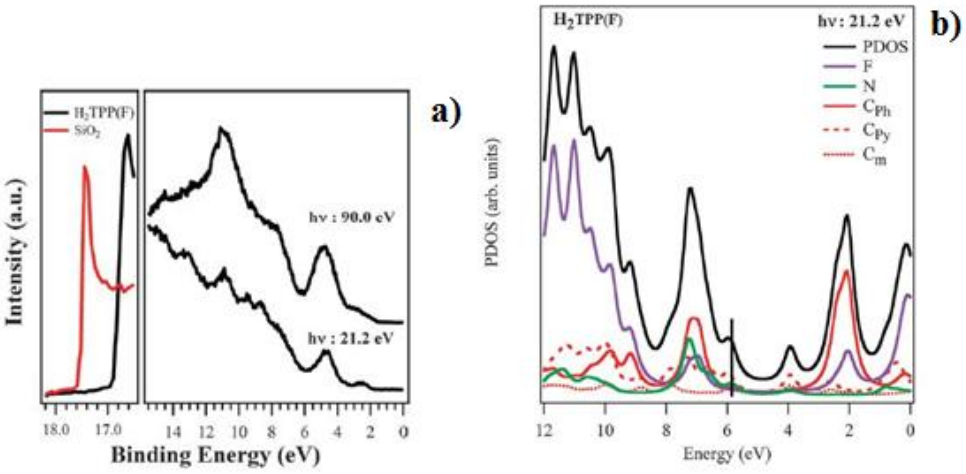

Figure 6.24: (a) Valence band photoemission of a $H_2TPP(F)$ film, 40 nm thick. (b) $H_2TPP(F)$ 2p PDOS, calculated taking into account the F2p, N2p and C2p atomic subshell photoionization cross sections [265].

6.7 $H_2TPP(F)$ thick film on SiO_2/Si(100) planar surface properties

We investigated the properties of $H_2TPP(F)$ in form of thick film (bulk phase) deposited on a SiO_2/Si(100) planar surface, with a nominal thickness of about 40 nm evaluated by a quartz microbalance, using He as carrier gas for a molecule KE of about 25eV. A detailed XPS and UPS characterization will be shown in order to have the organic electronic properties that will be used as reference to discuss the film growth process (see next paragraph), such as the distribution of the more external molecular orbitals and that of core levels, for all chemical species and elements present in the molecule.

Regarding XPS analysis, C1s, F1s and N1s core levels have been examined. The composition, i.e. the stoichiometry, is displayed in the following Table 6.2, where the calculated values are compared with the theoretical ones: the atomic concentrations (±2.5%) are consistent with those expected and are expressed as atomic percentages.

Figure 6.25 shows the C1s core level where it is possible to identify five components that reflect the carbon chemical species present in the molecule. The main peak is located at 288.28eV and it is due to emission from C atoms of phenyl rings involved in the C-F bonds (labeled as C-F in Figure 6.25).

ATOMIC PERCENTAGE (±2.5%)			
	%C	%F	%N
Calculated	61.4	33.2	5.4
Theoretical	64.7	29.4	5.9

Table 6.2: Atomic percentages calculated and expected for H_2TPP(F) bulk film.

Its intensity, that represents the 48.0% of the total C, is thus related to the photoemission of about 21 C atoms, with respect to the expected value of 20. Such a discrepancy (that affects also the weight of all other C1s components) has already been observed and attributed to a possible different photoemission efficiency of the carbon atoms directly involved in the fluorine bond [35,265].

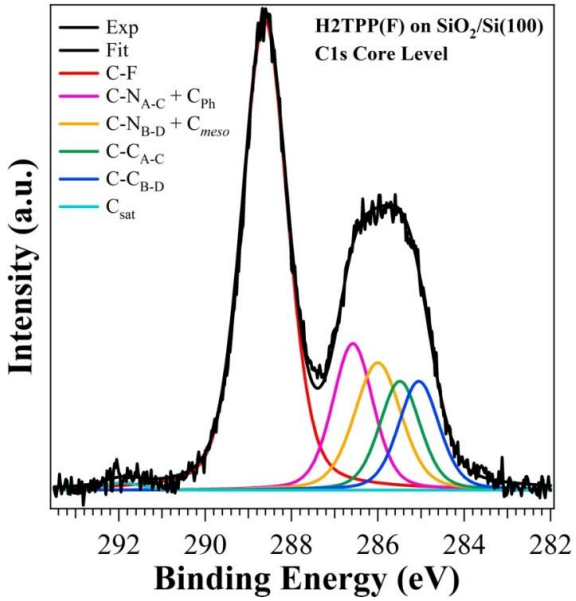

Figure 6.25: C1s core level from a H_2TPP(F) thick film.

Its high position in BE is connected with the fluorine electronegativity: valence electron withdrawing substituents decrease the electron density on the carbon atoms causing an increase of the C BE. Such an electron charge distribution, showing a strong deficiency on carbon ($C^{\delta+}$) and an electron excess on fluorine ($F^{\delta-}$) has been observed also in theoretical calculations [265]. The other carbon atoms in the four phenyl rings, characterized by bonds only with other C atoms, are not strongly influenced by the fluorine presence, so it is reasonable that they are located at lower BE. According to the model described above, these contributions add up to the C atoms showing a bond with N, giving rise to the

component at 286.25eV related to the 4 carbon atoms in α position in A and C rings, and the aforementioned 4 C atoms not involved in C-F bond in the phenyl rings (marked as C-N_{A-C} + C_{Ph} in Figure 6.25).

The peak at 285.62eV is due to the 4 carbon atoms in β position in B and D rings involved in C-N bonds with aza-N and the 4 C in *meso* positions (marked as C-N_{B-D} + C_{meso} in Figure 6.25). Each of these components corresponds to about 6.9 atoms with respect to the expected for the theoretical system, representing the 15.6% of the total C emission. The other two peaks at 285.14 and 284.64eV are associated to the C-C bonds in the macrocycle by the C atoms in β positions in A-C (C-C_{A-C}) and B-D (C-C_{B-D}) rings, respectively and each represents emission from about 4.3 C atoms. In addition to the five peaks proposed in the theoretical model, there is a further contribution at 291.43eV, named as Cs: a satellite structure related to a shake-up process due to a transition π→π* of the C in aromatic rings [55]. Interestingly, if this peak is associated to electron coming from C-F carbon species and experiencing the mentioned energy loss process, it can be argued that the HOMO-LUMO energy gap of this molecule is at least 3.2 eV, while if contributions some also from carbon in the macrocycle, this value is significantly higher. The following Table 6.3 summarizes the main features of all the components for the H_2TPP(F) C1s core level.

Component	**BE [eV]**	**Distance from C-F peak**	**C1s peak area percentage (±2.5%)**	**Number of C atoms**	**FWHM [eV]**
C-F	288.28	0.0	48.0	21.1	1.25
C-N_{A-C} + C_{Ph}	286.25	-2.0	15.6	6.9	1.17
C-N_{B-D} +Cmeso	285.62	-2.7	15.6	6.9	1.17
C-C_{A-C}	285.14	-3.1	9.7	4.3	1.00
C-C_{B-D}	284.64	-3.6	9.7	4.3	1.00
C_S	291.43	+3.2	1.4	0.6	1.10

Table 6.3: C1s core level main features of H_2TPP(F) thick film: BE, distance from main peak, FWHM are expressed in eV, while percentage on total C1s area and corresponding number of emitting C atoms are also shown.

It is noteworthy the shift of the whole spectrum of about -1.0eV with respect to values presented in Ref. 265, probably related to different charging effects in the experiments performed using synchrotron radiation light and a film showing different thickness. In fact,

the same effects have been found also in our experiments (see BEs values for core levels for thick film in the next paragraph) and we definitely assign it to differences in the organic film thickness. The same (or slightly lower) BE difference has been found also for N1s and F1s peaks, thus our data are totally in agreement with the interpretation proposed in Ref. 265.

The H_2TPP(F) N1s core level (see Table 6.4) shows two main peaks at low BE (Figure 6.26) that can be assigned to the aza-N atoms with the lone electron pair (398.35eV, N^{Aza}) and the pyrrolic bonded with H (400.30eV, N^{Py}) which represent the 45.0% and the 47.2% of the total N signal, respectively.

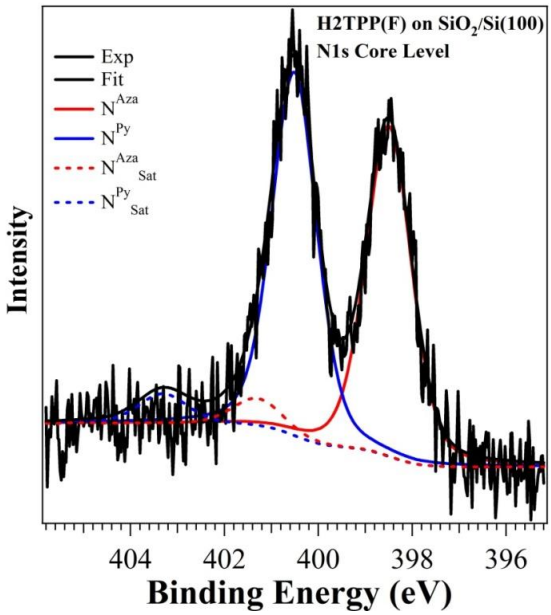

Figure 6.26: N1s core level from a H_2TPP(F) thick film.

Component	BE [eV]	Distance from N^{Py} peak	N1s peak area percentage (±2.5%)	Number of N atoms	FWHM [eV]
N^{Aza}	398.35	-2.0	44.3	1.8	1.22
N^{Py}	400.30	0.0	47.9	1.9	1.20
N^{Aza}_{Sat}	401.15	+0.9	3.9	0.2	1.30
N^{Py}_{Sat}	403.05	+2.8	3.9	0.2	1.30

Table 6.4: Components' parameters of N1s core level from H_2TPP(F) thick film: BE, distance from main peak, FWHM are expressed in eV, while percentage on total N1s area and corresponding number of emitting N atoms are also shown.

The broader components at higher BE (401.15 and 403.05eV) are satellite due to π→π* excitation process related to N^{Aza} (3.9%) and N^{Py} (3.9%), respectively [263,265,266]. Distances between single components and relative weight are once more in good agreement with the proposed scheme in Ref [265].

The F1s core level is constituted of a single main peak at 688.23eV, as shown in Figure 6.27, in agreement with the presence of only one chemical species for fluorine related to the F-C bond in the phenyl rings.

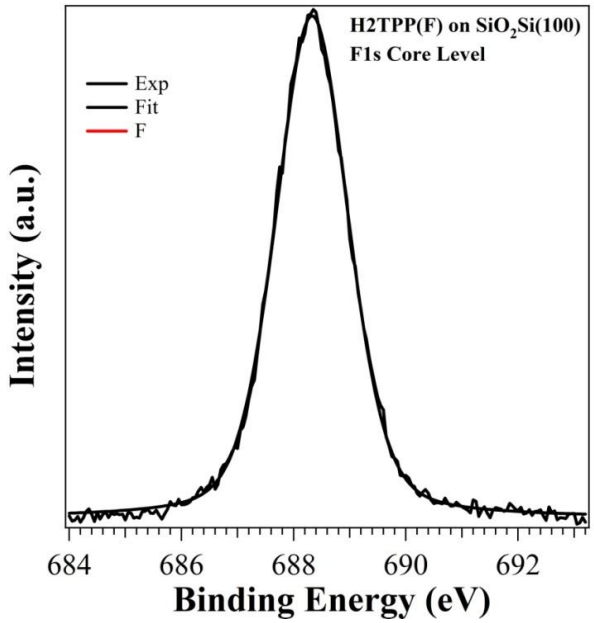

Figure 6.27: F1s core level from a H_2TPP(F) thick film.

Component	BE [eV]	Distance from F1s main peak	F1s peak area percentage (±2.5%)	FWHM [eV]
F	688.23	0.0	100	1.56

Table 6.5: Components' parameters of F1s core level from H_2TPP(F) thick film BE, distance from main peak, FWHM are expressed in eV, while percentage on total F1s area are also shown.

The valence band of H_2TPP(F) (Figure 6.28) is particularly complex and the first analysis for this molecule was developed in Trento [265]. The peak at 3.0 and 5.0eV are related to the HOMO and HOMO-1 bands, while the feature at about 11eV is certainly correlated to

F2p photoemission. The ionization potential (IP) value, calculated as the difference between the photon energy and the spectrum energy length (see Chapter 3), is equivalent to 6.64±0.1eV.

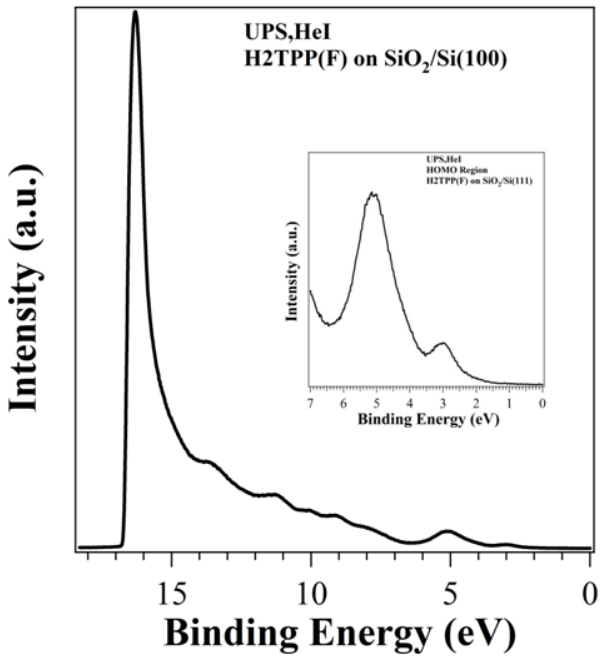

Figure 6.28: Valence band spectrum of H_2TPP(F) thick film with close-up of the SECO region.

While the overall lineshape is in agreement with previous results, the main bands BE are about +0.5eV higher and the IP value is slightly lower with respect to 7.0±0.1eV in Ref. 265. These discrepancies concerning bands BEs could be once more related to different charging effects using synchrotron radiation light, as well as the IP difference is probably due to more intense charging processes at the interface, not present in our in-house experiments.

In summary, we conclude we are dealing with a film of H_2TPP(F) where the molecule did not experience any damage during the deposition by SuMBD. Thus, the observed value represents a good basis and a reference for the following study of thin film growth on SiO_2/Si(100) surface.

6.7.1 H_2TPP(F) film growth on SiO_2/Si(100) planar surface

A consecutive series of H_2TPP(F) depositions on planar surface have been performed using He as carrier gas for a H_2TPP(F) KE of about 25eV keeping the substrate at room temperature. After each deposition a surface electron spectroscopy analysis was carried out by means of low resolution XPS (Passing Energy = 20eV) of C and F coming from the organic molecule and Si and O from the substrate, in order to investigate the growth process. Some growth times relative to the first part of the growth curve have been repeated in order to investigate in detail by XPS high resolution analysis (Passing Energy = 10eV) the chemical species involved in the interaction at the interface. Each film, corresponding to a specific deposition time (100, 240, 350, 470, 550, 2000 minutes), has been prepared depositing a suitable quantity of material on a Si(100)/SiO_2 planar surface previously cleaned. C, F, N, O and Si core levels were studied at low and high resolution. Furthermore, for O and Si measurements at grazing electron acceptance angle (θ=70°) have been carried out to analyze the interface from the point of view of the uppermost inorganic surface. Films have been characterized also with UPS spectroscopy. A second series of these samples, deposited at the same conditions, have been investigated by AFM and microfluorescence by Prof. Cristofolini group at Parma University (Department of Physics and Earth Sciences), as described in the paragraphs 3.6.3 and 3.6.6.

In order to study the growth mechanism, the intensity evolution of low resolution XPS core levels signals from substrate (Si2p and O1s) and organic molecule (C1s and F1s) have been analyzed as a function of the deposition time (Figure 6.29). The peaks area have been evaluated and normalized to the value of the clean surface for the substrate signals, and of the C and F values in the bulk state for the organic molecule. Any contribution coming from the adventitious C (<0.1ML on clean surface) has been taken into account and properly subtracted.

As displayed in Figure 6.29, the observed growth kinetics (XPS core levels emission signals vs. deposition time) are extremely complicated and cannot be described by the typical trends explained in the paragraph 2.7.1. The growth curve shows a sigmoid trend (S-shaped curve), typically observed in biological systems where the growth of population density of organisms in a new environment is studied [267].

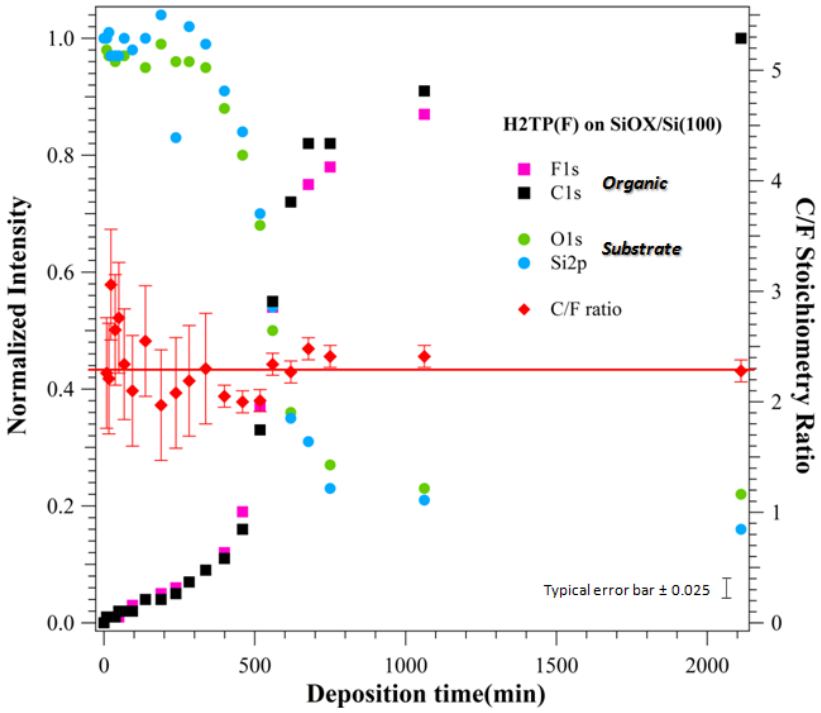

Figure 6.29: Growth kinetic (XPS core level signals vs. deposition time) for a $H_2TTP(F)$ deposition on $SiO_2/Si(100)$.

The graphic can be divided in four steps, in analogy to the system employed by the biologists:

- Lag phase between 0-400 minutes: the growth is very slow. The substrate signal could be considered as unchanged and the emission from the overlayer does not increase significantly. Indeed, at 400 min F1s and C1s signals are about 12% of the final value and shows a linear trend vs. time, while substrate signals decrease correspond to a film thickness < 1ML of $H_2TTP(F)$, where a signal reduction of 25% is expected (1ML thickness of 0.5nm, escape depth of 1.92 nm for Si2p, $H_2TTP(F)$ nominal density of 1.95 g/cm^3).
- Exponential phase 400-700 minutes: the curves change suddenly the slope becoming almost vertical for both substrate and overlayer signals, suggesting a strong increase in the growth velocity. The substrate signals decrease up to 30% of the initial signal, while F1s and C1s signals increase up to 75% and 82%, respectively.
- Transitional phase between 700-1100 minutes: this part of the curves is characterized by a decelerating growth rate. The substrate signal is still about 25%

and the emissions from the overlayer reach 78% and 82% for F1s and C1s, respectively.

- Plateau phase between 1100-2000 minutes: the curves reach a saturation state and no further variation occurs. In this last part of the curve the signal from the substrate is still present (~20% of the initial value).

To get information about the stoichiometry of the growing film, in Figure 6.29 is also plotted the atomic ratio between carbon and fluorine, calculated by the intensity of the XPS signals corrected by the specific sensitivity factors. The error bars displayed for the first points up to about 300 minutes are rather large (±0.5) because of the low coverage of organic molecule on the surface that enhances the error. The C/F ratio remains anyhow coherent with the expected value (2.2) during whole growth.

From a first analysis of the growth kinetic, it seems necessary to create a first organic layer, i.e. to complete a first interface with inorganic before starting a quick and efficient organic film deposition, probably characterized by formation of islands as suggested by the final substrate signals reduction different from zero for the thick film. This reminds of a sort of Stransky-Krastanov growth, where the formation of a wetting layer is required before island growth, is nevertheless different from what observed with other deposition approaches. In terms of sticking coefficient of H_2TTP(F) on the oxide surface, it is clear that in the first linear and slow regime it is very low, thus most of molecules are scattered from the surface and/or formation of very high aspect ratio nanoislands is possible. They cover a small portion of the substrate surface and thus give origin to the observed low organic signals and to the low inorganic intensity reduction. Once a critical coverage is reached, the sticking coefficient increases, the growth is sudden and efficient leading to the formation of the complete molecular film.

It has been shown by M. Nardi that, at a lower H_2TTP(F) KE of 0.5eV, the growth is completely different, similar to that of a non fluorinated porphyrin H_2TTP (Figure 6.30), with a quasi layer by layer growth where the organic/inorganic interaction is characterized by physisorption processes [35], with a high sticking coefficient right from the growth beginning. It is worth noting the different molecular arrival rate used in growth experiment present in Figure 6.30, being about ten times higher than in our deposition set-up (1 nm/min instead of 0.1 nm/min). Our result suggests that the high H_2TTP(F) KE induces formation of

different chemical reactivity at the interface, a process that competes with molecule repulsion and scattering from the surface.

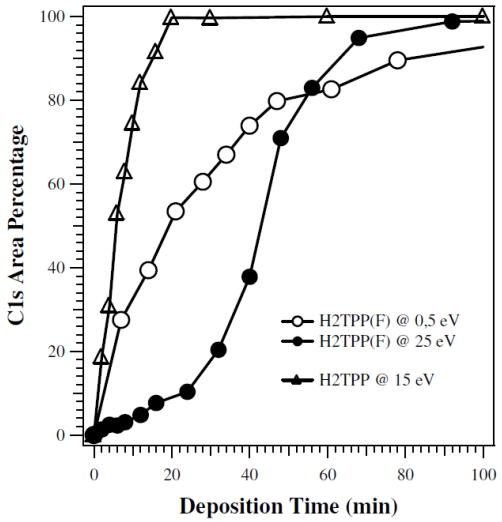

Figure 6.30: Growth kinetics of H_2TTP and $H_2TTP(F)$ on SiO_2/S1(100) surface by SuMBD ad different organic precursor kinetic energies [35]. Molecular nominal arrival rate was about ten times higher than in our experiments (1 nm/min instead of 0.1 nm/min) leading to the observed total lower deposition times.

Detailed high resolution XPS analysis and UPS characterizations have been carried out with the aim to shed further light on the chemical interactions that occur at the interface between $H_2TPP(F)$ and the oxide layer in SiO_2/Si(100) planar surface. For this purpose, the mentioned several depositions at 100, 240, 350, 470, 550 and 2000 minutes (as displayed in Figure 6.31), have been performed, where the latter represents the thick film phase and they will be named as D1, D2, D3, D4, D5 and Bulk from now on.

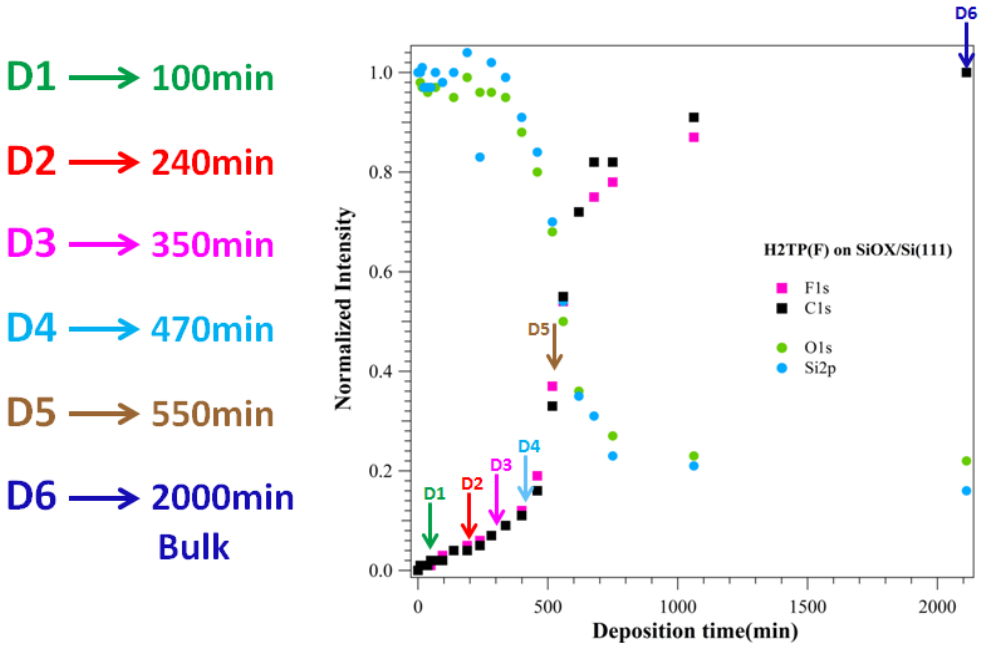

Figure 6.31: Points of the $H_2TPP(F)$ growth curve on $SiO_2/Si(100)$ planar surface analyzed by XPS and UPS high resolution: D1(100min), D2(240min), D3 (350min), D4 (470min), D5 (550min), D6 (Bulk).

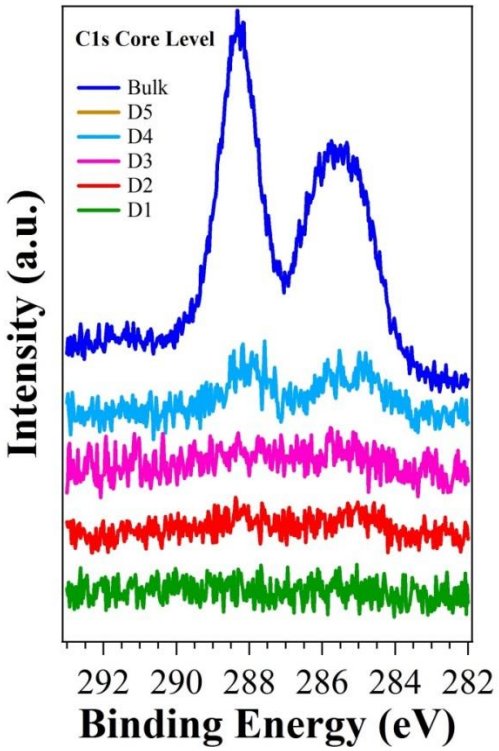

Figure 6.32: XPS C1s core level emission as a function of the $H_2TPP(F)$ film coverage.

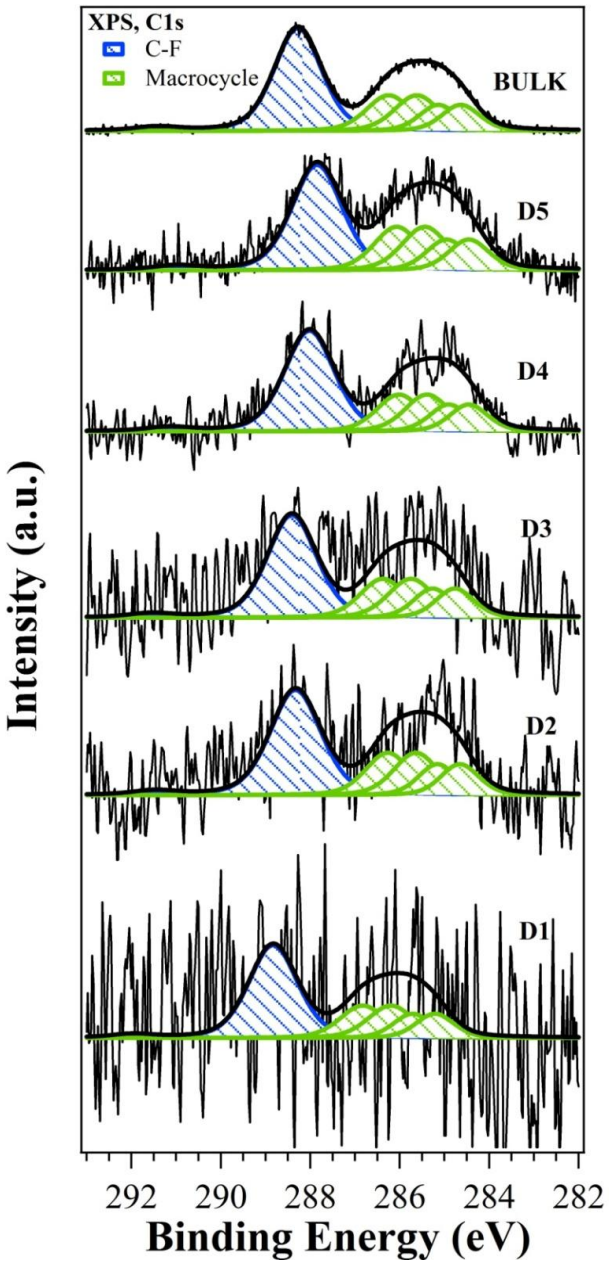

Figure 6.33: Comparison of the C1s lineshape deconvolution as function of the film coverage (Spectra normalized in height).

The C1s core level spectra as a function of the deposition time are displayed in Figure 6.32, where it is always possible to distinguish the main feature related to the C atoms involved in C-F bonds at high BE and the larger band associated to the C-C and C-N bonds in the macrocycle at lower BE. The comparison of all the spectra for each deposition time and their correspondent lineshape analysis is reported in Figure 6.33. The signal shown has not been first processed, so that the noise is the original coming from the data acquisition

system. The signal to noise ratio (S/N) is low for the initial growth stages, due to the small amount of organic molecule analyzed but it is possible to distinguish the typical two main bands of H_2TPP(F) for each grown film.

Taking as reference the main peak related to the C-F bond, it is possible to observe an energy shift from D1 (288.83eV) to the bulk (288.28eV) spectrum of about Δ = -0.55eV, reaching the maximum values in D4 (288.02eV, Δ = -0.81eV) and D5 (287.85eV, Δ = -0.98eV). The FWHM of the main peak (1.3eV) does not change significantly with the coverage.

If C1s core levels do not show evidence of new chemical species due to the interaction at the interface, important indications are provided by F1s analysis, taking also into account that the higher photoionization cross section as well as the single chemical species of emitting atoms (and thus a simpler peak lineshape) give rise to a higher signal intensity and better S/N ratio. The F1s core level evolution is showed in Figure 6.34.

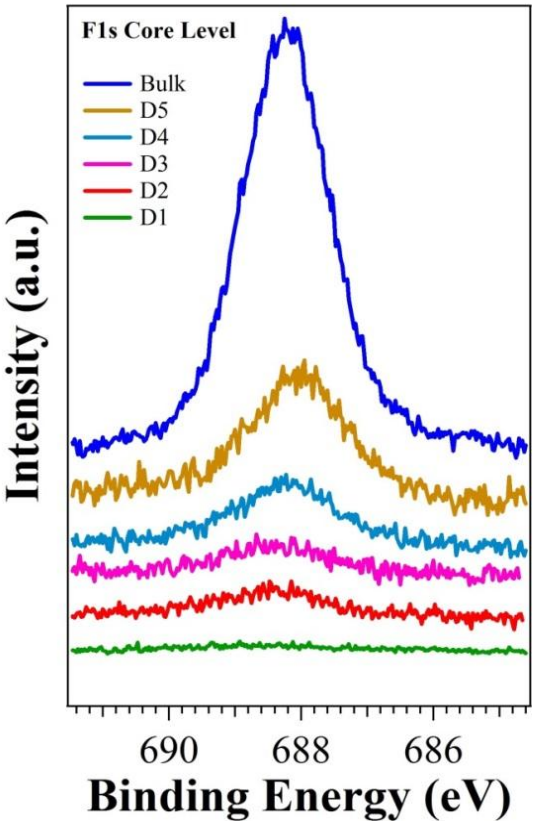

Figure 6.34: XPS F1s core level emission as a function of the H_2TPP(F) film coverage.

Furthermore, even though it is expected only one main feature due the F-C species, two components have been identified at low coverages (D1 and D2), as illustrated in Figure 6.35.

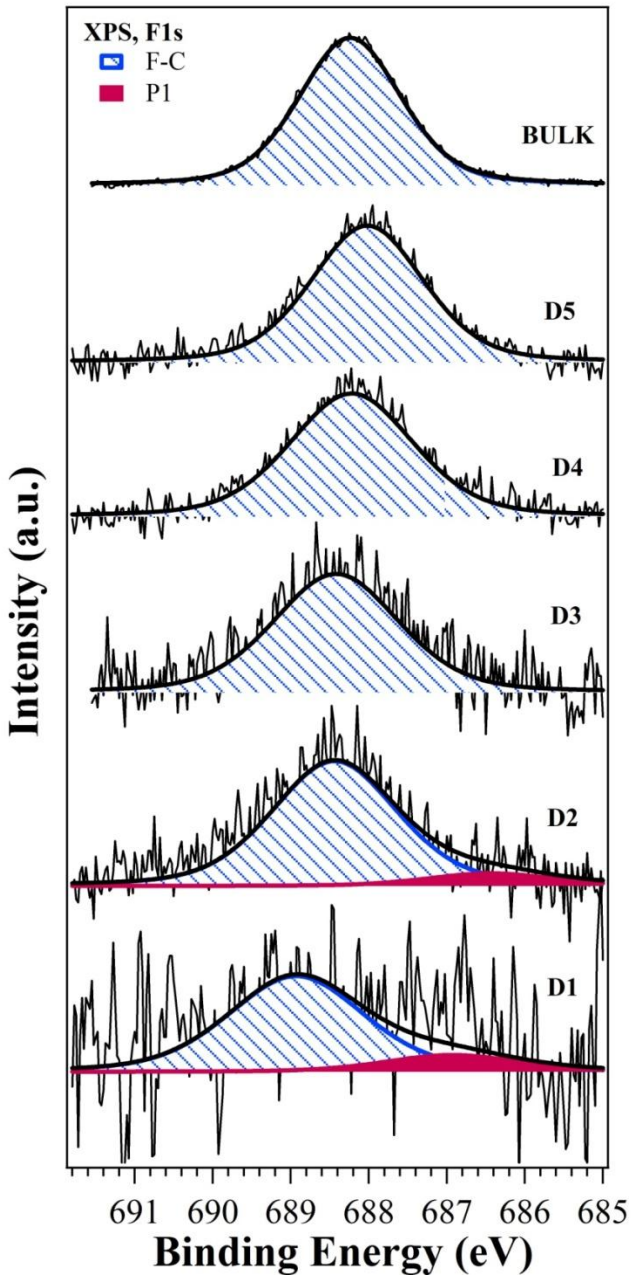

Figure 6.35: Comparison of the F1s lineshape deconvolution as function of the film coverage (Spectra normalized in height). The new P1 component is coloured in magenta.

The main peak can be straightforwardly ascribed to F-C in the phenyl rings and it is confirmed by the energy position of this peak in the bulk phase, where only this component is visible. The new contribution at lower BE, labeled as P1, is located at about 2eV from the main peak and is present (i.e., detectable) only for the two lower coverages, D1 and D2. Moreover, similarly to what obseved for C1s, also the main component shows an energy peak shift from D1 (688.93eV) to bulk (688.23eV) of about Δ = -0.07eV, reaching the maximum change in D5 (688.02eV, Δ = -0.91 eV).

It can be observed that at increasing film coverage, also the P1 contribution shifts towards lower BE from D1 (696.93eV) to D2 (696.44eV). The FWHM of the main peak at high BE decreases with the coverage from 1.89eV in D1 up to 1.56eV in the Bulk. The second contribution, instead, shows a FWHM of 1.89eV in D1 and 2.0eV in D2. The weight of D2 over the whole fluorine emission is 14.7% in D1 and 9.2% in D2.

The ratio between the intensity of the whole C1s and F1s emission and phenyl/macrocycle components are coherent for all the depositions with the theoretical expected values, as shown in Table 6.6. This once more confirms that the organic molecule integrity is not affected by SuMBD deposition approach.

	CF/F	***C_{TOT}/F***	***CF/C_{macro}***
D1	1.10	2.34	0.95
D2	1.02	2.19	0.89
D3	0.98	2.40	0.89
D4	1.02	2.14	0.94
D5	0.98	2.18	0.82
Bulk	1.01	2.11	0.95
Theoretical Values	1.00	2.20	0.83

Table 6.6: Carbon and fluorine chemical species ratio as function of the film coverage.

Regarding the N1s core level Figure 6.36 and Figure 6.37 show the N1s spectra as a function of the deposition time and the lineshape deconvolution, respectively.

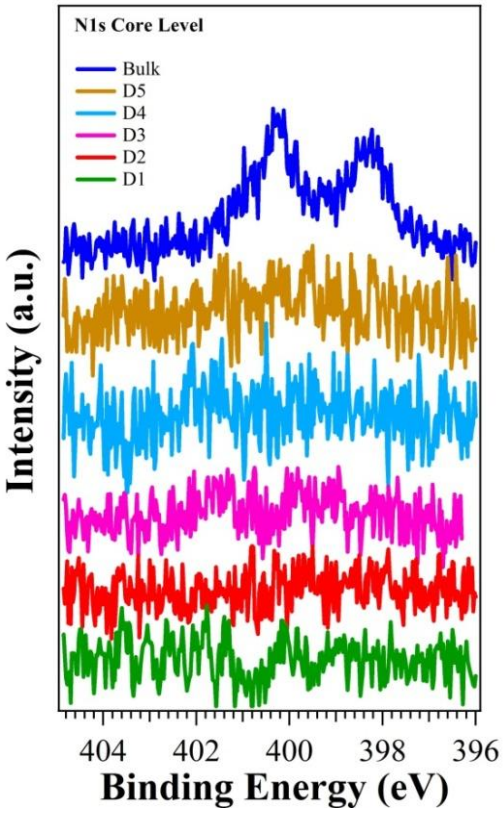

Figure 6.36: XPS N1s core level emission as a function of the $H_2TPP(F)$ film coverage.

The S/N ratio of the experimental data is very low because of the specific low intensity of the nitrogen emission from $H_2TPP(F)$, making very difficult any reliable evaluation of N1s contribution at the lower coverages. Nevertheless, the N1s peak for all coverages is well reproduced by the standard components, so that it can be argued that, whatever is happening at the interface, the nitrogens are not involved in the formation of any kind of chemical activity, within our experimental sensitivity.

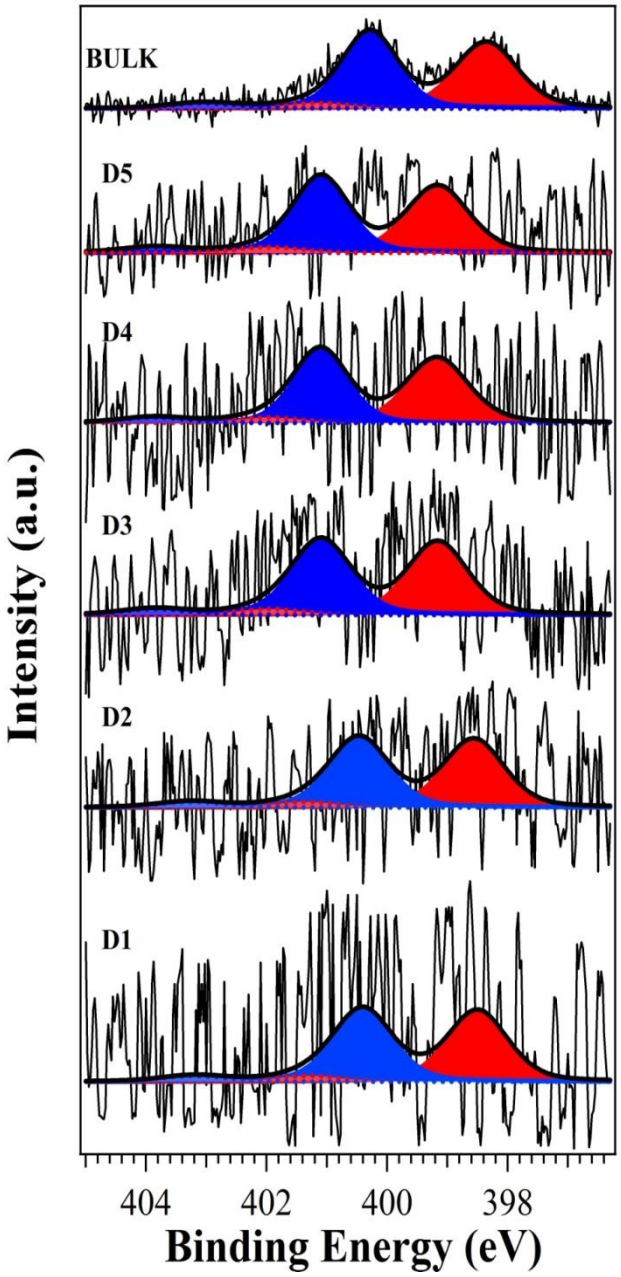

Figure 6.37: Comparison of the N1s lineshape deconvolution as function of the film coverage (Spectra normalized in height).

Let's consider now the silicon and oxygen core level analysis from the SiO_2/Si(100) substrate. In Figure 6.38 are shown O1s and Si2p core levels evolution from clean surface to D5 coverage: as can be clearly seen, no significant lineshape changes can be identified. Taking into account the very low amount of organic molecule interacting with the oxide surface, it is expected that the possible presence of new chemical species, testifying the

chemical processes at the interface, would be characterized by a very weak Si2p and/or O1s component, probably not detectable in these experimental conditions.

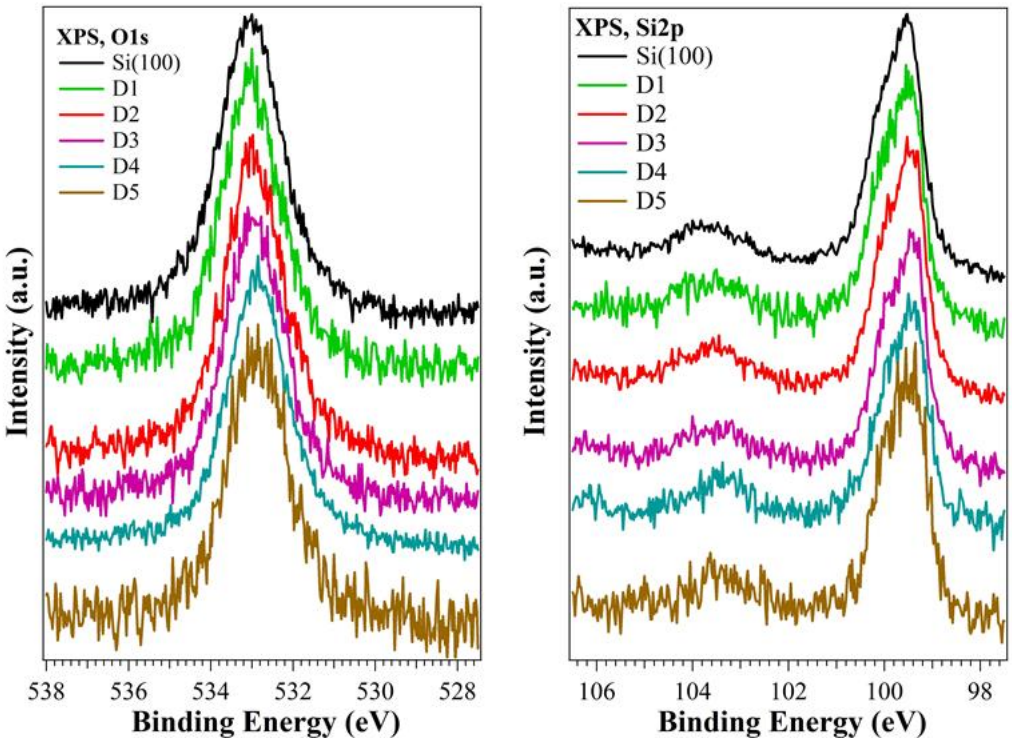

Figure 6.38: XPS O1s (on the left) and Si2p (on the right) core levels emission as a function of the $H_2TPP(F)$ film coverage (Spectra normalized in height).

So far all the characterizations have been performed in normal acceptance condition, but in order to possibly distinguish the Si and Oxy components involved in the chemical interaction at the interface aiming at increasing surface sensitivity, we have acquired the Si2p and O1s core levels at grazing acceptance geometry (Figure 6.39), performed keeping the angle between the normal to the surface and the emitted electrons at θ=70°. Figure 6.39 (panel on the right), shows that the main lineshape differences are observed for the Si2p core level, where a decrease of the band at ~99eV and an increase of the band at 104eV put in evidence the components related to the uppermost surface layer, i.e. the oxide layer having its main emission right at ~104eV. It is noteworthy we did not analyzed the photoemission signal from the $H_2TTP(F)$ molecule: in fact, while the oxide layers as a thickness of about 1.5 nm and Si2p core level is mainly dominated by the contribution

from Si in the bulk (band at ~99eV), the molecular film thickness corresponds to about 0.5 nm and thus there is no need to put in evidence a surface contribution.

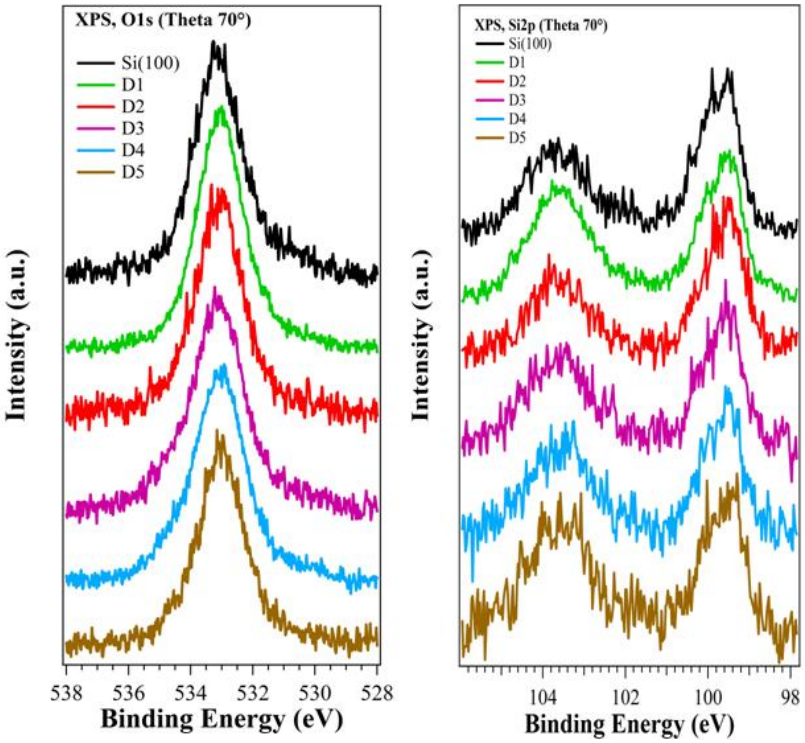

Figure 6.39: XPS O1s (on the left) and Si2p (on the right) core levels emission acquired in grazing angle (θ=70°) as a function of the $H_2TPP(F)$ film coverage (Spectra normalized in height).

Moreover, as can be clearly seen from Figure 6.39, there is a significative reduction of photoemission signals and signal-to-noise ratio, an effect that would worsen the already low intensity of C1s, N1s and F1s core levels at low film coverages.

Regarding the Si2p core level, in agreement with the literature [268], it is possible to distinguish all the components related to the different intermediate oxidation states between SiO_2 and Si. As a matter of fact (see Figure 6.40), the lineshape deconvolution of the SiO_2/Si(100) clean surface is composed of five peaks corresponding to Si^0 (99.51eV), Si^{1+} (Si_2O, 100.34eV), Si^{2+} (SiO, 100.82eV), Si^{3+} (Si_2O_3, 102.11eV) and Si^{4+} (SiO_2, 103.61eV). The composition percentage of the cleaned surface is summarized in the Table 6.7.

Si Oxidation State	BE [eV]	Composition Percentage
Si^{0}	99.51	48.4
Si^{1+} (Si_2O)	100.34	3.4
Si^{2+} (SiO)	100.82	1.0
Si^{3+} (Si_2O_3)	102.11	5.7
Si^{4+} (SiO_2)	103.61	41.5

Table 6.7: Substrate Si(111) calculated composition percentage

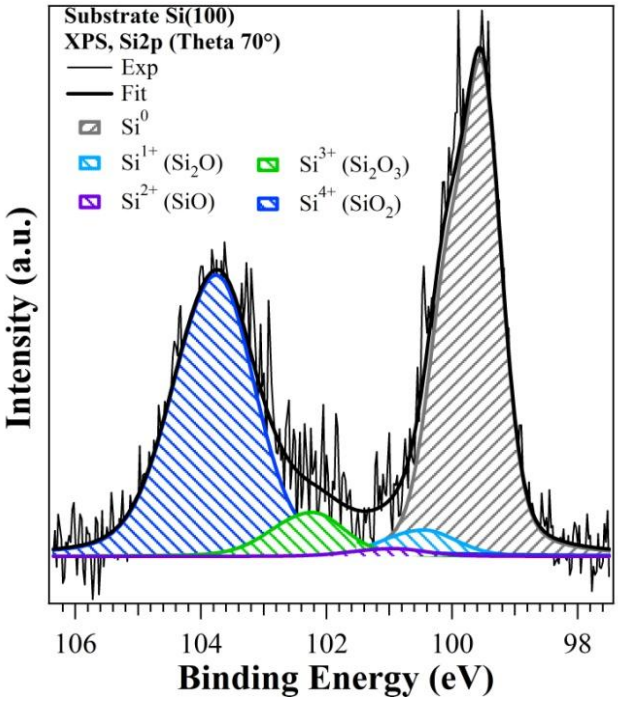

Figure 6.40: XPS Si2p lineshape deconvolution. All the oxidized species (Si_2O, SiO, Si_2O_3, SiO_2) are present.

The model used for the analysis of the Si2p clean surface core level can be effectively used also for all the surfaces with $H_2TPP(F)$ coverage (Figure 6.41), without significant differences from one surface to the other.

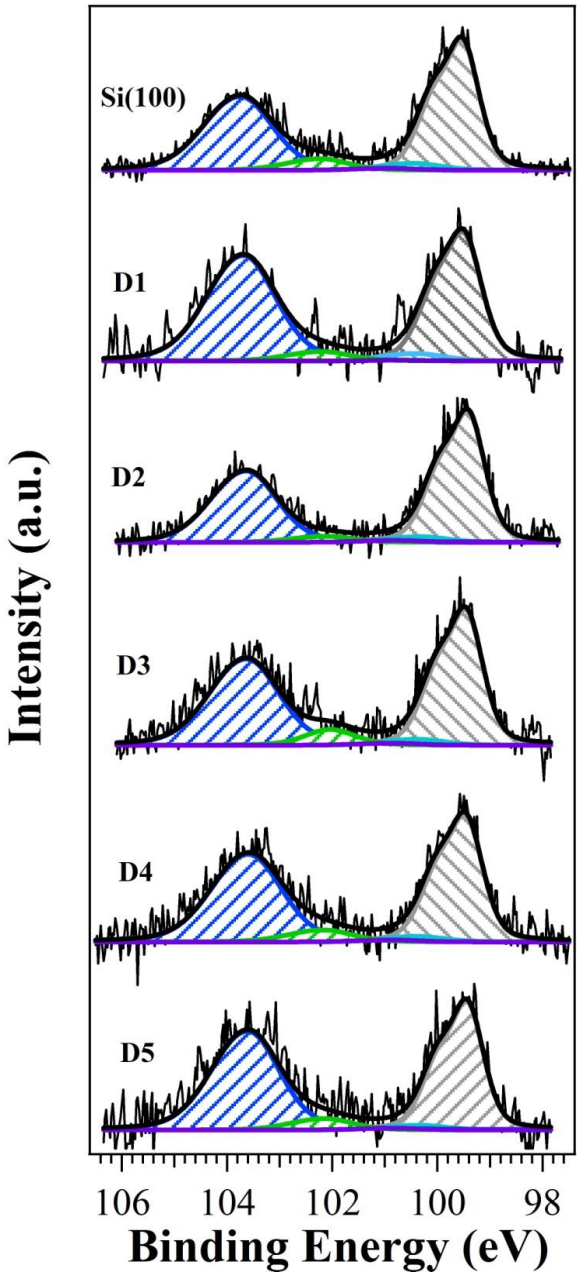

Figure 6.41: Comparison of the Si2p lineshape deconvolution as a function of the film coverage (Spectra normalized in height).

This suggests that no detectable peaks, thus other chemical species related to organic/inorganic interaction can be identified during the organic film growth. In fact, it is very hard to identify any possible new component in Si2p core level involved in the interaction at the interface. Pereira and coworkers demonstrated that it is almost impossible to distinguish Si-O, Si-F and Si-O-F contributions in Si2p core level because of the superposition of all the components at the same energies [269].

Likewise to what observed before, also Si2p emission shows an energy shift. If for Si^0 peak a small variation from clean surface (99.51eV) to D5 (99.42eV, Δ = -0.09eV) has been found, for Si^{4+} (SiO_2) a higher change has been observed. The SiO_2 component in fact exhibits a variation of Δ = -0.13eV from cleaned surface (103.61eV) to D5 (103.48eV), reaching the maximum value in D4 (Δ = -0.16eV). The FWHM of the peaks remains unchanged at the different coverages.

The O1s spectrum of the clean SiO_2/Si(100) surface, similarly to Si2p core level, shows the same components related to the different oxidation states of the substrate as displayed in Figure 6.42.

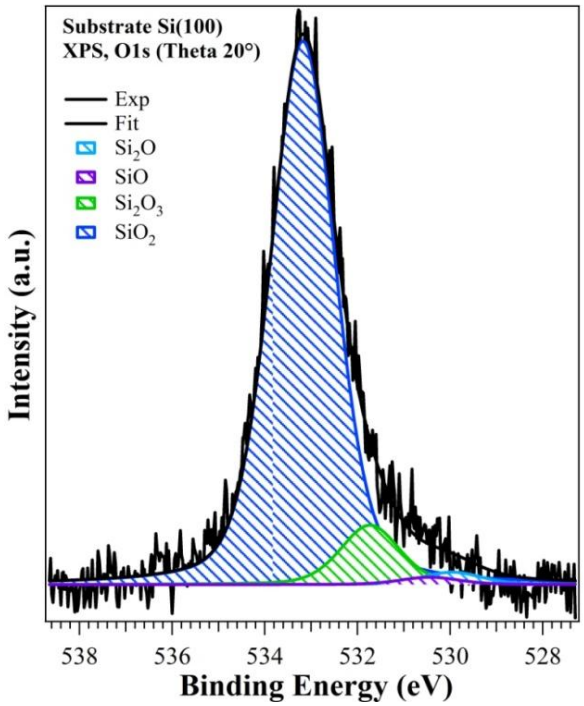

Figure 6.42: XPS O1s lineshape deconvolution. All the oxidized species (Si_2O, SiO, Si_2O_3, SiO_2) are present.

The main peak is associated to SiO_2 (533.18eV) and it is possible to distinguish the other contributions at low BE such as Si_2O_3 at 531.73eV, SiO at 530.44eV and Si_2O at 529.95eV. During the $H_2TPP(F)$ film growth the model used for the O1s clean surface is no longer adeguate and it is necessary to introduce a further component, named as P1, at about 534.4eV. The O1s spectra evolution is illustrated in Figure 6.43.

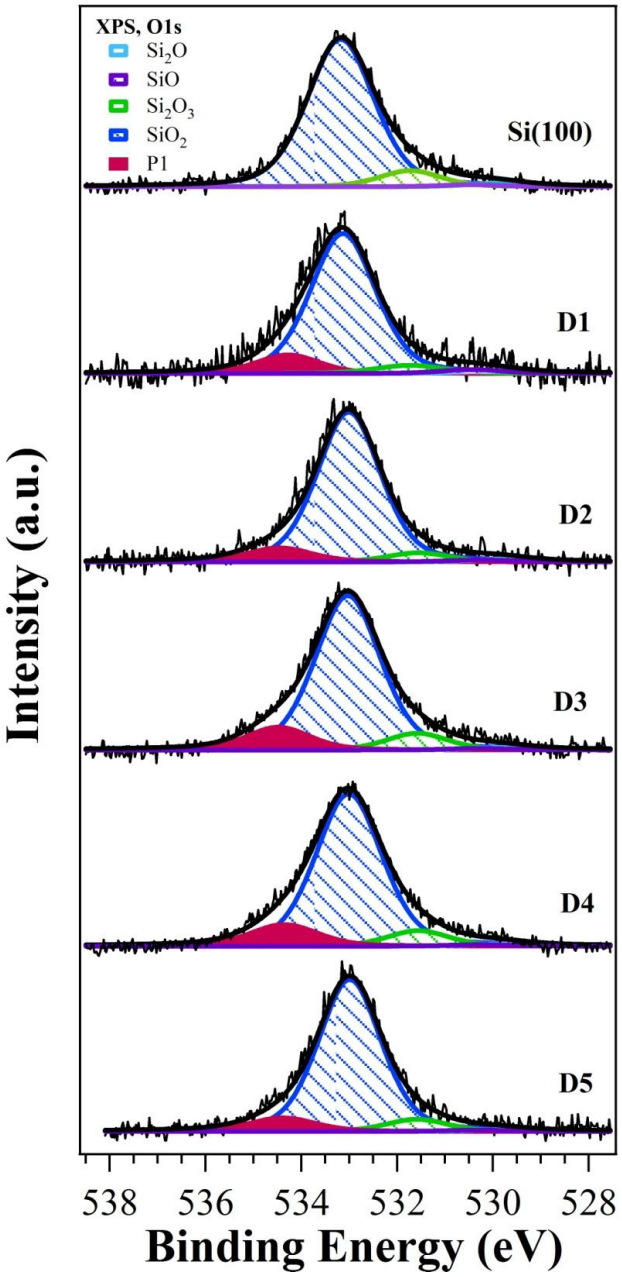

Figure 6.43: Comparison of the O1s lineshape deconvolution as function of the film coverage (Spectra normalized in height). The new P1 component is coloured in magenta.

The P1 peak represents about 5-10% of the total oxygen signal at each deposition time and it is located at about 1.5eV from the main peak of the SiO_2. This distance is shortened at the highest coatings, becoming 1.4eV at D4 and D5. If we evaluate the absolute intensity of the O1s SiO_2 peak and that of the new P1 component, as shown in Figure 6.44 (values

for bulk film have not been measured), while the former is characterized by a constant decrease, the latter shows a slight increase up to D5.

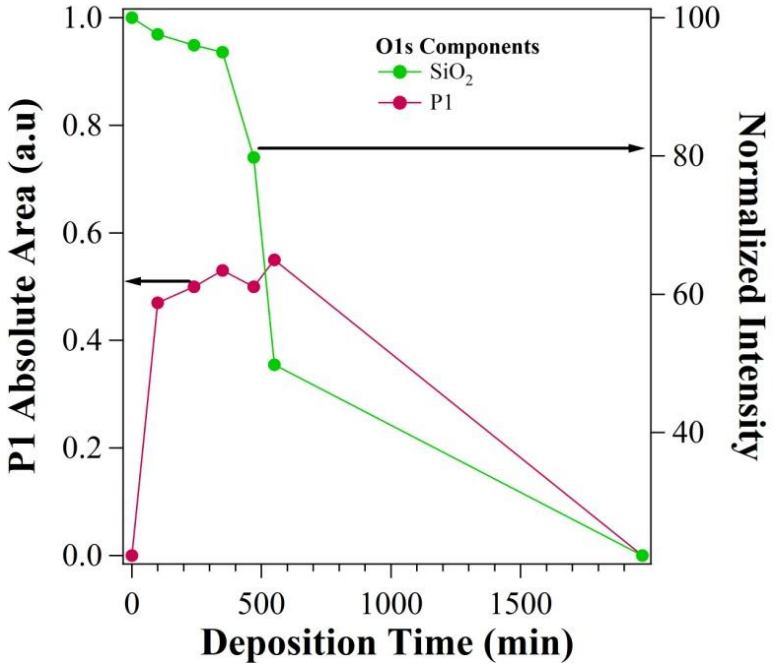

Figure 6.44: Evolution of O1s components (measured in grazing acceptance) vs. deposition time. Normalized SiO_2 component (green curve, right axis) and absolute P1 peak area (red curve, left axis).

This suggests that P1 is related to the formation of the organic/inorganic interface, that reaches a maximum around D4/D5 deposition, when the quick growth starts. This could be the reason at the origin of the (relatively) high P1 area percentage over the whole O1s emission peak at all deposition times. Due to the presence of several components in the O1s peak, as well as the lower S/N ratio related to grazing acceptance XPS analysis, it is difficult to say which oxygen chemical species gives origin to the new P1, however its intensity, being at least comparable or higher than that of SiO, Si_2O and Si_2O_3, suggests that only SiO_2 can be related to the new peak. P1 intensity is high from the early growth stages and increase slightly vs. deposition time, an evidence of an evolving organic/inorganic interface but being well developed and expanded right from D1. Differently, emission from SiO_2 starts to decrease significantly at D4 due to the onset of thicker organic layer growth, an event occurring before the observed deposition times in Figure 6.29 and Figure 6.31. This can be easily explained in terms of the higher surface

sensitivity we have at grazing XPS acceptance, better showing the evolution of the interface formation. On these basis, we can argue that at least about 5-10% of the oxide layer surface is interested by the interaction with the porphyrin, and that D4 rather than D5 represents the onset of the fast $H_2TTP(F)$ film growth.

In Figure 6.45 are shown all the BE shifts calculated for photoemitted peaks from silicon (Si^0 and SiO_2) and oxygen (SiO_2) in grazing angle acceptance, fluorine (F-C contribution) and carbon (C-F component) in normal acceptance as a function of the deposition time.

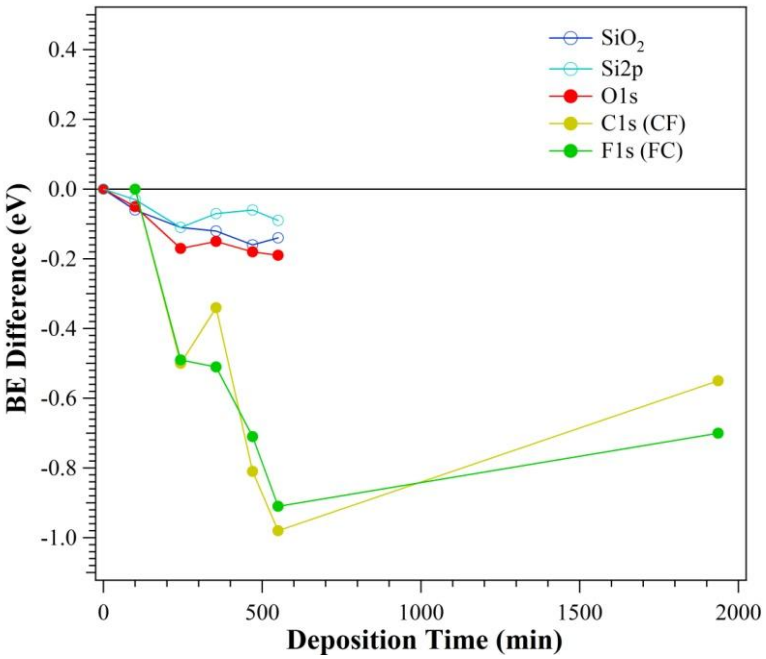

Figure 6.45: Position energy shift of SiO_2, Si^0, O1s main peak (SiO_2), C-F and F-C components compared to clean surface (Si, O) and D1 film (C, F).

The energy shift of the O1s main peak associated to SiO_2 is comparable to that observed in the corresponding component in Si2p core level. Both silicon and oxygen energy shifts represent an evidence of the formation of a weak dipole or charge transfer involving the organic molecule at the interface, that will be better described in the following. Regarding the contributions from the substrate, the values related to the bulk phase are not reported since the signal of Si2p and O1s was too low to be acquired in grazing acceptance with a low S/N ratio.

The peak energy from C1s (C-F) and F1s (F-C) show a very important shift, higher than for substrate signals, suggesting that the whole fluorinated phenyl rings are directly involved in the interaction at the interface, i.e. carbon over fluorine. This evidence is confirmed by the presence of a new component in the F1s core level, which suggests the occurring of an interaction at the interface, weak if we consider the relative peak weight but strong in terms of energy shifts. On the other hand, C1s does not show any new component and chemical reactivity is testified only by the same energy shifts of F1s. But this is expected, since considering the F1s P1 intensity, we should observe a related C1s C-P1 peak having such a low area that would become not detectable (or distinguishable) in our experimental conditions.

On the other hand, O1s is characterized by a new peak (P1) present at each deposition time but not in the clean surface, and located in the topmost oxide layers, as it has been revealed only by XPS analysis in grazing acceptance. Thus, this is the inorganic counterpart of F1s P1 new peak it can be associated to the chemical interaction between the H_2TPP(F) organic molecule and the inorganic surface. C1s, F1s and O1s core level analysis does not show the clear evidence of the formation of covalent bonds, suggesting that the interaction could be different. Covalent interaction would require the rupture of the C-F bond in the phenyl ring, an event that is hard to believe considering the strength of this bond, thus something else is happening. Furthermore, all XPS data suggest that the molecule is still intact, no loss of fluorine, carbon or nitrogen chemical species during the whole film growth, thus no modification occurred in the phenyl rings. O1s and F1s new peaks show an energy distance with respect to the main component of about +2.0 and -1.5 eV, very high values but similar, that can be explained in terms of charge transfer from the oxide layer to the fluorinated phenyl rings. Even though it is difficult to quantify such a charge transfer, the high energy distance of new peaks from the unperturbed core levels, as well as the high energy shift of the latter vs. deposition time, suggest anything but a negligible process involving a large substrate surface area. We can suppose that fluorine atoms interact with defects on the silicon oxide surface, with their electron withdrawing property collecting electrons from donor sites, such as the well known -OH^- hydroxyl ion [270]. This would lead to the observed phenomena, but further evidences are necessary to confirm such an hypothesis.

UPS characterization have been carried and the valence band as function of the coverage is illustrated in Figure 6.46 (panel on the left), where the clean silicon oxide surface spectrum is also shown for comparison.

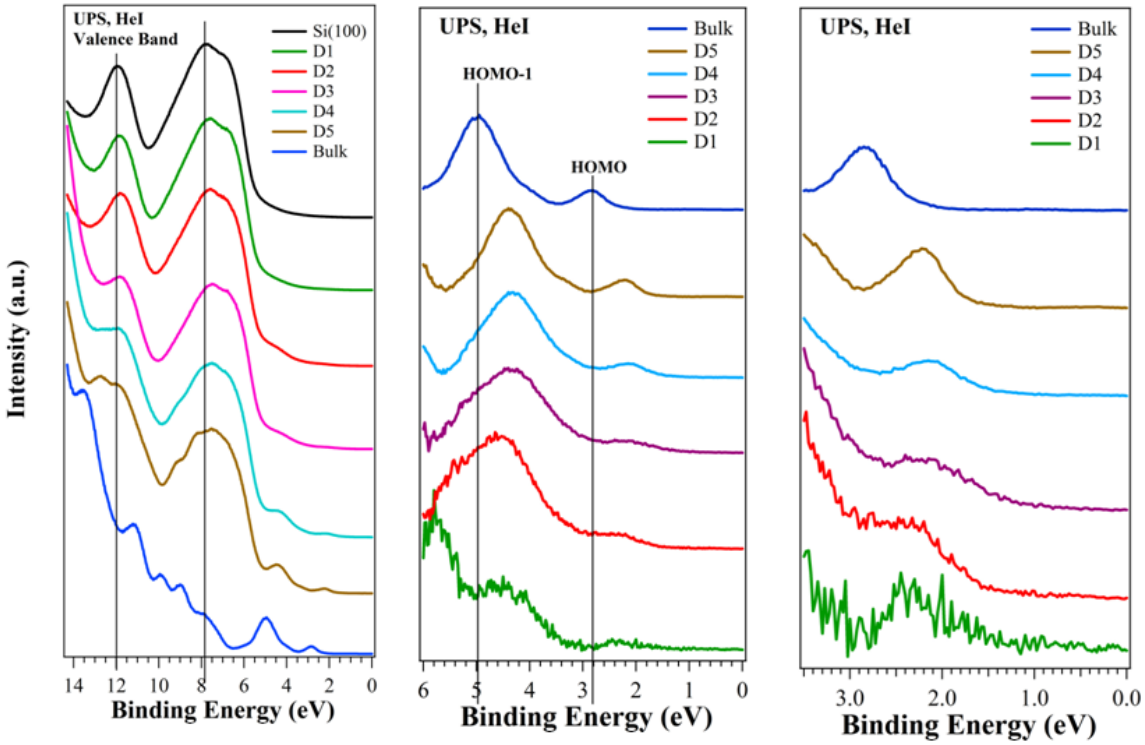

Figure 6.46: UPS spectra as function of the film coverage: valence bands (on the left) and detailed view of the HOMO region (in the middle) (Spectra normalized in height). In the right is shown a magnification of the HOMO bands.

With the exception of bulk phase, the valence bands lineshape is dominated by the O2p level hybridized band of the oxide surface in the 6-10eV BE region. In the 7-13eV BE range it is possible to observe the increasing contributions due to π and σ orbitals from phenyl rings C atoms as well as from σ orbitals from nitrogens [271,272,273], that are visible above all in the bulk phase. It is noteworthy the small but detectable energy shift towards lower BEs of the SiO_2 bands, reaching a maximum of -0.23eV at D3 (see vertical lines in Figure 6.46, left panel). The thick molecular film (labelled Bulk) is characterized by the known features and bands previously observed (see paragraph 6.7), in particular in the 0-6eV region we can identify the HOMO and HOMO-1 peaks at 2.5 and 4.5eV. Concerning the other spectra, the organic molecular features in the HOMO-HOMO-1

region are not so visible because of both the very low organic coverage and the masking effect by the steep substrate signal. In order to put them in evidence, the clean substrate spectrum has been subtracted to the other spectra, as displayed in the detail of the region between 0-6 eV in the middle and right panels of Figure 6.46. The intrinsic difficulties and possibility to introduce artifacts in this kind of analysis are evident, so we prefer to put our attention only on the HOMO region, disregarding the HOMO-1 band which analysis we consider less reliable after the subtraction procedure.

The organic features become more intense with the coverage and it is visible a clear shift and a complex width evolution of the HOMO band from D1 to the bulk. In particular, the zoom in the HOMO region of Figure 6.46 (left panel) shows an asymmetric HOMO right from D1, with a maximum broadening at D3/D4 that gradually reduces leading to a symmetric and well defined band for the thick bulk film. These are evidences that the chemical-physical properties at the interface change with the film coverage and they are quite different with respect to those of the bulk.

The SECO (Secondary Electron Cut Off) region is illustrated in Figure 6.47 and its trend clearly show the formation of dipoles at the interface. The dipole intensity changes with the film coverage in fact if D1 and D2 samples show an energy shift with respect to the substrate of -0.15 and -0.24eV, respectively, this value increases up to D4 (about Δ=-0.36eV) and then slightly decreases in D5. The SECO energy position in the bulk, instead, is very similar to that of the Si(100) substrate (Δ=-0.05eV).

Starting from the information acquired from the valence band spectra, we could calculate some important parameters for each analyzed system, such as the ionization potential (IP), the work function (WF), the HOMO centroid and leading edge energy and the expected LUMO position from the theoretical band gap [265].

Analysis performed in previous works have suggested a H_2TPP(F) band gap of about 4eV [274], a value not so far from the observed 3.2 eV in the C1s analysis (see paragraph 6.7), so that it is possible to develop a scheme of the energy levels starting from the SiO_2/Si(100) surface up to the bulk organic film summarizing all analyzed systems, as shown in Figure 6.48.

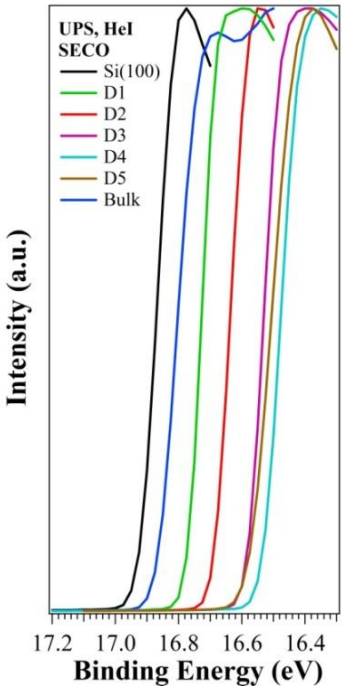

Figure 6.47: UPS spectra as function of the film coverage: SECO region.

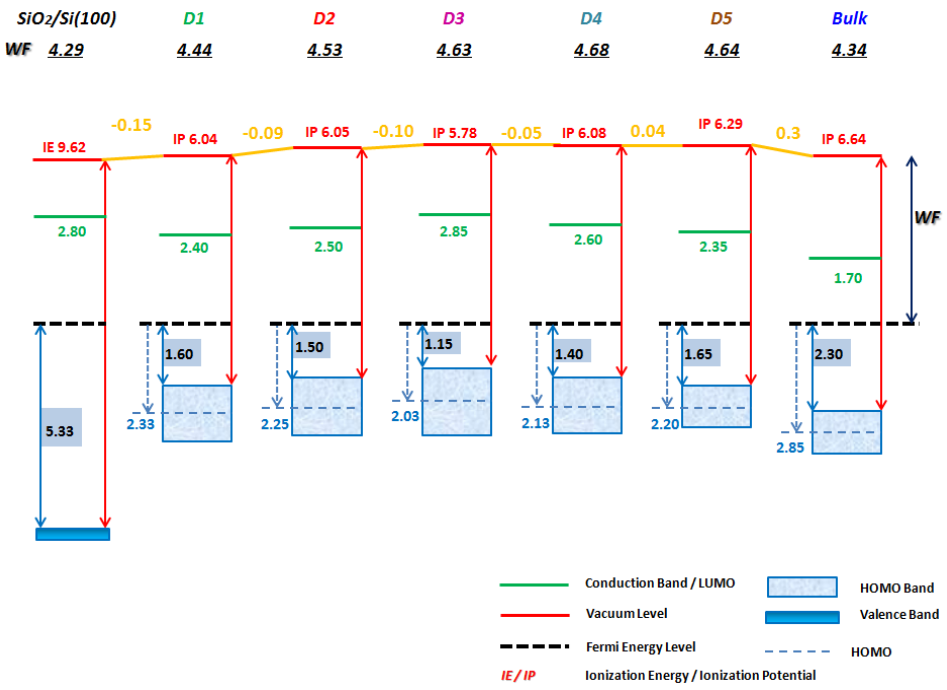

Figure 6.48: Energy level scheme of Si(100) substrate, H_2TPP(F) thick film and D1, D2, D3, D4, D5 samples. Organic film IP, WF, and the extrapolated LUMO position are displayed. The HOMO band and centroid position are also illustrated. All values are in eV.

Surprisingly, Si(100) substrate and H_2TPP(F) bulk (i.e., the two non interacting inorganic and organic systems) show very similar WF values, so that we would expect no significant variations during film growth, i.e. physisorption. Indeed, this has been observed for the growth by SuMBD at low molecular precursor KE, but in case of the large KE value of 25eV it is clear we are dealing with far more complex processes.

The native silicon oxide layer is characterized by a large band gap (>8eV), that is a strong insulating character. Nonetheless, being the Fermi level significantly closer to the conduction rather than to the valence band, it can be considered a n-type semiconductor, with the presence of electron donor levels near the Fermi level that are due to defects spatially located in the most external surface layer [270,275].

IP seems to be almost unchanged from D1 to D5 apart from the D3 value, that is however influenced by the particularly large width and broad shape of the HOMO band. On the other hand, WF shows a maximum at D3/D4. WF increase from the clean inorganic surface up to D4 film and then decrease down to the thick film value.

To go deeper in the interpretation of the level scheme in Figure 6.48, let we compare the kinetic energy (and not binding energy) shifts of the XPS and UPS signals coming from the substrate with those of WF, using the clean surface values as a reference. As can be seen in Figure 6.49, O1s, Si2p emitted from oxide layer and SiO_2 valence band features show similar trends and values (within errors), being slightly lower for bulk (Si^0).

This can be expected if we think all processes are related to the organic/inorganic interface, not involving bulk silicon. Kinetic energy shifts of all components from the native silicon oxide layer shows the same trend, increasing from D1 up to D3 and then being almost stable. This is a fingerprint of formation of band bending in the inorganic surface and, given the total WF shift, the difference with the band bending can be attributed to formation of surface dipole at the interface [57,276].

This suggests that the band bending increases from D1 up to D3, then seems stable at a value of about +0.2eV, while a dipole of about 0.08eV is present for D1 and D2, then increases reaching about 0.2eV at D4, then slightly decreases. Considering that H_2TTP(F) HOMO feature presents large broadening from D1 to D3, a fingerprint of charge transfer from the inorganic surface, we can properly suppose we are dealing with this type of process producing a maximum shift of +0.2eV up to D3/D4 in the inorganic photoemission

features and a band bending in the oxide VB. Comparing with results for the oxygen-fluorine interaction, this would be a further evidence of a charge transfer mechanism.

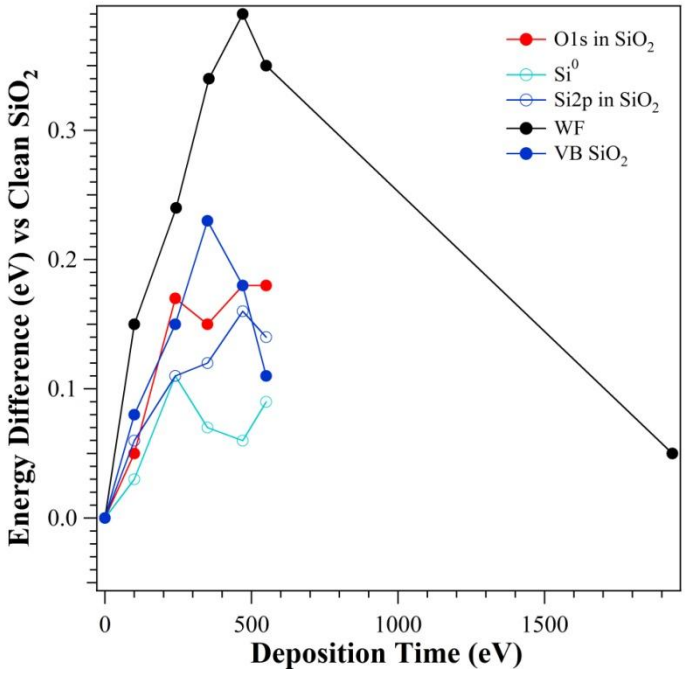

Figure 6.49: Energy shifts of different photoemission features related to the substrate and of work function vs the deposition time. Values are referred to those of clean sample.

Electron capture in fluorine atoms scattering on MgO(100) surface through charge exchange with oxygen anions, as well as fluorine anions electron loss processes with metal cations has been reported [277], but in our case we are dealing with different collision geometries. Being the oxide layer an insulator with surface defects, it is feasible an electron transfer from the related electron donor levels to fluorine. The process has not been observed in SuMBD experiments at lower H_2TTP(F) KE of 0.5eV [35] and is thus enhanced by the higher energy value used here, enabling a different chemical interaction not allowed in physisorption processes. It is worth mentioning the absence of possible electron tunneling effects from the underlying n-doped silicon bulk, an effect considered unlikely for the CuPc/SiO_2/Si(100) n/p doped that has a lower HOMO-LUMO band gap (2.3eV instead of 4eV) and thus fully negligible in our system [278]. For the case of organics on metals , when inorganic WF is lower than the organic IP, probability of charge transfer from metal to the LUMO is high [157]: in our case, likening the n-doped insulator

to a metal, the charge transfer could be reasonable. Moreover, comparing D1/D2/D3 with bulk film HOMO-LUMO levels, at the interface there is a shifts towards the Fermi level, as indeed occurs in the case of electron transfer from the inorganic to the organic LUMO [276].

We do observe band bending in the inorganic, but it is small (+0.2eV) and thus involving low carrier densities, in agreement with the proposed scheme of a n-doped silicon oxide layer due to surface defects. On the contrary, we do not clearly observe the HOMO'-LUMO' features, but it has been shown they cannot be detected in case of band bending of +0.2eV [57], while they are visible for a value of +0.7eV. It is worth noting that the electron excess on the organic molecule is probably at the origin of the observed strong decrease of the IP from D1 to D4, with an overall higher probability to extract electrons from the molecule itself due to the higher electron density.

On these basis, we finally claim that there is an electron transfer from a donor level in the defected silicon oxide layer to the organic molecule through the fluorine atoms. This process leads to formation of an accumulation layer of holes in the substrates bands and of electrons in the molecules at the interface, with the consequent band bending in the insulating material [58]. The process evolves from D1 up to D4, and involves only a single layer of molecules at the interface, as close vicinity between oxygen and fluorine atoms is required to achieve charge transfer. Having in mind the proposed formation of an organic wetting layer, necessary to enable the quick growth in D5, we think this is the case. As the LUMO has a significant contribution from fluorine atoms unoccupied molecular orbitals, we can state that it is populated leading to the HOMO'-LUMO' rearrangement that we identify in the broadening of the HOMO peak, that has a maximum in D3.

Being involved directly oxygen (from silicon oxide) and fluorine (from the molecule) atoms at the interface, the charge transfer is highly localized and occurs only on molecules in contact with the inorganic on the surface. If we consider that in D1, about 15% of the F1s emission is due to fluorine atoms involved in the interaction mechanism, this means that about 3 atoms per molecule experience the charge transfer. It is difficult to suppose the observed electron excess confined on three fluorines in only one phenyl, more reliable is a charge distribution over four or three rings. This is in agreement with the C1s and F1s energy shifts that indeed involve the whole molecule, phenyls and macrocycle, suggesting a charge distribution on a single molecule affecting all organic molecular species and

properties, as suggested also from the decrease in the IP value. If three phenyls interacts with the inorganic surface this means that the molecule is laying on the surface, an effect already seen for porphyrins on metal deposition [279], but further comments would lead to pure speculations.

Having in mind the supposed formation of a wetting layer necessary for the quick growth of the organic layer, the overall picture is even more complex, with formation of a first organic/inorganic interface that rapidly evolves in something different.

The formation of a wetting layer related to the charge transfer process at the interface up to D3, D4 is in good agreement with the results found for the P1 peak in O1s core level, that is present for all films, while the new P1 component in F1s core level is detectable only for D1 and D2 and decrease its weight at increasing coverage. This could be due to the presence of different types of H_2TTP(F) molecules, not experiencing the charge transfer from the inorganic because deposited on the wetting layer, thus masking contributions from the layer below. Also the maximum HOMO broadening is achieved at D3 and not D4, suggesting once more presence of a second or more layers of molecules reducing signal from the wetting layer. Considering the particular type of growth, it is likely we are dealing with islands growth on the wetting layer right from D2, D3.

Such a hypothesis becomes true if we analyze the WF trend. As suggested in several reviews [57, 276], the difference between the observed BE (band bending) and the WF shifts is due to the presence of a dipole at the interface, that is present from the early growth stages and increases from D3 to D5. Typically, when the inorganic/organic interface is completed, a plateau for the WF is achieved and both band bending and surface dipole are constant. Our results are very different, WF shows a maximum at D4 than decreases towards the porphyrin thick film value. A new evolution of the growth mechanisms must be hypothesized, involving not only the inorganic/organic interface, which is almost completed in D4, but also an organic/organic one lying in-between the first silicon oxide functionalizing H_2TTP(F) layer and the layers of physisorbed molecules in the thick film. Such an intermolecular interface would be the source of the surface dipole increase from D3 to D5.

At a glance, from Figure 6.29, the sticking coefficient in the 0-400 min deposition time is about eight time lower than in the 400-800 min region, so once the wetting layer is complete, growth is quick and sudden. What could happen is that, on those inorganic

surface regions where the wetting layer is almost complete, there the sticking coefficient for incoming molecules is by far higher and the growth of new layers is more probable. Considering the very long time required to complete the first organic/inorganic interface, island growth is for sure highly probable.

If the proposed mechanism is correct, we should find its fingerprints from the evolution of $H_2TTP(F)$ related chemical species and properties. To this end, it can be useful analyze the evolution of the C1s, F1s, HOMO kinetic energies and system WF vs. the deposition time but referring to the values in the thick molecular film (bulk) (Figure 6.50), similarly to what done for inorganics signals (see Figure 6.49) where values reference was the clean substrate. The two core levels trend is different to that of HOMO, and all are different to that of WF. The presence of core level shifts is typically associated to formation of band bending in inorganics, as stated before, while in case of absence of band structure as in organic π-conjugated molecules we should rather observe the formation of an accumulation (or depletion) layer, whose thickness can be also very high. The proposed approach for inorganics to evaluate presence of band bending and surface dipoles has never been applied for the organic counterpart [57,250], nor will be in our system.

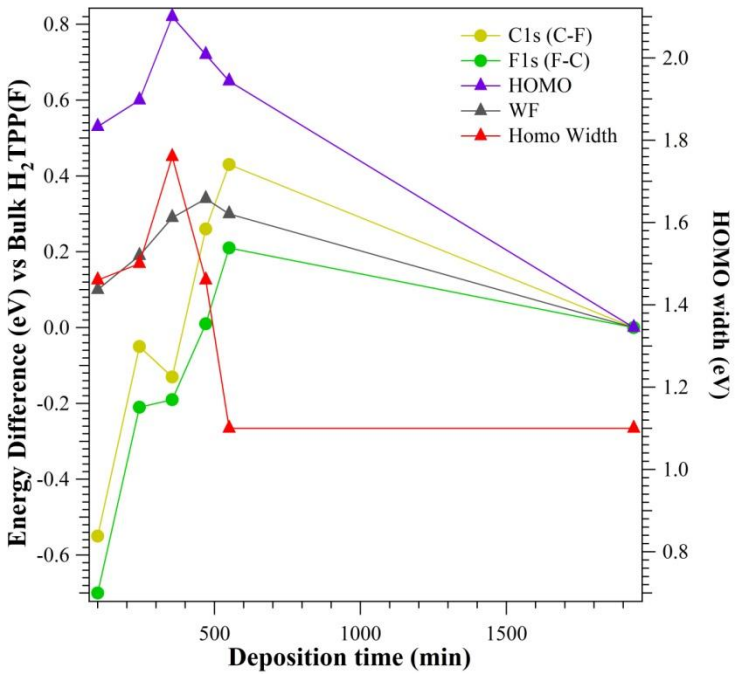

Figure 6.50: Energy shifts of different photoemission features related to the $H_2TTP(F)$ molecule and of work function vs the deposition time. Values are refereed to those of a thick molecular film.

With respect to bulk values, WF is always higher and this leads to lower C1s and F1s kinetic energies but in D4 and D5, HOMO kinetic energy instead is always higher than in bulk, probably better reflecting the different interaction processes occurring in the growing film.

In case of a charge transfer process involving only organic molecules, fingerprints should be present also in the H_2TTP(F) molecular orbitals density of states. If, previously, a +0.2eV band bending in the inorganic gave rise to an enlargement of the HOMO band, we can expect something more intense given the observed higher core level shifts.

As shown in Figure 6.50, the HOMO width vs. deposition time is characterized by a trend similar to that of the HOMO energy: this means that its centroid energy value is very influenced by its shape and broadening, at D3 being respectively highly asymmetric and 60% higher than in the bulk film. Having in mind that charge transfer from the inorganic surface is almost completed in D3, the lower HOMO width in D4 and D5, comparable to that of bulk film, suggests the onset of some new process involving only organic molecules but unlikely charge transfer among them.

The answer can be achieved comparing the D5 and bulk film electronic levels. Bulk formation is characterized by a surface dipole of +0.3eV, but the +0.7eV energy difference of HOMO in D5 still requires presence of band bending, let we say a depletion layer (using common jargon for inorganics). This means there is presence of positive charges in D5 whose excess must be balanced by a band bending from D5 to bulk film. The process of charge compensation is then complete when also IP value achieve its natural value. The presence of layers of positive charges can be intuitive if we think to the excess of negative charges in the wetting layer: the first layers interfacing it will try to balance such an excess. However, it is difficult to define where those positive charges are brought. The very high energy differences we observe with respect to the bulk film values suggest occurrence of intense processes. For a charge transfer process it is not possible to define the chemical species involved, and this seems strange since we observe significant energy shifts of the C1s and F1s core levels, higher than those of the inorganic counterpart in the functionalizing wetting layer. A possible reason could be that we are not dealing with charge transfer but the growth of a film showing a different molecular arrangement, structural order, as variation in WF has been widely reported in such case [280,281].

Moreover, in case of strong WF changes for SAM on metals, a sort of self-rearrangement has been observed [282,283].

With this scheme, the first wetting layer would be followed by formation of a second (or more) one, i.e. islands where molecular spatial rearrangement occurs leading to a WF change and positive charge compensation of the electron excess at the interface. During completion of the first functionalizing layer, as soon as a minimum nanometric surface area is properly covered the growth of further layers can start in these small and selected regions, being the sticking coefficient eight time higher than for the wetting layer. Probably, also in D2 and D3 there is formation of islands with high aspect ratio, but when the first functionalizing layer is complete, a far more efficient growth starts.

In summary, such a complex charge distribution during the film growth can lead to the observed peculiar growth kinetics, C1s and F1s shifts as well as HOMO energies so different from that of the bulk porphyrin. While the first wetting layer is very likely a single layer, the growth mechanisms of the other layers require formation of islands growing in area and thickness. Moreover, the electron charge excess in the wetting layer leads to the formation of a positive charge compensation thanks to a different structural rearrangement of the molecules.

6.7.2 *Ex-situ* analysis

A series of H_2TPP(F) depositions on Si(111)/SiO_2 planar surface at 100, 240, 350, 470, 550 and 2000 minutes, similarly to those analyzed by XPS and UPS, has been prepared for ex-situ characterization. AFM and microfluorescence have been carried out by Prof. Cristofolini group in Parma University, as described in paragraphs 3.6.3 and 3.6.6.

Figure 6.51 shows the AFM images for the D1, D2 and Bulk samples: film height in D1 has been normalized at 10 nm while in the other are normalized at 70 nm, and the topography is related to an area of 10x10 μm.

These analysis give an indication about the morphology of H_2TPP(F) films, showing the presence of islands which become wider and higher with the deposition time. Indeed, if D1 sample is mainly flat, the islands become visible only in D2 and the surface area covered by the islands increases with the deposition time, whereas their average height remains

constant at about 40 nm. It is interesting to observe that in the bulk phase there is not a complete and uniform coverage of the substrate, in agreement with the final XPS intensity reduction of the substrate (different from zero) observed in the growth kinetic (see Figure 6.29).

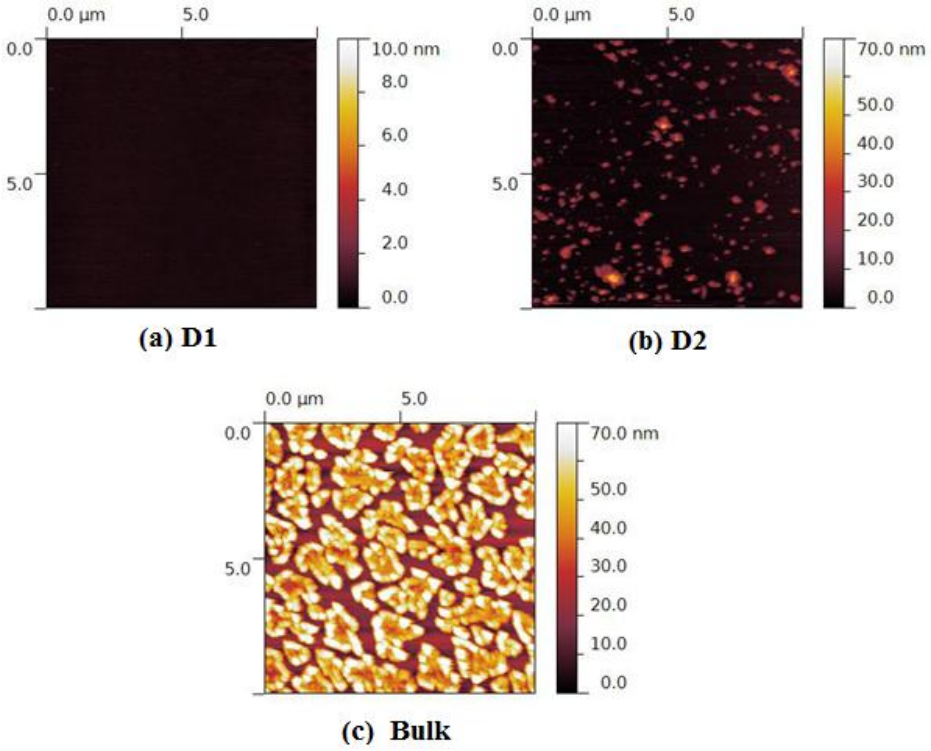

Figure 6.51: AFM images of D1 (a), D2 (b) and Bulk (c)

The microfluorescence analysis (photon energy 473 nm) has been carried out both on islands and between them (flat zone), providing very important information. In Figure 6.52 (top panel) the D1 and D2 spectra of the flat zones between islands are shown (blue and red lines, respectively), in comparison with that of H_2TPP(F) powder (bulk crystal) taken as reference (black line).

The spectra of the organic molecules deposited onto the planar surface are different with respect to the solid state phase, showing only a peak in the region between 650-670 nm but not the second one at about 710 nm. The real intensity of the two depositions spectra, not normalized in height, is displayed in the bottom panel in Figure 6.52: D2 is slightly more intense with respect D1 according to the higher amount of material deposited at that time. These results suggest the presence of an organic wetting layer that is formed from the first

step of deposition at D1 and is almost completed in D2. It is possible to exclude that this signal is related to the substrate since its signal has been opportunely considered and subtracted.

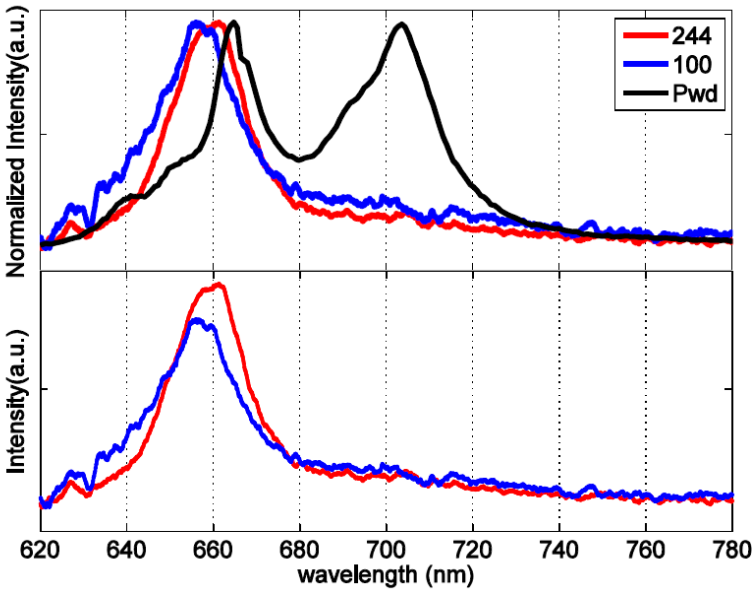

Figure 6.52: Microfluorescence spectra (normalized in height) acquired between islands (flat zones) in D1 and D2 samples (blue and red lines, respectively) compared with H_2TPP(F) powders (panel in the top). The panel in the bottom shows the comparison of the same spectra not normalized in height.

Moreover, comparing the fluorescence spectrum of the islands and the flat zone in D2, as shown in Figure 6.53, it is evident that they have a different shape: the spectrum acquired on the island (green line) is much more similar to that of the porphyrin powder (black line), showing the two components at about 663 nm and 705 nm, differently from the signal in the flat zone (red line). The panel in the bottom of Figure 6.53 shows a comparison of the spectra not normalized in height, showing that the signal from the islands is higher with respect to the flat zones, thus the organic material quantity is larger in the islands, as expected.

The difference between the spectra observed in the islands and in the flat zone is a clear indication of the presence of two different molecular organization. In agreement with the hypothesis described in paragraph 6.7.1, the flat zone can be related to the wetting layer

experiencing the charge transfer from the inorganic surface: the electron excess on the phenyls rings could be responsible of the different fluorescence spectrum observed in the flat zone with respect to the island one and the H_2TTP(F) powders. At increasing coverage, the islands formation occur, so that the organic molecules prefer to deposit on them giving rise to structures characterized by a 40 nm height as observed in AFM analysis.

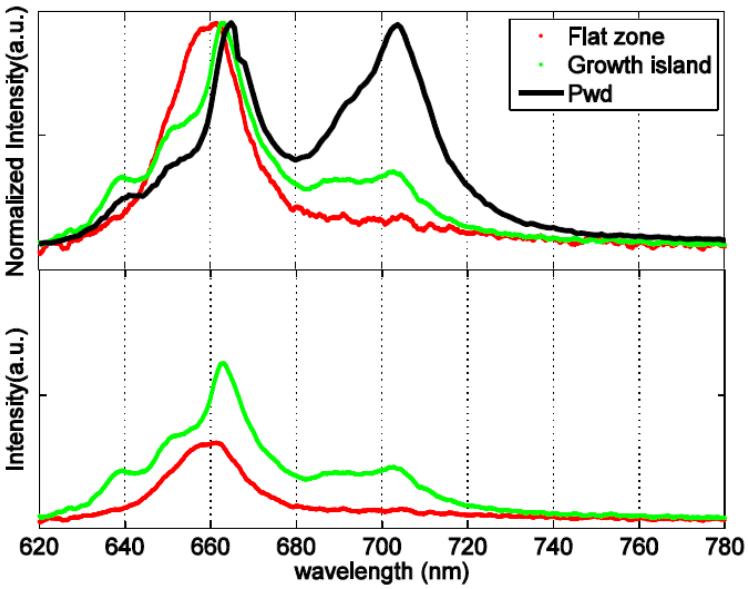

Figure 6.53: D2 microfluorescence spectra acquired on the islands (green line) and on the flat zone (red line), compared with that of a H_2TPP(F) bulk crystal (black line), normalized in height. In the panel in the bottom is shown the comparison of the spectra in the islands and flat zone not normalized in height.

Increasing the deposition time the spectra for D4, D5 and Bulk, have been acquired only on the islands because of their spread which does not allow to focalize the laser spot only in a flat zone. Spectra show the same shape and increase in intensity with the deposition time (Figure 6.54). The panel in the bottom shows the comparison of the spectra not normalized in height, showing the increase of the signal with the deposition time.

These results are completely in agreement with the proposed growth scheme, with a wetting layer in D1 and D2 with H2TTP(F) molecules showing different electronic properties, and with formation of small islands that starts right from D2, as supposed

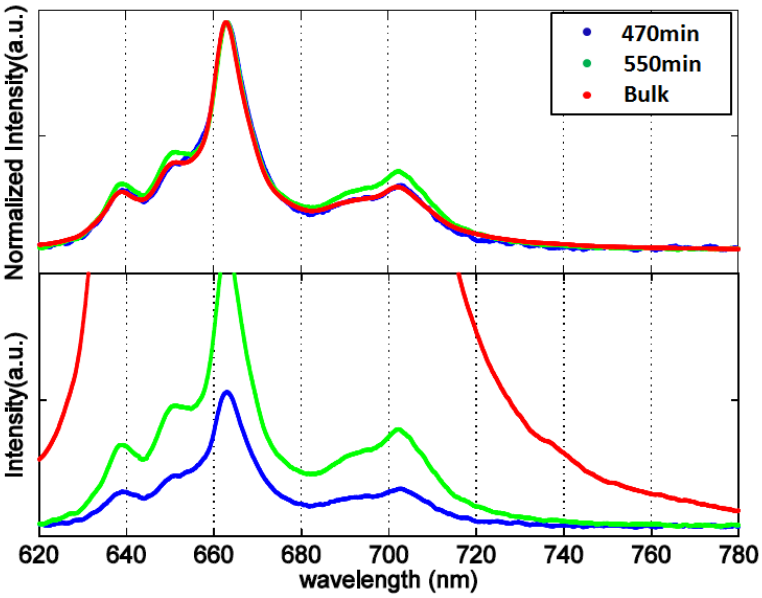

Figure 6.54: Comparison of the microfluorescence spectra for D4 (blue), D5(green) and Bulk (red) normalized in height. In the bottom the spectra are shown not normalized in height.

6.7.3 Summary of results on the film grown on the silicon surface

In order to establish which are the processes that occur at the $H_2TPP(F)/SiC\text{-}SiO_2$ core shell NWs interface, a simple inorganic surface has been functionalized by $H_2TPP(F)$ supersonic beams and studied: the $Si(100)/SiO_2$ planar surface, indeed showing a similar silicon oxide layer. The first mandatory step is the evaluation of the properties of a $H_2TPP(F)$ thick film on $Si(100)/SiO_2$: the core levels analysis is in very good agreement with the theoretical/experimental model proposed by M. Nardi in previous works [265].

The growth kinetic has been studied analyzing the evolution of the XPS core levels signals from the organic molecule (C1s, F1s) and from the substrate (Si2p, O1s), giving rise to a very complex process, characterized by a sigmoid character: very slow in the first part up to significative deposition times (0-400min) then very rapid in the 400-800 min region. At higher deposition times, a complete molecular film is achieved but with presence of islands, as confirmed by the AFM and microfluorescence ex-situ analysis. Films at different deposition times have been studied in details in order to better understand the type of interaction at the interface and to identify all the components and mechanisms involved both from the $H_2TPP(F)$ and the substrate points of view.

Our XPS and UPS studies have highlighted the interaction at the organic/inorganic interface being localized on the fluorinated phenyl rings, as shown by the presence of a new component in F1s core level. Moreover, we identified a new component also in O1s core level (emerging by the analysis at grazing angle) that can be recognized as the inorganic counterpart in the interaction mechanism, i.e. a charge transfer process from the oxide surface defects related to an electron donor level, to the fluorine atoms in the phenyl rings, due to the high electron withdrawing property of the halogen species.

This leads to formation of a layer of holes in the inorganic, with a 0.2eV band bending, as well as of an organic single layer of molecules, laying on the surface, showing an electron excess localized on the phenyl rings. Sticking coefficient ruling the formation of the wetting layer is very low, and in those regions where it is complete, a far more efficient island growth can start. This further, complex, film growth is characterized by the compensation of the negative charge excess by creating a layer with positive charges. Once achieved such a charge equilibrium, a band bending, depletion zone occurs to match the electronic properties of a positively charged molecular film to that of the bulk molecular film. The occurrence of an organic/organic interface, following the organic/inorganic interface formation is achieved probably by a different intermolecular rearrangement, leading to the observed changes in core levels BEs, WF and IP.

The AFM and microfluorescence studies confirmed the formation of a wetting layer of H_2TTP(F) having optical properties different from that of the organic powders, probably related to the electron charge excess hindering specific electronic transitions. Islands presence too has been confirmed, showing luminescence properties more similar to that of the bulk H_2TTP(F) film. This is a clear indication of a different molecular organization on the surface, a phenomenon already investigated by computational analysis [265].

The observed phenomena are totally due to the high kinetic energy of the organic precursor, about 25eV, as they have not been reported at 0.5eV, where only physisorption occurs. Thus the SuMBD approach is able to induce and activate a great number of chemical/physical and electronic processes: formation of covalent bond has not been observed, but charge transfer processes occurs at the organic/inorganic interface leading to formation of a electron excess whose compensation is achieved only by means of different and complex processes, probably related to a molecular rearrangement during growth.

It is noteworthy that the observed charge transfer process on the SiO_2 native oxide interface has been reported also in Chapter 4, where perylene molecules instead of partially fluorinated molecule were used. In that case, due to the very short distance of the organic LUMO from the Fermi edge, the charge transfer process was by far more feasible and probable than in the case of H_2TTP(F), a molecule exhibiting two times higher HOMO-LUMO gap.

6.8 Properties of H_2TPP(F) film growth on SiO_2/SiC NWs

The H_2TPP(F) thick film deposited on SiC/SiO_2 core-shell NWs, with a nominal thickness of about 40nm, has been characterized in detail by means of XPS spectroscopy. A He carrier gas has been used to produce the supersonic H_2TPP(F) seeded beam, leading to a final precursor KE of about 25eV. As stated before, due to the high insulating character of the NWs, it has not been possible to perform UPS analysis, but only XPS. Moreover, as we will see in the following, several effects have been observed ascribable to the specific properties of these nanostructures. Also taking into account the exposed charging problems, studies of the organic films have been carried out in order to verify the feasibility of the envisaged XPS analysis.

In agreement to the case of the planar surface, C1s, F1s and N1s core levels have been examined. The stoichiometry has been evaluated and the calculated values are in agreement with the expected atomic concentrations (±2.5%) as summarized in Table 6.8. This suggests that the H_2TTP(F) molecule, also in case of deposition on these NWs, has not been damaged by the SuMBD deposition approach.

ATOMIC PERCENTAGE (±2.5%)			
	%C	%F	%N
Calculated	66.2	28.0	5.8
Theoretical	64.7	29.4	5.9

Table 6.8: Atomic percentage values calculated and expected for H_2TPP(F) bulk film.

The C1s lineshape deconvolution is achieved with five contributions related to the organic molecule, as observed for the planar surface. Having in mind the previously discussed

notation regarding the chemical species present in the molecule, a detailed lineshape analysis can be performed (see Table 6.9). The main peak ascribed to the C-F is located at 289.0eV and it represents the 46.9% of the C total signal associated to the photoemission of about 20.6 C atoms, with respect to the theoretical 20 atoms. The analysis of the H_2TPP(F) thick film C1s core level is displayed in Figure 6.55.

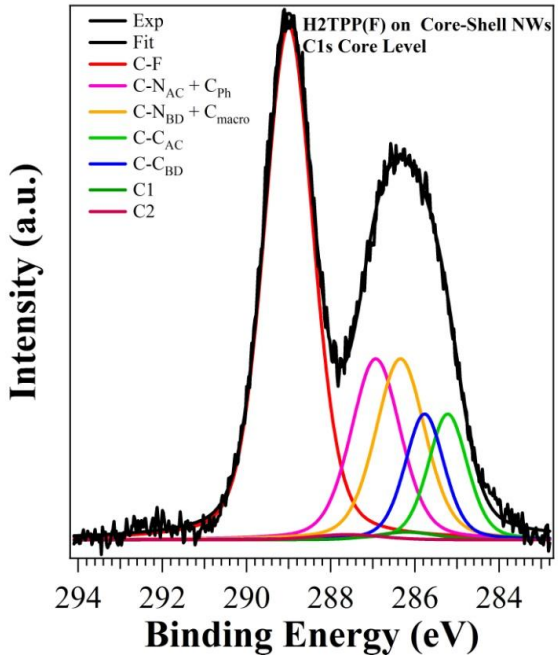

Figure 6.55: C1s core level from a H_2TPP(F) thick film.

Component	BE [eV]	Distance from C-F peak	C1s peak area percentage (±2.5%)	Atoms Number	FWHM [eV]
C-F	289.00	0.0	46.4	20.6	1.38
C-N$_{A-C}$ + C$_{Ph}$	286.93	-2.1	16.5	7.3	1.39
C-N$_{B-D}$ +Cmeso	286.35	-2.7	16.5	7.3	1.39
C-C$_{A-C}$	285.77	-3.2	9.1	4.0	1.1
C-C$_{B-D}$	285.22	-3.8	9.1	4.0	1.1
C$_{Sat}$	292.10	+3.1	0.9	0.4	1.1
C1	286.20	-2.8	0.8		1.7
C2	287.60	-1.4	0.6		1.9

Table 6.9: C1s core level main features from H_2TPP(F).

The components correlated with the C-N bonds in the pyrrole rings are located at 286.93eV (C-$N_{A\text{-}C}$ + C_{Ph}) and 286.35eV (C-$N_{A\text{-}C}$ + C_{meso}) and they correspond to the 33.2% of the total C signal, i.e. about 14.6 carbon atoms instead of the theoretical 16. The peaks at lower BE at 285.77eV and 285.22eV due to the C-C bonds in the A-B and B-D rings in the macrocycle respectively, are 18.4% of the C signal and are associated to 8.0 C atoms, as expected. A weak contribution at 292.20eV is also present: a satellite structure related to a shake-up process due to a transition $\pi \rightarrow \pi^*$ of the C in aromatic rings [55].

It is noteworthy that, with respect to the H_2TPP(F) corresponding film deposited on the planar surface, in the NWs the peaks are shifted towards high BE. Considering the C-F contribution found in planar surface located at 288.28eV, the difference in BE can be estimated of about Δ = +0.7eV, and the same occurs for all other peaks. Moreover, all the components in the C1s core level have a larger FWHM of about +0.15eV. The large width and energy shift of the peaks, with respect to those observed in the planar surface, are likely due to the mentioned charging phenomena common in this type of NWs.

Moreover, aside from the typical component of H_2TPP(F) just described in the previous paragraph, it is necessary to introduce two further contributions at 286.20eV and 287.60eV (labelled C1 and C2, respectively), both representing about 1.5% of the C total signal. These components will be explained in detail in the next paragraphs.

Figure 6.56 shows the N1s core level and, according to the theoretical model used for the planar surface, it is possible to distinguish the contribution related to the aza-N atoms with the lone electron pair (399.22eV, N^{Aza}) and the pyrrolic N atoms bonded with H (401.15eV, N^{Py}) which represent the 42.8% and the 49.6% of the total N signal, respectively. The two satellite peaks at high BE are related to the $\pi \rightarrow \pi^*$ excitation process related to N^{Aza} (3.8%) and N^{Py} (3.8%) and they are located at 402.02 and 403.92eV.

Component	BE [eV]	Distance from N^{Py} peak	N1s peak area percentage (±2.5%)	Atoms Number	FWHM [eV]
N^{Aza}	399.22	-1.9	42.8	1.7	1.41
N^{Py}	401.15	0.0	49.6	2.0	1.41
N^{Aza}_{Sat}	402.02	+1.0	3.8	0.1	1.50
N^{Py}_{Sat}	403.92	+2.8	3.8	0.1	1.50

Table 6.10: N1s core level main features from H_2TPP(F).

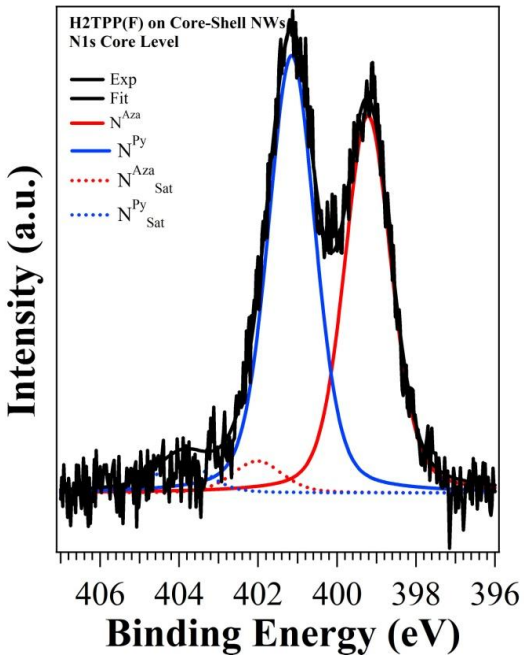

Figure 6.56: N1s core level from a H_2TPP(F) thick film.

Once more, the N1s properties are those of the H_2TTP(F) molecule observed in the thicker films deposited on planar surfaces, apart from a higher BE (+0.7eV) and larger FWHM (+0.19eV) as observed for the C1s emission.

The F1s peak analysis is illustrated in Figure 6.57. A main peak at 689.23eV is present and can be ascribed to the F-C bonds in phenyl rings, showing once again a BE shift (Δ = +0.3eV) with respect to the H_2TPP(F) film deposited on SiO_2/Si(100) planar surface. This peak represents the 96.2% of the F total signal. Differently from what observed for C1s and N1s emissions, the peak width does not show a significant increase with respect to the H_2TPP(F) films on SiO_2/Si(100) surface: this, together with the lower BE shift can be related to the originally larger width of the F1s emission with respect to C1s and N1s, probably leading to less noticeable effects in case of charging phenomena.

However, as observed for C1s peak, there is a second component at 688.67eV, representing about 3.8% of total F1s emission. It is for sure related to fluorine coming from the H_2TTP(F) phenyl rings, being the only fluorine source and we will see in the following its origin.

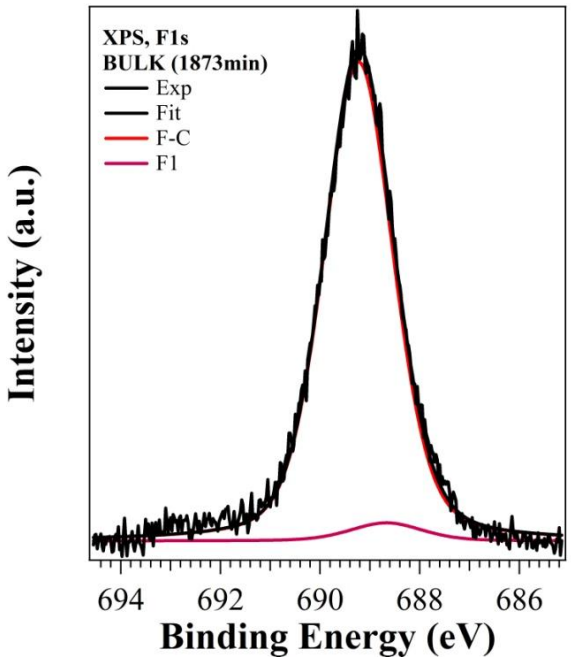

Figure 6.57: XPS F1s core level from H_2TPP(F) thick film.

Component	BE [eV]	Distance from F1s main peak	F1s peak area percentage (±2.5%)	FWHM [eV]
F	689.23	0.0	96.2	1.64
F1	688.67	-0.6	3.8	1.70

Table 6.11: F1s core level main features from H_2TPP(F).

6.9 H_2TPP(F) film grown on SiC/SiO_2 core-shell NWs

A consecutive series of H_2TPP(F) depositions has been performed on SiC/SiO_2 core/shell NWs keeping the substrate at room temperature, and using He as carrier gas leading to a final precursor KE of 25eV. For each deposition step, XPS analysis at low resolution has been performed, similarly to the planar surface, obtaining important information about the growth mechanism. In particular, the growth process of H_2TPP(F) on SiC/SiO_2 core-shell NWs has been examined in detail studying the low resolution signals from the substrate (Si and Oxy XPS emission) and from the organic molecule (C and F XPS emission) as a function of the coverage. The peaks area has been evaluated and normalized to the value of

the clean surface for the Si2p, O1s substrate signals and of the C1s and F1s molecule values in the bulk state.

In order to study in detail the interactions in the first few layers of coverage, the early points of the growth curve have been investigated (6, 12, 25, 45, 64, 84, 106, 130, 280 and 480 minutes), examining by XPS at high resolution C, F, N, O and Si core levels. Unlike the planar surface, SiC/SiO_2 core/shell NWs functionalized with $H_2TPP(F)$ cannot be characterized by UPS spectroscopy because of the sample charging that does not make the measure reliable.

SiC/SiO_2 core/shell NWs clean surface is characterized by the presence of silicon oxide compounds, but also by specific carbon chemical species. As can be seen in Figure 6.58, Si2p and O1s emissions show a single component at 105.67eV and 535.26eV (FWHM of 1.82eV and 2.00eV), respectively, related to the silicon oxide shell in the NWs.

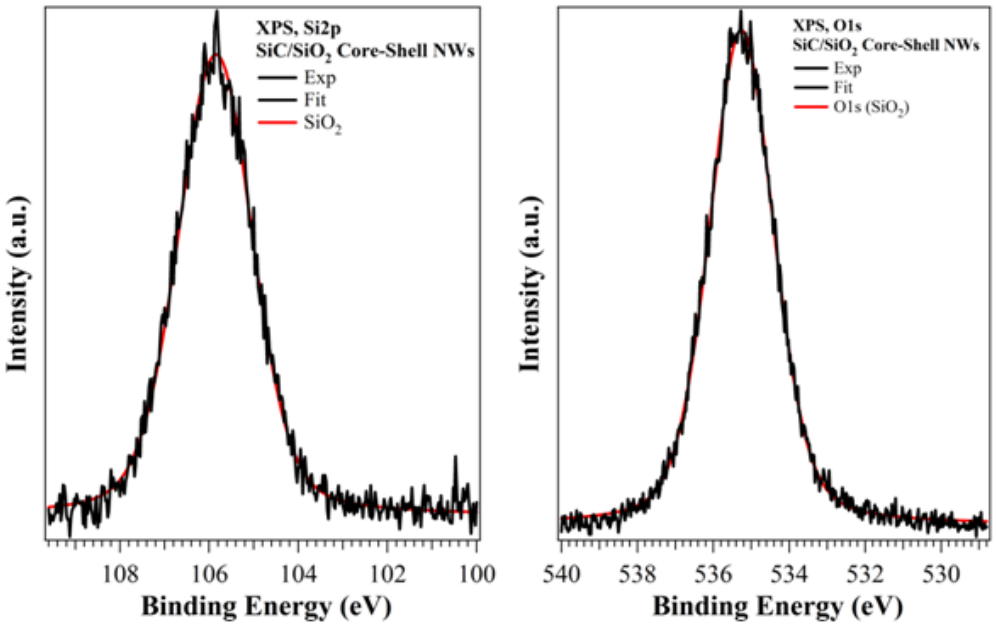

Figure 6.58: Si2p (on the left) and O1s (on the right) core levels related to the SiO_2 present on the NWs surface.

The large FWHM could suggest presence of more than one chemical species, but the broadening due to NWs insulating character prevents from making any further comment. As observed for the organic molecule, the BE values are about +1.0eV higher than expected for silicon oxide due to the charging effects typical of these nanostructures. We

decided to not re-align the binding energy, maintaining the experimentally observed values to avoid introduction of possible artifacts.

The quantitative analysis has demonstrated that the oxide is under stoichiometric in oxygen with a O/Si of 1.34. This was expected, due to the nanodimensions of the one dimensional system, and is important since it leads to presence of a great number of defects on the surface, possibly being the origin of electron donor levels in the oxide gap. However, this has not been checked because of the impossibility of performing UPS analysis.

The C1s peak has been deconvolved by three components and their interpretation has been achieved in a work proposed by our group in Trento, in collaboration with IMEM-CNR in Parma [254]. In agreement with this study, as shown in Figure 6.59 the peak at low BE (286.87eV) is related to the carbide in the surface. The other two components are related to C-C bonds (288.11eV), either embedded in the NWs or not, and to oxycarbide (289.72eV), such as Si-O-C, and/or C-O compounds. The C contributions have been taken into account in the following quantitative and qualitative analysis and properly considered.

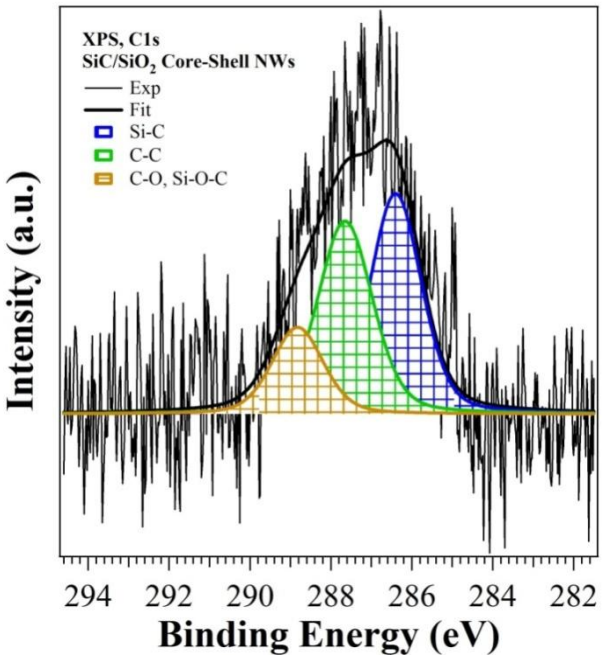

Figure 6.59: C1s core level of the residual carbon present on the NWs surface.

Figure 6.60 displays the peculiar growth kinetic observed for the H_2TPP(F) on core-shell NWs as a function of the photoemission signals from the organic molecule and the

substrate as a function of the deposition time. At a first glance, the growth trend is quite different with respect to the process observed for H_2TPP(F) on the planar surface (see Figure 6.29). Indeed, the growth seems to be faster and characterized by logarithmic trends.

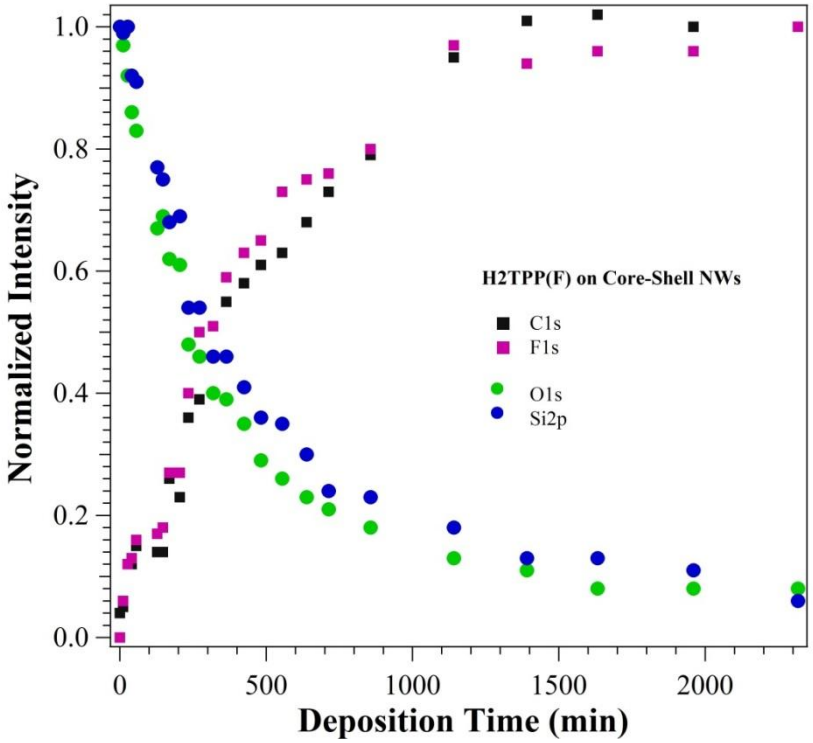

Figure 6.60: Growth kinetic (XPS core level signals vs. deposition time) for a H_2TTP(F) deposition on SiC/SiO_2 core-shell NWs.

While in the first 500 min of deposition time for the growth on planar surface we observed an almost linear growth leading to a C1s and F1s intensity being less than 15% of the thick final film, in this case the corresponding value is 60% and a further steep increase is never observed. Except for the first three points, in which the intensity of the signal from the substrate remains almost unchanged (97% of the original), the deposition leads to a constant substrate signal decrease and organic signal increase. In the 1400-2300 min region the system reaches a saturation state and no further variations occur. Similarly to the H_2TPP(F) on the planar surface, at high coverage the signal from the substrate is still present and it represents 16% of the initial value. All curves are characterized by presence of sort of steps, showing a not-monotonic trend that, however, could be related also to typical errors in this type of analysis, probably enhanced on these nanostructures. In fact,

while in Figure 6.28 a constant and proper C/F stoichiometry value has been found during the whole growth, in this case the scattering of the C1s and F1s data clearly suggests a higher variability of the chemical species ratio, as the same variability can be also found for the Si/O ratio. It seems clear that the observed steps and trend variations are due to the peculiar electronic and morphological characteristics of the NWs.

Before analyzing in details the growth mechanisms, some preliminary considerations should be made. We performed organic depositions on NWs grown on Si substrate. The typical NWs density is about 5-10 NWs μm^{-2} [284], while each NWs has a diameter of 60 nm and a length of about 50 μm. Density has been calculated by SEM images, i.e. by counting only those NWs visible within the microscope depth field, that is an underestimated value, but let's consider this is the same density seen by the incoming molecules, that are deposited with a direction normal to the main substrate surface. These numbers lead to a number of NWs exposed to the SuMBD beam of $3.2\text{-}6.4 \times 10^8$, with a total surface of about 30-60 cm^2, being the SuMBD spot diameter of about 0.9 cm. The real exposed surface would be the half, as impinging molecules "see" only the upward portion of the NW, not the downward. However, TEM analysis has shown the functionalize NWs are completely and uniformly covered by the organic molecules, as can be seen in Figure 6.61.

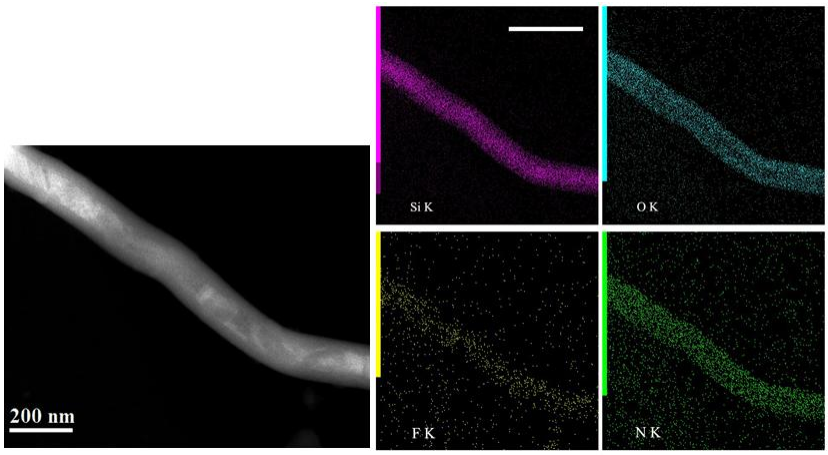

Figure 6.61: TEM analysis of a single NWs functionalized by the H_2TTP(F) molecule. the whole NW surface is completely covered by the organic molecule.

Thus we can consider the 30-60 cm^2 as proper and correct and not its half: also considering that when we analyze by XPS only the upward part and not the hidden downward part are measured, we know that the growth process lead to a complete NW surface coverage. By comparing to the SiO_2/Si(100) case, where the functionalized area was a spot with 0.9 mm diameter, i.e. 0.64 cm^2, in the case of NWs we are depositing molecules on a surface about two order of magnitude larger. Nevertheless, by comparing the two growth kinetics, the shapes and slopes are totally different: the formation of a 40 nm thick layer is achieved in about the same time, but the first growth stages suggest the mechanisms for growth on NWs are far more efficient. The larger surface to be covered has the higher sticking coefficient, i.e. the functionalization mechanism is more efficient than in the case of the planar surface.

In order to determine the variations in terms of chemical/physical properties of the H_2TPP(F) films on NWs at different coverage times, high resolution XPS analysis has been performed only for C1s and F1s. Regarding the N1s core level analysis, as already seen in the case of the planar surface, the signal from the organic molecule is too weak so that it is quite difficult to obtain reliable information also after long acquisition times. Moreover, on the NWs substrate N1s shows a significative broadening that makes unreliable any interpretation based on its analysis. For this reason we did not acquire the nitrogen spectra and we focused our attention on the C1s and F1s core level interpretation. Furthermore, concerning signals from substrates, experiments on the planar surface suggest the need to perform XPS in grazing acceptance angles. In case of NWs, we are dealing with curved surfaces and photoelectron acquisition is characterized at the same time by a continuous of acceptances angles, from normal to grazing, so the analysis of Si2p and O1s core levels would lead to not reliable interpretation, being convolution of different acquisition geometries. The analysis have been performed at different deposition times in the first fast part of the growth curve at 6min, 12min, 25min, 45min, 65min, 85min, 105min, 130min, 280min, 480 min (labeled as D1, D2, D3, D4, D5, D6, D7, D8, D9, D10) and 1880 min: the latter being representative of the bulk phase. As a matter of fact, we analyzed the same growth deposition time window as for the H_2TTP(F) on SiO_2/Si(100) case.

In Figure 6.62 the core levels of Si2p and O1s from substrate are shown. Due to the aforementioned characteristics of the XPS analysis in normal acceptance of curved surfaces, the core level lineshape analysis does not supply useful indications about

contributions of NWs chemical species involved in the interaction at the interface, as on the contrary seen for planar system. What can be mentioned is the presence of a BE shift of both peaks toward lower values, being about 1.0eV the difference between the clean and bulk cases.

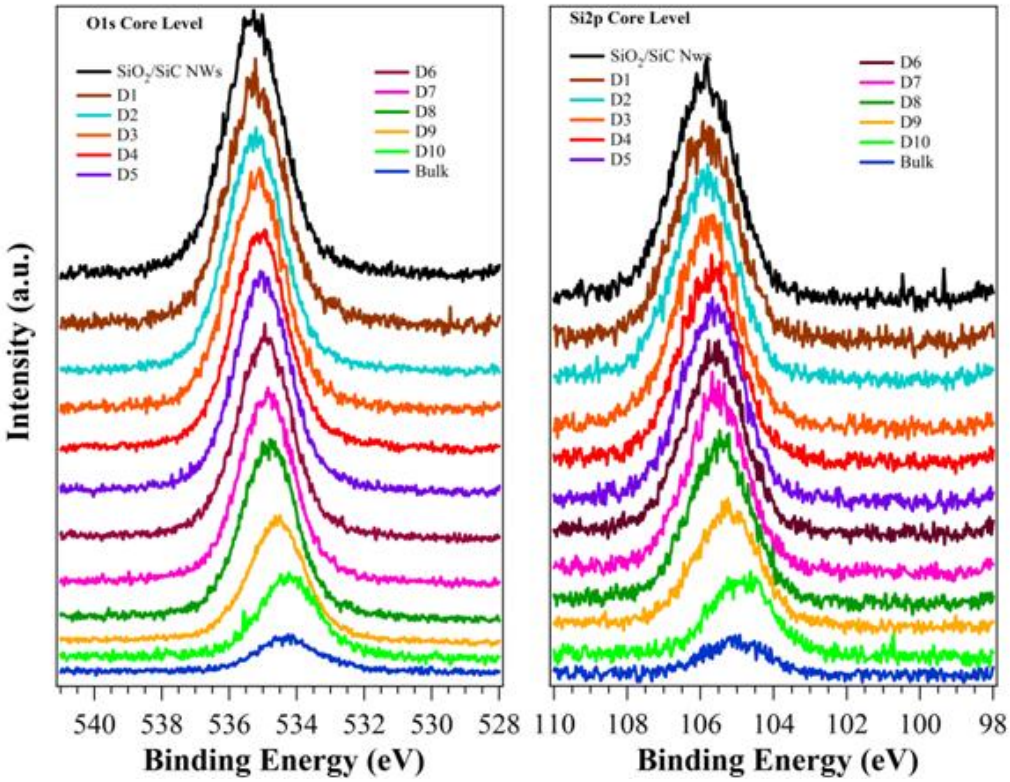

Figure 6.62: XPS O1s (on the left) and Si2p (on the right) core levels emission as a function of the $H_2TPP(F)$ film coverage.

The C1s core level spectra as a function of the deposition time are shown in Figure 6.63. At a first glance, it is possible to recognize the two typical features of the lineshape related to the C-F bonds at high BE and C-C and C-N contributions at lower BE for all deposition time. Only at higher coverages the ratio between the two main bands seems to be that of a $H_2TPP(F)$ molecule, in fact from D1 to D9 films there is a higher weight of the band related to emission from the macrocycle with respect to that from the fluorinated phenyl rings. This is a clear evidence of the presence of different types of organic molecules.

Considering the intrinsic complexity of the $H_2TPP(F)$ C1s deconvolution from a pristine $H_2TPP(F)$, characterized by the presence of five components, and the presence of three other peaks coming from the carbon species present at the NW surface, we decide to adopt

a specific strategy to analyze the C1s emission. At very high coverage we observe the fingerprints of a typical H_2TTP(F) molecule, physisorbed and not chemically interacting with anything else, as shown in paragraph 6.8. Moreover we can claim that, due to the very large exposed surface and the great number of NWs, we are dealing with organic/inorganic interfaces on each single NW and it is hard to think that organic growth will be completed and developed at the same time on all nanostructures.

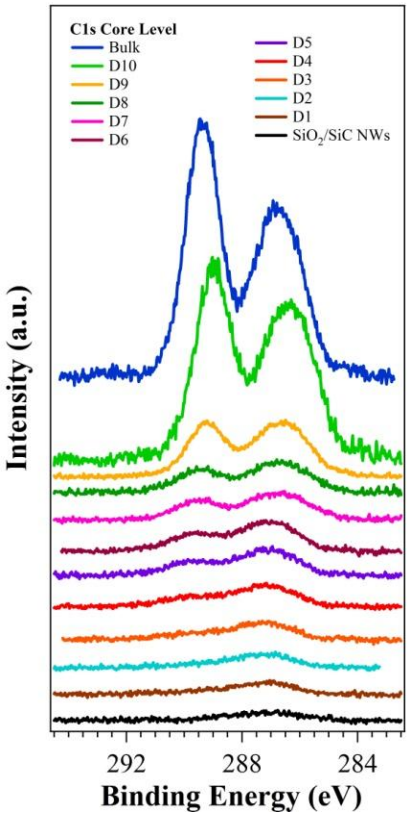

Figure 6.63: XPS C1s core level emission as a function of the H_2TPP(F) film coverage.

Thus, we will always deal with analysis of NWs presenting at the same time a different degrees of functionalization and organic film thickness. In other words, we are dealing with a diffused interface where formation of a complete molecular film is achieved not by means of a coherent growth process on the whole available surface (as occurs for a planar surface) but by a sequence of single growth processes on each NW. Such a sequence will lead to coexistence of NWs at different growth stages, so that the whole photoemission

signal from the surface will constantly increase but we will examine at the same time single NWs characterized by different organic film thicknesses.

We decided to deconvolve the C1s peak by using the lower possible number of varying peaks and related variables, having in mind to achieve reliable information for the chemical/physical processes occurring at the interface and not just a good lineshape fit, an error that is possible when the deconvolution process is so difficult. We used i) a set of five components representing emission from physisorbed molecules (disregarding emission from the shake-up satellite, not significant for the final purpose) that we labeled "Physisorbed" in the following and whose intensity is expected to grow with the deposition time; ii) a set of three components representing emission from carbon-based NWs surface species, labeled "NW C", whose intensity will decrease with growth according to a factor weighted between the observed decrease in intensity for Si2p and O1s (being the C1s energy, thus also escape depth, in-between that of the other two peaks). By using this approach, it was necessary to introduce two further new components to properly reproduce the observed C1s lineshape, located at about 3.5 and 1.5eV from the main peak of the physisorbed species (representing C-F atoms in phenyls) and labeled C1 and C2, respectively. These components have been already shown for the bulk film, suggesting once more that we are dealing with a very diffused organic/inorganic interface, leading to presence of interacting species which fingerprints are detectable also at very high deposition times.

Going back to C1s analysis, as can be seen in Figure 6.64, the contributions related to the residual carbon from the NWs are visible only at low coverages, while they almost disappear when other contributions from organic molecule strongly increase and become the most important one with deposition time.

C1s lineshape from every H_2TPP(F) deposition step can be well reproduced by the proposed approach: only the relative intensity of the physisorbed peaks, NW C species and C1/C2 components have been varied, together with BE shifts involving all species at the same time and with the same values. Apart from the expected increase in signal intensity at increasing coverage, there is indeed a significant energy shift: C-F main component (physisorbed) shifts gradually from 290.26eV in D1 up to 289.00eV in the Bulk (see Table 6.12).

The same energy shift has been observed also for the macrocycle components of physisorbed species. The FWHM of C-F peak remains unchanged (1.7eV) up to the D9 (1.44eV), but then slightly decreases reaching the lower value in the Bulk film (1.38eV). Regarding C1 and C2, they show a continuous but less intense shift towards lower BE, being about Δ = -1eV for C2 and Δ = -0.6eV for C1. Their FWMH (1.7eV and 1.9 for C1 and C2, respectively) does not change with the coverage.

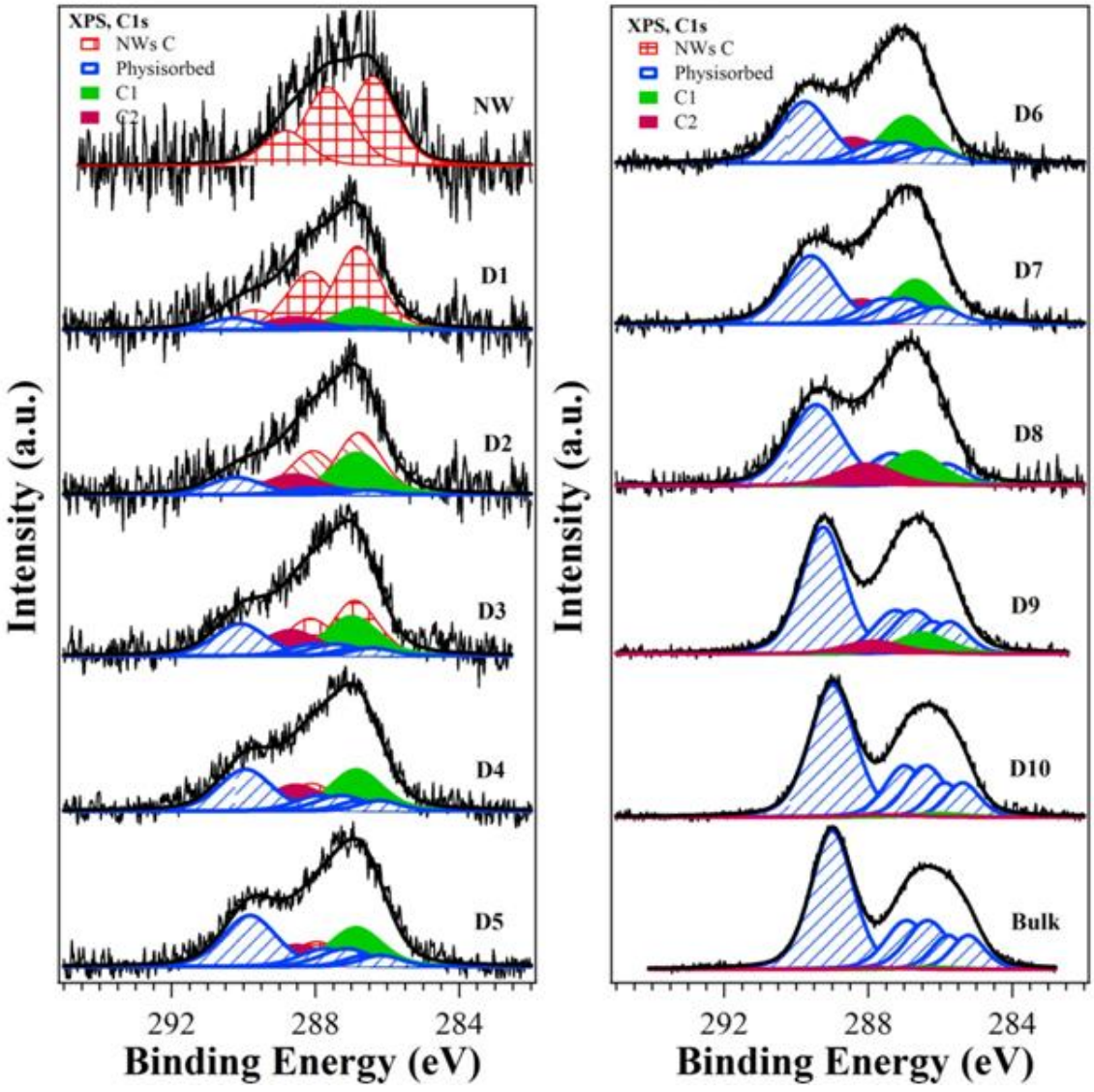

Figure 6.64: C1s core level emission as a function of the H_2TPP(F) film coverage (spectra normalized in height).

The F1s core level spectra as a function of the coverage are reported in Figure 6.65, while the lineshape analysis for each film is shown in Figure 6.66.

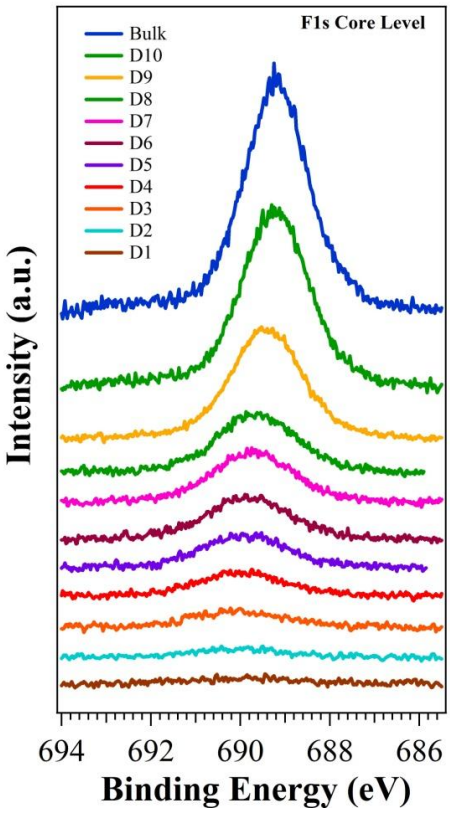

Figure 6.65: XPS F1s core level emission as a function of the $H_2TPP(F)$ film coverage.

Similarly to the C1s core level, F1s is characterized (see Table 6.12) by two different peaks: i) a main one whose evolution with the deposition time leads to the formation of the typical F1s components of the $H_2TTP(F)$ molecule and, in analogy to C1s, defined as "Physisorbed" (blue line in Figure 6.66), ii) a second one labelled as F1 (purple line in Figure 6.66). The "Physisorbed" contribution is located at higher BE with respect to F1 and during the deposition it gradually shifts towards lower BE, with a difference between the D1 (691.1eV) and the Bulk (689.23eV) films of about Δ = 1.87eV. The FWHM decreases with the coverage from 1.90eV in D1 up to 1.64eV in the Bulk. The F1 peak is located at about -1.6eV from the other at higher BE and this distance decreases with the deposition time down to -0.6eV in the bulk film, thus showing a shift in energy with the coverage from 689.47eV in D1 up to 688.67eV in the Bulk film. Similarly to the "Physisorbed" contribution, also the F1 FWHM reduces from 1.90eV in D1 down to 1.74eV in the Bulk film.

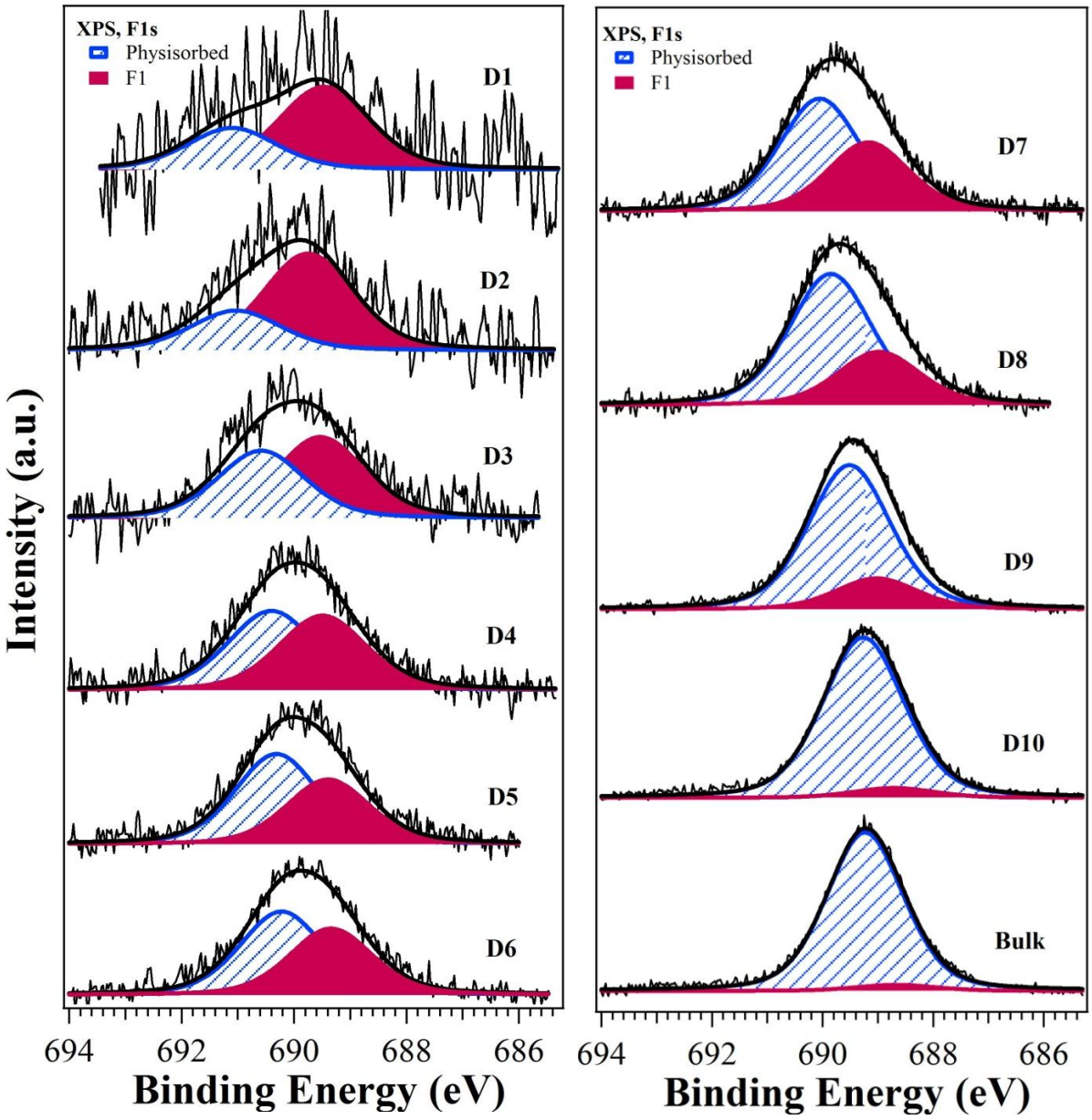

Figure 6.66: XPS F1s core level lineshape deconvolution as a function of the H_2TPP(F) film coverage (Spectra normalized in height).

The presence of significant BE shifts, as well as broadening of all components from the lowest coverage up to the bulk film suggest once more we are studying a highly diffused interface. It is characterized by the presence of contributions from different growth stages (i.e. NWs showing different coverages) during the whole organic growth and by the existence of strongly interacting chemical species at the interface itself.

	D1		Bulk	
	BE [eV]	**FWHM [eV]**	**BE [eV]**	**FWHM [eV]**
C-F	290.26	1.64	289.00	1.38
C1	286.76	1.70	286.20	1.70
C2	288.56	1.91	287.60	1.90
F-C	691.1	1.90	689.23	1.64
F1	689.47	1.90	688.67	1.70

Table 6.12: Main features of the C-F, C1, C2, F-C and F1 components in D1 and Bulk deposition.

An interesting result has been obtained calculating the ratio between the C1s and F1s components giving important indication about their chemical origin, definitely confirming the supposed definition of physisorbed species. It has been found, indeed, that the ratios between the components (CF carbons in phenyl rings showing C-F bonds, C_{macro} carbon in the macrocycle) in C1s and the peak at higher BE in fluorine are coherent with the values of the organic molecules $H_2TPP(F)$, as reported in Table 6.13.

$H_2TPP(F)$ PHYSISORBED			
	CF/F	***C_{TOT}/F***	***CF/C_{macro}***
D1	0.89	1.87	0.91
D2	0.97	2.03	0.92
D3	0.91	1.91	0.91
D4	0.92	1.93	0.91
D5	0.93	1.91	0.95
D6	0.92	1.88	0.95
D7	0.90	1.89	0.92
D8	0.92	1.95	0.89
D9	0.89	1.89	0.88
D10	0.95	2.00	0.90
Bulk	0.95	2.02	0.88
Theoretical Values	1.00	2.20	0.83

Table 6.13: Ratio between the different features in C1s and F1s of the "Physisorbed" species as function of the film coverage. Theoretical values are also shown.

The intensities of C1, C2 and F1 peaks decrease with the deposition time, so it is reasonable to claim they are mainly present when the organic thickness is very low, i.e. at the organic/inorganic interface, representing the fingerprint of the occurring chemical/physical processes. By calculating the ratio between the new carbon and fluorine photoemission features it has been found that it is still comparable with that of the organic molecule, as showed in the Table 6.14, even if slightly lower that is suggesting a carbon deficiency. More in details, F1 and C2 belong to the fluorinated phenyls involved in the chemical interaction at the interface, while C1 peak is representative of the carbon atoms in the macrocycle. Taking into account the difficulties in evaluating the C1s components and the higher reliability in analyzing the F1s ones, it is reasonable that the errors for the former are higher than for the other, leading to a possible underestimation of the carbon content and overestimation of fluorine. Also the observed general peak broadening can generate less severe artifacts for the F1s emission rather than for C1s, considering the presence of only two components for the fluorine peak.

H_2TPP(F) NEW COMPONENTS			
	C2/F1	***C1+C2/F1***	***C2/C1***
D1	0.54	1.40	0.63
D2	0.50	1.43	0.53
D3	0.64	1.53	0.73
D4	0.66	1.61	0.70
D5	0.58	1.54	0.61
D6	0.53	1.43	0.60
D7	0.74	1.86	0.67
D8	0.64	1.55	0.70
D9	0.54	1.34	0.68
D10	0.72	1.69	0.74
Bulk	0.69	1.59	0.77

Table 6.14: Ratio between new components found in C1s and F1s core levels, as function of the film coverage.

These results suggest that the two components, both in C1s and F1s, are representative of the "Chemisorbed" molecules directly involved in the interaction. This explanation justifies, moreover, the different BEs of the two species. The "Chemisorbed" species, indeed, being involved in the interaction suffer a charge rearrangement on the all organic

molecule determining their positioning at lower BE with respect to the "Physisorbed" components, in a similar way as observed for the H_2TTP(F) growth on planar silicon oxide surface. The interaction with the NWs, localized above all on the fluorinated phenyl rings, has the effect to neutralize the charge density on the molecule so that these peaks are situated at low BE, i.e. draw electrons from the surface to the fluorinated phenyls leading to a decrease in binding energy for both carbon and fluorine species in the rings.

To further confirm that the three peaks, C1, C2 and F1 belong to the same molecular species, we compared the C1+C2 and F1 peak area to that of physisorbed carbon and fluorine, respectively, as a function of the film coverage. The same qualitative trend has been found (Figure 6.67), finally suggesting the proposed interpretation.

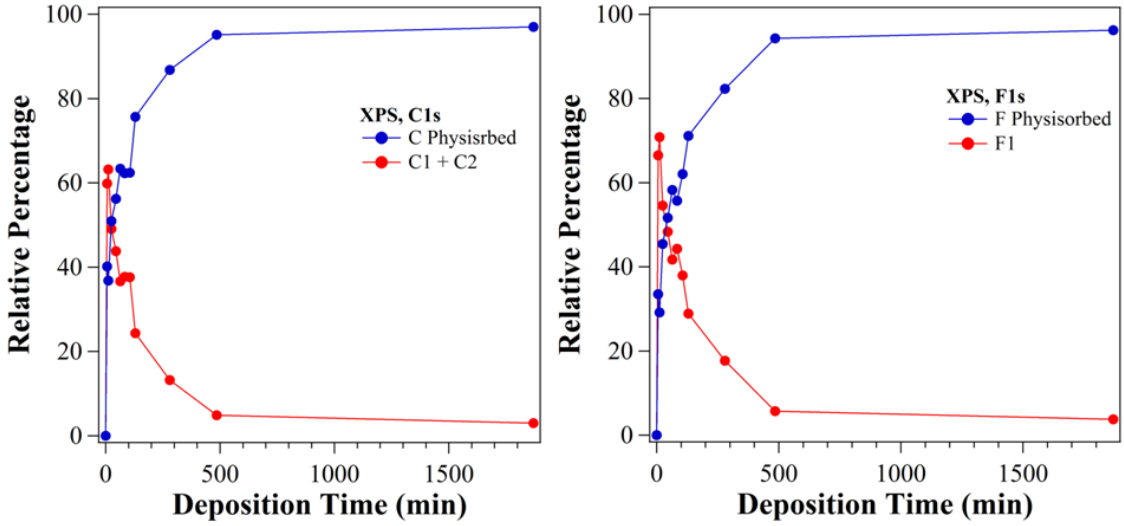

Figure 6.67: Relative percentage calculated for the "Physisorbed" and "Chemisorbed" species in C1s and F1s core levels.

Thus, we confirm that the C1, C2 and F1 components are representative of a different type of H_2TTP(F) molecules, that are not physisorbed but rather directly involved in the interaction at the interface, i.e. "chemisorbed".

It is difficult to further comment the type of chemical interaction occurring at the interface. The absence of UPS analysis makes not fully reliable any consideration on WF function position, charge transfer processes, band bending. However, taking into account what we have observed for the H_2TTP(F) growth on the planar surface and the strong hints coming from the XPS analysis, some further considerations can be made.

For the growth on planar surface we observed formation of surface dipoles and charge transfer processes involving extraction of electrons from donor levels in the SiO_2 surface, leading to the observed fluorine peak at lower binding energy and band bending phenomenon for both inorganic and organic counterparts, causing significant BE shifts.

For the $H_2TTP(F)$ growth on NWs we observe stronger BE shifts for the substrate species during the film deposition, in complete analogy with previous case ascribable to a band bending at the more external part of the NW. Thus a source of donor electronic levels from the silicon oxide surface also for NWs is reasonable, if we think that the SiO_2 shell is characterized by a larger amount of surface defects with respect to a planar oxide. Moreover, all molecular photoemission peaks exhibits very large BE shifts, in complete analogy with the previous case and we can attribute these to the formation of a complex intermediate layer with charge compensation between the charged interface and the neutral thick film.

The growth process on NWs is by far quicker than for the planar surface case, so higher amount of organic materials are present also at the initial growth stages and, together with the presence of a larger surface, this led to a more reliable analysis of the C1s core level of the real interface. Conversely, the initial growth stages on the planar surface had such a small quantity of organic material that any introduction of new C1s components (namely, the observed C1 and C2 peaks) would have been just pure speculation. F1s core level, for both growth on NWs and SiO_2/Si(100) surfaces, has shown the presence of a single new component at lower BE with respect to the main peak related to physisorbed molecules. We can therefore argue that interaction mechanisms at the organic/inorganic interface involve in both cases fluorine, and thus the bonded carbon atoms in the phenyl rings whose evolution we are finally able to observe in the NWs case.

We claim that we are dealing once more with charge transfer processes at the interface, from electron donor levels of NWs to fluorine atoms. The high electron withdrawing property of fluorine will further enhance the electron density excess in the phenyl rings of the pristine molecule, but being the original electronic density totally located on fluorine atoms [265], this new provision of negative charge will be partially shared also with the bonded carbon atom, the C-F species which core level would in turn move to lower binding energies. The new carbon atoms bonded to fluorine will therefore experience a charge redistribution, becoming more similar to a tetraphenyl porphyrin H_2TTP without

fluorine [285], where carbon in the phenyl rings have a lower BE while carbon species in the macrocycle have the same electronic properties. Having this in mind, the C2 peak can be reliably attributed to carbon atoms in a phenyl ring interacting with the NWs by charge transfer processes through fluorine atoms (F1 component), while C1 peak represents the macrocycle part of the chemisorbed H_2TTP(F) molecule. The C2/C1 ratio expressed in Table 6.13 confirms (within the commented errors) this hypothesis.

If the mechanisms at the basis of the organic/inorganic interaction at the interface are the same, it is worth discussing their efficiency. We can imagine the overall growth on all NWs is just the sum of several single NW growth, this would lead to a growth kinetic characterized by smoothed form of a sigmoidal curve, also considering that the growth does not start at the same time on each NW, as confirmed by the presence of the C1, C2 and F1 peak also for the very thick film. The shape is totally different, suggesting that the efficiency to complete the organic interface layer on NWs, necessary for the growth of the physisorbed film, is by far higher than for SiO_2/Si(100). The different collision geometries in the former case, characterized by a curved surface rather than planar, could enhance the efficiency but also reduce it. In fact, in case of multiple scattering phenomena, leading to KE losses of the molecules in the supersonic beam, the creation of the charge transfer process results less probable.

Considering the previous arguments on the presence of a diffused interface, the overall efficiency of the growth process must be by far higher than for the silicon oxide planar surface, i.e. the same charge transfer mechanism observed in previous paragraph but with higher efficiency, probably related to a higher density of electron donor levels for the NW surface.

6.9.1 Summary of results on the film grown on NWs

In view of the development of a challenging application, i.e. the synthesis of a new class of hybrid PS for photodynamic therapy induced and activated by x-rays, the functionalization of SiC/SiO_2 core-shell NWs by H_2TPP(F) supersonic beams has been analyzed. We based our studies having in mind the results achieved for the porphyrin growth on the planar native silicon oxide surface. Studies on NWs has been characterized by lower resolution and charging effects during measurements, due to the intrinsic highly insulating nature of

this material. That's why the results previously achieved have been a good and fundamental guide for interpretation of NWs functionalization process.

The first evident result is the quite different H_2TPP(F) growth kinetic on NWs, which follows a logarithmic trend instead of the sigmoid observed for the functionalization of the Si(100)/SiO_2 planar surface. The deposition process, thus the sticking coefficient seems to be much more efficient since the signal from the organic rapidly increases starting from very low deposition time. An interesting drawback is the difficulty to study early growth stages where a significant amount of organic molecule was present, differently from what happened for the H_2TTP(F) growth on planar surface.

Analyzing in detail several deposition steps by XPS spectroscopy, a chemisorption process at the interface has been suggested characterized by the strong interaction of unbroken porphyrins. The C1s and F1s lineshape analysis has brought to the identification of the specific contributions from unreacted, physisorbed H_2TPP(F) molecules and of new features located at lower BE and related to H_2TTP(F) molecules experiencing a chemical interaction at the interface. The strong charge reorganization which occurs on the organic inside the fluorinated phenyls is suggested as being the main process, increasing electron density also on carbon atoms and leading to the downward shift of the corresponding C1s component. This is true if the interaction is strong enough to induce the charge exchange between the organic molecule, where the withdrawing properties of fluorine atoms play the major role, and the NWs outer shell, characterized by dangling bonds and defects. In complete analogy to what observed for porphyrin deposition on the planar silicon oxide surface, electron donor levels are very likely present also on NWs (that show an understoichiometric oxygen silicon oxide surface, also with presence of carbon species) and enable the charge transfer towards the fluorine atoms. This process is also at the origin of the observed negative BE shift of Si2p and O1s, that in turn is due to the formation of band bending phenomenon in the inorganic materials.

Concerning the two analyzed systems (NWs and planar surface functionalized by H_2TPP(F)), the SuMBD kinetic activation of interface processes is the main driving force of all the strong interactions experienced by the organic molecules, but the surface nature, such as the presence of a more defective oxide shell and dangling bonds, plays as well an important role on the mechanism efficiency leading increasing it in NWs, even though the NWs facing surface is about 100 times higher than the planar one.

6.10 Carbon-doped silicon dioxide NWs

The aim of our group in Trento is to study new materials and/or hybrid interfaces with innovative properties for application in several fields, including biomedical. To this purpose, we are studying a new class of inorganic NWs constituted by carbon-doped silicon dioxide, that are promising candidates for the functionalization with organics, fully exploiting our knowledge and experience acquired during the study of SiC/SiO_2 core shell NWs (see paragraph 6.9).

The SiO_x nanostructures own a high emission yields [286] which can be increased with a doping process as widely demonstrated in literature [287]. A preliminary study concerning these new batch of NWs, without any functionalization, will be here exposed and has been subject of a publication in "Nanotechnology" journal [284].

Silicon oxide NWs have been grown in IMEM-CNR Institute in Parma by DR. M. Bosi and G. Attolini by means of chemical vapor deposition technique, using Si(100) as substrate and carbon monoxide as dopant precursor. Metallic Ni has been used as catalyst in the growth process, as described by M.A.A. Elmasry *et al*. [288]. The NWs, after the removal of contaminants by means of the wet procedure described in paragraph 3.7.1, have been outgassed at 300°C in UHV for several hours and then analyzed by XPS at low (PE=50eV) and high resolution (PE=10eV). Moreover, with the intention to determine if the carbon phase due to the doping process is sited on the uppermost surface or deeper, the NWs were sputtered with an ion-gun sputtering facility (ions energy at 1keV, raster $5x5mm^2$) present in the analysis chamber (see paragraph 3.2.3) and characterized by XPS and AES [284].

Figure 6.68 shows the XPS low resolution analysis both for the outgassed and sputtered NWs, putting in evidence the presence of carbon, silicon and oxygen species. Traces of nickel used as catalyst in the growth process are visible only after sputtering.

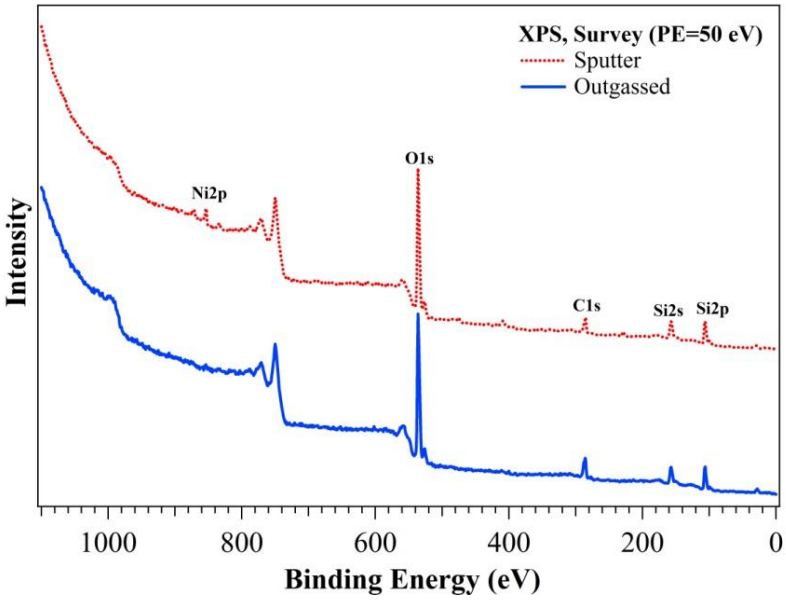

Figure 6.68: Outgassed and sputtered SiO_2 NWs XPS wide spectra (PE=50eV) [284].

Figure 6.69 shows the C1s (a), Si2p (b) and O1s (c) core levels. The first evidence in the analysis of the C1s lineshape is the presence of two main structures related to the NWs and substrate.

The NWs contributions result shifted towards high BE due to charging phenomena at the surface during measurements, in fact the typical features related to Si-O in Si2p and O1s core levels fall into a BE range totally unreliable but permitting us to calculate the shift related to charging. Taking this consideration into account, it is possible to identify some shifted components related to the NWs and other unshifted due to the substrate.

Considering C1 analysis, from the point of view of the substrate in the outgassed sample (bottom curve in Figure 6.69-a), the component C-Sub1 (285.24eV) is associated to the C-C bonds (38.7% of the total emission signal), whereas C-Sub3, located at 286.15eV, is related to C-O bonds (9.8%) of the unreacted and adventitious carbon (Table 6.15). C-Sub2 at 284.00eV is due to Si-C bonds (1.1%), as found by R. Verucchi and co-workers in their study of the SiC synthesis by SuMBD at room temperature [21]. In the same way, the components related to NWs have been identified as the C-C bonds at 288.00eV (30.5%, C-NW1), C-O and Si-O-C at 289.29eV (7.8%, C-NW3). C-NW2 (287.00eV), being located at the same energy of the difference between C-Sub1 and C-Sub2, can be associated to carbide (Si-C) in NW shell (12.1%.).

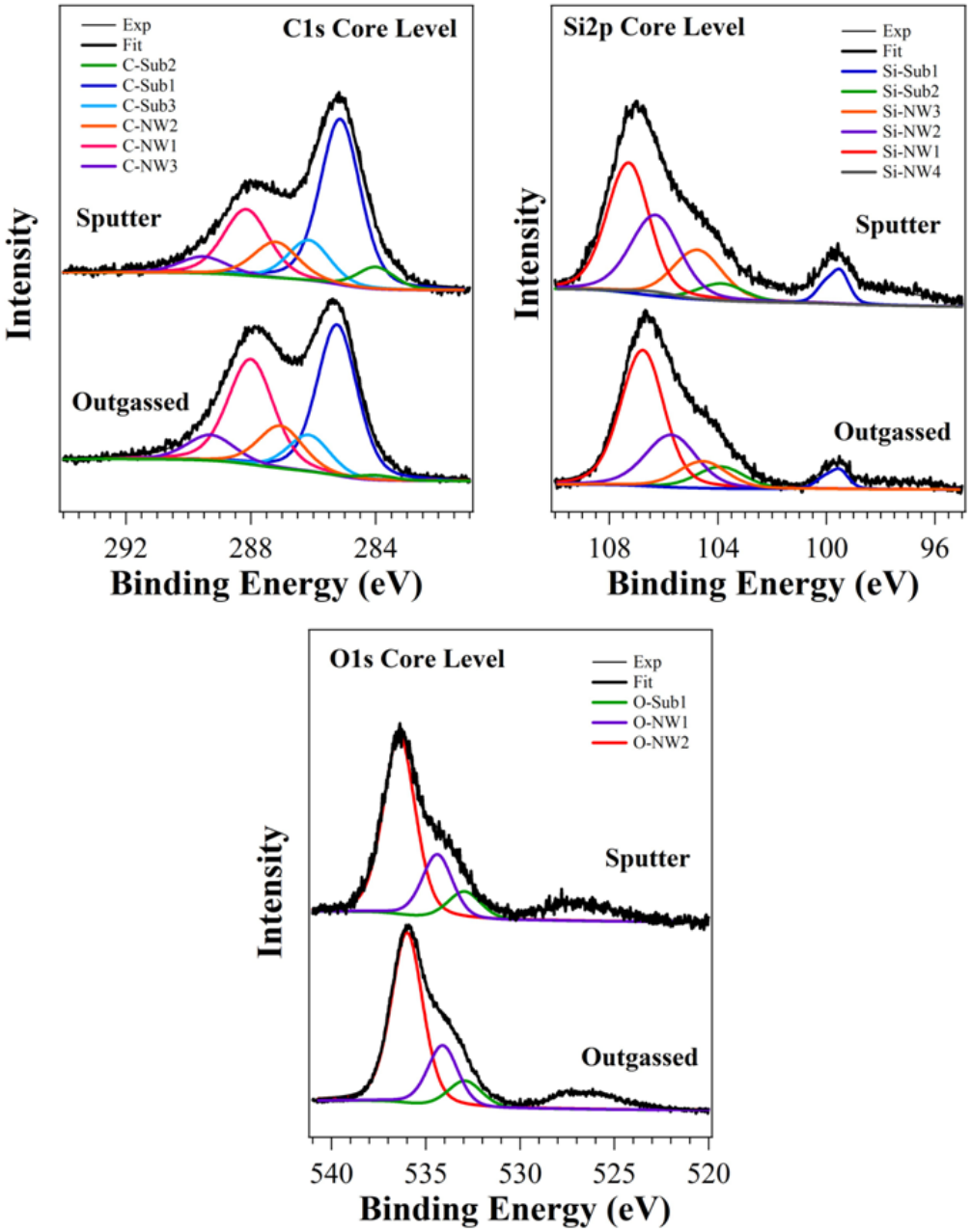

Figure 6.69: C1s (a), Si2p (b) and O1s (c) lineshapes deconvolution for the outgassed (bottom) and sputtered (top) NWs [284].

After sputtering (top curve in Figure 6.69-a), the core level shows an energy shift towards lower BE and a reduction of the components at high BE related to the NWs components, in particular C-NW1 and C-NW3, reaching a value of 15.5% and 4.1% respectively. It is then possible to extract from the change of the relative percentages of the peaks the indication about the distribution of the carbon species in the NWs, in particular we suggest the presence of C-C, Si-O-C, Si-C and Si-O compounds, respectively, from the outside

inwards. The main features of the components related to NWs and substrate are summarized in Table 6.15.

	C1s BE [eV]				Si2p BE [eV]				O1s BE [eV]		
	Outgas.	**Sput.**	**Peak**		**Outgas.**	**Sput.**	**Peak**		**Outgas.**	**Sput.**	**Peak**
C-NW1	288.00	288.15	C-C	**Si-NW1**	106.62	107.08	Si-O oxy	**O-NW1**	534.09	534.43	Si-O-C
C-NW2	287.00	287.20	Si-C	**Si-NW2**	105.67	106.05	Si-O-C	**O-NW2**	536.00	536.38	Si-O oxy
C-NW3	289.29	289.53	C-O S-O-C	**Si-NW3**	104.37	104.57	Si-C				
C-Sub1	285.24	285.14	C-C	**Si-NW4**	--------	106.20	NiO-SiO				
C-Sub2	284.00	284.00	Si-C	**Si-Sub1**	99.51	99.48	Si-Si	**O-Sub1**	532.92	533.00	Si-O oxy
C-Sub3	286.14	286.14	C-O	**Si-Sub2**	103.71	103.68	Si-O oxy				

Table 6.15: C1s and Si2p peaks position for outgassed and sputtered NWs.

Regarding Si2p core level analysis, the outgassed sample displays the two typical components (bottom curve in Figure 6.69-b) from the substrate at 99.5eV, related to the Si-Si and representing the 4.4% of the total Si2p photoemission signal, and at 103.7eV, associated to SiO_x and representing the 9.1% [55].

Moreover, it is possible to identify three peaks related to NWs, similarly to what observed in C1s core level, representing the SiO_x contribution (Si-NW1 with $x \approx 1.4$) at 106.62eV (45.9%), the oxycarbides Si-O-C at 105.67eV (Si-NW2, 27.1%) and Si-C at 104.37eV (Si-NW3, 13.3%). The sputtering process causes a shift of all the components, as reported in the Table 6.15, and it is necessary to introduce a further peak in order to deconvolute the lineshape, achieving the correct stoichiometry of the other components (panel in the top in Figure 6.69-b). This component (Si-NW4) is very low and it is located at 106.20eV representing the 1.3% of the total Si2p signal, is present only in the sputtered sample. It can be related to the interaction between the silicon oxide and the nickel/nickel oxide used as catalyst in the growth process.

O1s core level is shown in Figure 6.69-c. The outgassed sample lineshape is characterized by three peaks related to the SiO_x component of the substrate (O-Sub1, 532.92eV) and to the NWs contributions Si-O (O-NW2, 536.00eV) and Si-O-C (O-NW1, 534.09eV) contributions. The broad component at lower BE is associated to a satellites due to the non-monochromatic source used for the analysis [55]. After sputtering, the components related

to NWs are shifted towards higher BE of about +0.36eV, whereas the substrate contribution is unchanged. Moreover the weight of these components is not affected by the sputtering process and they can be estimated at about 66.5% the main peak O-NW2, 22.2% the O-NW1 and 11.3% the O-Sub1.

The evaluation of the total atomic composition of the samples after outgassing and sputtering provide additional information about the components distribution. After sputtering, as shown in the Table 6.16, the C1s contributions from NWs decreases and, moreover, it was calculated that the Si-C/C-C ratio increase whereas NW2/NW1 ratio does not vary.

ATOMIC COMPOSITION								
	OUTGASSED SAMPLE				SPUTTERED SAMPLE			
	C1s	O1s	Si2p	N2p	C1s	O1s	Si2p	N2p
NW	13.46	50.78	35.76	0.00	7.53	51.94	39.44	1.09
Sub	52.08	25.72	22.21	0.00	48.17	24.63	20.89	0.00
TOT	21.30	45.80	33.00	0.00	16.3	46.8	36.00	0.87

Table 6.16: Atomic percentages of the C1s, O1s, Si2p and N1s peaks for the NWs surface.

These evidences could suggest the presence of the carbide species inside the NWs while the oxycarbide are concentrated in the outer shell together with a small quantity of C-C, still present after the treatment. The intensity of Si-C and Si-Si components in Si2p increase after treatment: the sputtering process indeed induces the removal of carbon contamination from the substrate and from NWs, increasing the contribution due to the carbide compounds on the substrate and highlighting the presence of nickel compounds on NWs surface.

This observation is in agreement with the introduction of a new component into the Si2p peak. The oxide components both in O1s and Si2p do not show variations, confirming the hypothesis that the oxycarbides are concentrated in the outer NW shell.

As mentioned previously, the samples were routinely characterized by means of AES, giving rise to an interesting evidence. When the sample in the UHV chamber is subject to the electron beam (3 keV, 50 nA electron current) a white luminescence appears, as shown in Figure 6.70. This phenomenon decreases lowering the intensity (current) of the electron

beam, while when the electron beam spot is broadened (lower surface electron density), the luminescence becomes weaker. As a matter of fact, the white emission is the cathodoluminescence due to the interaction between electron beam and NWs.

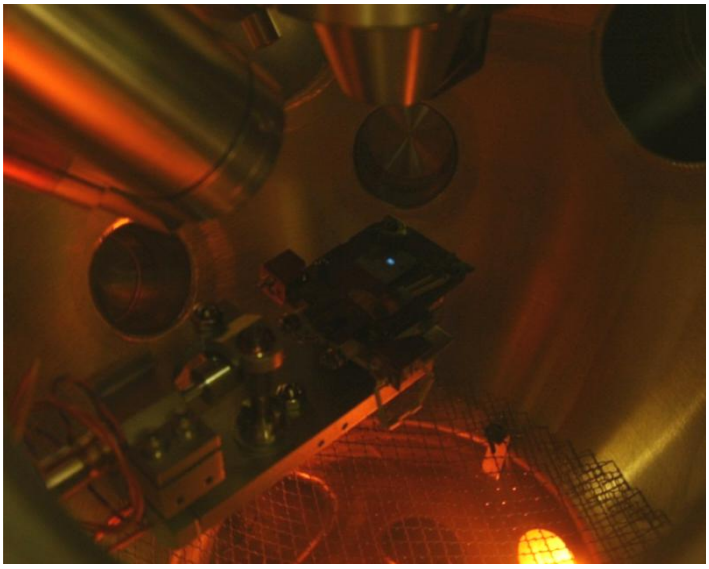

Figure 6.70: Spot due to the white cathodoluminescence emission induced by the electron beam in the UHV analysis chamber [284].

The light emission properties of these carbon-doped silicon dioxide NWs have been evaluated by cathodoluminescence spectroscopy at IMEM-CNR Institute in Parma and reveal a rather different situation with respect to similar analysis on undoped silica NWs. Without going deeper in details (see Ref. 284), the CL analysis suggests an important role of the carbon clusters as dopants in the NWs enhancing the green emission, so giving rise to the observed white spot. A similar behaviour has been proposed by L. Skuja that worked with germanium atoms as isoelectronic dopant [289]. The germanium clusters obtained in the conformation ≡Ge-Ge≡ are responsible of the peculiar 3.1-3.2eV emission, commonly observed for germanium-doped silica.

These cathodoluminescence properties make the Silica C-doped NWs a good candidate for nanostructured photosensitizers, once a functionalization with organic molecules, such as the previously used H_2TTP(F) has been performed. The idea is the same for the SiC/SiO_2 core/shell NWs, exploit their luminescence induced by electrons and thus photons to excite a porphyrin molecule, in turn being able to generate singlet oxygen and other highly reactive species for tumour therapy. This activity will be developed during 2015.

Chapter 7

Conclusions and perspectives

We have confirmed and expanded the idea that supersonic molecular beams seeded by organic precursors can pave the way to a new approach for the synthesis of materials in form of thin films. In the last years, several relevant examples have been presented by the group of IMEM-CNR in Trento that has originally proposed, developed and implemented the SuMBD technique. The main point is the kinetic activation that induces formation of chemical/physical processes, improve surface mobility during the film growth mainly exploiting the high kinetic energy of the precursors in the supersonic beam. As a matter of fact, the SuMBD approach enables to work in condition that are far from thermodynamic equilibrium, as it occurs for most of techniques used for thin film growth, and in this way it is possible to overcome potential barriers hindering specific chemical processes, or surface mobility of molecules and aggregates.

These potentialities have been addressed to specific scientific cases, aiming at realization of devices or applications in fields like electronics, optoelectronics, sensing, biomedicine. Even though significant successes have been achieved, the comprehensive knowledge of the mechanisms at the basis of the observed phenomena is far from fully being achieved. Moreover, results have already paved the way for the study of other intriguing scientific problems towards challenging applications.

This Thesis contributes to deeply understand the physical/chemical processes ruling the materials growth and synthesis by SuMBD, fully exploiting its potentialities by exploring the use of supersonic seeded beams for different scientific problems.

Three different test cases have been addressed investigating: i) the SuMBD ability to control electronic properties in organic thin films; ii) induce synthesis of nanostructured carbon-based materials; iii) functionalize inorganic surfaces.

In particular, we studied the growth of organic thin films suitable for realization of electronic devices (OFET), exploring the SuMBD ability to control electronic properties at the organic/inorganic interfaces other than morphology and device performances. The synthesis on metal of one the most promising and investigated materials, graphene, has been studied exploiting results previously achieved on other systems, were the ability of fullerene supersonic beams to break the cage and induce formation of carbon-based materials at room temperatures was shown. Finally, the complex functionalization process of inorganic nanostructures and surfaces by organic molecules with SuMBD has been addressed, towards applications of these hybrid systems in biomedicine. The approach used to investigated these different cases was based mainly on surface electron spectroscopies in in-situ experiments performed at the IMEM-CNR labs in Trento, aiming at comprehension of the electronic and structural properties of surfaces and interfaces. Ex-situ analysis have been performed as well, in collaboration with other groups, for characterization of films morphology, optical properties and performances of electronic devices.

Thin film growth by SuMBD of N,N'-1H,1H-perfluorobutil dicyanoperylenediimide (PDIF-CN_2) perylene derivative molecule on SiO_2 substrates has been studied, towards the realization of organic field effect transistors based on these π-conjugated molecules showing n-type semiconducting characteristics. Being most of organic molecules p-type semiconductors, the possibility to use this type of materials paves the way for the realization of new promising devices and p-n junctions based only on organics. The analysis of the electronic properties of organic/inorganic interfaces in these kind of devices is particularly difficult, as a number of processes rule the final behaviour of the OFET. In particular, formation of dipole at the interface, charge transfer processes, accumulation layer of carriers and possibility of doping are just few of these. In order to better tune the

ability of our analytical techniques to study these scientific problems, we analyzed an organic/organic interface based on Sexithiophene (T6) and N,N-bis(n-octyl)-dicyanoperylenediimide **(**PDI-8CN_2), a perylene derivative similar to that used in the main experiment. In this complex system, showing both organic/organic and inorganic/organic interfaces, we identified formation of surface dipole and charge transfer processes between organics, leading to an interface doping whose origin was only hypothesised but never verified before in this systems. Turning back to our main experiment, by performing deposition on SiO_2 at room temperature of the PDIF-CN_2 perylene molecule by both SuMBD and organic molecular beam (OMBD) techniques, we demonstrated the strong improvement of the structural order in the former case. This leads to the best performances for the corresponding realized OFET devices, with currents being three order of magnitude higher than for the corresponding OMBD films. From the point of view of the electronic properties, the formation of surface dipoles have been shown and most important we identified the presence of charge transfer processes from the silicon oxide layer to the organic, exploiting the presence of electron donor levels in the oxide energy gap. Even though unlikely, this process leads to a perylene LUMO location on the Fermi level and is at the origin of the observed OFET negative voltage threshold. The role of SuMBD was clearly demonstrated in the ability to improve the morphology and structure of the organic film at growth temperatures much lower than those required by OMBD (20°C instead of 120°C), fully exploiting the organic energy excess given by the supersonic beam approach in improving mobility and growth process towards a highly ordered film, thus the carrier mobility in the final device. Concerning electronic properties, structural order reflects in a higher carrier mobility, with an energy level positioning by means of a charge transfer process that allows the n-type conductance.

We studied the idea to synthesize carbon-based nanostructures, in particular graphene, on copper surfaces (polycrystalline and single crystal) by using fullerene carbon precursors by SuMBD. The IMEM-CNR group in Trento has shown that C_{60} molecule cage breaks in the collision with silicon surface at room temperature and induce the formation of nanocrystalline 3C-SiC nanoislands. Considering the known chemical/physical similarities between fullerene and graphene, we decided to investigate the rupture of the molecule in a collision with a metal surface (not showing formation of carbides), copper, in order to unwrap it, just opening the cage and create a nanofoil of graphene, with hexagons and

pentagons, but still a single layer of graphene. Theoretical modelling (LISC-FBK) suggests a possible threshold of cage rupture around 35-40 eV, similar to that observed for the C_{60} on silicon case hence achievable by our experimental set up. Supersonic beams of fullerene at 15 and 35 eV have been used to grow thin film on copper poly and Cu(111) surface, a material widely used for graphene synthesis by CVD with hydrocarbons at process temperatures higher than 1000°C. Our preliminary study of the electronic properties of this interface has clearly shown a strong chemical interaction at the interface of the first layer, with chemisorption leading to a sort of metallic character of the first C_{60} monolayer. We identified the presence of the few carbon atoms interacting with the copper ones, in agreement with a model where a surface metal reconstruction has been hypothesized, a sort of cup where the fullerene cage is placed. What seems clear is that the C_{60}/Cu interface is ruled by the mobility of the organic on the metal, in order to find the most favourable atomic site and create a (4x4) rearrangement thanks to the good lattice matching between C_{60} crystal and Cu(111). In fact, we have found the absence of cage rupture an all copper surfaces, at both C_{60} kinetic energies, with a substrate temperature from 20°C to 500°C. This is a clear indication that the energy excess given by the supersonic beam is being used to promote processes different than the cage rupture. The strong and favourable superposition of organic molecular orbitals and metal 3d surface states, proved by the efficient chemisorption process, probably enables the energy transfer from C_{60} to copper surface with dissipation of the original kinetic energy in lattice phonons, or promotion of the organic surface mobility. The cage rupture observed for the C_{60}/Si case occurred on a chemically active but semiconducting surface, where probably these kind of effects are less important. We finally achieved cage rupture by thermal treatments of fullerene single layer films on poly Cu/Cu(111) deposited at 15/35 eV, at temperatures of 550/645°C respectively. The carbon based film on the surface have shown electronic properties different from that of a C_{60} single layer, similar to that of defected graphene, especially for the first case where sulphur contamination (from copper surface) was observed and that, once exposed to air, has been subject of a strong oxidation as confirmed by ex-situ Raman characterization. The film on Cu(111) at 645°C has shown about the same electronic properties of the former, with a great stability up to about 800°C, Raman analysis revealed a highly defected but single layer graphene film, with no oxidation. Synthesis of graphitic layers after fullerene fragmentation have been reported, but never graphene formation. We found presence of the cage portion located in the copper surface cup even after the cage

rupture, so we think the break occurs when the cage is in its most favourable surface location, inside the copper cup and bonds breaking occurs in the molecule portion just outside the cup itself, as already hypothesized for the C_{60}/Ru(111) surface. In this case, formation of a complete graphene layer was achieved only at 1200K (930°C) while graphene quantum dots have been found also at 650K (380°C). This suggests that the role of the fullerene kinetic energy could be that the molecule really reach the best surface location, as rupture cannot be achieved during the first organic/metal surface collision, at least at the used experimental conditions. Anyway, the SuMBD approach seems to be a promising and viable technique for synthesis of graphene.

The third scientific case was the functionalization by supersonic beam of partially fluorinated tetraphenylporphyrin (H_2TTP(F)) of silicon oxide based surfaces, in forms of planar film and SiC/SiO_2 core shell nanowires. The final aim was to create nanohybrid systems that could be suitable as photosensitizers in photodynamic therapy (PDT) activated by X-rays instead of visible light, on the basis of a scheme proposed few years ago to overcome limitations of the traditional PDT approach. SiC/SiO_2 core shell NWs are composed of a SiC core surrounded by a silicon oxide layer: the favourable electronic level coupling of the two material leads to a strong luminescence induced by electron and photon at high energies, a luminescence spectrum which well matches the optical absorption characteristics of the H_2TTP(F) molecule. Shortly, a photon beam would induce the excitation and luminescence of the inorganic counterpart, that would be absorbed, transferred to the porphyrin, this in turn becomes able to produce highly oxidizing chemical species, like singlet oxygen, able to induce death in tumour cells. Due to the highly insulating character of NWs, we studied the most simpler case of deposition of H_2TTP(F) on a native silicon oxide layer, showing similar chemical characteristic of a SiO_2 NW surface but with lower density of surface defects. While it is known that at molecule kinetic energies of 0.5 eV, only physisorption occurs during the film growth, at 25 eV we have found evidence of a strong chemical activity. We observed the formation of an initial wetting layer, characterized by a sticking coefficient being 8 times lower than after its completion, when a quick and sudden film growth occurs. The wetting layer is formed by a single layer of molecule experiencing a charge transfer from the electron donor levels in the oxide layer, in particular from the oxygen atoms on the surface to the fluorine on the phenyl rings. This electron charge transfer, that is due to the electron withdrawing property

of fluorine, leads to a band bending in the inorganic and formation of surface dipoles. Once completed the wetting layer, the growth starts quickly and is characterized by the mentioned higher sticking coefficient. However, island formation before the layer completion has been found, probably on specific surface regions where a local wetting layer completion at the nanoscale has been achieved. The electron charge excess at the organic/inorganic interface is compensated by the presence of positively charged layers, as put in evidence by the occurrence of a depletion layer that matches the properties of the film after completion of the first functionalizing layer and the thick molecular film. These matching layers are probably due to a different molecule rearrangement and film structure rather than on organic/organic charge transfer processes, that indeed have not been observed. The possibility to achieve chemisorption and charge transfer processes from insulating inorganics also in molecule showing so large HOMO-LUMO gap, and a energy level matching far less favourable than what observed for perylene (that has lower gap and ionization potential), is a consequence of the high organic molecule kinetic energy given by the SuMBD approach. The number and quality of physical/chemical processes induced by the oxide functionalization is impressive, leading to film with a growth trend never observed before for deposition of organics on inorganics. The study of the H_2TTP(F)/NWs interaction has taken great advantage from the former results. The film growth kinetic is characterized by a higher sticking coefficient, right from the very early stages. This is surprising since, if we compare the surface area of NWs and native silicon oxide exposed to molecule deposition, the total NWs value is about 40 times higher but formation of a complete molecular film is achieved in the same deposition times. The processes occurring at the interface are once more characterized by charge transfer from the oxide layer to the fluorinated phenyls, but in this case the efficiency is by far higher than in the planar oxide case. Band bending occurs for the inorganic counterpart. Thanks to the higher sticking coefficient, it has been possible to find evidence of the charge transfer also in carbon atoms of the fluorinated phenyls, that experience a binding energy shift towards lower binding energies such as fluorines, due to the electron charge excess. This means that a significant charge rearrangement occurs in the fluorinated rings, probably on all four rings. More in details, two different kinds of molecules can be identified, one chemisorbed experiencing the mentioned charge transfer, and a second one physisorbed, related to not interacting porphyrins. This suggests a very diffused interface, with the presence at the same time of NWs being partially or totally functionalized, as also clean or at early growth stages. The

efficiency of the chemical/physical processes at the organic/inorganic interface is very high, probably due to the higher defects density on the NWs surface that are at the basis of the charge transfer process in chemisorption. These results clearly demonstrate the feasibility of the SuMBD approach to create nanohybrids systems for PDT, with results at least comparable but more reliable than for functionalization achieved by wet chemistry approach with other porphyrins.

The results achieved in this Thesis led (and will lead) to publication of several papers on international high impact journal, as reported in the list below.

[1] L. Aversa, R. Verucchi, R. Tatti, F.V. Di Girolamo, M. Barra, F. Ciccullo, A. Cassinese and S. Iannotta, Surface doping in T6/PDI-8CN_2 heterostructures investigated by transport and photoemission measurements, Appl. Phys. Lett. 2012, 101, 233504;

[2] M. Bosi, G. Attolini, M. Negri, C. Frigeri, E. Buffagni, C. Ferrari, T. Rimoldi, L. Cristofolini, L. Aversa, R. Tatti and R. Verucchi, Optimization of a buffer layer for cubic silicon carbide growth on silicon substrates, Journal of Crystal Growth, 2013, 383, 84-94;

[3] D. Pontiroli, M. Aramini, M. Gaboardi, M. Mazzani; S. Sanna, F. Caracciolo, P. Carretta, C. Cavallari; S. Rols, R. Tatti, L. Aversa, R. Verucchi and M. Riccò, Tracking the Hydrogen Motion in Defective Graphene, The Journal of Physical Chemistry C, 2014, 118 (13), 7110-7116;

[4] F. Chiarella, T. Toccoli, M. Barra, L. Aversa, F. Ciccullo, R. Tatti, R. Verucchi, S. Iannotta, A. Cassinese, High mobility PDIF-CN2 n-type thin-film transistors deposited at room temperature by supersonic molecular beam deposition, Applied Physics Letters, 2014, 104, 143302

[5] F. Fabbri, M. Negri, F. Rossi, R. Tatti, L. Aversa, S. Chander, R. Verucchi, G. Attolini, G. Salviati, Carbon doped SiOx nanowires with large yield white emission, Nanotechnology, 2014, 25, 185704;

[6] M. Bosi, G. Attolini, M. Negri, C. Frigeri, E. Buffagni, C. Ferrari, T. Rimoldi, L. Cristofolini, L. Aversa, R. Tatti and R. Verucchi, High quality 3C-SiC/Si grown on an optimized SiC buffer layer, Material Science Forum, In press;

[7] R. Tatti, L. Aversa, R. Verucchi, S.Iannotta, S. Taioli, Synthesis of graphene on copper surfaces by C_{60} supersonic molecular beams, to be submitted to Physical Chemistry Chemical Physics

[8] R. Tatti, L. Aversa, R. Verucchi, T. Rimoldi, L. Cristofolini, F. Rossi, F. Fabbri, G. Salviati, S.Iannotta, Functionalization of SiOx surfaces by supersonic beams of H_2TPP(F), to be submitted to Physical Review B

Outcome and perspectives.

The relevant results achieved give answers to scientific problems that were known but not still solved, paving the way to the realization of the envisaged applications previously described. Moreover, some themes are still open and some other emerged right during the Thesis work.

Regarding growth of organic thin films for electronics application, the achieved results will be useful to realize new organic-based electronic devices, such as p-n heterojunctions fully based on SuMBD deposition and codeposition of different type of molecule in order to achieve doping effects in three-dimensional structures rather than only localized at an interface between bi-dimensional films. Relevant application could be light organic emitting transistors (LET), exploiting the specific molecular optical properties and the use of supersonic beams to grow highly ordered thin films.

Study of C_{60} deposition on metal surfaces in order to achieve graphene synthesis will continue. We will perform other studies in order to better clarify the role of C_{60} kinetic energy in determining the observed process. We envisage the possibility to induce the fullerene (4x4) rearrangement at room temperature instead of 300-400°C by using suitable molecule kinetic energies, improving fullerene surface mobility. Due to the different de-excitation channels, they could be used to improve mobility on surface. We will try also to increase the maximum reachable kinetic energy, but this will require some significant changes in our SuMBD source, moreover already programmed. Another case of study will be the use of different metals surfaces, characterized by different reactivity like nickel, or other showing decoupling of surface states and molecular orbitals, as could be for a highly insulating material like SiO_2, TiO_2.

Finally, functionalization of NWs will continue with other kinds of materials. At the end of Chapter 6, we presented the characterization of silica NWs, that show interesting white fluorescence similarly to the SiC/SiO_2 core/shell type, thus they could be once more used as inorganic counterpart for photosensitizers for PDT. Their surface presents different types of oxides and compounds, together also with carbon-based compounds, probably at the origin of the observed white fluorescence. This lead probably to presence of several defects states in the surfaces, being possible source of electrons for charge transfer processes achieved during H_2TTP(F) functionalization by SuMBD.

References

[1] M.J. Cardillo, C.S.Y. Ching, E.F. Greene, G.E. Becker, J. Of Vacuum Science and Technology 15, 423, 1978

[2] G. Scoles, Atomic and Molecular Beam Methods, Oxford University Press, Oxford, 1988

[3] P. Milani and S. Iannotta, *Cluster Beam Synthesis of Nano-structured Materials*, Springer-Verlag, Berlin, 1999

[4] W. Gerlach and O. Stern, *Z.* Physik 8, 110, 1921; 9, 349, 1921

[5] A. Kantrowitz and J. Grey, Rev. Sci. Instr. 22, 328, 1951

[6] E.W. Becker and K. Bier, Zeitschrift Fuer Naturforschung A 9, 975, 1956

[7] E.W. Becker and W. Henkes, Z. Physik. 146, 320, 1956

[8] O. Hagen and W. Henkes, Zeitschrift Fuer Naturforschung A 15, 851, 1960

[9] J.B. Anderson, *Molecular Beams and Low Density Gasdynamics*, edited by P.P. Wegener, New York, Dekker, 1974

[10] A. Podestà, T. Toccoli, P. Milani, A. Boschetti, S. Iannotta, Surf. Sci. 464, L673, 2000

[11] S. Iannotta, T. Toccoli, A. Boschetti, M. Ferrari, Appl. Phys. Lett. 76, 1845, 2000

[12] S. Iannotta, T. Toccoli, Journal of Polymer Science: Polymer Physics 41, 2501, 2003

[13] T Toccoli, A. Pallaoro, N. Coppedè, S. Iannotta, F. De Angelis, L. Mariucci, and G. Fortunato, Appl. Phys. Lett. 88, 132106, 2006

[14] Y. Wu, T. Toccoli, N. Koch, E. Iacob, A. Pallaoro, P. Rudolf, S. Iannotta, Phys. Rev. Lett. B 98, 076601, 2007

[15] L. Casalis, M.F. Danisman, B. Nickel, G. Bracco, T. Toccoli, S. Iannotta, G. Scoles, Phys. Rev. Lett. 90, 206101, 2003

[16] A. Graham and J.P. Toennies, Surf. Sci. 427, 1, 1999

[17] T. Toccoli, S. Capone, L. Guerini, M. Anderle, A. Boschetti, E. Jacob, V. Micheli, P. Siciliano and S. Iannotta, IEEE Sensors Journal 3, 199, 2003

[18] O. Hagena and Obert, J. Chem. Phys. 56, 1793, 1972

[19] M. Henini, Thin Solid films 306, 331, 1999 and references therein

[20] M. Nardi, R. Verucchi, R. Tubino, S. Iannotta, Phys. Rev. B 79, 125404, 2009

[21] R. Verucchi, L. Aversa, M.V. Nardi, S. Taioli, S. a Beccara, D. Alfè, L. Nasi, F. Rossi, G. Salviati and S. Iannotta, J. Am. Chem. Soc. 134, 17400, 2012

[22] F. Rosei, R. Rosei, Surf. Sci. 500, 395, 2002

[23] A.P. Graham, Surf. Sci. Rep. 49, 115, 2003

[24] J. Palisaitis, Physics of Advanced Materials Winter School, 2008.

[25] S.R. Forrest, Chemical Reviews 97, 1793, 1997

[26] S.A. Ustin, K.A. Brown, W. Ho, Rev. Sci. Instr. 71, 1479, 2000

[27] J-H. Boo, S.A. Ustin, W. Ho, Thin solid films 343-344, 650, 1999

[28] R. Malik, E. Gulari, S.H. Li, P.K. Bhattacharya, J. Singh, J. of crystal Growth 150, 984, 1995

[29] R. Verucchi, L. Aversa, G. Ciullo, A. Podestà, P. Milani and S. Iannotta, European Phys. J. B 26, 509, 2002

[30] L. Aversa, R. Verucchi, G. Ciullo, L. Ferrari, P. Moras, M. Pedio, A. Pesci and S. Iannotta, Appl. Surf. Sci. 184, 350, 2001

[31] S. Lee, B. Koo, J. Shin, E. Lee, H. Park and H. Kim, Appl. Phys. Lett. 88, 162109, 2006

[32] R. Ruiz, D. Choudhary, B. Nickel, T. Toccoli, K.C. Chang, A.C. Mayer, P. Clancy, J.M. Blakely, R.L. Headrick, S. Iannotta and G.G. Malliaras, Chem. Mater. 16, 4497, 2004

[33] J.W. Chang, H. Kim, B.K. Ju, J. Jang and Y.H. Lee, J Korean Phys. Soc. 42, 647, 2003

[34] F. Detto, PhD Thesis in Science and Technology of Innovative Materials, Parma University, 2012

[35] M.V. Nardi, PhD Thesis in Material Science, Milano “Bicocca” University, 2007

[36] T.S. Kang, B.S. Harrison, T.J. Foley, A.S. Knefely, J.M. Boncella, J.R. Reynolds, K.S. Schanzea, Adv. Mater. 15, 1093, 2003

[37] R. Pizzoferrato, L. Lagonigro, T. Ziller, A. Di Carlo, R. Paolesse, F. Mandoj, A. Ricci, C. lo Sterzo, Chem. Phys. 300, 217, 2004

[38] J.B. Oh, K.L. Paik, J.W. Ka, S.G. Roh, M.K. Nah, H.K. Kim, Mater. Sci. Eng. C 24, 257, 2004

[39] A. Kahn, N. Kock, W. Gao, J. Polym. Sci., Part B: Polym. Phys. 41, 2529, 2003

[40] H. Morkoç, S. Strite, G.B. Gao, M.E: Lin, B. Sverdlov, M. Burns, J. Appl. Phys. 76, 1363, 1994

[41] W.A. Nevin, H. Yamagishi, M. Yamaguchi, Y. Tawada, Nature, 368, 529, 1994

[42] B.J. Baliga, Mater. Res. Soc. Symp. Proc. 512, 77, 1998

[43] A.J. Steckl, IEEE Trans. Electron. Devices 39, 64, 1992

[44] A.W. Dunn, P. Moriarty, P.H. Beton, J. Vac. Sci. Technol. A 15, 1478, 1997

[45] G.L. Harrys, *Properties of Silicon Carbide*, Ed. INSPEC: London, 1995

[46] K. Sakamoto, T. Susuki, M. Harada, T. Wakita, S. Suto, A. Kasuya, Phys. Rev. B 57, 9003, 1998

[47] M. de Seta, N. Tomozeiu, D. Sanvitto, F. Evangelisti, surf. Sci. 460, 203, 2000

[48] S. Taioli, G. Garberoglio, S. Simonucci, S. a Beccara, L. Aversa, M.V. Nardi, R. Verucchi, S. Iannotta, M. Dapor and D. Alfè, J. Chem. Phys. 138, 144701, 2013

[49] J. Hutter, J. Chem. Phys. 118, 3928, 2003

[50] W.C. Wiley, I.H. McLaren, Reviews of Scientific Instruments 65, 1150, 1994

[51] P. Piseri, Tesi di Laurea in Fisica, Università degli Studi di Milano, A.A. 1993-1994

[52] L. Aversa, PhD Thesis in Physics, Trento University, 2004

[53] G.A. Somorjai, introduction to surface chemistry and catalysis, Wiley-Interscience USA 199

[54] S. Hüfner, Photoelectron Spectroscopy, Springer-Verlag, Berlin 1995

[55] Handbook of X-Ray Photoelectron Spectroscopy, Ed. By J. Chastain and r.C. King, Physical electronics Inc., 1992, USA

[56] Y. Gao, Materials Science and Engineering R 68, 39, 2010

[57] W. Chen, D. Qi, X. Gao, A.T.S. Wee, Progress in Surface Science 84, 279, 2009

[58] W. Chen, D.C. Qi, H. Huang, X. Gao and A.T.S. Wee, Adv. Funct. Mater. 21, 410, 2011

[59] D. Briggs and M. Seah, Practical Surface Analysis, Wiley Frankfurt 1990

[60] E.G. McRae, Surface Science 124, 106, 1983

[61] M.A. VanHove, W.H. Weinberg, C.M. Chan, Low-Energy Electron Diffraction, Springer-Verlag, Berlin 1996

[62] T.W. Collette and T.L. Williams, J. Environ. Monit. 4, 27, 2002

[63] This algorithm was originally developed by R. Kwok: http://www.chem.qmw.ac.uk/surface

[64] L.E. Davis, N.C. MacDonald, P.W. Palmberg, G.E. Riach, R.E. Weber, Handbook of Auger Electron Spectroscopy, pub. By Physical Electronics Industries, USA 1978

[65] R.L. Carroll and C.B. Gorman, Angew. Chem. Int. Ed 41, 4378, 2002

[66] R.F. Pierret, "Semiconductor Device Fundamentals". Reading, Massachusetts: Addison Wesley Longman 1996

[67] M.J. Małachowski and J. Zmija, Opto-Electron. Rev. 18, 121, 2010

[68] E. Menard, Y. Sun, J.U. Park, D.J.L. Shir, Y.S. Nam, S. Jeon and J.A. Rogers, Chem. Rev. 107, 1117, 2007

[69] C.D. Dimitrakopoulos and P.R.L. Malefant, Adv. Mater. 14, 99, 2002

[70] Th.B. Singh and N.S. Sariciftci, Annu. Rev. Mater. Res. 36, 199, 2006

[71] Y. Diao, B.C.K. Tee, G. Giri, J. Xu, D.H. kim, H.A. Becerril, R.M. Stoltenberg, T.H. Lee, G. Xue, S.C.B. Mannsfeld, Z. Bao, Nat. Mater. 12, 665, 2013

[72] A.Y. Amin, A. Khassanov, K. Reuter, T. Meyer-Friedrichsen, M. Halik, J. Am. Chem. Soc. 134, 16548, 2012

[73] N. Kurihara, A. Yao, M. Sunagawa, Y. Ikeda, K. Terai, H. Kondo, M. Saito, H. Ikeda, H. Nakamura, Jpn. J. Appl. Phys. 52, 05DC11, 2013

[74] H. Minemawari, T. Yamada, H. Matsui, J. Tsutsumi, S. Haas, R. Chiba, R. Kumai, T. Hasegawa, Nature, 475, 364, 2011

[75] A. Facchetti, Materials Today 10, 28,2007

[76] G. Horowitz, R. Hajlaoui and F. Kouki, Eur. Phys. J. AP 1, 361, 1998

[77] M. Mas-Torrent and C. Rovira, Chem. Soc. Rev. 37, 827, 2008

[78] Th.B. Singh, N.S. Sariciftci, M. Jaiswal and R. Menon, Handbook of Organic Electronics and Photonics, Vol.3, Edited by Hari Singh Nalwa, 153-176, 2008

[79] Y.Y. Lin, D.J. Gundlach, S.F. Nelson, T.N. Jackson, IEEE Trans. Electron Dev. Lett. 18, 606, 1997

[80] Y. Sun , Y. Liu and D. Zhu, J. Mater. Chem. 15, 53, 2005

[81] C. Goldman, S. Haas, C. Krellner, K.P. Pernstich, D.J. Gundlach and B. Batlogg., J. Appl. Phys. 96, 2080,2004

[82] A. Facchetti, Y. Deng, A. Wang, Y. Koide, H. Sirringhaus, T.J. Marks and R.H. Friend, Angew. Chem. Int. Ed. 39, 4547, 2000

[83] M.H. Yoon, S.A. Di Benedetto, A. Facchetti, T.J. Marks, J. Am. Chem. Soc. 127, 1348, 2005

[84] H. Dong, C. Wang and W. Hu, Chem. Commun. 46, 5211, 2010

[85] M.M. Ling and W. Hu, Chem. Mater. 16, 4824, 2004

[86] Y.D. Park, J.A. Lim, H.S. Lee, K. Cho, Mater. Today 10, 46, 2007

[87] K. Xiao, Y. Liu, G. Yu and D. Zhu, Appl. Phys. A 77, 367, 2003

[88] C.D. Dimitrakopoulos, S. Purushothaman, J. Kymissis, A. Callegari, J.M. Shaw, J. Appl. Phys. 80, 2501, 1996

[89] C.D. Dimitrakopoulos and D.J. Mascaro, IBM J. Res. Dev. 45, 11, 2001

[90] C. Kim, K. Bang, I. An, C.J. Kang, Y.S. Kim, D. Jeon, Current Applied Physics 6, 925, 2006

[91] J.A. Lim, H.S. Lee, W.H. Lee and K. Cho, Adv. Funct. Mater. 19, 1515, 2009

[92] D.H. Kim, H.S. Lee, H. Yang and K. Cho, Adv. Funct. Mater. 18, 1363, 2008

[93] D.J. Gundlach, J.E. Royer, S.K. Park, S. Subramanian, O.D. Jurchescu, B.H. Hamadani, A.J. Moad, R.J. Kline, L.C. Tague, O. Kirillov, C.A. Richter, J.G. Kushmerick, L.J. Richter, S.R. Parkin, T.N. Jackson and J.E. Anthony, Nat. Mater. 7, 216, 2008

[94] H.Y. Choi, S.H. Kim, J. Jang, Adv. Mater. 16, 732, 2004

[95] S. Steudel, S. De Vusser, S. De Jonge, D. Janssen, S. Verlaak, J. Genue, P. Heremans, Appl. Phys. Lett. 85, 5550, 2004

[96] A.L. Briseno, S. CB Mannsfeld, M.M. Ling, S. Liu, R.J. Tseng, C. Reese, M.E. Roberts, Y. Yang, F. Wudl, Z. Bao, Nature 444, 913, 2006

[97] Langmuir-Blodgett Films, ed. G. Roberts, Plenum Press, USA, 1990

[98] D.E. Bornside, C.W. Macosko, L.E. Scriven, J. Imaging Tech. 13, 122, 1987

[99] N. Sahu, B. Parija and S. Panigrahi, Indian J. Phys. 83(4), 493, 2009

[100] R. Tubino, A. Borghesi, L. Dalla Bella, S. Destri, W. Porzio, A. Sassella, Optical Materials 9, 437, 1998

[101] S.R. Forrest, Chem. Rev. 97, 1793, 1997

[102] T. Toccoli, A. Boschetti, C. Corradi, L. Guerini, M. Mazzola and S. Iannotta, Synth. Met. 137, 3, 2003

[103] G. Horowitz, R. Hajlaoui, R. Bourguiga, M. Hajlaoui, Synthetic Metals 101, 401, 1999

[104] S.M. Sze, Semiconductor Devices, Physics and Technology, John Wiley & Sons, Inc., 2002

[105] J. Ristein, Science 313, 1057, 2006

[106] K. Szacłowski, Infochemistry: information processing at the nanoscale, John Wiley & Sons, United Kingdom, 2012

[107] J. Ristein, J. Phys. D: Appl. Phys. 39, R71, 2006

[108] W. Chen, D. Qi, X. Gao and A.T.S. Wee, Progress in Surface Science 84, 279, 2009

[109] F. Dinelli, M. Murgia, P. Levy, M. Cavallini, F. Biscarini and D.M. de Leeuw, Phys. Rev. Lett. 92, 116802, 2004

[110] W. Chen, S. Chen, D.C. Qi, X.Y. Gao, A.T. Wee, J. Am. Chem. Soc. 129(34), 10418, 2007

[111] I.G. Hill, A. Rajagopal, A. Kahn, Y. Hu, Appl. Phys. Lett. 73(5), 662, 1998

[112] X. Crispin, V. Geskin, A. Crispin, J. Cornil, R. Lazzaroni, W.R. Salaneck and J.L. Bredas, J. Am. Chem Soc. 124, 8131, 2002

[113] H. Wang, Z. Liu, T.W. Ng, M.F. Lo, C.S. Lee, D. Yan and S.T. Lee, Appl. Phys. Lett. 96, 173303, 2010

[114] A. Rajagopal, C.I. Wu, A. Kahn, J. Appl. Phys. 83, 2649, 1998

[115] W. Chen, S. Chen, S. Chen, Y.L. Huang, H. Huang, D.C. Qi, X.Y. Gao, J. Ma and A.T.S. Wee, J. Appl. Phys. 106, 064910, 2009

[116] W. Chen, H. Huang, S. Chen, Y.L. Huang, X.Y. Gao and A.T.S. Wee, Chem. Mater. 20, 7017, 2008

[117] I. Salzmann, S. Duhm, G. Heimel, M. Oehzelt, R. Kniprath, R.L. Johnson, J.P. Rabe and N. Koch, J. Am. Chem. Soc. 130, 12870, 2008

[118] S. Duhm, G. Heimel, I. Salzmann, H. Glowatzki, R.L. Johnson, A. Vollmer, J.P. Rabe and N. Koch, Nat. Mater. 7, 326, 2008

[119] F.V. Di Girolamo, M. Barra, F. Chiarella, S. Lettieri, M. Salluzzo, and S. Cassinese, Phys. Rev. B 85, 125310, 2012

[120] A.C. Hosokawa, H. Higashi, T. Kusumoto, Appl. Phys. Lett. 62, 3238, 1993

[121] A. Jones, A. Facchetti, M.R. Wasielewski, T.J. Marks, J. Am. Chem. Soc. 129, 15259, 2007

[122] H. Wang, J. Wang, H. Huang, X. Yan, D. Yan, Org. Electron. 7, 369, 2006

[123] L. Aversa, R. Verucchi, R. Tatti, F.V. Di Girolamo, M. Barra, F. Ciccullo, A. Cassinese and S. Iannotta, Appl. Phys. Lett. 101, 233504, 2012

[124] Y. Ge and J.E. Whitten, Chem. Phys. Lett. 448, 65, 2007

[125] J. Ivanco, J.R. Krenn, M.G. Ramsey, F.P. Netzer, T. Haber, R. Resel, A. Haase, B. Stadlober and G. Jakopic, J. Appl. Phys. 96, 2716, 2004

[126] M. Grobosch and M. Knupfer, Org. Electron. 8, 625, 2007

[127] A. Chandekar and J.E. Whitten, Synth. Met. 150, 259, 2005

[128] O. Pellegrino, M. Rei Vilar, G. Howitz, F. Kouki, G. Garnier, J.D. Lopes da Silva and M. Botelho do Rego, Thin solid Films 327, 291, 1998

[129] D. Jin, W. Wang, A. Rahmana, J. Lizhen, H. Zhang, H. Li, P. Hea, and S. Bao, Appl. Surf. Sci. 257, 4994, 2011

[130] F. Chiarella, T. Toccoli, M. Barra, L. Aversa, F. Ciccullo, R. Tatti, R. Verucchi, S. Iannotta and A. Cassinese, Appl. Phys. Lett. 104, 143302, 2014

[131] R.T. Weitz, K. Amsharov, U. Zschieschang, E. Barrena Villas, D.K. Goswami, M. Burghard, H. Dosch, M. Jansen, K. Kern, H. Klauk, J. Am. Chem. Soc. 130, 4637, 2008

[132] H.W. Kroto, J.R. Heat, S.C. O'Brien, R.F. Curl and R.E. Smalley, Nature 318, 162, 1985

[133] S. Iijima, Nature 354, 56, 1991

[134] R.E. Smalley, in Transcript of Panel Discussion for Workshop on fundamentals of carbon/carbon, 7 December 1990 (Ed.: L.W. Burggraf) Air Force Office of Scientific Research, Bolling AFB, 16, D.C. 1993

[135] K.S. Novoselov, A.K. Geim, S.V. Morozov, D. Jiang, Y. Zhang, S.V. Dubonos, I.V. Grigorieva, A.A. Firsov, Science 306, 666, 2004

[136] A.K. Geim, Science 324, 1530, 2009

[137] L. Landau, Phys. Z. Sowjetunion 11, 545, 1937; N.D. Mermin, Phys. Rev. 176, 250, 1968

[138] A.K. Geim and K.S. Novoselov, Nat. Materials 6, 183, 2007

[139] M.S. Dresselhaus, G. Dresselhaus, P.C. Eklund, Science of Fullerene and CarbonNanotubes, AcademicPress, San Diego, 1996

[140] C. Riedl, C. Coletti and U. Starke, J. Phys. D: Appl. Phys. 43, 374009, 2010

[141] P.R. Wallace, Phys. Rev. 71, 622, 1947

[142] A.C. Neto, F. Guinea, N.M. Peres, K.S. Novoselov, A. K. Geim, Rev. Mod. Phys. 81, 109, 2009

[143] T. Ando, NPG Asia Mater. 1, 17, 2009; E.Y. Andrei, G. Li and X. Du, Rep. Prog. Phys. 75, 056501, 2012

[144] M. Batzill, Surf. Sci. Rep. 67, 83, 2012

[145] A.C. Neto, F. Guinea, N.M. Peres, Physics World 19, 33, 2006

[146] T. Ohta, A. Bostwick, T. Seyller, K. Horn and E. Rotenberg, Science 313, 951, 2006

[147] K.S. Novoselov, E. McCann, S.V. Morozov, V.I. Fal'kp, M.I. Katsnelson, U. Zeitler, D. Jiang, F. Schedin and A.K. Geim, Nature Phys. 2, 177, 2006

[148] E. McCann, Phys. Rev. B 74, 161403, 2003

[149] P. Byszewski and Z. Klusek, Opto-Electron. Rev. 9, 203, 2001

[150] D. Bonchev and D.H. Rouvray (Eds.), C*hemical Topology: introduction and fundamentals*, Gordon & breach, Amsterdam 1999

[151] K. Hedberg, L. Hedberg, D.S. Bethune, C.A. Brown, H.C. Dorn, R.D. Johnson and M. de Vries, Science 254, 410, 1991

[152] M.S. Dresselhaus, G. Dresselhaus and P.C. Eklund, Science of fullerene and carbon nanotubes, Elsevier Science USA, San Diego, 1996

[153] M. Prato, J. Mater. Chem. 7, 1097, 1997

[154] R.C. Haddon, Accounts Chem. Res. 25, 127, 1992

[155] S.B. Singh and A. Singh, Int. J. Chem. Tech. Res. 5, 167, 2013

[156] K.D. Tsuei, J.Y. Yuh, C.T. Tzeng, R.Y. Chu, S.C. Chung and K.L. Tsang, Phys. Rev. B 56, 15412, 1997

[157] S. Braun, W.R. Salaneck, M. Fahlman, Adv. Mater. 21, 1450, 2009

[158] N. Koch, ChemPhysChem 8, 1438, 2007

[159] T.R. Ohno, Y. Chen, S.E. Harvey, G.H. Kroll and J.H. Weaver, Phys. Rev. B 44, 13747, 1991

[160] S. Modesti, S. Cerasari, P. Rudolf, Phys. Rev. Lett. 71, 2469, 1993

[161] A.J. Maxwell, P.A. Bruhwiler, A. Nilsson, N. Martensson, and P. Rudolf, Phys. Rev. B 49, 10717, 1994

[162] G.K. Weitheim and D.N.E. Buchanan, Phys. Rev. B 50, 11070, 1994

[163] A. Sellidj and B.E. Koel, J. Phys. Chem.. 97, 10076, 1993

[164] M. Pedio, K. Hevesi, N. Zema, M. Capozi, P. Perfetti, R. Gouttebaron, J.-J. Pireaux, R. Caudano, P. Rudolf, Surface Science 437, 249, 1999

[165] T.R. Ohno, Y. Chen, S.E. Harvey, G.H. Kroll, P.J. Benning, J.H. Weaver, Phys. Rev. B 47, 2389, 1993

[166] M.W. Ruckman, Bo Xia, S.L. Qiu, Phys. Rev. B 48, 15457, 1993

[167] Y.Z. Li, M. Chander, J.C. Patrin, J.H. Weaver, L.P.F. Chibante and R.E. Smalley, Phys. Rev. B 45, 13837, 1992

[168] H. Xu, D.M. Chen and W.N. Creager, Phys. Rev. Lett, 70, 1850, 1993

[169] B.S. Itchkawitz, J.P. Long, T. Schedel-Niedrig, M.N. Kabler, A.M. Bradshaw, R. Schlogl, W.R. Hunter, Chem. Phys. Letters 243, 211, 1995

[170] T. Hashizume, K. Motai, X.D. Wang, H. Shinohara, Y. Saito, Y. Maruyama, K. Ohno, Y. Kawazoe, Y. Nishina, H.W. Pickering, Y. Kuk and T. Sakurai, Phys. Rev. Lett. 71, 2959, 1993

[171] A. Tamai, A.P. Seitsonen, F. Baumberger, M. Hengsberger, Z.-X. Shen, T. Greber and J. Osterwalder, Phys. Rev. B 77, 075134, 2008

[172] B.J. Benning, F. Stepniak, J.H. Weaver, Phys. Rev. B 48, 9086, 1993; J.H. Weaver, Acc. Chem. Res. 25, 143, 1992

[173] D.W. Yan, W. Liu, H.Z. Wang, C.R. Wang, Materials Transactions 48, 700, 2007

[174] X. Yao, T.G. Ruskell, R.K. Workman, D. Sarid and D. Chen, Surf. Sci. 366, L85, 1996

[175] X. Yao, T.G. Ruskell, R.K. Workman, D. Sarid and D. Chen, Surf. Sci. 367, L743, 1996

[176] C. Tindall, O. Takaota, T. Kobayashi, Y. Hasegawa, T. Sakurai, Sci. Rep. Res. Inst. Tohoku Univ. Ser. A 44, 51, 1997

[177] T. Sakurai, X.D. Wang, Q.K. Xue, Y. Hasegawa, T. Hashitume and H. Shinohara, Prog. Surf. Sci. 51, 263, 1996

[178] E.I. Altman and R.J. Colton, Surf. Sci. 279, 49, 1992; E.I. Altman and R.J. Colton, Phys. Rev. B 48, 18244, 1993

[179] S. Von Gersum, T. Kruse and P. Roth, Ber. Bunsenges. Phys. Chem. 98, 979, 1994; E.Kolodney, B. Tsipinyuk and A. Budrevich, J. Chem. Phys. 100, 8452, 1994

[180] S.D. Leifer, D.G. Goodwin, M.S. Anderson and J.R. Anderson, Phys. Rev. B 51, 9973, 1995

[181] C. Cepek, A. Goldoni, S. Modesti, Phys. Rev. B 53, 7466, 1996

[182] V. Saltas and C.A. Papageorgopoulos, Surface Science 488, 23, 2001

[183] A.V. Hamza and M. Balooch, Chem. Phys. Lett. 201, 404, 1993

[184] D. Chen and D. Sarid, Phys. Rev. B 49, 7612, 1994

[185] S.S. Wong, W.W. Pai, C.H. Chen and M.T. Lin, Phys. Rev. B 82, 125442, 2010

[186] L.M.A. Perdigão, S.N. Sabki, J.M. Garfitt, P. Capiod, P.H. Beton, J. Phys. Chem. C 115, 7472, 2011

[187] J. Perdereau, G.E. Rhead, Surf. Sci. 24, 555, 1971; J. Wintterlin and M.-L. Bocquet, Surf. Science 603, 1841, 2009

[188] J.M. Wofford, S. Nie, K.F. McCarty, N.C. Bartelt, O.D. Dubon, Nano Lett. 10, 4890, 2010

[189] J. Lu, P.S.E. Yeo, C.K. Gan, P. Wu, K.P. Loh, Nature Nanotech. 6, 247, 2011

[190] N.C. Bartelt and K.F. McCarty, MRS Bulletin 37, 1158, 2012

[191] J.M. Wofford, S. Nie, K.F. McCarty, N.C. Bartelt, O.D. Dubon, Nano Lett. 10, 4890, 2010

[192] W. Bao, F. Miao, Z. Chen, H. Zhang, W. Jang, C. Dames, C.N. Lau, Nat. Nanotechnol. 4, 562, 2009

[193] C. Mattevi, H. Kim, M. Chhwala, J. Mater. Chem. 21, 3324, 2011

[194] X. Li, W. Cai, J. An, S. Kim, J. Nah, D. Yang, R. Piner, A. Velamakanni, I. Jung, E. Tutuc, S.K. Banerjee, L. Colombo and R.S. Ruoff, Science 324, 1312, 2009

[195] R. Tatti, L. Aversa, R. Verucchi, S. Iannotta, S. Taioli, to be submitted to Phys. Chem. Chem. Phys.

[196] E. Sacher, Langmuir 26, 3807, 2010

[197] C. Mosser, A. Mosser, M. Romeo, S. Petit, A. Decarrean, Clays and Clay Minerals 40, 593, 1992

[198] M.T. Greiner, L. Chai, M.G, Helander, W.M. Tang, Z.H. Lu, Adv. Funct. Mater. 22, 4557, 2012

[199] M. Bauer, S. Pawlik, M. Aeschlimann, Surface Science 377-379, 350, 1997

[200] H. Estrade-Szwarckopf, Carbon 42, 1713, 2004

[201] F. Sette, G.K. Wertheim, Y. Ma, G. Meigs, Phys. Rev. Lett. B 41, 9766, 1990

[202] I.V. Antonova, Phys-Usp 56, 3807, 2013

[203] M. Filippi and L. Calliari, Surf. Interface Anal. 38, 595, 2006

[204] J.A. Leiro, M.H. Heinonen, T. Laiho, I.G. Batirev, J. Electr. Spectros. & Rel. Phen. 128, 205, 2003

[205] N. Sato, Y. Saito, H. Shinohara, Chem. Phys. 162, 433, 1992

[206] A. Urbina, J.S. Park, J.M. Lee, S.O. Kim, J.S. Kim, Nanotechn. 24, 484013, 2013

[207] J.H. Kim, J.H. Hwang, J. Suh, S. Tongay, S. Kwon, C.C. Hwang, J. Wu, J.Y. Park, Appl. Phys. Lett. 103,171604, 2013

[208] K.D. Tsuei, J.Y. Yuh, C.T. Tzeng, R.Y. Chu, S.C. Chung and K.L. Tsang, Phys. Rev. B 56, 15412, 1997

[209] M.R.C. Hunt, A. Rajogopal, R. Caudano, P. Rudolf, Surf. Sci. 454-456, 267, 2000

[210] W.W Pai, H.T. Jeng, C.-H Lin, X. Xiao, A. Zhao, X. Zhang, G. Xu, X.Q. Shi, M.A. Van Hove, C.S. Hsue, , K.D. Tsuei, Phys. Rev. Lett. 104, 036103, 2010

[211] G. Xu, X.Q. Shi, R.Q. Zhang, W.W. Pai, H.T. Jeng, M.A. Van Hove, Phys. Rev. B 86, 075419, 2012

[212] A. Tamai, F. Baumberger, M. Hengsberger, J. Lobo-Checa, M. Muntwiler, M. Corso, C. Cirelli, L. Patthey, Z.-X. Shen, T. Greber, and J. Osterwalder, Phys. Rev. B 81, 045423, 2010

[213] X.-Q. Shi, M.A. Van Hove, R.-Q. Zhang, Phys. Rev. B 85, 075421, 2012

[214] D. Pontiroli, M. Aramini, M. Gaboardi, M. Mazzani, S. Sanna, F. Caracciolo, P. Carretta, C. Cavallari, S. Rols, R. Tatti, L. Aversa, R. Verucchi, M. Riccò, J. Phys. Chem. C 118, 7110, 2014

[215] S.W. Lee, C. Mattevi, M. Chhowalla and R.M. Sankaran, J. Phys. Chem. Lett. 3, 772, 2012

[216] S. Stankovich, D.A. Dikin, R.D. Piner, K.A. Kohlhaas, A. Kleinhammes, Y. Jia, Y. Wu, S.T. Ngueyen, R.S. Ruoff, Carbon 45, 1558, 2007

[217] M. Boutchich, A. Jaffrè, D. alamrguy, J. Alvarez, A. Barras, Y. Tanizawa, R. Tero, H. Okada, T.V. Thu, J.P. Kleider, A. Sandhu, J. Phys.: Conf. Ser. 433, 012001, 2013

[218] L.Jaber-Ansari, M.C. Hersam, Mat. Res. Bull. 37, 1167, 2012

[219] T. Hayashi, Y. Baba, T. Taga, A. Kishimoto, H. Takahashi, K. Tohji, Fullerenes, Nanotubes, and Carbon Nanostructures 19, 684, 2011

[220] J. Hodkiewicz, Thermo Fisher Scientific, Madison, WI, USA 2010

[221] P. Juzenas, W. Chen, Y.P. Sun, M.A.N. Coelho, R. Generalov, N. Generalova, and I.L. Christensen, Adv. Drug. Deliv. Rev. 60, 1600,2008

[222] Y. Rio, M.S. Rodriguez- Morgade, T. Torres, Org. Biomol. Chem. 6, 1877, 2008

[223] B. Ortel, C.R. Shea, P. Calzavara-Pinton, Front. Biosci. 14, 4157, 2009

[224] P. Agostinis, K. Berg, K.A. Cengel, T.H. Foster, A.W. Girotti, S.O. Gollnick, S.M. Hahn, M.R. Hamblin, A. Juzeniene, D. Kessel, M. Korbelik, J. Moan, P. Mroz, D. Nowis, J. Piette, B.C. Wilson, J. Golab, CA: Cancer J. Clin. 61, 250, 2011

[225] M.C. DeRosa, R.J. Crutchley, Coordination Chemistry Reviews, 233-234351, 2002

[226] I.J. MacDonald and T.J. Dougherty, J. Porph. Pthalocyn. 5, 105, 2001

[227] K. Berg, P.K. Selbo, A. Weyergang, A. Dietze, L. Prasmickaite, A. Bonsted, B.Ø. Engesaeter, E. Angell-Petersen, T. Warloe, N. Frandsen, A. Høgset, Journal of Microscopy 218, 133, 2005

[228] B.C. Wilson, P.J. Muller, J.C. Yanch, Phys. Med. Biol., 31, 125, 1986

[229] A.P. Castano, T.N. Demidova, M.R. Hamblin, Photodiagnosis and Photodynamic Therapy 1, 279, 2004

[230] J.A. Barreto, W. O'Malley, M. Kubeil, B. Graham, H. Stephan and L. Spiccia, Adv. Mater. 23, H18, 2011

[231] S. Wang, R. Gao, F. Zhou and M. Selke, J. Mater. Chem. 14, 487, 2004

[232] D. Bechet, P. Couleaud, C. Frochot, M.L. Viriot, F. Guillemin and M. Barberi-Heyob, Trends in Biotechnology 26, 612, 2008

[233] M.L. Hans, A.M. Lowman, Current Opinion in Solid state and Materials Science 6, 319, 2002

[234] I. Grizzi, H. Garreau, S. Li, M. Vert, Biomaterials 16, 305, 1995

[235] D. Avnir, S. Braun. O. Lev, O. Ottolenghi, Chem. Mater. 6, 1605, 1994

[236] T.K. Jain, I. Roy, T.K. De, A.N. Maitra, J. Am. Chem. Soc. 120, 11092, 1998

[237] I. Roy, T.Y. Ohulchanskyy, H.E. Pudavar, E.J. Bergey, A.R. Oseroff, J. Morgan, T.J. Dougherty, and P.N. Prasad, J. Am. Chem. Soc. 125, 7860, 2003

[238] D.C. Hone, P.I. Walker, R. Evans-Gowing, S. FitzGerald, A. Beeby, I. Chambrier, M.J. Cook and D.A. Russell, Langmuir 18, 2985, 2002

[239] P. Juzenas, W. Chen, Y.P. sun, M.A.N. Coelho, R. Generalov, N. Generalova, and I.L. Christensen, Adv. Drug. Deliv. Rev. 60, 1600,2008

[240] P. Alivisatos, Pure Appl. Chem. 72, 3, 2000

[241] B. Dubertret, P. Skourides, D.J. Norris, V. Noireaux, A.H. Brivanlou, A. Libchaber, Science 298, 1759, 2002

[242] A.C.S. Samia, X. Chen and C. Burda, J. Am. Chem. Soc. 125, 15736, 2003

[243] W. Chen and J. Zhang, J. Nanosci. Nanotechnol. 6, 1159, 2006

[244] P.A. Rodnyi, *Physical Processes in Inorganic Scintillators*, CRC Press, NY, 1997; C. van Eijk, Phys. Med. Biol. 47, R85, 2002

[245] S. Tabassum, W.M. Al-Asbahy, M. Afzal, F. Arjmand, R.H. Khan, Mol. BioSyst. 8, 2424, 2012

[246] P. Gómez-Romero and C. Sanchez, *Functional Hybrid Materials*, Wenheim: Wiley-VCH, 2004

[247] Coletti C, M.J. Jaroszeski, A. Pallaoro, A.M. Hoff, S. Iannotta and S.E. Saddow, *Proc. 29th Annu. Int. Conf. IEEE EMBS* vol. 5849, 2007

[248] S.E. Saddow, C. Frewin, M. Reyes, J. Register, M. Nezafati, S. Thomas, ECS Trans. 61, 101, 2014

[249] R. Yakimova, R.M. Jr Petoral, G.R. Yazdi, C. Vahlberg, A. Lloyd Spetz and K. Uvdal, J. Phys. D: Appl. Phys. 40, 6435, 2007

[250] C.L. Frewin, M. Jaroszeski, E. Weeber, K.E. Muffly, A. Kumar, M. Peters, A. Oliveros and S.E. Saddow, J. Mol. Recognit. 22, 380, 2009

[251] P. Prete, *Nanowires*, Vukovar: Intech, Rijeka, Croatia, 2010

[252] S. E. Saddow, Silicon Carbide Biotechnology: A Biocompatible Semiconductor for Advanced Biomedical Devices and Applications, Elsevier LTD, UK, 2011

[253] C. Louis, S. Roux, G. Ledoux, C. Dujardin, O. Tillement, B.L. Cheng, P. Perriat, Chemical Physics Letter 429, 157, 2006

[254] F. Fabbri, F. Rossi, G. Attolini, G. Salviati, S. Iannotta, L. Aversa, R. Verucchi, M. Nardi, N. Fukuta, B. Dierre and T. Sekiguchi, Nanotechnology 21, 345702, 2010

[255] Y. Goldberg, M.E. Levinshtein and S.L. Rumyantsev, *Properties of Advanced Semiconductor Materials GaN; AlN; SiC; SiGe*, ed. M.E. Levinshtein, S.L. Rumyantsev and M.N. Shur, New York: Wiley, 2001

[256] L. Skuja, J. Non-Cryst. Solids 239, 16, 1998

[257] S. Gallis, V. Nikas, M. Huang, E. Eisenbraun and A.E. Kaloyerosb, J. Appl. Phys. 102, 024302, 2007

[258] V.V. Efanas'ev, M. Bassler, G. Pensl and M.J. Schulz, J. Appl. Phys. 79, 3108, 1996

[259] F. Bechstedt, P. Kackell, A. Zywietz, K. Karch, B. Adolph, K. Tenelsen and J. Furthmuller, Phys. Status Solidi B 202, 35, 1997

[260] M.E. Pistol and C.E. Pryor, Phys. Rev. B 78, 115319, 2008

[261] L. Liu, J.Y.P. Ko, M.J. Ward, Y.M. Yiu, T.K. Sham and Y. Zhang, J. Phys.: Conf. Ser. 190, 012134, 2009

[262] F. Rossi, E. Bedogni, F. Bigi, T. Rimoldi, L. Cristofolini, S. Pinelli, R. Alinovi, M. Negri, S.C. Dhanabalan, G. Attolini, F. Fabbri, M. Goldoni, A. Mutti, G. Benecchi, C. Ghetti, S. Iannotta and G. Salviati, Sci. Rep. 5, DOI: 10.1038/srep07606

[263] B. Park, Y. Ryu and K. Yong, Surf. Rev. Lett. 11, 373, 2004

[264] SC. Dhanabalan, M. Negri, F. Rossi, G. Attolini, M. Campanini, F. Fabbri, M. Bosi, G. Salviati, Silicon Carbide and Related Materials, Materials Science Forum, 740-742, 494, 2012

[265] M. Nardi, R. Verucchi, L. Aversa, M. Casarin, A. Vittadini, N. Mahne, A. Giglia, S. Nannarone and S. Iannotta, New J. Chem. 37, 1036, 2013

[266] K. Diller, F. Klappenberger, M. Marshall, K. Hermann, A. Nefedov, Ch. Wöll and J.V. Barth, J. Chem. Phys. 136, 014705, 2012

[267] J.P. Sharma, Comprehensive Biology, Laxmi Publications (P) LTD, New-Delhi, 2014

[268] F.J. Himpsel, F.R. McFeely, A. Taleb-Ibrahimi, J.A. Yarmoff, Phys. Rev. B 38, 6084, 1988

[269] J. Pereira, L.E. Pichon, R. Dussart, C. Cardinaud, C.Y. Duluard, E.H. Oubensaid, P. Lefaucheux, M. Boufnichel and P. Ranson, Appl. Phys. Lett. 94, 071501, 2009

[270] K.L. Mittal, H.R. Anderson, Acid-base interactions: relevance to adhesion science and technology, Vol. 2, VSP, 1991

[271] L. Scudiero, D.E. Barlow, U. Mazur, K.W. Hipps, J. Am. Chem. Soc., 123, 4073, 2001

[272] N. Papageorgiou, Y. Ferro, E. Salomon, A. Allouche, J. M. Layet, L. Giovanelli, G. Le Lay, Phys. Rev. B, 68, 235105, 2003

[273] E.J. Baerends, G. Ricciardi, A. Rosa, S.J.A. van Gisbergen, Coord.Chem. Rev., 230, 5, 2002

[274] S.R. Abramson, R. Baer, L. Kronik, Phys. Rev. B 84, 075144, 2011

[275] J. Mizsei, Vacuum 67, 59, 2002

[276] D.C. Qi, W. Chen, X. Gao, L. Wang, S. Chen, K.P. Loh, A.T.S. Wee, J. Am. Chem. Soc. 129, 8084, 2007

[277] S. Ustaze, R. Verucchi, S. Lacombe, L. Guillemot, and V. A. Esaulov, Phys. Rev. Lett. 79, 3526, 1997

[278] L. Grzadziel, M. Krywiecki, H. Peisert, T. Chassé, J. Szuber, Org. Elect. 13, 1873, 2012

[279] A. Pignedoli, CA Pignedoli, G. Di Santo, C. Castellarin-Cudia, E. Magnano, F. Bondino, A. Verdini, D. Passerone, ACS Nano 6, 10800, 2012

[280] V. Palermo, M. Palma, Z. Tomovic´, M.D. Watson, R. Friedlein, K. Mullen, P Samorì, ChemPhysChem 6, 2371, 2005

[281] D.A. Egger, E. Zojer, J. Phys. Chem. Lett. 4, 3521, 2013

[282] T. Nishi, K. Kanai, Y. Ouchi, M.R. Willis, K. Seki, Chem. Phys. Lett. 414, 479, 2005

[283] H. Ishii, N. Hayashi, E. Ito, Y. Washizu, K. Sugi, Y. Kimura, M. Niwano, Y. Ouchi, K. Seki, Phys. Stat. Sol. A, 201, 1075, 2004

[284] F. Fabbri, F. Rossi, M. Negri, R. Tatti, L. Aversa, S.C. Dhanabalan, R. Verucchi, G. Attolini and G. Salviati, Nanotechnology 25, 185704, 2014

[285] M. Nardi, R. Verucchi, C. Corradi, M. Pola, M. Casarin, A. Vittadini, S. Iannotta, Phys. Chem. Chem. Phys. 12, 871, 2010

[286] Y.Y. Choi, S.J. Park, Y. Kim and D.J. Choi, CrystEngComm. 14, 5552, 2012

[287] H.J. Fitting, J. Lumin. 129, 1488, 2009; C.M. Chen, H.C. Pan, D.Z. Zhu, J. Hu and M.Q. Li, Nucl. Instr. Meth, Phys. Res. B 159, 81, 1999

[288] M.A. Elmasry, A. Gaber and E.M.H. Khater, J. Therm. Anal. Calorim. 52, 489, 1998; J. Szekely and C.I. Lin, Metall. Mater. Trans. B 7, 493, 1976

[289] L. Skuja, J. Non-Cryst. Solids 239, 16, 1998

Ringraziamenti

Siamo giunti alla fine di questa importante avventura durata tre anni ed il primo pensiero va a tutte le persone che ho conosciuto e con cui ho avuto la fortuna di lavorare in questo periodo all'IMEM-CNR di Trento.

Vorrei ringraziare per questo il mio relatore, Dott. Salvatore Iannotta, per avermi accolto in questo gruppo, dandomi la possibilità di affacciarmi ad un mondo per me completamente sconosciuto, quale quello delle spettroscopie, e per i suoi preziosi consigli ed incoraggiamenti nei momenti di confusione.

Un ringraziamento particolare va a Roberto, per tutto quello che mi ha insegnato e per avermi guidato in questi anni aiutandomi a crescere. Il mio grazie non è solo per la sua grande professionalità, ma anche per la bella persona che si è sempre rivelata, incoraggiandomi in ogni cosa, nonostante le difficoltà e aumentando la voglia di continuare questo lavoro con sempre più passione. Un grazie di cuore a Lucrezia e Giovanni, che mi sopportano tutti i giorni in ufficio, per il loro aiuto e la loro pazienza e per la bellissima amicizia che si è instaurata.

Un grazie a Claudio, per la sua grande disponibilità e per l'avermi insegnato tutto sui sistemi da vuoto. Un grazie a Marco, per le sue ventate di positività del venerdì, a Matteo, per essersi dimostrato un amico sempre pronto ad ascoltarmi ed a Tullio, per la sua disponibilità. Non posso poi non ringraziare Marina e Monica, che con il loro prezioso contributo mi hanno aiutato a sopravvivere nel caos della burocrazia.

Vorrei inoltre ringraziare tutti i gruppi con cui ho avuto il grande piacere di collaborare in questi anni: Dott. G. Salviati ed i suoi collaboratori, Francesca e Filippo (IMEM-CNR, Parma), Dott. Bosi e Dott. Attolini (IMEM-CNR Trento), Prof. G. Cristofolini (Università di Parma), Dott. M. Riccò e Dott. D. Pontiroli (Università di Parma), Prof. E. Dalcanale (Università di Parma), Dott. Cassinese (Università di Napoli "Federico II"), Dott. G. Carotenuto e Dott.ssa A. Longo (IPCB-CNR, Napoli), Prof. N. Pugno (Università di Trento), Dott.ssa A. Sanson (ISTEC-CNR, Faenza), Dott. S. Taioli (LISC-FBK, Trento), Dott. G. Speranza (CMM-FBK, Trento) e Dott. G. Baldi (IMEM-CNR, Parma).

E poi c'è la mia famiglia, e non ci sono parole per spiegare il grande amore e la grande riconoscenza verso ognuno di loro, a partire dai miei genitori e poi le mie sorelle e le loro bellissime famiglie. Un grazie non basta per tutto quello che mi hanno insegnato e per

quello che mi regalano ogni giorno: il loro affetto, il loro appoggio e la certezza che ci saranno sempre, nonostante le distanze.

Ora che questo percorso è finito, guardo al futuro e non posso che sperare di continuare questo sogno, quello di fare ricerca, e nonostante le difficoltà che mi aspettano, continuerò ad alimentare questa grande passione e come diceva Rita Levi Montalcini "Pensate al futuro che vi aspetta, pensate a quello che potete fare, e non temete niente".